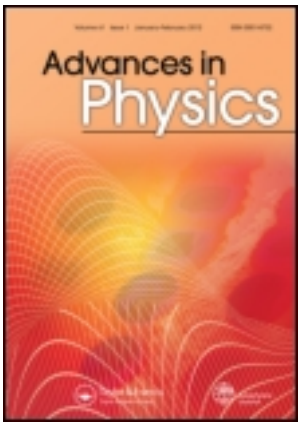

Advances in Physics
Publication details, including instructions for authors and subscription information:
http://www.tandfonline.com/loi/tadp20

Friction and energy dissipation mechanisms in adsorbed molecules and molecularly thin films

Jacqueline Krim [a]
[a] Physics Department, North Carolina State University, Raleigh, NC, 27695, USA
Version of record first published: 13 Aug 2012.

To cite this article: Jacqueline Krim (2012): Friction and energy dissipation mechanisms in adsorbed molecules and molecularly thin films, Advances in Physics, 61:3, 155-323

To link to this article: http://dx.doi.org/10.1080/00018732.2012.706401

Advances in Physics
Vol. 61, No. 3, May–June 2012, 155–323

Taylor & Francis
Taylor & Francis Group

REVIEW ARTICLE

Friction and energy dissipation mechanisms in adsorbed molecules and molecularly thin films

Jacqueline Krim*

Physics Department, North Carolina State University, Raleigh, NC 27695, USA

(*Received 21 June 2012; final version received 22 June 2012*)

This review provides an overview of recent advances that have been achieved in understanding the basic physics of friction and energy dissipation in molecularly thin adsorbed films and the associated impact on friction at microscopic and macroscopic length scales. Topics covered include a historical overview of the fundamental understanding of macroscopic friction, theoretical treatments of phononic and electronic energy dissipation mechanisms in thin films, and current experimental methods capable of probing such phenomena. Measurements performed on adsorbates sliding in unconfined geometries with the quartz crystal microbalance technique receive particular attention. The final sections review the experimental literature of how measurements of sliding friction in thin films reveal energy dissipation mechanisms and how the results can be linked to film-spreading behavior, lubrication, film phase transitions, superconductivity-dependent friction, and microelectromechanical systems applications. Materials systems reported on include adsorbed films comprised of helium, neon, argon, krypton, xenon, water, oxygen, nitrogen, carbon monoxide, ethane, ethanol, trifluoroethanol, methanol, cyclohexane, ethylene, pentanol, toluene, tricresylphosphate, *t*-butylphenyl phosphate, benzene, and iodobenzene. Substrates reported on include silver, gold, aluminum, copper, nickel, lead, silicon, graphite, graphene, fullerenes, C60, diamond, carbon, diamond-like carbon, and $YBa_2Cu_3O_7$, and self-assembled monolayers consisting of tethered polymeric molecules.

PACS: 68.35.Af Atomic scale friction, 68.43.Jk Diffusion of adsorbates, kinetics of coarsening and aggregation, 68.43.Pq Adsorbate vibrations, 81.40.Pq Friction, lubrication, and wear, 63.22.Kn Clusters and nanocrystals, 46.55.+d Tribology and mechanical contacts

Keywords: nanotribology; adsorbed films; electronic friction; phononic friction; electrostatic friction; physical adsorption; chemical adsorption; energy dissipation; nano-lubrication; quartz crystal microbalance; diffusive Brownian motion

Contents

*Email: jkrim@ncsu.edu

ISSN 0001-8732 print/ISSN 1460-6976 online

http://dx.doi.org/10.1080/00018732.2012.706401
http://www.tandfonline.com

List of Acronyms

AFM	atomic force microscope
CNT	carbon nanotubes
DLC	diamond-like carbon
EELS	electron energy loss spectroscopy
FEM	field emission microscopy
FFM	frictional force microscopy
FIM	field ion microscopy
FM	frequency modulation
HAS	helium atom scattering
HeSE	helium spin echo
IRAS	infrared adsorption spectroscopy
LEED	low-energy electron diffraction
LFM	lateral force microscopy
LITD	laser-induced thermal desorption
LOD	linear optic diffraction
MD	molecular dynamics
MEMS	microelectromechanical systems
MFT	mesoscale friction tester
MWCNT	multi-walled carbon nanotubes
NEMS	nanoelectromechanical systems
OTS	octadecyl-trichlorosilane
PEEM	photoemission electron microscopy
PFPE	perfluoropolyether
PFTS	perfluorodecyl-trichlorosilane
PSD	position sensitive detector
QHAS	quasi-elastic helium atom scattering
QCM	quartz crystal microbalance
QSE	quantum size effects
QWS	quantum well states

SAMs	self-assembled monolayers
SFA	surface forces apparatus
SHD	second harmonic diffraction
STM	scanning tunneling microscopy
TBBP	*t*-butylphenyl phosphate
TCP	tricresylphosphate
TFE	triflouroethanol
UHV	ultra-high vacuum

List of Symbols

A	area of the crystal
$\vec{A}$	amplitude of oscillation
A_c	area of contact
a	substrate lattice constant
a_c	area of the two-molecule unit cell
α	decay constant
B_{tot}	total viscous drag
b	vector defining the placement of the dislocations
C_m, C_l	capacitance per unit length of comb-drive actuators of main and loading shuttles
C_{sense}	capacitance per unit length of the sense combs
D	self-diffusion constant
D_i, D_s	island and spreading diffusion coefficient
d	thickness of the metal film
d_{nn}	nearest-neighbor distance of the substrate atoms
ΔK	parallel momentum transfer of the beam
$\Delta\rho$	adsorbate-induced increase in film resistivity
δA_c	average area occupied per particle
E_b	adsorbate binding energy
E_d	energy barrier
e	electron charge
ε	depth of the potential well
η	viscous friction damping parameter
η_3	bulk fluid viscosity
F	friction
F_C	critical force
F_{ext}	external force
F_f	force of friction
F_k	kinetic friction
f	frequency of the crystal
f_0	fundamental frequency of the crystal
f_i	fluctuating force due to thermal effects
g	reciprocal lattice vectors
γ_A, γ_B	surface tension of solid and liquid
γ_{AB}	interfacial tension
h	Planck's constant
κ	attempt frequency

k	force constant
k_{F}	Fermi wave vector
k_{m}, k_{l}	spring constant of the main and loading shuttle's folded flexures
L_{ov}	distance between the sliding layer and the substrate
l	length
$\hat{l}_{\beta}$	unit vectors of the molecular axis
λ	slip length
m	adsorbate mass
m_{q}	mass of the quartz crystal
N	normal load
N_{e}	number of conduction electrons
n	number of conduction electrons per unit volume
n_{a}	number of adsorbates per unit area in direct contact with the adsorbate
n_{N}	number of normal state electrons
Ω	drive frequency
ω	oscillation frequency
ω_{F}	Fermi frequency
ω_{p}	plasma frequency
ω_z, $\omega_{\|\|}$	frequencies of the frustrated translations perpendicular and parallel to the substrate
p	dipole moment of the adsorbate
ϕ	film-spreading pressure
ρ_2	mass per unit area of the adsorbed film
ρ_3	bulk density
$\vec{\rho}_{\beta}$	position of the molecules
ρ_{q}	density of quartz
Q^{-1}	inverse quality factor
q	induced charge in the substrate
r	vector in the plane of the substrate
s	stress
σ	separation distance at which the interparticle potential is zero
σ_0	bulk conductivity of the metal substrate
σ_{p}	Peierls stress
T_{m}	melting point temperature
t_{d}	decay time
t_{ph}	lifetime of the photons
t_{q}	thickness of the quartz
τ	slip time
τ_{U}	free flight time between nonconservative collision processes
θ	quadrupole moment
U	energy
U_0	surface corrugation
μ	coefficient of friction
μ_{v}	coefficient of viscous friction
μ_0	permeability of vacuum
μ_{e}, μ_{p}, μ_{subs}	electronic and phononic friction
μ_{eh}	electronic component of friction

V	adsorbate–adsorbate interaction potential
V_o, V_g	amplitudes of the constant and periodic components of the adsorbate–substrate potential
V_{bias}	constant voltage applied to the sense combs
V_{push}, V_{pull}	voltages applied to the push and pull actuators of the main shuttle
V_{load}, V_{unload}	voltages applied to the load and unload actuators of the loading shuttle
v	velocity
v_d	dislocation velocity
v_{ext}	externally imposed translational velocity
v_q	speed of sound in quartz
v_s	sliding velocity
w	width
γ	line width of the adsorbate variations
Z	number of contacts per particle
Z_f	acoustic impedance of the film
Z_m	mechanical impedance
z	height of the adsorbate with respect to the surface

1. Introduction

When an object moves along a surface or through a viscous liquid or gas, the force resisting its motion is referred to as friction. Frictional forces are nonconservative, converting the kinetic energy of materials in sliding contact to internal energy. Friction and its consequences are of great concern from both a sustainability and quality-of-life point of view, and the economic impact is massive. Indeed, by one estimate, improved attention to tribology (the study of friction, lubrication, and wear) would save developed countries up to 1.6% of their gross national product [1], or close to $225 billion annually in the USA alone.

Irrespective of whether the application involves length scales associated with turbine engines or nanogears, a complete understanding of friction will be attained only through probing dissipative phenomena at the atomic scale. This is where the kinetic energy associated with relative motion at interfaces is transferred into thermal energy and where a first principles' understanding of dissipative mechanisms originates. Investigations of friction ideally involve characterization of the sliding interface not only at atomic length scales, but at atomic time scales as well. Adsorbed films, whether in the form of intentionally applied lubricants or physisorbed contaminants, are ubiquitous at interfaces and must be taken into account by all realistic treatments of the topic [2,3]. It is well known that adsorbed films in the form of lubricants can greatly reduce friction forces between sliding surfaces, but less studied is the fact that they have been implicated in producing static friction and jamming effects. Although studies of the atomic-scale origins of friction have traditionally been quite challenging, experimental and theoretical techniques have emerged in recent years that allow examination of friction at atomic scales that have heretofore been inaccessible. An era of science and engineering is thus emerging where control of mechanical and electrical systems at the atomic level will be the new focus. While the exact form of tomorrow's electronics and machinery remains unclear, the impact of molecularly thin adsorbed films is a certainty.

This review focuses on recent advances that have been achieved in understanding the basic physics of frictional phenomena in adsorbed films and the associated impact on friction at microscopic and macroscopic length scales (Figure 1). Measurements performed on adsorbates

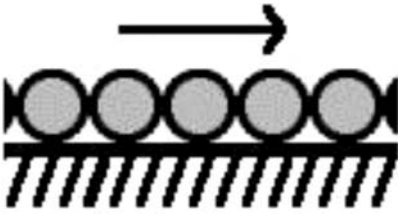

Figure 1. Simplest geometry of adsorbed film particles sliding on a solid substrate, the primary focus of this review.

sliding in unconfined geometries with the quartz crystal microbalance (QCM) technique receive particular attention, as the information is unavailable elsewhere in a compiled form. The review begins with a brief historical overview of progress in fundamentals of macroscopic friction, followed by three introductory examples to demonstrate the scope of applications that are impacted by studies of adsorbed film friction. Section 2 covers experimental techniques that are capable of measuring dissipative phenomena in adsorbed films and related geometries, as well as highlights how measurements of sliding friction in thin films are linked to experimental techniques that probe spreading, lubrication, and diffusive phenomena. Section 3 covers theoretical treatments of thin-film dissipative phenomena, with a focus on first principles' derivations based on phononic and electronic energy dissipation mechanisms. Literature reports (both numerical and experimental) of friction in specific thin-film systems are reviewed in Section 4 and are categorized by the material system studied. The reader is referred to the list of reviews on closely related topics compiled at the end of this section for further reading, as well as to current monographs on sliding friction [4–6].

1.1. *Fundamentals of macroscopic friction*

Modern study of friction began at least 500 years ago, when Leonardo da Vinci recorded in unpublished notebooks the laws governing the motion of a rectangular block sliding over a planar surface [7] (Figure 2). But the friction between two macroscopic solid objects is virtually always discussed within the context of "Amontons' law" [8]

$$F = \mu N, \tag{1}$$

which was published hundreds of years later. The normal load N in Equation (1) is the force that presses surfaces in sliding contact together and μ is the coefficient of friction. Amontons also reported that the friction force did not depend on the apparent area of contact: a small object encounters as much friction as a large block of the same material so long as their weights are equal. A third well-known law, attributed to Coulomb (who is better known for his work on electrostatics), states that the friction force is independent of velocity for the ordinary sliding speeds [9]. Coulomb, who did not have the benefit of atomic-scale knowledge of surface morphology, or even the knowledge that atoms existed, was particularly interested in the fundamental origins of friction and whether it might arise from interlocking asperities and surface roughness. He was able to rule this out as a viable mechanism however, since the energy gained in lifting a surface over an asperity can be completely regained when dropping it back down. The idea that increased surface roughness will increase friction persisted nonetheless well into the 1970s before being definitively discounted by surface science experiments, demonstrating that films of one-molecule thick can substantially change friction, while having minimal impact on surface roughness. A macroscopic analog of this effect is easily demonstrated by comparing the friction of onions with and without the thin outer layer removed. While the overall shape and mass is virtually unchanged, the friction

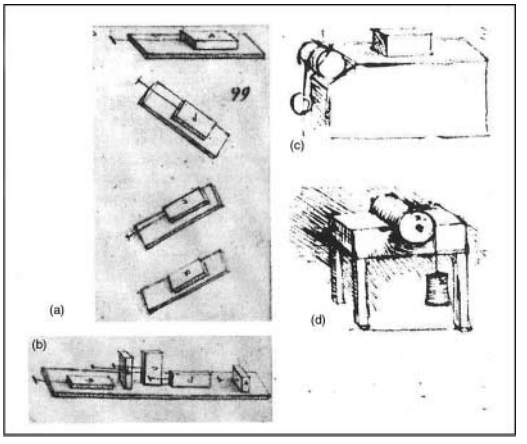

Figure 2. Leonardo da Vinci's sketch from the *Codex Atlanticus* and *Codex Arundel* showing: (a) the force of friction between horizontal and inclined planes, (b) the influence of macroscopic apparent contact area on friction, (c) a friction force measurement horizontal plane using a weight and a pulley, and (d) measurements of frictional torque on a roller and half bearing.

coefficient of a peeled onion can be six or more times greater than before it was peeled, despite having nominally the same roughness.

Improvements in ultra-high vacuum (UHV) technology throughout the 1950s to 1970s redefined the concept of surface roughness and crystallinity [10–14] and allowed preparation of unprecedented, well-characterized crystalline surfaces, frequently covered with well-characterized films. Three major advances that occurred in this period include: (1) the development and construction of routinely demountable vacuum-tight metallic enclosures in which residual pressures between 10^{-9} and 10^{-10} Torr could be established and maintained without excessive difficulty; (2) the use of these enclosures to perform the elemental analysis of the constituents of a surface by means of Auger electron spectroscopy [15]; and (3) the deployment of the diffraction of low-energy electrons (LEED) for structural studies of single-crystal surfaces. A great number of LEED/Auger studies were carried out starting in the 1970s on the structure of a wide range of single-crystal surfaces and the two-dimensional phases of atoms and molecules adsorbed on them [16–18].

During the same time, Tabor and Winterton developed the first apparatus where forces between surfaces could be measured for separations as little as 5–30 nm [19,20]. The technique was adapted by Israelachvili and Tabor for friction measurements 5 years later in 1973 [21]. Employing this newly developed surface forces apparatus (SFA) technique, it was established that friction at a sliding crystalline interface could be present in the complete absence of wear. A major discovery followed years later with the discovery by means of an SFA that friction correlated with adhesion hysteresis, rather than adhesion itself [22]. The collective results ushered in a new era of detailed studies of the mechanisms of friction in well-controlled interfaces separated by molecularly thin lubricant films ([20] and references therein) [23–25]. Measurements with the SFA established that when two surfaces touch each other, the actual microscopic area of contact A_c is much less than the apparent macroscopic area. The vast majority of surfaces are not atomically flat, and when two such surfaces touch, contact between them takes place only at their asperities. Although A_c is typically 10,000 times less than the apparent contact area, many asperities do come into contact and locally they exhibit very high yield stresses, not unlike tiny cold welds. The result is that while friction is independent of *apparent* (macroscopic) contact area, it is in fact proportional to *true* contact area. Macroscopic tribological behavior is, therefore, highly sensitive to the details of

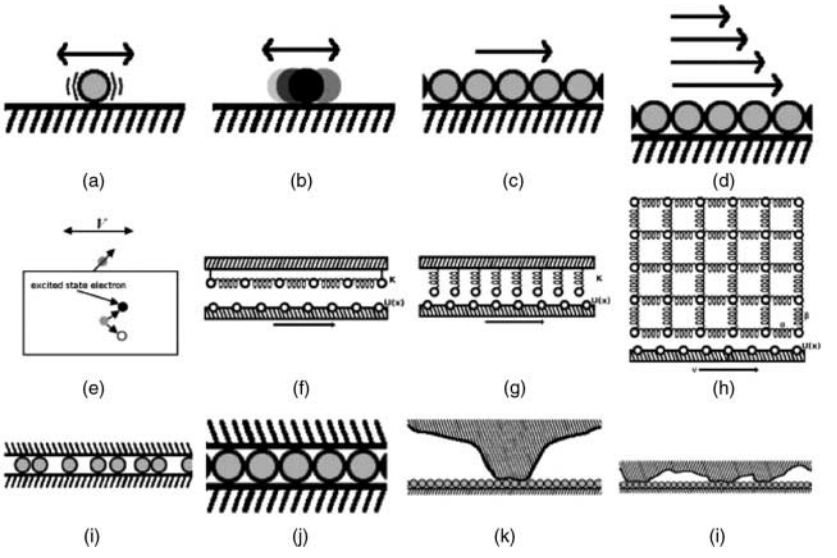

Figure 3. Sliding friction geometries spanning atomic (a) to macroscopic (l) configurations. (a) Atomic vibration, (b) diffusive motion along a surface, (c) sliding of an adsorbed monolayer along a surface, (d) monolayer slippage at the interface of a solid and a bulk liquid or gas, (e) electronic contributions to friction of an adsorbate, (f)–(h) phononic models of frictional sliding, (i) disordered submonolayer coverages of confined layers, (j) confined layers at full monolayer coverages, (k) single-asperity contact, and (l) multi-asperity contact.

interfacial contact at the atomic scale, and there are many levels of geometric complexity at which frictional energy dissipation can be explored, all of which are rightly considered "fundamental" (Figure 3).

A first-principles' theory of "wearless" friction [26,27] was suggested as early as 1928 by Prandtl ([28]; translated to English by Popov in [29]), involving phononic or lattice vibration mechanisms, whose lifetimes may range from picoseconds to nanoseconds. Decades later, the model came to be known as the "Tomlinson" model, based on a 1929 paper by Tomlinson entitled "Molecular origins of friction" that focused on adhesive contributions to friction [30]. Ironically, the paper by Tomlinson in 1929 does not contain the model now known as "Tomlinson's model", but Prandtl's 1928 publication does [28]. In this review, it will be referred to as the "Prandtl–Tomlinson" model.

Tabor [14,31] attempted to experimentally document the existence of phonons, but the proper technology was not available at the time to perform experiments at suitably small length or time scales. Major advances in the atomic-scale characterization of surfaces, however, came with the development of scanning probe microscopes in the 1980s, which were quickly adapted for nonconducting surfaces and for probes of microscopic-scale friction. Inspired by the concept of phonon friction, Gary McClelland collaborated with C. Mathew Mate at IBM Almaden in the mid-1980s to measure nanometer-scale friction. They did so by adapting a newly invented instrument: the atomic force microscope (AFM), for measurements of lateral forces (LFMs). With it, they published their first observations of friction, measured atom-by-atom, in a landmark 1987 paper. Their instrument revolutionized studies of friction at atomic length scales [32]. Over the same time period, Krim *et al*. [34] recorded sliding friction measurements of krypton monolayers adsorbed on Au(111) utilizing a QCM technique. The data were modeled with molecular dynamics (MD) simulation by Robbins and coworkers, assuming that the friction was due to phonons excited in

the adsorbed layers [35]. The combined QCM and numerical results provided the first definitive evidence for the existence of a phononic mechanism for friction. Evidence for phononic friction mechanisms in an AFM geometry was first reported in 2007 [36,37].

The discovery of phononic contributions to friction was symptomatic of a renewed interest in fundamental areas of tribology that began in the late 1980s, sparked by the new experimental and theoretical techniques capable of studying the force of friction in well-defined contact geometries [38–41]. These techniques benefited directly from advances in surface science throughout the 1970s. Surface scientists new to the field of tribology now prepared well-defined interfaces in advance of the measurements rather than trying to characterize innumerable hidden interfaces. It is in this sense that mainstream tribologists are distinguished from nanotribologists. Tribologists generally seek information on the nature of the "imperfect" contact between two macroscopic objects, while nanotribologists seek to gather information in situations where the two surfaces (each frequently a single crystal) are in 100% surface contact. Nanotribologists can thus begin to address issues involving the origin of friction through direct measurements of shear stress in known contacting geometries. The dividing line between nanotribology and macroscale geometry is, however, by no means a distinct one, as demonstrated in Figure 3. Various levels of increasingly complex energy dissipation geometries are present, spanning damped motion of in-plane vibration of adatoms to lubricated multi-asperity contact. The geometry of a sliding adsorbed film falls at the crossroads between atomic and macroscale phenomena and as such is highly relevant to both regimes. The following examples demonstrate the wide range and scope of applications that motivate studies of frictional phenomena in adsorbed films.

1.2. *Introductory examples*

1.2.1. *Unconfined contact: nanoscale transport and atomic machinery*

Machine components with incredibly small dimensions are rapidly approaching the length scales routinely probed by the nanotribological community. Whether the long-range goal is to separate, deliver, assemble, or to remove materials, energy transfer issues are integral to true control of motion at the nanoscale. This is clearly apparent when considering device energy efficiency from a profitability point of view, but equally important is the fact that any frictional heat released in an inefficient transport process is available to destroy the device function: if any portion melts, the device itself is destroyed.

Consider the force $F = swl$ required to slide a carbon nanotube (CNT) of length l and contact width w along a relatively low friction surface such as graphite [42] (Figure 4). The quantity s is the surface stress assuming a quasistatic friction law, typically 2×10^6 N m^{-2} for the nanotube/graphite interface [43–46]. The force needed to manipulate a 25-nm long, 0.3-nm wide single-walled nanotube is $F = 15$ pN, and the energy lost to friction over a distance of 1000 nm is $U = Fd = 15 \times 10^{-18}$ J. The smallest manipulator system fabricated to date employ microelectromechanical system (MEMS) technology. (It is well recognized that scanning probe microscopes are far less energy efficient for directing motion. They of course plan an essential and indisputable role in characterization and development of nanomaterials.) In an ideal efficiency scenario, an energy $U = 1/2kx^2$ is expended in displacing a manipulating structure with a force constant k. Reducing k could of course lower the energy expended, but large values are usually required to maintain structural stability and high-frequency operation. For an MEMS structure with a spring constant of 3 N m^{-1}, the energy to move the nanotube 100 nm would be $U = 15$ fJ. The energy efficiency of this process is only $\sim$0.001. Practical nanoscale manufacturing processes will clearly seek additional, more efficient methods for directing motion.

One such method for directed motion of nanoscale objects has recently been reported by Porto *et al*. [47,48]. The authors have reported a theoretical design of microscopic engines on the atomic

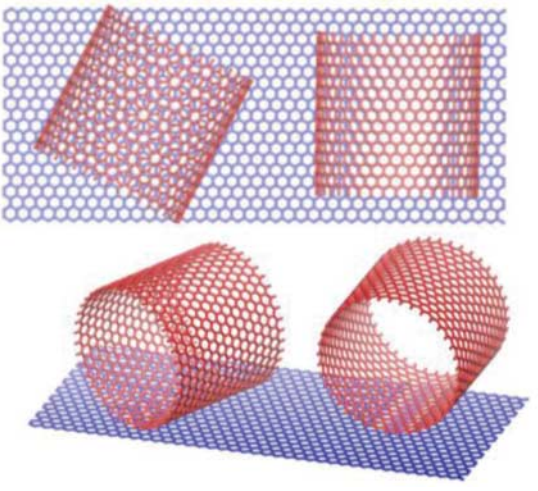

Figure 4. (color online) MD simulation of rolling of a single-wall nanotube. The orientation of the nanotube lattice with respect to the substrate will have great impact on the friction associated with its motion. These are both 40, 0 nanotubes, out of registry (left, which should slide), and in registry (right, which should roll). Image courtesy of J.D. Shall and D.W. Brenner.

scale that both translate and rotate and can perform useful functions such as the pulling of a cargo. The approach is based on the transformation of the energy fed into directed motion through a dynamical competition between the intrinsic lengths of the moving object and the supporting carrier (Figure 5).

The motor and machine components suggested by this group are driven by frictional push-off forces along a surface. In one scenario, the dynamics of a classical particle are investigated in a one-dimensional two-wave potential composed of two periodic potentials that have the same amplitude and periodicity. One of the periodic potentials is externally driven and performs a translational motion with respect to the other. If one of the potentials is of the ratchet type, translation of the potential in a given direction leads to motion of the particle in the same direction, whereas translation in the opposite direction leaves the particle localized at its original location. Moreover, even if the translation is random, but still has a finite velocity, an efficient directed transport of the particle occurs.

The nanomachines described by Porto *et al*. [47–50] bear a striking resemblance to atoms connected by springs, as treated in classical treatments of phononic friction mechanisms in adsorbed

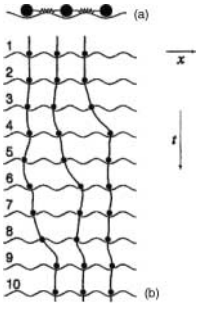

Figure 5. An atomic-scale "car". Reprinted figure with permission from M. Porto *et al.*, Physical Review Letters 84, p. 6058, 2000 [47]. Copyright (2000) by the American Physical Society.

layers. Their design illustrates how astoundingly small future machine components are envisioned and how closely one must monitor energy dissipative processes in order to assure a viable system. The authors are quick to point out, however, that the actual "cars" built according to their design concepts need not be atomic in scale, as the general concept scales up in size to the mesoscale. The approach makes use of the nonlinear properties of friction, which can be achieved by superimposing time-dependent external fields that break the spatial symmetry. The motion can be controlled and optimized by adjusting the system parameters, which clearly includes the frictional shear stress between the machines and the substrates over which they travel.

Given that the shear stresses associated with the sliding of adsorbed films on surfaces can vary by many orders of magnitudes, knowledge of the frictional energy dissipation of atoms and very small "objects" is a key element of successful design of these future machines. Indeed, physisorbed molecules and their diffusive properties are becoming increasingly prominent in the emerging arena of nanoelectromechanical systems (NEMS) [51–54].

1.2.2. *Confined contact: static friction and jamming effects*

Stick–slip phenomena are frequently blamed for excessive interfacial wear rates and as such have received much attention from the mainstream tribological community. The key to understanding static friction and stick–slip phenomena appears to lie buried in the atomic-scale structure of the myriad of contacts formed between the two sliding surfaces and, in particular, the nature of adsorbed molecules confined between them [55–57].

One question that is routinely raised involves how static friction can be so ubiquitous when two clean interfaces in sliding contact are not theoretically expected to exhibit it. The answer may involve "third body" effects, whereby additional adsorbed molecules act to initially pin the interface. Robbins, Muser, and coworkers have published a series of articles suggesting that static friction is related to adhesive forces of thin adsorbed films (water, hydrocarbons, etc.), known to be present on most surfaces [55,58–60] (Figure 6). They have demonstrated with computer simulations that these ubiquitous films behave like particles which roll or migrate to the open niches of an incommensurate interface composed of irregular topologies. The particles always find a local energy minimum, so it always takes some energy to initiate sliding. The effect can be thought of as a microscopic analog of a glass transition, whereby a system develops mechanical rigidity with either cooling or compression (Figure 7). In the absence of contamination, numerical studies have also revealed that the degree of commensurability arises from a competition between interfacial and elastic interactions and depends sensitively on the size of the contact [61]. Friction in this case increases with decreasing cluster size and the clusters eventually become pinned at a critical size (Figure 8).

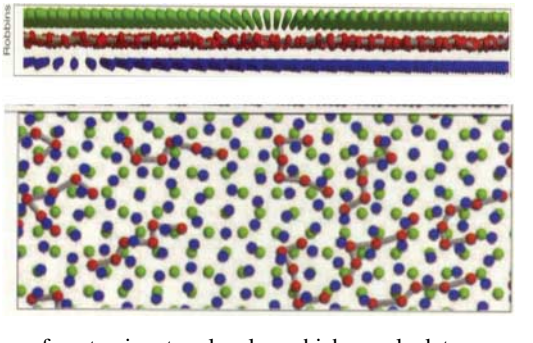

Figure 6. Top and side views of contaminant molecules, which may lock two macroscopic surfaces together resulting in the occurrence of static friction. Image courtesy of M.O. Robbins.

Figure 7. (color online) Stacks of fruit provide macroscopic examples of the impact of friction on jamming phenomena. On the left, the unpeeled onions provide a weak foundation for the apples and oranges higher up in a tilted fruit tray. Next to the left, after removal of just one onion from the base, the pile becomes unjammed and almost all the constituents fall off. A pile whose base is made of peeled onions remains jammed after numerous constituents are removed, an effect which is directly attributable to higher friction levels. Reprinted figure with permission from J. Krim *et al.*, Physics Today 62, p. 66, 2009 [626]. Copyright (2009) by the American Institute of Physics.

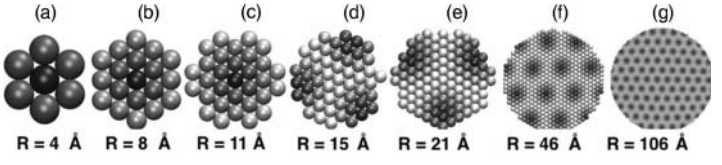

Figure 8. Equilibrium structures of a Kr island on Cu(111). The grayscale is indicative of particle distance from the minima of the substrate potential. The friction of the adsorbed clusters is found to decrease with size, and below a critical size, the island become commensurate and pinned to the substrate. Reprinted figure with permission from M. Reguzzoni and M. C. Righi, Physical Review B 85, art#201412(R), 2012 [61]. Copyright (2012) by the American Physical Society.

Experimental determination of the structure of films trapped between solid surfaces, and not just the structure of the surface contact points, thus remains one of the most important goals of both the macro- and nanotribological communities [62,63].

1.2.3. *Multiasperity contact: macroscopic blocks on planes*

Consider a block on a substrate sliding on a monolayer of adsorbed atoms or molecules that is sliding at a constant speed v and pushed by an external force F_{ext}. The substrate may have been intentionally lubricated with a molecularly thin film, as is the case in hard-disk drive technology, or it may simply be "lubricated" by ever-present atmospheric species (water, hydrocarbons, etc.). The block is not accelerating, so the same force must be acting on the lubrication layer, and an equal but oppositely directed frictional resistance force will be present. If A_{c} is the area of contact, then the block will act with a tangential stress $s = F_{\text{ext}}/A_{\text{c}}$ on the lubrication layer and with a corresponding average value of $s\delta A_{\text{c}}$ per lubrication particle, where δA_{c} is the average area occupied per particle. Figure 8 from [64] depicts three fundamental energy dissipation mechanisms associated with asperity sliding on a film-covered surface: phononic molecular vibrations, conduction electron drag forces, and electrostatic friction associated with electrostatic effects (Figure 9). This review focuses primarily on the friction of film constituents on the open surface: this is intimately related to how the contact is supplied with lubricant and whether a film will be squeezed out of a contact.

In a mean field treatment, it is common to remove the block and replace it by the shear stress applied to the film. Correct from a mathematical point of view, the frictional forces associated with films adsorbed on open surfaces vary radically, however, in both functional form and magnitude from their confined counterparts. The block, moreover, is in contact with the substrate at only a small fraction of the apparent contact area, typically less than 1%, so the system as a whole involves a combination of films adsorbed on surfaces that are in both open geometries and confined between asperity contacts. This interfacial region is not only extremely difficult to characterize,

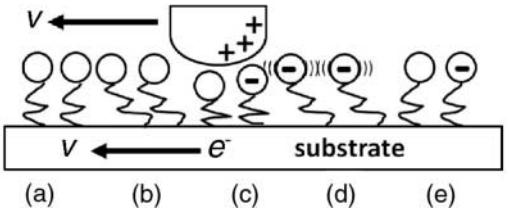

Figure 9. Schematic of phononic, conduction electron, and electrostatic tribo-electric friction mechanisms for surface molecules excited by an AFM tip sliding at speed V. Phononic friction mechanisms are molecular vibrations excited by the passing asperity that damp away after it passes (a)–(e). For conducting materials, conduction electronic effects such as electron–hole pair creation or electron wind drag effects may result in frictional energy dissipation as electrons are dragged along with the asperity. (a)–(c) For insulating materials, contact electrification and subsequent charge transfer to the passing tip result in large electrostatic frictional forces (c)–(e). Studies of the latter effect are quite challenging, yet increasingly important, if all contributions are to be accounted for. Reprinted figure with permission from I.B. Altfeder *et al.*, Journal of Applied Physics 111, art#094916, 2012 [64]. Copyright (2012) by the American Institute of Physics.

but is also continuously evolving as the microscopic irregularities of the sliding surfaces touch and push into one another. The constant changing of the nature of the interfacial geometry of the contacting areas gives rise to variations in friction coefficients and sliding events. Moreover, the friction force at an individual asperity may or may not increase with applied load, depending on the structure of the contacting solids, and molecules confined within them. Small changes in film coverage meanwhile can be associated with large changes in frictional energy dissipation levels. Knowledge of their frictional properties is therefore a key element to a fundamental understanding of overall system behavior.

A comprehensive treatment of the fundamental origins of energy dissipation in adsorbed films and their impact on sliding friction is clearly a wide-ranging topic with many closely related areas of research interest. Experimental and theoretical methods will be reviewed in Sections 2 and 3, with results presented in Section 4 categorized according to the material systems studied. This section ends with a list of selected reviews on closely related topics that provide detailed information on areas that the reader may wish to explore in further detail.

1.3. *Review articles on closely related topics*

1.3.1. *Adatom vibrations*

Chabal *et al*. [65]: This review describes major experimental vibrational-spectroscopic techniques (i.e. infrared absorption, Raman scattering, high-resolution electron loss, helium atom scattering, and sum frequency generation) along with selected results. Particular emphasis is given to (a) complex surface reactions and (b) vibrational adatom dynamics with an emphasis on energy dissipation at surfaces.

Tobin [66]: This review examines experimental and theoretical developments that explain adsorbate effects on electronic conduction in metals, with applications in nanotechnology, chemical sensing, and tribology. Specific quantitative predictions regarding the optical effects of surface resistivity are compared to current experimental results, and a discussion of which aspects of theory are confirmed, and which are not.

1.3.2. *Diffusion*

Barth [67] has reviewed the theoretical and experimental literature on aspects and evolution of surface diffusion, with an emphasis on nonmetallic adsorbates at metal surfaces. The main

experimental values are tabulated, and both theoretical and experimental studies on transient mobility in the adsorption of gases on metal surfaces are summarized. See also [53].

1.3.3. *Adsorbed monolayers*

Krim [14,68] described the historical origins of the field of nanotribology, with an emphasis on how surface science has influenced our understanding of friction and a list of resources on tribology at all length scales.

Braun and Naumovets [69] reviewed recent progress in nanotribology, with a focus on MD simulation of tribological systems from the perspective of surface science and physics. The main goal of this review is to connect recent MD results with experiment.

Dedkov [70] has reviewed experimental and theoretical studies of nanotribology pertaining to investigations of atomic-scale friction, adhesion, wear, and lubrication. A major focus of the work involves "dry" adhesion friction between the tip of an AFM and an atomically smooth surface. However, many other physical effects are considered as well, including tribochemistry, triboemission of particles, and conduction in metallic nanocontacts. In addition, an overview of theoretical results for static and dynamical (velocity-proportional) friction are discussed, as well as some results obtained using the computer simulations.

Bruch *et al*. [71] reviewed progress in the field of physisorption. Advances in the knowledge of microscopic structures and interactions of weakly bound adsorbates are reviewed, focusing on the adsorption sites of rare gases on flat metal surfaces and at surface steps, the structures of higher-order commensurate solids, collective excitations in rare-gas monolayers, molecular orientations, and growth processes in alkane films, and adsorbate diffusion. Experimental techniques are thoroughly reviewed, including high-resolution thermal desorption spectroscopy and ellipsometry for studying thermodynamics; low-temperature scanning tunneling microscopy (STM), very low current electron diffraction, and surface X-ray diffraction for studying structures; inelastic atom scattering for studying collective excitations; quasielastic helium atom and neutron scattering and laser techniques for studying diffusion; and the QCM for studying interfacial friction. Finally, the present state of knowledge for physical adsorption potentials and the role of the van der Waals interaction are discussed in the context of the widespread use of density-functional theory. Experimental and theoretical results for many adsorption systems are described and tabulated.

1.3.4. *Confined monolayers*

Muser *et al*. [55] provided an extensive and systematic review of the statistical mechanics of friction in the slow sliding and static regime, focusing on static and stick–slip phenomenon and the impact of mobile adsorbed species on system response.

Christenson [72] has written an extensive review of experimental work on freezing and melting in confined geometries, with a thorough treatment of SFA studies of shear force measurements of thin films (see also [20,73] for reviews of SFA). Chaudhury [74] has also reviewed the topic of studies of friction studies in SFA geometries with an emphasis on the role of self-assembled organic layers. See also [75].

1.3.5. *Asperity contacts*

Szlufarska *et al*. [76] reviewed recent advances in the experimental, theoretical, and computational studies of single-asperity nanotribology, with a strong focus on the latest developments in AFM and MD simulations and their applications. This is an extensive review and a must-read for up-to-date and detailed information on the status of single asperity, particularly AFM studies of sliding friction (see also [77,78]).

Quasicrystalline systems provide unique settings for studies of the impact of interfacial commensurability on sliding friction. Park and Thiel [79] highlighted recent studies of the atomic-scale friction and adhesion properties of quasicrystals. Their review focuses on tribological studies carried out in different mechanical regimes (elastic and inelastic) and at different length scales (macroscale and nanoscale). They address the role of the surface oxide and the nature of mechanical contact in determining friction and adhesion properties and discuss the relationship between the aperiodic atomic structure of quasicrystals and their low friction, for both elastic and inelastic regimes.

Johannsmann [80] has reviewed the diverse variety of interactions and response of a QCM electrode in contact with a variety of counterface geometries.

1.3.6. *Multiasperity contacts*

For many years, a fundamental problem in contact mechanics, both tribology and indentation problems, has been the inability to see what is taking place at a buried interface. Marks *et al.* [81] reviewed recent developments that allow it to become possible to perform contact mechanics experiments *in situ* within a transmission electron microscope. These new experiments have been enabled by both the miniaturization of sensors and actuators and improvements in their mechanical stability and force sensitivity. New information is now becoming available about the nanoscale processes of sliding, wear, and tribochemical reactions, as well as microstructural evolution during nanoindentation such as dislocation bursts and phase transformations. Their review provides an overview of some of these developments, in terms of both the advances in technical instrumentation and some of the novel scientific insights.

1.3.7. *Hydrodynamic slip*

The topic of boundary slip is closely related to that of slippage of adsorbed monolayers. Lauga *et al.* [82] provide an extensive review of the current status of the "no-slip" boundary condition, that is, the assumption that when a liquid flows over a solid surface, the liquid molecules adjacent to the solid are stationary relative to the solid. This no-slip boundary condition has been applied successfully to model many macroscopic experiments, but has no microscopic justification. The authors review experimental studies regarding the phenomenon of slip of liquids at solid interfaces and the interplay of factors such as surface roughness, surface charge, wetting, and the presence of gaseous layers might have on the measured interfacial slip.

Ellis and Thompson [83] reviewed the no-slip boundary condition which, as a precept of interfacial fluid dynamics, has become a topic of some controversy because of the proliferation of theoretical and experimental evidence for the existence of slip, especially at micro- and nanoscopic scales. In their review, they considered the models, techniques, and results, both experimental and by simulation, concerning interfacial slip and mechanical coupling at solid–liquid (outer slip) and adsorbate–substrate (inner slip) interfaces. Outer slip is a viscous process, normally described by a planar discontinuity between the upper layer of surface particles and the adjacent liquid layer. A number of factors can lead to slip, including surface–liquid affinity, high shear rates, surface roughness, and the elasticity of any intermediary film layer. Inner slip can be a viscoelastic process and is related to adhesion and friction. Although it has received little attention, it will be important when dealing with self-assembled monolayers (SAMs) and more complex biosensor applications. Finally, they consider stochastic coupling as an aspect of the concept of slip, whereby liquid molecules near a surface in contact with a flow interact with or bind for a short period of time, before jumping to a new location on the surface or back into the bulk. See also [84,85].

1.3.8. *Statistical mechanics and molecular dynamics*

Modeling and simulation techniques have been reviewed in two separate publications by Muser *et al*. [55,60]. The topics reviewed include stick–slip motion, sliding friction, atomistic models of friction, molecularly thin films, CNTs, charge-density waves, and asperity contacts. MD and related simulation techniques are described, and the major results for comparisons of theory with experiment are overviewed.

1.3.9. *Nanotribology: topical comments, updates, and monographs*

The topic of nanotribology in the last 20 years has received regular attention in terms of updates and commentaries in the literature. A partial list includes [38,39,81,86–97]. Four comprehensive monographs on the topic include [4–6,98].

2. Experimental techniques

When considering the attributes of various experimental techniques that are in use for studies of fundamental investigations of sliding friction, it is useful to compare the geometries, length, and time scales that are probed, to cast the results within context and to determine the range of scales over which experimental observations may be relevant. The techniques described in this section focus primarily on probes of sliding friction in adsorbed particles and films and organized according to experimental geometry, beginning with the simplest geometries depicted in the first row of Figure 3 (from Section 1), and progressing in complexity towards multi-asperity contact.

When considering an one-atom- or -molecule-thick film adsorbed on a solid substrate, one might ask whether the film will slide at all, in light of the no-slip boundary condition of fluid hydrodynamics. It seems intuitively clear that if a sufficiently strong shear stress is applied, a film will eventually slide if the shear strength between it and the substrate is weaker than the internal shear strength of the substrate material. But the friction law that governs thin-film sliding has no *a priori* reason to resemble Amontons' law, $F_{\mathrm{f}} = \mu N$ (Figure 10). In addition, there is no *a priori* reason why static friction, which is ubiquitous at the macroscale, need be present in an adsorbed layer system. It is entirely reasonable to expect the friction law governing a thin film to be closer in form to that of a macroscopic body moving through a viscous fluid, since the film is in 100% contact with the substrate. "Viscous friction" is described at low velocity v by

$$F_{\mathrm{f}} = \frac{mv}{\tau} = \eta v = m\mu_{\mathrm{v}} v, \tag{2}$$

where m is the mass of the object and τ is the characteristic time for the object's velocity to decay to $1/e$ of its initial velocity if given an initial velocity and then released. The constants η and μ_{v} in Equation (2) are commonly employed to parameterize viscous friction (the symbol η_3 is reserved here for three-dimensional fluid viscosity). It is thus becomes important at the outset

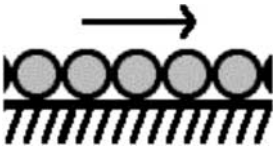

Figure 10. The frictional force law that governs thin-film sliding is not obviously $F_{\mathrm{f}} = \mu N$ since there is no externally applied normal force, and not obviously $F_{\mathrm{f}} = mv/\tau$, given the no-slip boundary condition in hydrodynamics.

to establish whether films do in fact slide at boundaries, and if so, what force law is applicable. This section describes common experimental techniques that have been employed for fundamental measurements of friction and frictional force laws in adsorbed layers, beginning with techniques devoted to dissipation associated with damping of vibration of the adsorbed adatoms, whose friction is well described by $F_f/A = \eta_2 v$, where η_2 is $\eta/A = m\mu_v/A$.

2.1. *Frictional damping of atomic vibrations*

2.1.1. *Helium atom scattering*

A community of surface scientists emerged in the late 1980s, whose members studied phononic and electronic contributions to energy dissipation within the context of small vibrational motions of atoms on surfaces [99] (Figure 11). This community was motivated by a desire to map out the magnitude and corrugation of the potential energy surface for adsorbed atoms and molecules, importantly to a wide range of topics in surface science such as diffusion, catalysis, and molecular epitaxy. In order to determine the detailed shape of the lateral potential energy surface, particularly the amplitude of its surface corrugation U_o, it is necessary to determine not only the diffusion barrier to atomic motion along a surface, but also the number and type of adsorption sites in the unit cell and the local shape of the potential at those sites. By studying how atoms vibrate on surfaces, such information can be inferred. Studies of how the vibrations are damped also provide first principles' information on the simplest forms of frictional energy dissipation.

Whenever atoms or molecules adsorb on surfaces, new vibrational modes emerge that are not present in either an isolated surface or the adsorbate alone. The modes that appear include both "internal" stretching or torsional vibrations and "external" modes whereby an entire molecule or atom moves as a whole with respect to the surface. The modes have characteristic energies that can be probed by a number of spectroscopic techniques. The line width (defined as the lifetime or damping) of such vibrations is indicative of the rate at which the energy of the phonon mode is dissipated into heat and can also be inferred from spectroscopic techniques. Frustrated, or damped, translational modes, both parallel and perpendicular to the substrate, have been probed for a range of adsorbate–substrate combinations [71]. Perpendicular modes (referred to as S or FT_z modes) mainly probe the energy and damping of the perpendicular interaction between the adsorbate and the substrate. Low-frequency (~ 10 meV, or $\sim 2.4 \times 10^{12}$ Hz) FT_z modes are reflective of physically adsorbed particles, while high-frequency (higher than physisorbed modes by a factor of ~ 10 or more) modes are indicative of chemisorption [100]. Modes parallel to the surface (T-modes) probe the curvature or corrugation of the adsorbate–substrate interaction potential [101–104] and the commensurability between the adsorbate and the substrate [103,104].

Before the mid-1980s, the only external vibrations to have been studied were the "frustrated" (i.e. damped) perpendicular vibrations of physisorbed molecules on graphite. Their energies were determined using inelastic scattering of thermal energy neutrons, the standard technique for vibrational studies in bulk materials [105]. Only graphite surfaces could be studied at the time on account of high-surface-area sample requirements. (The graphite samples were obtained from the

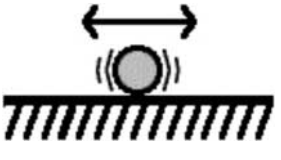

Figure 11. Simple geometry of an adsorbed atom whose vibration is damped. Friction in this geometry is generally described by $F_f = mv/\tau$.

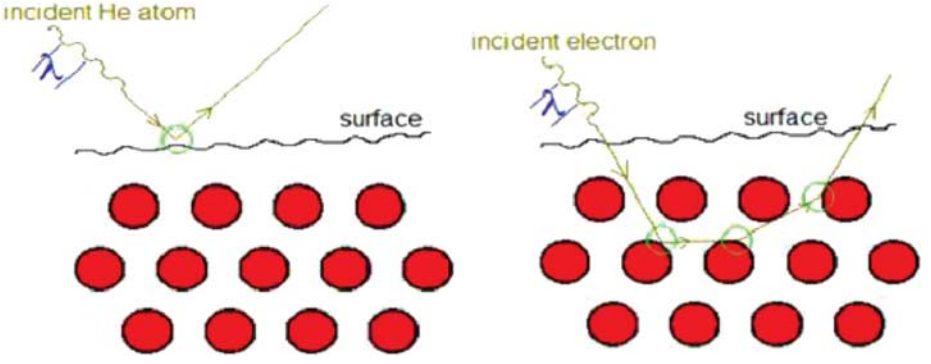

Figure 12. (color online) Helium at thermal energies can be modeled classically as scattering from a hard potential wall, with the location of scattering points representing a constant electron density surface. Since single scattering dominates the helium–surface interactions, the collected helium signal easily gives information on the surface structure without the complications of considering multiple electron scattering events (such as in LEED; http://en.wikipedia.org/wiki/File:Helium_atom_scattering_1.jpg).

carbon industry, which coincidentally manufactured them for use as high-surface-area lubricants.) Frustrated vibrations parallel to a surface, perhaps more directly relatable to sliding friction, were reported for the system nitrogen on graphite in 1990 [106], but no connections with nanotribology were made at that time. Indeed, even if the notion had been advanced, it would not have been obvious that the dissipation associated with small molecular vibrations of atoms adsorbed on a surface was comparable to frictional energy dissipation of atoms sliding several lattice spacings or more along a surface.

The first direct observation of external vibrations of a molecule adsorbed on a nongraphitic substrate was reported in 1986 for CO molecules adsorbed on Pt(111) [107], obtained by means of an inelastic scattering of thermal energy of He atoms [108] (Figure 12). A large number of systems were subsequently explored by means of He scattering, and later advances in other techniques also made possible the probing of external vibrational modes [71,99,109,110].

The position of minima in the potential energy can be determined by means of LEED measurements, infrared adsorption spectroscopy (IRAS), and analysis of electron energy loss spectroscopy (EELS) data. In a few cases, EELS data have also revealed the T-modes, which are parallel to the surface. EELS measurements of inelastic T-modes have also provided details on the curvature of the potential energy minima as well as an independent measurement of the friction parameter. IRAS data have been employed to measure the energy difference between adsorption sites, yielding direct information on barriers to diffusion for a limited number of systems. High-resolution helium atom scattering (HAS) techniques have provided the most extensive number of information on surface potentials and parallel vibration modes. Analysis of the diffusional broadening of the quasi-elastic peak as a function of momentum transfer and temperature also provides details of the static diffusion barriers and viscous friction parameters.

A typical high-resolution HAS apparatus incorporates a supersonic helium atom beam that is targeted at a sample held within an UHV chamber, and a time-of-flight arm 1–2 m in length that is positioned at about 90° from the direction of the incoming helium beam (Figure 13). The parallel momentum transfer of the beam, ΔK, is varied by changing the incidence angle of the beam with respect to the surface normal direction. The angular resolution is typically a few tenths of a degree, which yields a momentum transfer resolution of the order of hundredths of an inverse angstrom. Adsorbed film dynamics are probed by dividing the beam into short pulses (of order 10 μs) and

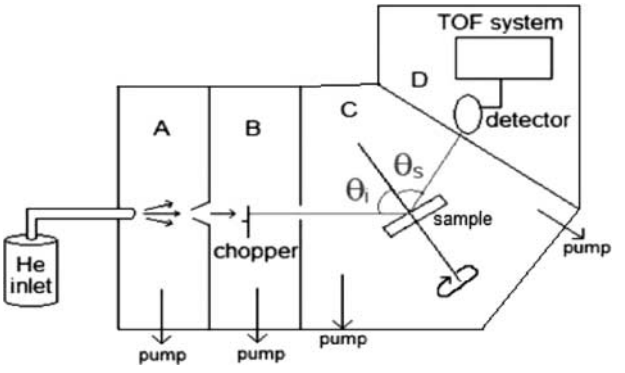

Figure 13. Schematic of helium scattering apparatus (http://en.wikipedia.org/wiki/File:Helium_atom_scattering_3.jpg).

measuring the flight time to the detector. The energy transfer resolution obtained in this manner is typically of the order of 0.1 meV. Quasi-elastic peak broadening information is obtained via deconvolution of the data with the measured instrument response function (Figure 14).

Analysis of quasi-elastic helium atom scattering (QHAS) data is performed in a manner very similar to that developed for neutron scattering data, by taking into account the differences between the interactions of helium atoms and neutrons with adsorbate atoms and molecules [111–114]. Information on adsorbate vibration modes thus allows estimates to be made of the magnitude of a surface's corrugation, or how much the binding energy to a surface varies as an atom moves from one position to another along a surface.

From the information given by the phonon dispersion curves obtained from HAS and related spectroscopies, it is possible to estimate sliding friction parameters for a given adsorbate–substrate system. In particular, using a viscous friction coefficient as defined by $F_f = m\mu_v v$ and written in a form that separates out the dissipation that occurs within the substrate μ_{subs}:

$$\mu_v = \mu_{subs} + aU_o^2, \tag{3}$$

parameters obtained from HAS experiments can be used to estimates the values for both μ_{subs} and U_o. The second term in Equation (3) is the predicted form for phononic contributions to friction occurring within the adsorbed film. Bruch has used the energies (frequencies) of the frustrated (damped) translational phonon modes to determine the surface corrugation amplitude U_o for krypton on graphite and generalized the results to other adsorbate–substrate combinations by adapting the parameters to reflect the surface structure [71,115].

Bruch employs the form for the interaction potential suggested by Steele [116], which can be written as

$$V_s(\boldsymbol{r}, z) = V_o(z) + \Sigma_g V_g(z)\ \exp(i\boldsymbol{g} \cdot \boldsymbol{r}), \tag{4}$$

where V_o and V_g are the amplitudes of the constant and periodic components of the adsorbate–substrate potential, $\boldsymbol{g}$ are the reciprocal lattice vectors, z is the height of the adsorbate with respect to the substrate, and $\boldsymbol{r}$ is the vector in the plane of the substrate.

The sign of V_g is assigned to be positive for systems exhibiting "conventional corrugation" and negative for those exhibiting "anti-corrugation". The amplitude of the periodic component of the adsorbate–substrate potential is then related to the vibrational frequencies as follows.

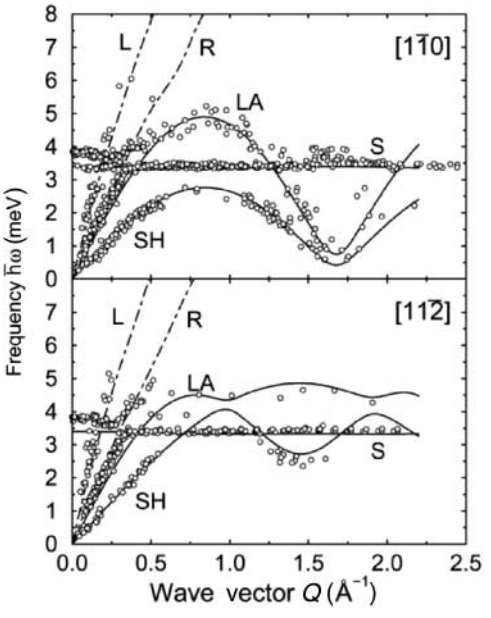

Figure 14. Reduced zone plot of the experimental dispersion curves for an incommensurate monolayer of xenon on Pt(111) for the Pt(111) [1$\bar{1}$0] and [11$\bar{2}$] azimuths at a surface temperature of $T_s = 50$ K. The experimental points, taken by inelastic HAS at incident energies between 6 and 17 meV (○) fall into five distinct phonon branches labeled R, L, S, LA, and SH, where R and L designate the Rayleigh wave and the longitudinal resonance of the Pt(111) surface, respectively (dot-dashed lines) and S, LA, and SH refer to vibrations of the Xe monolayer. The S-mode is the perpendicular vibration of the Xe atoms. The solid curves are calculations of the monolayer phonons based on the McLachlan-modified HFD-B2 Xe–Xe gas-phase potential of Aziz *et al.* for the measured lattice constant $L_{Xe}^{exp} = 4.33$ Å with the xenon monolayer rotated by $\pm 2.6°$ with respect to the given azimuths. The good agreement with the calculations identifies the lower frequency dispersive Xe monolayer mode as shear horizontal (SH), whereas the higher frequency mode is longitudinal (LA). The good agreement is also a strong support for the assumption of transferability of interactions from three-dimensional dense phases that underlies most modeling in physical adsorption. Reprinted figure with permission from L.W. Bruch *et al.*, Journal of Chemical Physics 112, p.3314, 2000 [115]. Copyright (2000) by the American Institute of Physics.

For $V_g < 0$ ("anti-corrugation": counterintuitively, adsorption first occurs atop substrate atoms):

$$\omega_z = \left(\frac{V_o - 3V_g}{m}\right)^{1/2} \quad \text{and} \quad \omega_{||} = g_o \left(\frac{-3V_g}{m}\right)^{1/2} \tag{5}$$

and for $V_g > 0$ ("conventional corrugation", where atoms first adsorb in threefold hollow sites):

$$\omega_z = \left(\frac{V_o + 6V_g}{m}\right)^{1/2} \quad \text{and} \quad \omega_{\|} = g_o \left(\frac{1.5V_g}{m}\right)^{1/2}, \tag{6}$$

where ω_z and ω_Π are the frequencies of the frustrated translations perpendicular and parallel to the substrate, respectively, and m is the adsorbate mass. The reciprocal lattice vector, g_o, is

$$g_o = \frac{4\pi}{d_{nn}(3)^{1/2}}, \tag{7}$$

where d_{nn} is the nearest-neighbor distance of the substrate atoms. The surface corrugation, U_o, can then be estimated using $U_o = -8V_g$, for $V_g < 0$, and $U_o = V_g$, for $V_g > 0$.

The damping term, μ_{subs}, in Equation (3) can also be estimated using HAS and related spectroscopies. B.N.J. Persson [117,118] has used the following approach for adsorbates on the (100) surface of an fcc crystal, writing the damping term for the motion of adsorbate i as a matrix:

$$m\frac{d^2r_i}{dt^2} + m\mu_v\frac{dr_i}{dt} = -\frac{\partial U}{\partial r_i} - \frac{\partial V}{\partial r_i} + \boldsymbol{f}_i + \boldsymbol{F}, \tag{8}$$

$$\begin{matrix} \mu_\parallel & 0 & 0 \\ 0 & \mu_\parallel & 0 \\ 0 & 0 & \mu_\perp \end{matrix}$$

where m is the mass of the adsorbate, U the periodically corrugated adsorbate–substrate interaction potential, V the adsorbate/adsorbate interaction potential, $\boldsymbol{f}_i$ a fluctuating force due to thermal effects, and $\boldsymbol{F}$ is an external force.

The components of the friction or dissipation matrix μ_v are related to the stochastically fluctuating forces arising from the irregular thermal motion of the substrate. The damping term is thus dependent on coupling of the adsorbate and substrate phonon modes and also by the excitation of electron–hole pairs in the substrate by the adsorbate. Persson relates the line width, γ, of the adsorbate vibrations to μ_v via the expression

$$\hbar\mu_v = \gamma. \tag{9}$$

In summary, various theorists have demonstrated that the coefficients of friction can be inferred from phonon dispersion curves if they are available for the adsorbate–substrate combination.

2.1.2. *Surface resistivity*

The vibrations at surfaces community remained distinct from the tribology community until 1991, when Mats Persson [119] (not to be confused with B.N.J. Persson) estimated the electronic contribution to sliding friction for a rare gas adsorbed on a metal surface from surface resistivity data and noticed that it was consistent in magnitude with sliding friction data reported for Kr monolayers adsorbed on Au. In particular, Persson related the electronic component of friction, μ_{eh}, theoretically to the surface resistivity of an adsorbate–substrate system via

$$\mu_{eh} = \frac{n^2e^2d\Delta\rho}{mn_a}, \tag{10}$$

where n is the number of conduction electrons per unit volume, e the electron charge, d the thickness of the metal film, $\Delta\rho$ the adsorbate-induced increase in film resistivity, m the adsorbate mass, and n_a the number of adsorbates per unit area in direct contact with the adsorbate (Figure 15). This is derived for a viscous friction law of the form

$$F_f = m\mu_{eh}v, \tag{11}$$

where F_f is the force of friction and v the sliding speed. Schumacher [120] employed Equations (10) and (11) to infer friction coefficients for a range of adsorbates and found the characteristic damping times to be in the range 10^{-9}–10^{-12} s. The values compare favorably with those reported by means of QCM for sliding adsorbed films, a technique which will be described in Section 2.3. The approach has been explored extensively by the group of Tobin and coworkers, who have

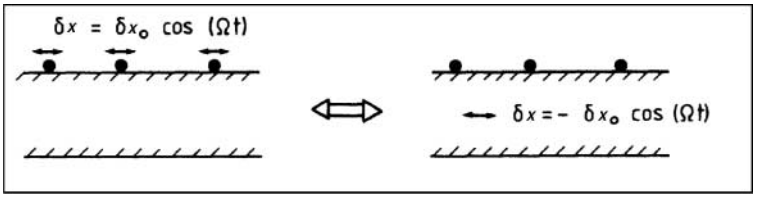

Figure 15. Schematic of how electronic contributions to frictional energy dissipation in an adsorbed species can be inferred from measurement of thin-film resistivity. The damping of the parallel frustrated translations in the adsorbates (left) is related to adsorbate-induced increases in film resistivity by a change of reference frame (right). Reprinted figure with permission from B.N.J. Persson, Physical Review B 44, p. 3277, 1991 [412]. Copyright (1991) by the American Physical Society.

regularly reported inconsistencies with models in which the increase in film resistance arises solely from scattering of conduction electrons by the adsorbates [121]. Nonetheless, while questions remain concerning the relative contributions of phononic and electronic mechanisms to frictional energy dissipation damped atomic vibration, it does appear that the fundamental mechanisms of dissipation are similar, if not identical. Although the vibrations at surfaces community has focused on vibrations of isolated atoms, it is becoming increasingly evident that their atomic and molecular energy dissipation levels provide good approximations for higher coverages, particularly if the adsorbed layers are incoherent, as is the case for two-dimensional sliding of fluid layers.

For sufficiently high temperatures, adsorbed particles are able to begin diffusing laterally along surfaces, with their diffusion rates limited by friction, as discussed in the following section.

2.2. *Diffusion*

Studies of the sideways movement of thin films across surfaces elucidate how friction and lubrication occur at the molecular level and generally originate in some fashion with Einstein's discovery that frictional transport coefficients could be related to diffusion coefficients [122]. Einstein noted that what appeared as friction in one experimental situation would appear again as diffusion in another. In particular, Einstein noted that the same random forces which cause the erratic motion of a particle in Brownian motion would also cause drag if the particle were pulled through the fluid. Therefore, fluctuations of the particle have the same origins as dissipative frictional forces which one must perform work against if one tries to perturb the system in a particular direction. From this, Einstein was able to use statistical mechanics to link the self-diffusion constant D of a particle with the proportionality constant η between its drift velocity v and an applied force, $F = \eta v$:

$$D = \frac{k_B T}{\eta}. \tag{12}$$

The diffusion coefficient in Equation (12) corresponds to that of a single-molecule self-diffusion, that is, that associated with a "random walk" whereby the average displacement of a particle is directly proportional to the square root of time (Figure 16). This self-diffusion coefficient of an individual particle originates in the simple theoretical model given by Pisov *et al.* [123], in an approach that dates back to Eyring, Kramers, and others [124]:

$$D(T) = \frac{\kappa a^2}{4} \exp\left(-\frac{E_d}{k_B T}\right), \tag{13}$$

where a is the jump step, κ the attempt frequency, and E_d the energy barrier to be overcome. The diffusion coefficient is thus connected to adsorbed film sliding friction, and measurement of one

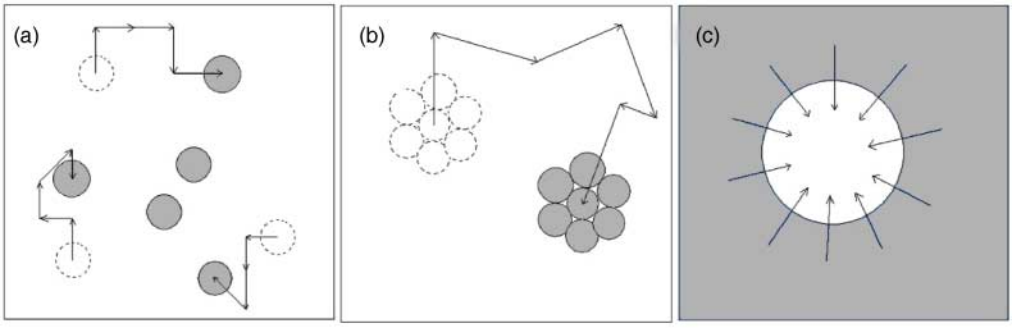

Figure 16. Schematic of the three types of diffusion coefficients: (a) the single-molecule self-diffusion coefficient D associated with a random walk of individual particles (Equation (12)), (b) the self-diffusion coefficient D_i associated with a random walk of two-dimensional islands (Equation (15)), and (c) the spreading diffusion coefficient associated with refilling of a two-dimensional hole associated with the rate that the hole will be refilled (Equation (16)). Reprinted figure with permission from B.P. Miller *et al.*, Journal of Low Temperature Physics 157, p. 252, 2009 [536]. Copyright (2009) from Springer.

quantity allows the other to be inferred. A schematic of three types of diffusion is depicted in Figure 16: (a) single-particle self-diffusion, characterized by the diffusion coefficient D, which is associated with the area swept out by a random walk of diffusive particles; (b) island "self-diffusion" associated with random Brownian motion of clusters and/or two-dimensional islands, characterized by an "island" diffusion coefficient D_i; and (c) the collective spreading diffusion coefficient associated with refilling of a two-dimensional hole associated with the rate that the hole will be refilled. Single-particle and cluster mobilities are far more fundamental quantities than the highly density-dependent collective diffusion coefficient. They are defined in an identical manner, but are distinguished here on account of the fact that clusters are known to diffuse in a very different manner from their single-atom counterparts [54,125]. A two-dimensional cluster meanwhile might be considered to be more comparable to a sliding monolayer than an individual atom exhibiting Brownian motion [124].

A number of experimental and theoretical treatments have been reported that treat self-diffusion of individual particles to self-diffusion of island clusters to spreading diffusion within complete monolayers [67,123,126] (Figure 16(c)). The diffusion and spreading coefficients referred to here are two-dimensional quantities that are defined in an entirely distinct manner from the spreading rate of a macroscopic droplet placed on a surface. But the collective spreading coefficient that describes two-dimensional refilling of an area free of adsorbate is clearly linked to the manner in which a three-dimensional droplet spreads over a surface to reach its equilibrium configuration. This is especially true for the precursor film: the later stages become governed by macroscopic hydrodynamics, viscosity, and spreading parameters.

The most common experimental techniques that have been employed to measure self-diffusive and collective diffusion are given in the following sections (see [67,127] for a more extensive treatment and [128] for very recent experimental advances).

2.2.1. *Field emission microscopy*

The field emission microscopy (FEM) technique has been reviewed in detail in a highly cited review on the diffusion of adsorbates on metal surfaces [129]. In an FEM experiment, a high electric field causes electrons to be emitted from a very small area at the end of a metal tip. The electrons are magnified and displayed on a fluorescent screen. Since the magnitude of the field

emission current depends very sensitively on the local work function at the surface, adsorbates present on the surface have a significant and directly observable effect. Adsorbate diffusion is probed via a shadowing method, whereby only a fraction of the investigated area is exposed to an adsorbate beam, and the spreading of the adsorbate distribution is monitored as a function of time. The FEM technique is very limited in terms of the substrates that can be probed. In addition, the adsorbate systems must induce substantial work function changes and also be able to withstand high electric fields without their surface mobility being affected.

2.2.2. *Field ion microscopy*

Field ion microscopy (FIM) studies typically explore surface migration of adsorbed atoms [130]. The adsorbate distribution on a metal tip is first visualized at a low temperature by an inert imaging gas ionized at the surface by means of a high electric field [131]. The tip is next heated to a desired temperature in the absence of the imaging field, in order to induce adsorbate migration. The motion is documented by imaging after the sample is recooled, to stop migration and to allow for the determination of the particle distribution. From a series of images, the mean-square displacement of adatoms is obtained and the self-diffusion coefficient can be inferred.

FIM has successfully been applied to investigate the diffusion of single-metal adatoms and clusters strongly bound at metal surfaces [132,133]. But studies of adsorbed nonmetals are rare: the primary problem with FIM for nonmetals is that the adsorbates tend to desorb or be otherwise invisible when being probed by this technique.

2.2.3. *Laser-induced thermal desorption*

In the 1980s, laser-induced thermal desorption (LITD) was introduced for the investigation of surface diffusion phenomena [134,135]. LITD is conceptionally straightforward, which probes collective or spreading diffusion (Figure 16(c)). A layer is first adsorbed uniformly on a surface. A focused laser pulse then desorbs adsorbate particles from a very well-defined area on the surface. The spot left bare is refilled by surface diffusion from the surrounding area. A second laser impulse is applied to desorb the transported adsorbates after a fixed time interval t between it and the first pulse. The amount of material that desorbs is quantified by mass spectrometry, which allows for monitoring of the rate that species are diffusing and refilling the hole [136].

The LITD technique has been employed for investigating surface mobility of a range of physisorbed gases and large molecules on single-crystal surfaces. The advantages of this technique include both simplicity and the fact that virtually all adsorbates which can be thermally desorbed and detected by a mass spectrometer are amenable to the LITD technique. LITD is of course limited to adsorbates which can be desorbed without being destroyed by the strong power associated with lasers. A frequently discussed problem is the possible effect of substrate imperfections in the area under investigation, and whether the laser itself may be creating surface imperfections. The issue of surface steps and imperfections is, however, ever present in all types of experimental probes of diffusion.

2.2.4. *Scanning tunneling microscopy*

STM observations of surface diffusion of atoms have been reported since the very early studies with this technique [137,138]. In these measurements, characteristic spikes were observed in the tunneling tracks, which were attributed to highly mobile adsorbates moving faster than the tunneling tip. The spikes are indicative of a fluctuating adsorbate density in the area probed by the STM tip. It has therefore been suggested that the spreading diffusion coefficient can, in principle, be measured by recording the current fluctuations of the tunnel junction quite analogous to the

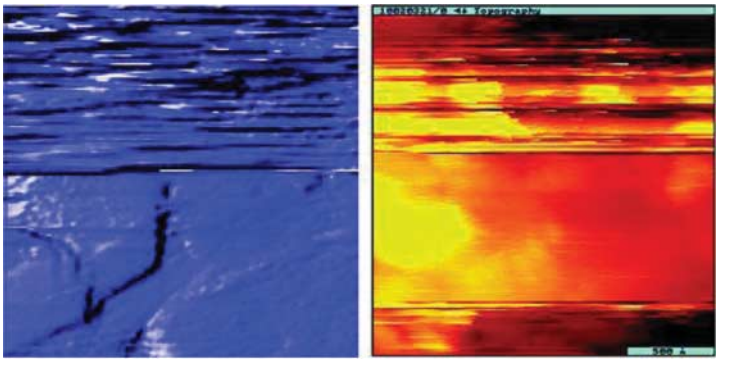

Figure 17. (color online) STM images of TBPP on platinum and TCP on Cu(111) that have been recorded, while the QCM is stationary (noisy regions) and oscillating. The noise is attributed to mobile adsorbed species diffusing in and out of the contact region. Reprinted figure with permission from M. Abdelmaksoud *et al*., Langmuir 22, p. 9606, 2006 [272]. Copyright (2006) by the American Chemical Society.

FEM method. Data interpretation can be ambiguous however, and the means for removing adatoms from a specified region is not always straightforward. Further work will be required in order to establish STM current fluctuation measurements as a reliable method for surface diffusion [139]. Nonetheless, the technique remains quite viable in principle. Figure 17 shows images from one recent report, whereby the STM measurements were performed on mobile atoms adsorbed onto the surface electrodes of a QCM. The images are noisy when the QCM is stationary, indicative of diffusion. When the QCM is set in oscillation, the regions scanned become clear, an indication that the area brushed free by the STM tip-QCM oscillating contact is not replenished in one oscillation cycle.

Concerning single-particle self-diffusion (Figure 16(a)), STM measurements are well suited for systematic studies by simply tracking the motion of individual adsorbate particles. This has been achieved for a variety of systems including adsorbed gas atoms and molecules at metal surfaces. In favorable cases, where the mean-square displacement of adatoms is determined, data can be analyzed directly in terms of the definition of the diffusion coefficient and its direct association with Brownian motion. While STM is a very powerful technique for diffusion studies, it can be labor-intensive for studies of individual atom tracking, and great care must be taken to avoid interaction effects between the tip and the migrating species.

2.2.5. *Optical techniques: photoemission electron spectroscopy, linear optic diffraction, and second harmonic diffraction*

Direct optical observations of thermal spreading of a concentration profile of surface adsorbates have been performed by spatially resolved photoelectric current measurements employing photoemission electron microscopy (PEEM) methods [140]. Similar to FEM, the PEEM method exploits the local work function changes induced by adsorbates. PEEM allows, however, a complete image of the photoelectron energies from adsorbate layers on single-crystal surfaces to be formed. In PEEM experiments for surface diffusion, a coverage gradient is generated on the surface by laser-induced desorption, or by deposition through a mask. The subsequent spreading of the adsorbate layer is monitored as a function of temperature. Due to the spatial resolution of about 100 nm, a statistical analysis can be performed, to infer the diffusion coefficients. This has been demonstrated for several systems, including adsorbed CO and O on Pd and Pt surfaces and alkali metal surface

diffusion. PEEM thus bridges the gap between atomic resolution microscopies and macroscopic observations of spreading.

Optical diffraction techniques with two lasers can also allow measurement of the spreading surface diffusion coefficient. This involves regular arrays of one-dimensional concentration profiles on an initially uniform adsorbate layer that are created by laser-induced desorption [141–144]. The grating amplitude is detected by the diffraction signal from a low-power probe laser. As adsorbate diffusion sets in, a uniform distribution is eventually arrived at, allowing spreading diffusion coefficients to be inferred.

2.2.6. *Quasi-elastic helium atom scattering*

Diffusion of an adsorbate is influenced by the potential energy surface over which the adsorbate spreads and also by thermal coupling between the adsorbate and the substrate. In principle, both factors are amenable to investigation through quasi-elastic broadening in the energy spread of a probing beam of helium atoms [112,113,145]. Jardine *et al*. [127] have published a thorough review on both the QHAS technique and the available data in relation to how diffusion parameters are determined by this method, which has been extensively used. Activation barriers are deduced from the experiment and their relation to the substrate potential, as well as the central role played by the friction parameter, with the CO/Cu(001) system used as a case study. The authors conclude that the main issues to emerge are the need for detailed MD simulations in the interpretation of data and the desirability of significantly greater energy resolution in the experiments themselves.

The QHAS technique can be applied over a wide temperature range and to anisotropic diffusion. One of its striking features is that it simultaneously provides information on short-time dynamics associated with local damping as well as information on long-time diffusion over barrier heights. QHAS is, however, limited to the case of high diffusivities (Table 1) and requires extensive data interpretation. Recent theoretical studies emphasize the role of additional contributions to the dynamical structure factor from the frustrated translation, and it has been pointed out that nondiffusive processes may also contribute to the peak broadening. QHAS has nonetheless been very successfully employed to obtain diffusion characteristics for weakly bound adsorbates at metal surfaces.

Table 1. Principal methods for surface diffusion studies of nonmetallic adsorbates on metals.

Method	Remarks	Studied adsorbates	Length scale	Range of D ($cm^2\ s^{-1}$)
STM	Tracer diffusion, direct observation, study of interactions	N, O, S, CO, O_2, C_{60}, organic molecules	10 Å	10^{-19}–10^{-16}
QHAS	Tracer diffusion, frustrated translation	CO, S, H, Xe	10 Å	$>5 \times 10^{-6}$
FEM	Refractory metal tips	H, N, O, CO		
Fluctuation	Collective diffusion		100 Å	10^{-14}–10^{-9}
Shadowing	Collective diffusion, averages over planes		100–1000 Å	10^{-12}–10^{-10}
LOD/SHD	Collective diffusion, coadsorbate systems	H, CO, NH_3	1 μm	10^{-15}–10^{-7}
PEEM	Collective diffusion, study of defects	CO, O	0.1–1000 μm	10^{-9}–10^{-5}
LITD	Collective diffusion, "macroscopic" coadsorbate systems	H, CO, O, organic molecules	100–1000 μm	10^{-8}–10^{-5}

Note: Reprinted with permission from J.V. Barth, Surface Science Reports **40**, pp. 75–149 [67]. Copyright (2000) with permission from Elsevier.

Hedgeland *et al*. [128] have recently combined helium and neutron spin-echo techniques to overcome these difficulties and obtain friction coefficients for the diffusion and Brownian motion of benzene molecules adsorbed on graphite. The helium spin echo (HeSE) measurements were performed on cleaved single crystals of highly oriented pyrolytic graphite. Neutron spin echo measurements were performed on high-surface-area-exfoliated graphite samples. The spin-echo techniques, which track motion at both atomic-scale time (ps) and length (nm) scales, revealed the motion directly through the time dependence of structural correlations on the surface and diffusion coefficients in the order of 10^{-9} cm^2 s^{-1} [128,146].

2.2.7. *Quartz crystal microbalance*

A QCM consists of a single crystal of quartz that oscillates in transverse shear motion (resonance frequencies are typically at 5–10 MHz) with very little internal dissipation. The oscillations are driven by applying an alternating voltage to metal electrodes deposited on the surface of the quartz, and the electrodes are generally prepared so as to present (111) metal orientations at their surfaces when surface science investigations are being performed [147]. Atomically thin films adsorbed onto the QCM electrodes produce shifts in both the frequency and the quality factor Q, which are indicative of the degree to which the films are able to track the oscillatory motion of the underlying substrate. The QCM was adapted for friction measurements in the late 1980s by Krim and Widom [149] and for decades beforehand it was routinely used for microweighing purposes [148]. It has been extended to a wide variety of nanotribological applications by using it in combination with alternative techniques such as SFA [150]. STM [63,151,152], and nanoindenters [153]. It is also being increasingly employed for studies of binding and shear strength for nanoscale biomedical applications [154].

Frequency shifts in the QCM are generally associated with mass uptake, while quality factor shifts, which are generally manifested as decreases in the amplitude of vibration, arise from dissipative effects such as frictional losses associated with adsorbate sliding and/or viscoelasticity [155]. For submonolayer clusters and monolayer adsorbates, dissipation associated with viscoelasticity can be neglected. Sliding friction and diffusion in this case are well described by the viscous friction law (Equation (2)) [156,157] and characteristic "slip times" τ and frictional damping coefficients η_2 are determined via [148]

$$\delta(Q^{-1}) = -4\pi\tau\delta f \quad \text{and} \quad \eta_2 = \frac{\rho_2}{\tau}, \tag{14}$$

where Q^{-1} and f are the inverse quality factor and the frequency of the crystal, respectively, and ρ_2 is the mass per unit area of the adsorbed film. A more extensive discussion of the QCM technique is contained in Section 2.3, within the context of sliding friction of complete monolayers. The following sections describe how QCM data can be analyzed to yield values for adsorbate self- and spreading-diffusion coefficients.

2.2.7.1 *Island diffusion coefficients* The diffusive and frictional behavior of clusters of particles can vary dramatically with size. Sliding friction values may drop for clusters of atoms, for example, because the formation of an island generally requires that some or all of the atoms in the layer becomes incommensurate with the substrate. Gold clusters of 250 atoms have been routinely observed to diffuse on graphite substrates with surprisingly large diffusion coefficients [158] ($D = 1000$ cm^2 s^{-1} and $E_\mathrm{d} = 0.5$ eV compared to single-atom values [159] of $D = 0.002$ cm^2 s^{-1} and $E_\mathrm{d} = 0.08$ eV). Similar behavior has been reported for other metal clusters as well [160].

Pisov *et al*. [123] have suggested that the diffusive behavior of such islands can be probed by means of QCM via the fluctuation–dissipation relation. In particular, they suggest that the cluster

drift mobility can be related to an island diffusion coefficient D_i through the Einstein relation, Equation (4), and is written as $D_i \eta_2 A = k_B T$, to obtain

$$\tau = \frac{D_i m N}{k_B T}, \tag{15}$$

where $\rho_2 = mN/A = \eta_2 \tau$ is the mass per unit area of an island consisting of N atoms, each with mass m. Island diffusion coefficients which are greater than 10^{-5} cm^2 s^{-1} should be detectable using a QCM. Given that the islands may be exhibiting self-diffusion at a much greater pace than individual particles, replenishment by means of diffusive motion of islands may become a mechanism for lubrication in cases where the island size is comparable to that of the contact. This mechanism is distinct from that of a spreading film replenishing regions of low density due to internal pressure gradient, which is associated with the spreading diffusion coefficient, as described in the following sections.

2.2.7.2 *Spreading diffusion of an adsorbed monolayer as determined by QCM* If a small amount of liquid is placed on a surface, then the rate of increase in surface area of the liquid as it spreads into a thin film defines how quickly the area can be replenished, as discussed already through the numerical work of Brenner *et al*. Experimentally obtained values for the parameters employed in such models, however, are generally not easy to obtain. Widom and Krim [126], however, described one such method in 1994, by deriving how the spreading diffusion coefficient D_s can be experimentally determined from slip times and adsorption isotherm information obtained from QCM measurements at subsaturation vapor pressures. By substituting Equation (6) into Equation (7) in the 1994 paper by Widom and Krim, the spreading diffusion coefficient, measured in cm^2 s^{-1}, is given by [126]

$$D_s = \tau \left(\frac{\partial \phi}{\partial \rho} \right)_T, \tag{16}$$

where ϕ is the film-spreading pressure, or the force per unit length exerted on an arbitrary boundary within the film. A more familiar form of this equation equates the diffusion constant D_s as the product of individual particle mobility, τ (m), times density, times the derivative of the chemical potential with respect to density (Equation (7) in [126]). The spreading pressure can, however, be obtained from adsorption isotherm data, since it can be written in the form

$$\phi(P') = \frac{k_B T}{m} \int_0^{P'} \frac{\rho_2(P)}{P} \mathrm{d}P, \tag{17}$$

where ρ_2 is the mass per unit area adsorbed at pressure P. The spreading diffusion coefficient obtained in this manner provides an intuitive gauge of whether a lubricant is able to spread back into a contact where it has been scraped off: simply stated, if $D_s = 1$ cm^2 s^{-1}, then a 1-cm^2 area brushed free of an adsorbed film will be replenished by sideways flow in a period of 1 s. In order for this to occur, it is of course necessary that a reservoir of lubricant be present to resupply the emptied area. This reservoir might be a resupply from the gas phase onto an adjacent area of the surface [161] or perhaps a nearby high-surface-area region that acts as a sponge or ballast for the film material to flow into the uncovered region.

2.2.8. *Impact of surface defects, pinning on diffusion coefficients*

Whenever experiments to study surface mobility, diffusion, and sliding are performed, the effects of ubiquitous surface imperfections and/or contaminations must be taken into consideration

[162,163]. These include, in particular, impurities from within the bulk of the substrate and technique-induced damage, as well as residual gases that have become pinned at the surface being studied. In addition, the presence of atomic steps or other lattice defects such as vacancies may severely inhibit surface diffusion and ultimately the ability of monolayers to slide along specific surfaces. Steps may even represent sources for two-dimensional substrate atom evaporation, and both the formation and concentration of defects may be temperature-dependent. For instance, adsorbates may preferentially bind to surface steps or other defects which implies reduced surface mobility. Frequently, however, such effects are implicitly contained in the experimental data and it is a challenging task to disentangle their contribution and that of the mobility on the perfect substrate areas, thus giving rise to lively discussions as to the interpretation of data. Diffusion studies provide the simplest geometries under which pinning is observed to occur. Whether one considers this to be "defective" behavior or simply an intrinsic characteristic of the fact that no experimental system is geometrically perfect impacts how one views pinning in more complicated geometries, such as the QCM technique to be described in the following sections. Pinning and static friction will be present in many different experimental system geometries associated with thin-film sliding, but less frequently reported in theoretical modeling.

2.3. *Adsorbed layers in unconfined geometries*

2.3.1. *The QCM technique*

A QCM is a surface-sensitive oscillating piezoelectric which can accurately measure mass uptake and energy dissipation of an adsorbed layer. The technique was adapted to friction measurements of adsorbed films in 1988 by Krim and Widom [148]. Through acoustic impedance calculations, they were able to show that if the shear stress between the film and the QCM surface is below approximately 10^3 N m^{-2}, then the film slippage arising from the oscillating nature of the QCM surface can be detected by monitoring the changes in the QCM resonance frequency and amplitude. QCM measurements yielded the first definitive experimental evidence for existence of both phononic [34] and electronic [164–166] friction mechanisms in sliding adsorbed layers. A frequent limitation of nanotribological techniques is their maximum sliding speed. For an AFM, the top lateral speed is in the order of 10 μm s^{-1}. The surface of the QCM, however, can easily reach peak speeds in the order of m s^{-1} with higher frequency oscillators [63,167,168]. Recent advances in SFA techniques have also allowed studies of sliding speeds to be increased by several orders of magnitude, from mm s^{-1} [169,170] to m s^{-1} [171,172].

A schematic of the QCM techniques is shown in Figure 18. By coating the two faces of the QCM with metal electrodes and applying an alternating voltage perpendicular to the electrodes, the QCM can be made to mechanically oscillate due to its piezoelectric properties. Quality factors (Q) are relatively high in this mode of oscillation, typically 10^5 or greater. Because of its high-frequency stability and high Q, a QCM can detect mass changes as small as 1 pg cm^{-2}. This technique can be employed up to 573°C, above which crystalline quartz loses its piezoelectric properties. Sliding friction measurements are highly sensitive to surface electrode uniformity, and QCMs have been prepared with a very wide range of surface topologies. These ranges from very disordered surfaces [173] to highly uniform surfaces with terraces large enough to allow helium atom scattering to be performed on them [174]. The surface roughness of QCM electrodes is discussed in great detail in Section 4.

Quartz crystals typically used for studies of micro-weighing and frictional sliding are cut in the "transverse shear AT-cut" orientation. This means that the crystal oscillates in the transverse shear mode (Figure 16(b)), which arises from the manner in which the quartz is cut relative to its crystallographic axes. The piezoelectric effect depends greatly on direction, for example, if stress is applied along the Z-axis, and no electric signal is generated. Therefore, the way the quartz disk

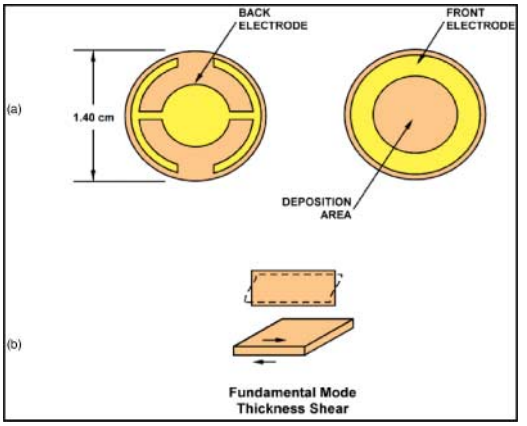

Figure 18. (color online) (a) Schematic of typical QCM, which consists of a thin (<1 mm) disk of single-crystal quartz with metal film electrodes deposited onto each face. (b) Illustration of transverse shear mode of oscillation.

is cut has a great impact on the crystal frequency as well as on its stress and temperature responses. The Z-axis is defined as the direction parallel to the quartz "trigonal" axis, named for the fact that it has three symmetric diagonal axes perpendicular to it. The X-axis is chosen parallel to one of the diagonal axes. The AT cut is oriented at angles of $\theta = 35°15'$ from the ZX-plane. These crystal cuts are used for the high-frequency thickness-shear mode of oscillation. Since the AT-cut crystals have zero temperature coefficient near room temperature, they are the most popular choice for most of the applications. Custom cuts can be obtained, exhibiting zero temperature coefficient at temperatures other than room temperature.

When the crystal oscillates, its two broad faces move in opposite directions. As the oscillation occurs, an acoustic wave travels across the thickness of the crystal at the speed of sound in quartz. Standing waves will occur for frequencies which have wavelengths that are odd multiples of the crystals thickness, that is, $t = n\lambda/2$. Therefore, the fundamental frequency of the quartz crystal oscillator and its thickness are related by the equation

$$f_0 = \frac{v_q}{2t}. \tag{18}$$

In Equation (18), f_0 is the fundamental frequency of the crystal and v_q the speed of sound in quartz. For AT-cut quartz, $f_0 t = 1670$ m s^{-1}. Differentiating Equation (18) and substituting back into the original expression yields

$$\frac{df_0}{f_0} = -\frac{dt}{t}. \tag{19}$$

Since the thickness and mass of the crystals are related by the equation $m_q = \rho_q A t$, where m_q is the mass of the quartz crystal, ρ_q the density of quartz (2.65 g cm^{-3}), and A the crystal area, one can relate changes in the frequency of the oscillation of the quartz crystal to changes in its mass:

$$\frac{df_0}{f_0} = -\frac{dm_q}{m_q}. \tag{20}$$

In 1959, Sauerbrey [149] observed that when a thin film is adsorbed onto a quartz crystal, the additional mass due to the film can be treated as a perturbation to the mass of the crystal. This

assumption results in Equation (21), which demonstrates how quartz crystals can be used as microbalances for the weighing of thin adsorbed film:

$$\mathrm{d}f_0 = -\left(\frac{m_\mathrm{f}}{A}\right)\left(\frac{f_0^2}{\rho_\mathrm{q} v_\mathrm{q}}\right) = -\frac{\rho_2 f_0^2}{2.21 \times 10^5}. \tag{21}$$

In Equation (21), $m_\mathrm{f}/A = \rho_2$ is the mass per unit area of the adsorbed film (in g cm^{-2}), and it is assumed that the film is adsorbed on both the electrodes. Equation (21) shows how changes in frequency can be related to changes in mass of an adsorbed film and is valid as long as the attached film is nondissipative. The change in frequency, for example, of a one-monolayer thick film of helium with mass per unit area 6.7 ng cm^{-2} adsorbed on a 10 MHz crystal would be close to 3 Hz. Given that frequency stabilities of 0.1 Hz or better are routine, this is well within the detection limit of the technique.

If the adsorbed film is sliding, or if the QCM is oscillating in the presence of a surrounding gas phase, then a more sophisticated analysis treatment must be employed, as follows.

Oscillations of a planar surface can be related to the oscillations of a mass M_m suspended from some fixed support by a spring having compliance C_m and subjected to some light damping force $R_\mathrm{m} v$, which is proportional to the velocity. If a periodic force $F = F_0 \cos(\omega t)$ is applied to the mass, the latter experiences forced oscillations at that frequency and under steady conditions the velocity at a give time will be

$$\upsilon = \frac{F}{R_\mathrm{m} - \mathrm{i}(\omega M_\mathrm{m} - 1/\omega C_\mathrm{m})}, \tag{22}$$

and the ratio $F/v = Z_\mathrm{m} = R_\mathrm{m} - \mathrm{i}X_\mathrm{m}$ defines the quantity known as the "mechanical impedance".

It is within this framework that shear oscillations of a planar surface in contact with a viscous fluid (gas or liquid) and/or a sliding adsorbed film are generally studied. For a plane oscillating in the x-direction with a velocity $v_0\cos(\omega t)$, the motion of the surrounding fluid obeys the Navier–Stokes equation for a viscous, incompressible fluid can describe the adsorbed film by

$$\rho_3 \frac{\partial \upsilon_x}{\partial t} = \eta_3 \frac{\partial^2 \upsilon_x}{\partial z^2}, \tag{23}$$

where ρ_3 is the bulk density and η_3 the bulk fluid viscosity. The mechanical "acoustic impedance" Z of the fluid to shear oscillations is defined in terms of the mechanical impedance per unit area, $Z = Z_\mathrm{m}/A$, where A is the surface area in contact with the film or the fluid.

Stockbridge [175] has shown that shifts in quality factor and frequency of a QCM are related to the acoustic impedance presented to its surface according to

$$\delta\left(\frac{1}{Q}\right) = \frac{2R}{\omega \rho_\mathrm{q} t_\mathrm{q}} \quad \text{and} \quad \delta\omega = \frac{X}{\rho_\mathrm{q} t_\mathrm{q}}, \tag{24}$$

where ρ_q and t_q are the density and thickness of quartz, respectively. These equations must be multiplied by a factor of 2 if both sides of the QCM are exposed to the film and/or gas phase that gives rise to the acoustic impedance. The task then remains to obtain expressions for the acoustic impedance of gaseous phases and sliding adsorbed layers that the QCM is impacted by. Before these expressions are presented, a few comments are included on the manner in which shifts in quality factor and frequency shifts are obtained experimentally.

Energy dissipation is directly related to changes in the inverse quality factor, which arises from dissipation within the crystal, including its mounting arrangement, and any additional dissipation

that is associated directly with the presence of an adsorbed film:

$$\frac{1}{Q} = \frac{1}{Q_q} + \frac{1}{Q_f}. \tag{25}$$

Measurements of changes in the QCM quality factor simultaneously with frequency shift information thus allows for monitoring of the dissipative factors associated with the film. In order to monitor ΔQ^{-1}, the QCM amplitude can be calibrated with a gas that has known viscoelastic properties, a ring down decay curves can be recorded, and/or an amplitude versus frequency sweep can be performed [176–178].

A wide variety of commercial and noncommercial electronics are available for driving and monitoring the frequency and amplitude response of a QCM setup. Bruschi *et al*. [179] have described some simple circuits that can be assembled from standard components in addition to circuits described in the standard electronics industry [180]. The group reports that their performance is as good as that of the much more expensive frequency modulation technique employed in very precise QCM measurements and which requires high-quality commercial radiofrequency generators and amplifiers. They have also reported how a QCM can be mounted within a UHV chamber for surface science studies in temperatures ranging from 4 to 400 K. The low-amplitude QCM oscillations achieved by this group have allowed them to perform extensive measurements of pinning effects in sliding adsorbed films [181,182].

An alternative approach, which avoids self-heating effects in the QCM technique, involving an "inductive pulse" method has been reported [156]. This method is based on radio-frequency electric pulse excitation and ring-down signal measurements of quartz crystal resonators located in an induction coil. The technique was tested by examining surface areas and adsorption strengths for nitrogen uptake, and the differences between this and conventional techniques were explained as suppression of the self-heating effect when the inductive pulse method was employed.

Once measured, shift in quality factors and frequency shifts generate values for the acoustic impedance via Equation (24), which are related to film slippage and friction as follows.

In analogy with exposing the oscillating surface to a bulk fluid, consider a flat surface oscillating in plane with velocity $v(t)$ with an adsorbed film of thickness d, with bulk density ρ_{3f} and bulk viscosity η_{3f}, adsorbed on top [148,177,178]. The oscillatory motion of the surface will cause shear oscillations to penetrate into the z-direction normal to the surface. Taking the x-direction to be parallel to the motion of the surface, the subscript f refers to the film (v refers to the vapor) and the subscript 3 refers to the 3D, or bulk values (2 refers to the 2D, or surface values). The Navier–Stokes Equation (23) for a viscous, incompressible fluid is now written as

$$\rho_{3f} \frac{\partial \upsilon_x(z,t)}{\partial t} = \eta_{3f} \frac{\partial^2 \upsilon_x(z,t)}{\partial z^2}, \tag{26}$$

where the x-direction is in line with the motion of the substrate. The solution to Equation (26) for a frequency f under the assumption that the film does not slip at the interface is given by

$$\upsilon_x(z,t) = u(t) \frac{\cos\, k(d-z)}{\cos(kx)}, \tag{27}$$

where $k = (1+\mathrm{i})(\omega\rho/2\eta)^{1/2}$. The acoustic impedance of the film, Z_f, can be obtained from the stress tensor component $\sigma_{zy} = \eta(\delta v/\delta z)_z = 0$, written as

$$Z_f = R_f - \mathrm{i}X_f = \eta_{3f} k \tan(kd), \quad k^2 = \mathrm{i}\frac{\omega\rho_{3f}}{\eta_{3f}}. \tag{28}$$

The real (resistive) component of Z_f relates to the energy dissipation, while the imaginary (reactive) component relates to the inertia of the oscillator.

In the thin-film limit, where $|kd| \ll 1$, $\tan(kd)$ reduces to kd and the real part of Z_f vanishes reducing the acoustic impedance to

$$Z_f = -iX_f = -i\omega\rho_{3f}d = -i\omega\rho_{2f}. \tag{29}$$

Substituting Equation (29) into Equation (24) produces the Sauerbrey result for the mass–frequency relationship given by Equation (20).

When the QCM is exposed to a gaseous environment, the acoustic impedance introduced to the oscillator results from the shear impedance of the gas. If adsorption from the vapor-phase occurs, then the acoustic impedance introduced has an additional component from the mass uptake. But for the case when there is only gas damping and no adsorption, the acoustic impedance to shear wave propagation is given by

$$Z_v = R_v - iX_v = (1 - i)\sqrt{\pi\rho_{3v}\eta_{3v}f}. \tag{30}$$

Substituting Equation (30) into Equation (24), one can calculate frequency shifts and $\delta(1/Q)$. However, at low pressures, the time τ_r for excess particle momentum to relax after collision with the vibrating crystal of the gas particles becomes similar to the period of oscillation. The time τ_r is expected to be in the order of 1–10 gas collision times (mean free path/velocity), since excess momentum may not be completely transferred after just one collision. The gas cannot be regarded as a simple viscous fluid but must be looked upon as viscoelastic. Its viscosity now becomes a function of frequency where

$$\eta^*_{3v} = \frac{\eta_{3v}}{1 + i\omega\tau_r}. \tag{31}$$

The resistance and reactance of Z^*_v of the viscoelastic gas are

$$\begin{aligned} R^*_v &= \sqrt{\pi\rho_{3v}\eta_{3v}f}\sqrt{\frac{\omega\tau_r}{1+(\omega\tau_r)^2}\left(\sqrt{1+\frac{1}{(\omega\tau_r)^2}}+1\right)},\\ X^*_v &= \sqrt{\pi\rho_{3v}\eta_{3v}f}\sqrt{\frac{\omega\tau_r}{1+(\omega\tau_r)^2}\left(\sqrt{1+\frac{1}{(\omega\tau_r)^2}}-1\right)}. \end{aligned} \tag{32}$$

For pressures higher than 300 Torr, $\omega\tau_r \ll 1$, the gas does not behave viscoelastically, so the gas can be regarded as a simple viscous fluid.

Now consider the case of adsorption occurring from the vapor phase. The shear waves produced by the QCM will diffuse through the film and into the surrounding gas. The acoustic impedance in this environment will now have contributions from both the adsorbed film and the vapor. Assuming a no-slip (no energy dissipation) condition at the film–substrate boundary, the acoustic impedance is given by

$$\begin{aligned} &Z_{fv} = Z_{3f}\tanh(\Psi + \gamma d),\\ &\text{where}\\ &\tanh(\Psi) = \frac{Z_{3v}}{Z_{3f}},\\ &Z_{3v} = (1 - i)\sqrt{\pi\rho_{3v}\eta_{3v}f},\\ &Z_{3f} = (1 - i)\sqrt{\pi\rho_{3f}\eta_{3f}f},\\ &\gamma = Z_{3v} = (1 - i)\sqrt{\frac{\rho_{3f}\omega}{2\eta_{3f}}}. \end{aligned} \tag{33}$$

Again, assuming a thin-film limit of $|kd| \ll 1$, then the acoustic impedance simplifies to

$$Z_{\mathrm{fv}} = -\mathrm{i}\omega\rho_{2\mathrm{f}}\left[1 - \left(\frac{Z_{3\mathrm{v}}}{Z_{3\mathrm{f}}}\right)^2\right] + Z_{3\mathrm{v}}, \quad |kd| \ll 1. \tag{34}$$

Since the acoustic mismatch factor $[1 - (Z_{3\mathrm{v}}/Z_{3\mathrm{f}})^2]$ is close to unity in many cases, Equation (34) can be additionally simplified to

$$Z_{\mathrm{fv}} = -\mathrm{i}\omega\rho_{2\mathrm{f}} + Z_{3\mathrm{v}} = Z_{\mathrm{f}} + Z_{\mathrm{v}}. \tag{35}$$

The damping effects of both the film and the gas vapor on the QCM can now be separated and one can write the frequency and quality factor shifts as

$$\begin{aligned} \delta(\omega) &= \delta(\omega)_{\mathrm{f}} + \delta(\omega)_{\mathrm{v}} = \frac{X_{\mathrm{f}}}{\rho_{\mathrm{q}} t_{\mathrm{q}}} + \frac{X_{\mathrm{v}}}{\rho_{\mathrm{q}} t_{\mathrm{q}}}, \\ \delta\left(\frac{1}{Q}\right) &= \delta\left(\frac{1}{Q}\right)_{\mathrm{f}} + \delta\left(\frac{1}{Q}\right)_{\mathrm{v}} = 0 + \frac{R_{\mathrm{v}}}{\omega\rho_{\mathrm{q}} t_{\mathrm{q}}}. \end{aligned} \tag{36}$$

The effect of film slippage introduces a film impedance $1/\eta_2$ that is added in parallel to the no-slip case arrived at earlier. The total acoustic impedance including film slippage is then given by [183]

$$\frac{1}{Z_{\mathrm{tot}}} = \frac{1}{\eta_2} + \frac{1}{Z_{\mathrm{fv}}}. \tag{37}$$

Solving for the dissipative and reactive terms yields

$$\begin{aligned} \frac{X_{\mathrm{tot}}}{R_{\mathrm{tot}}^2 + X_{\mathrm{tot}}^2} &= \frac{\omega\rho_2 + X_{\mathrm{v}}}{R_{\mathrm{v}}^2 + (\omega\rho_2 + X_{\mathrm{v}})^2}, \\ \frac{R_{\mathrm{tot}}}{R_{\mathrm{tot}}^2 + X_{\mathrm{tot}}^2} &= \frac{R_v}{R_{\mathrm{v}}^2 + (\omega\rho_2 + X_{\mathrm{v}})^2} + \frac{1}{\eta_2}. \end{aligned} \tag{38}$$

This approach is a small modification to the original derivation by Krim and Widom [148] where

$$Z_{\mathrm{tot}} = Z_{\mathrm{v}} + \frac{Z_{\mathrm{f}}\eta_2}{Z_{\mathrm{f}} + \eta_2} \tag{39}$$

was used in place of Equation (37). In the low-vapor density limit, the two approaches give identical results. However, as the vapor density increases, the Bruschi and Mistura approach [183] gives a 10–15% correction to the Krim and Widom approach.

To calculate the slip time, τ, associated with frictional sliding of the adsorbed layer, solve for η_2 from Equation (38) and use the relation

$$\tau = \frac{\rho_{2\mathrm{f}}}{\eta_2}, \tag{40}$$

where τ is the time that the total film momentum takes to fall to $1/e$ of its original value if the substrate were to stop abruptly. It is to be noted that τ is an average value over the entire film, since not all of the particles are sliding the same amount at any given time.

One can thus employ the experimentally measured change in inverse quality factor and frequency shift to determine the resistance and reactive components of the total impedance Z_{tot} and

from that the slip time and interfacial slippage. For a sliding adsorbed film without the surrounding vapor, the determination of τ is simpler. The resistive and reactive components of Z_2 are

$$\begin{aligned} R_2 &= \frac{\rho_2 \omega^2 \tau}{1 + \omega^2 \tau^2}, \\ X_2 &= \frac{\rho_2 \omega}{1 + \omega^2 \tau^2}. \end{aligned} \tag{41}$$

Substituting Equation (41) into Equation (24) and dividing, one obtains Equation (14) in the form

$$\delta\left(\frac{1}{Q}\right) = 2\tau\delta\omega. \tag{42}$$

The analysis that gives rise to Equation (42) is based on the assumption of a viscous friction law for the sliding adsorbed monolayer. The validity of this assumption for the QCM techniques was examined in 1998 [173], when the technique was employed to measure the vibrational amplitude dependence of quality factor shifts which occur when Kr monolayers adsorb on the microbalance's gold electrodes. Assuming that the friction force is proportional to some power of the sliding velocity of the film relative to its substrate, such measurements allow one to infer whether or not the friction force law is linear in form. A linear friction law was confirmed to be valid for a full monolayer of both liquid and solid krypton, for sliding speeds estimated to be in the range 3–8 cm s^{-1}. The form of the friction law at lower coverages appeared to be nonlinear, consistent with $n < 1$ in a more general law, $F = \eta v^n$ (Figure 19).

Bruschi *et al*. [181,184] have also employed the QCM technique to measure the sliding friction of krypton films physisorbed on gold, but at substantially lower drive amplitudes and on Au(111) electrodes prepared in a manner to obtain high degrees of crystalline order as well as distinct step edges between crystalline facets. By slowly increasing the amplitude of the substrate oscillations, they observed a sharp transition from a film locked to the substrate to a sliding one. The transition was characterized by hysteresis in both the dissipation and inertial mass as the amplitude is decreased (Figure 20), and the dependence of this transition on film coverage was studied in detail [185]. Regarding the coverage dependence, they reported sharp pinning transitions separating a low-coverage region, characterized by slippage at the solid–fluid boundary, from a high-coverage region where the film was locked to the oscillating electrodes. Sliding of a film could, however, be induced by slowly increasing the amplitude of the substrate oscillations. The group was able to determine, from various experimental runs, that the precise location of the transitions was strongly dependent on the state of the substrate surface, a feature that is very analogous to the large impact of step edges and features on adatom diffusive properties.

The effect of substrate step edges and pinning of adsorbed layers on a QCM was studied numerically in detail by means of numerical modeling in 1999 [186]. In particular, the effects of a step defect and a random array of point defects (such as vacancies or substitutional impurities) on the force of friction acting on a xenon monolayer film as it slid on a silver (111) substrate were studied by MD and compared with the results of lowest order perturbation theory in the substrate corrugation potential. For the case of a step, the magnitude and velocity dependence of the friction force were reported to be strongly dependent on the direction of sliding with respect to the step and the corrugation strength. When the applied force F was perpendicular to the step, the film was pinned for F less than a critical force F. Motion of the film along the step, however, was not pinned. Fluctuations in the sliding velocity in time provided evidence of both stick–slip motion and thermally activated creep. The critical force, however, was still much lower than the effective inertial force exerted on the film by the oscillations of the substrate in experiments done with a QCM. Nonetheless, experimental observations reveal that at sufficiently high oscillator amplitudes

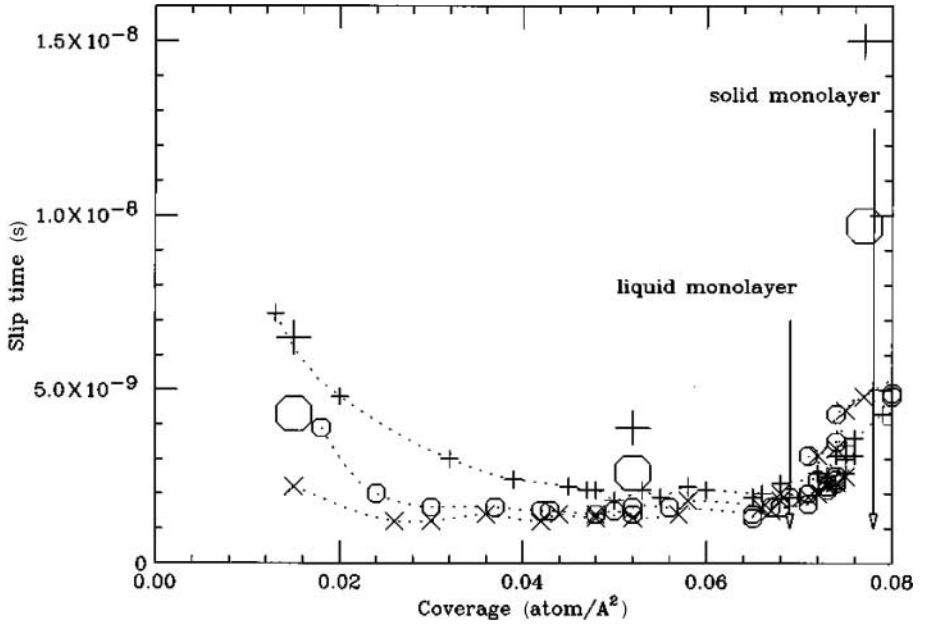

Figure 19. Slip time versus pressure for Kr/Au at 77.4 K. Symbols X, O, and + represent data recorded at different velocities having a ratio of 1, 2, and 3, respectively. The oversized symbols represent the theoretically predicted values for $n = 5$ for three different coverages: 0.015, 0.052, and 0.077 atoms Å^{-2}. The data are well described by a linear friction law at monolayer coverages and higher, as indicated by the fact that the slip time is independent of velocity at these coverages. At lower coverages, the slip times increase and the data appear nonlinear. Reprinted figure with permission from C. Mak *et al.*, Physical Review B 58, p. 5157, 1998 [173]. Copyright (1998) by the American Physical Society.

and monolayer coverages, the friction of adsorbed layers do slip and are well described by the linear friction (Equation (2)). QCM data for sliding film friction measurement for a variety of materials combinations are reviewed in Section 4.

2.3.1.1 *Spreading, wetting, and slip lengths* The diffusion and sliding friction phenomena discussed so far have been limited to two-dimensional adsorbed layers such as those depicted in Figure 16. As adsorbed layers thicken, they may or may not remain uniformly coated on the surface, depending on their three-dimensional wetting characteristics on that surface. Three-dimensional droplets may completely, incompletely, or not wet surfaces that they are in contact with, and it is common to define a "spreading coefficient" K to gauge whether wetting will occur:

$$K = \gamma_A - \gamma_B - \gamma_{AB}. \tag{43}$$

The term γ_A is the surface energy or surface tension of the solid, γ_B the surface tension of the liquid in question, and γ_{AB} the interfacial tension [187]. If K is positive, then the liquid will wet the surface, but if K is negative then it will dewet from the surface. In 1977, Dash employed thermodynamic arguments to demonstrate the correspondence between three types of vapor pressure adsorption isotherms and the three categories of macroscopic wetting behavior [188]. With increasing coverage, adsorbed films may form ever-thickening uniform layers, a uniform two-dimensional layer after which all material goes to form a bulk droplet at the bulk saturation vapor pressure (a), or only trace amounts may condense in advance of bulk droplet formation (b). Dash's

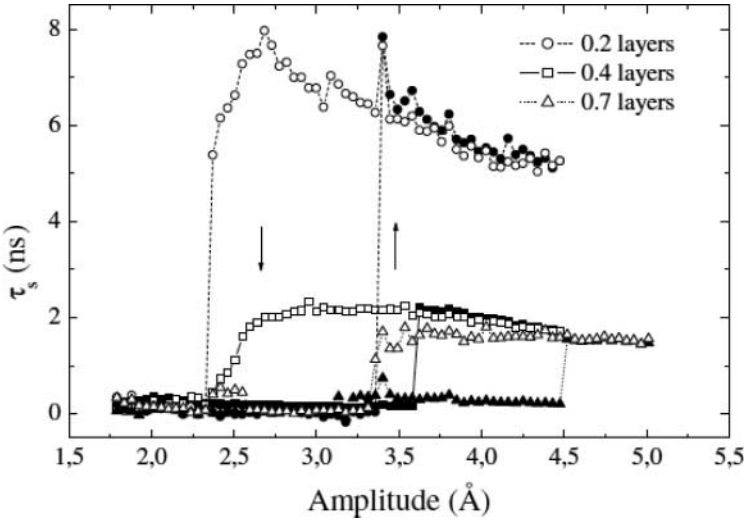

Figure 20. Slip time versus QCM amplitude of vibration for Kr/Au(111) at 77.4 at a coverage of 0.2 monolayers. The filled-up symbols correspond to data recorded as the amplitude was increased, and the open symbols are relative to decrease. The data are consistent in magnitude with those presented in Figure 19 and demonstrate that at low coverages and sliding speed, adsorbate particles may become pinned. Reprinted figure with permission from L. Bruschi *et al.*, Physical Review Letters 88, art#046105, 2002 [181]. Copyright (2002) by the American Physical Society.

correspondence between subsaturation adsorption behaviors and macroscopic wetting types is depicted in Figure 21 for the cases of (a) "complete", (b) "incomplete", and (c) "nonwetting" behaviors. Since the QCM technique is ideal for recording adsorption at subsaturation vapor pressure, both sliding friction and macroscopic wetting characteristics can thus be probed by this technique.

The fact that the adsorbed film might be sliding in response to the oscillatory motion of the QCM substrate might at first seem to be in contraction with the no-slip boundary condition of fluid hydrodynamics [189–194]. In particular, it was assumed for hundreds of years that when fluid flows over a solid surface, the liquid molecules adjacent to the solid are stationary relative to the solid and that the viscosity is equal to the bulk viscosity. Navier was the first to propose a general boundary condition that incorporated the possibility of fluid slip at a solid boundary. Navier's proposed boundary condition stated that the velocity at a surface is proportional to the shear stress at the surface:

$$v_s = \lambda \left(\frac{\mathrm{d}v_x}{\mathrm{d}y} \right). \tag{44}$$

Here, v_x is the sliding velocity and the term in parentheses is the local shear rate. λ is the constant referred to as "slip length". The slip length is the distance behind the interface at which the fluid velocity extrapolates to zero. The no-slip boundary condition corresponds to the case where $\lambda = 0$ (Figure 22). The physics of no-slip boundary states that flowing fluid comes to rest just at the point where it meets the solid surface. At the macroscopic level, it is well accepted that the boundary condition for a viscous fluid at the solid wall is one of "no-slip", that is, the fluid velocity matches the velocity of the solid boundary. Since the no-slip condition holds true for several rough surface systems, it is intuitive to postulate that surface roughness promotes stick at a fluid boundary [195].

MD simulations have in fact demonstrated the existence of slip for surfaces with no lateral corrugation of the potential of interaction [196–200]. In principle, in cases where there is strictly

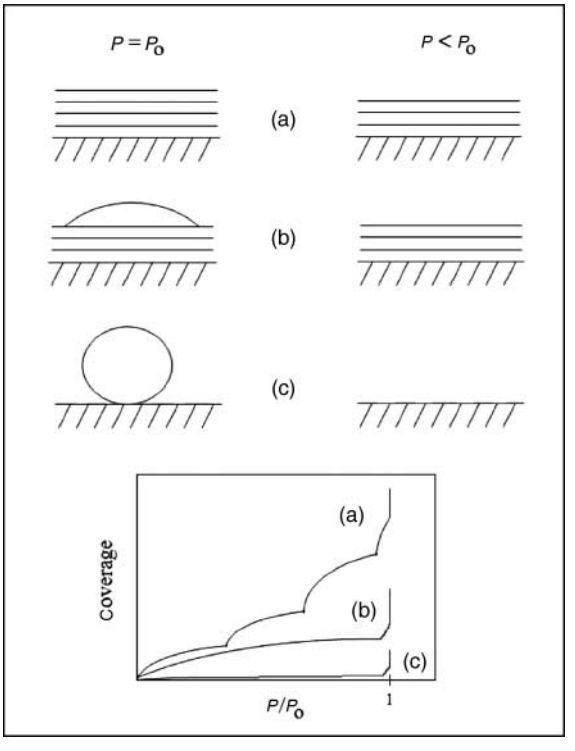

Figure 21. Three types of wetting behavior at (left) and below (right) the saturated vapor pressure, along with their corresponding forms for the vapor pressure isotherm. (a) Complete wetting, (b) incomplete wetting, and (c) nonwetting. The wetting behavior of an adsorbed material has been related to its frictional properties and slip length: the no-slip boundary condition may break down for cases of (b) incomplete and (c) nonwetting. Reprinted figure with permission from B.P. Miller *et al.*, Journal of Low Temperature Physics 157, p. 252, 2009 [536]. Copyright (2009) from Springer.

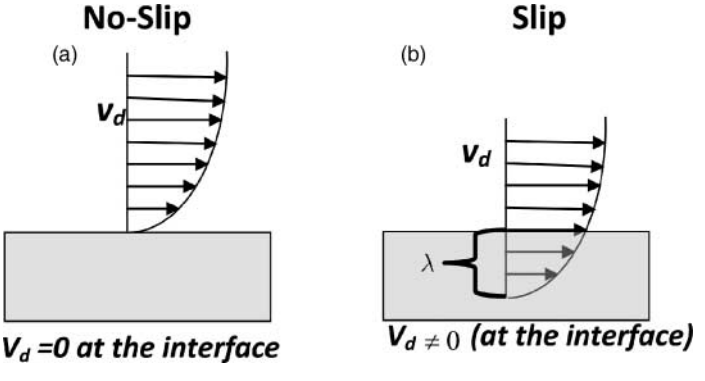

Figure 22. Schematic slip length, λ, definition: (a) velocity difference (v_d) between the film and the substrate for the no-slip boundary condition, where $\lambda = 0$ and (b) velocity difference when slip occurs, with $\lambda > 0$.

no corrugation, the slip length could be infinite. The situation is hypothetical, however, since in actual systems both surface atomic corrugation and surface roughness features are present, and friction arising from alternative mechanisms (electronic, electrostatic, etc.) must also be accounted for. Realistically, walls do possess structure and those points of localized preferential attachment

produce stick. The effects of topographical irregularity on fluid flow are thus likely to result in liquid pinning to the surface, giving rise to the no-slip boundary condition.

Barrat, Bocquet, and coworkers have [199–202] demonstrated that although it is well known that, at a macroscopic level, the boundary condition for a viscous fluid at a solid wall is one of "no slip" (i.e. the liquid velocity field vanishes at a fixed solid boundary), in the case of a liquid that partially wets the solid (i.e. Figure 21(b) and (c)) the no-slip condition may break down. The authors performed extensive MD simulations and showed that for sufficiently large contact angle, the boundary condition varied dramatically at the microscopic scale from that of the no-slip boundary condition (Figure 23). For example, slip lengths exceeding 30 molecular diameters were observed for a contact angle of 140°, characteristic of mercury on glass. A review of their primary results may be found in [202]. The findings have important implications for the transport properties and sliding friction in adsorbed films, as the slip length is directly related to the slip time and viscous friction damping coefficient η_{2f} defined in Equation (2) (written as $F = -\eta_{2f}v$, where v is the sliding speed of the film at the solid–film interface and F is the friction force resisting the sliding) according to

$$\lambda = \frac{\eta_{3f}}{\eta_{2f}}, \tag{45}$$

where η_{3f} is the bulk viscosity of the adsorbed film material. The slip length in many publications is denoted by $b = \eta_3/k$, where η_3 is the bulk viscosity and k the viscous friction coefficient denoted here as η_2.

To evaluate the friction in the system, one must consider what happens if the film slips at the film–substrate interface. Slip length is a term best understood by considering the velocity of the film and the substrate at the interface. In the no-slip limit, the difference in velocity between the film

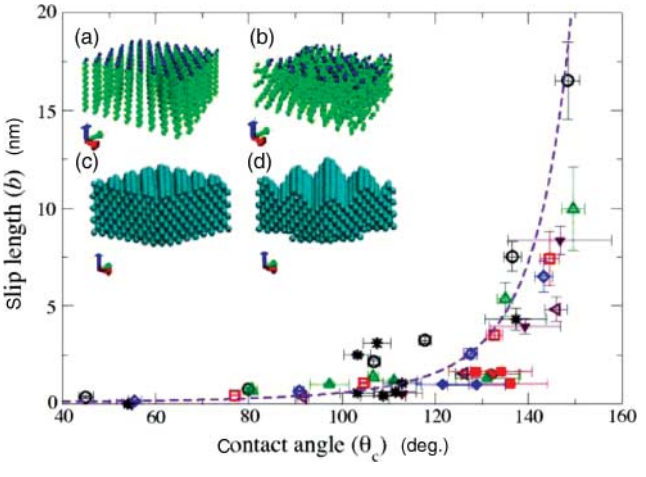

Figure 23. Water slip length b as a function of contact angle for various surfaces. Inset: MD simulations of an atomistic water model allow studies of hydrodynamic slippage of water at various surfaces, both inorganic (diamond-like and Lennard-Jones models) and organic (silane monolayers). Slippage, which is quantified by a slip length, is found to exhibit a 'quasi-universal' dependence on the macroscopic contact angle characterizing the surface wettability. Slippage is larger for more hydrophobic surfaces. This result can be understood on the basis of a scaling description of the molecular friction phenomena occurring at the water–solid interface. Various symbols correspond to various surfaces (diamond-like, Lennard-Jones, alkylsilane chains). The dashed line is a scaling law prediction. Reprinted figure with permission from D.M. Huang *et al.*, Physical Review Letters 101, art#226101, 2008 [201]. Copyright (2008) by the American Physical Society.

and the substrate at the interface is zero. Since the velocity of the film decays exponentially away from the interface, the velocity *difference* grows in the positive z-direction.

If the slip occurs at the interface, the velocity difference between the film and the substrate is not zero, but is of some finite value. The velocity difference grows in the positive z-direction. If one were to map the velocity profile in the no-slip case on to the velocity in the slip case, then there is some distance inside the substrate at which the velocity difference would again be zero (Figure 22). The distance into the substrate at which above condition is met is defined as the slip length λ. A longer slip length indicates that the velocity difference at the interface is greater and the frictional force between the layer and the substrate is low, and the total acoustic impedance of the material, if in contact with an oscillating substrate, includes an additional term due to slip

$$\frac{1}{Z_{\text{tot}}} = \frac{1}{\eta_{2\text{f}}} + \frac{1}{Z_{\text{f}}}. \tag{46}$$

Equation (46), which applies to solid surfaces in contact with arbitrarily thick fluids, is similar in form to Equation (37). The system treated by Equation (37) is a sliding adsorbed film in contact with a bulk gaseous or fluid phase, while Equation (46) applies to a uniform bulk fluid material that slips at the interface and would have acoustic impedance Z_{f} if no slippage was present. If, however, the viscosity of the fluid in contact with the substrate were to be locally reduced at the interface, then Equation (46) would generate an artifact, indicating apparent slippage even for no-slip boundary conditions (Figure 24) [92]. A reduced viscosity layer can in fact replace a slip length, and mechanical experiments alone do not distinguish the two representations. Techniques such as Neutron reflectivity [203] are, however, capable of detecting zones of reduced density, which are likely to be very thin and material system-dependent.

2.3.1.2 *Response of an immersed QCM with an adsorbed boundary layer* Given that QCMs have been increasingly utilized in the monitoring of the deposition of a wide range of macro- and micromolecular systems immersed both in bulk gaseous and liquid phases, a wide range of theoretical studies have been devoted to QCM acoustic response in immersed geometries more complex than those represented by Equations (37) or (46) (Figure 25). This section highlights selected contributions in this growing area.

One very important application that QCM has been used for involves chemical sensing of low levels of pollutant and contaminant materials in contact with chemically treated electrodes. Cowen *et al*. [204] derived a model that is applicable to this case, that is, surfaces that have been chemically

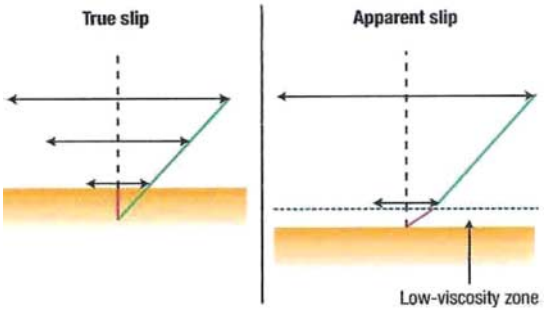

Figure 24. (color online) Schematic of how slip length λ may be mistaken for apparent slip in the event that the viscosity of the fluid becomes lower at locations close to the interface, from Granick (2003). Reprinted figure with permission from Macmillan Publishers Ltd, Nature Materials 2, pp. 221–227, 2003 [92]. Copyright (2003).

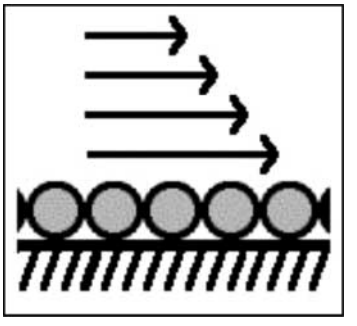

Figure 25. Sliding of an adsorbed film in the presence of a bulk medium (gas or liquid).

or physically modified to alter surface adhesion, or coated with one or more layers to amplify their response to any change of mass or material properties. They obtain a formalism that provides a unified view of the modification in the shear motion in acoustic wave systems by multiple finite thickness loadings of viscoelastic fluids. Their model encompasses QCM and other classes of acoustic wave devices based on a shear motion of the substrate surface and is also valid for both liquid and solid films. As a specific example, they examine the transition of a coating from liquid to solid that is modeled, and a correspondence between parameters from this physical model and parameters from alternative acoustic impedance models is explicitly provided. The characteristic changes in QCM frequency and dissipation as a function of thickness are presented for a single-layer device as the coating is varied from liquid as that of an amorphous solid. Results for a double-layer structure are also explicitly given, and the extension of the physical model to multiple layers is described. The author's approach provides a framework for considering how interfacial slip boundary conditions can be incorporated into the acoustic impedance used within circuit models of acoustic wave devices. Results are presented for interfacial slip occurring at the substrate–first layer interface using a single real slip parameter, s, which has inverse dimensions of impedance. In terms of acoustic impedance, such interfacial slip acts as a single-loop negative feedback. It is suggested that these results can also be viewed as arising from a double-layer model with an infinitesimally thin slip layer which gives rise to a modified acoustic load of the second layer.

Ellis and Hayward [205] have described a mathematical relationship between the slip parameter, which describes the relative motion of the surface and liquid in the transverse-shear model, and the slip length for a slip boundary condition applied to the transverse-shear model for a quartz-crystal acoustic wave device. Their theory reduces empirical determinations of slip to a one-parameter fit and shows that the magnitude and phase of the slip parameter can be linked to the slip length. The magnitude and phase of the slip parameter are shown to depend on one another, and an experiment is described to compare the effects of liquid–surface affinity on the resonant properties of a transverse-shear mode wave device by applying different polar and nonpolar liquids to surfaces of different polarity. The theory is validated with slip values determined from the transverse-shear model and compared to the slip length values from literature. The authors report that agreement with literature values of slip length is within one order of magnitude. The same group has written multiple reviews on this and related topics [83,206].

Du *et al*. [207] have obtained a formalism which predicts the influence of laterally heterogeneous slip (for instance, induced by nanoscopic air bubbles) on the shift of the resonance frequency and bandwidth of quartz crystal resonators immersed in liquids. The lateral heterogeneities are decomposed into their Fourier components, and the distribution of slip lengths provides a boundary condition, giving rise to a small, secondary flow field. They report that mean stress exerted by this secondary field induces a shift in resonance frequency and bandwidth. In addition, they report

that if the slip length is much smaller than the penetration depth of the shear waves and smaller than the lateral correlation length, the effects of the heterogeneities scale as $n^{3/2}$, with n being the overtone order. Their results are consistent with experimental results obtained with a gold-coated resonator in contact with various hydrophilic liquids.

The same group has examined by means of a continuum mechanics model the acoustic responses of molecular films with continuous viscoelastic profiles adsorbed on solid–liquid interfaces probed by QCM [207]. The numerical results show that the shift of resonant frequency and the change of dissipation factor of a QCM are determined mostly by the change of viscoelastic profile of the layers in solution adjacent to the quartz–solution interface due to the adsorbed molecular film. For films with the equal adsorbed mass, the changes in resonant frequency and the dissipation factor vary approximately linearly with the width of the film–solution interface in the profiles. They report that other viscoelastic properties of the adsorbed films are also affected by the profiles.

Kasemo and coworkers [208] have performed a theoretical analysis of dissipative effects in quartz crystal resonator applications in response to dynamics of complex biological fluids and soft polymer films. They show how viscosity (internal friction) and slippage (interfacial friction) of the sample influence the acoustic characteristics of the quartz resonator and present rigorous expressions for the resonant frequency and damping of the quartz crystal that allow quantification of friction effects. They also show that the QCM can be used as a "mechanical spectroscopy tool" by monitoring its response at different resonator frequencies. Possible applications of the results for biological sensor applications are discussed as examples of how the formalism that they derive can be applied to real-world applications.

Finally, Kanazawa and coworkers [209] report studies of how one can perform initial tests of an immersed QCM's response in order to perform a simple test by which the user could make a quick initial assessment of the instrument's performance. When a smooth quartz crystal resonator is immersed from air into a Newtonian liquid, they note that both the resonance and loss characteristics of the QCM are changed, and a minimum of two experimental parameters is needed to characterize these changes. One of the changes is that of the resonant frequency. The second is characterized by either a change in the equivalent circuit resistance or a change in the quality factor. They define "Newtonian signatures" and establish the sensitivity of these signatures to surface roughness and related experimental artifacts.

2.3.2. *The blowoff apparatus*

The viscous-friction law and frequent lack of static friction in the unconfined geometries associated with adsorption on QCM electrodes, while entirely consistent with atomic-scale theories of friction at clean crystalline interfaces (Section 3), are unheard of in the macroscopic world, where Amontons' law, Equation (1), and static friction phenomena are ubiquitous. The viscous friction law is also virtually absent for nanoscale measurements recorded for films present in molecularly confined geometries, for example, those associated with AFM and SFA techniques (Sections 2.4 and 2.5). For example, experiments by means of SFA have revealed that bulk fluid-like behavior tends to break down when two mica sheets are brought into very close contact (approximately one–six monolayers, depending on the specific material and shear conditions [210–213]; see also Sections 4.3.1 and 4.7.2), and the breakdown is frequently interpreted as a solidification or transition to glass-like behavior. Since the shear rate and sliding speeds for the QCM and the AFM and SFA techniques vary by more than five orders of magnitude, the question has arisen as to whether the difference between static and viscous friction originates from the difference in confinement geometry or from the shear rate at which the measurements are recorded.

Mate and coworkers [214–216] resolved this issue in 2000 by constructing a "blowoff apparatus" (Figure 26) to measure the shear response of molecularly thin liquid films on solid substrates

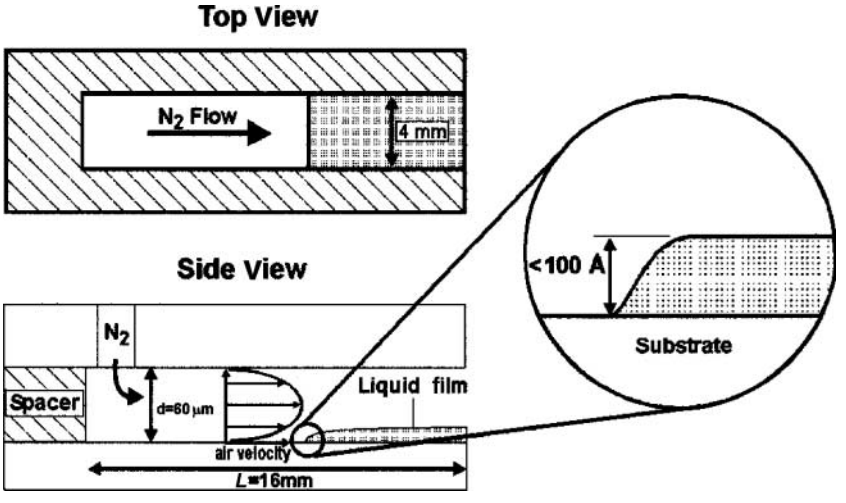

Figure 26. Schematic of the blowoff apparatus. No static friction is observed for a range of slow sliding speeds, and the viscous friction law is reported to govern the motion of the film in this unconfined geometry. Reprinted with permission from M.A. Scarpulla *et al.*, Journal of Chemical Physics 118, pp. 3368–3375, 2003 [216]. Copyright (2003) by the American Institute of Physics.

subjected to an applied air stress. Unlike the SFA, where the sheared film is confined between two solid surfaces, the film in the blowoff apparatus is confined by a single solid surface, resulting in a dramatically different rheological behavior. Having atoms and molecules slide against a single solid surface makes the blowoff technique similar to the QCM technique, but with four orders of magnitude slower sliding speeds ($10\,\mu$m s^{-1} versus 1 cm s^{-1}). Previous studies with the QCM technique demonstrated that the energy dissipation occurs through the viscous mechanisms of exciting phonons and electronic transitions for atoms sliding cross surfaces at speeds $\sim$1 cm s^{-1}. At slower sliding speeds, the slippage is less likely to occur, as atoms become trapped in the potential wells between the surface atoms; so energy dissipation during sliding becomes more like solid–solid friction then as viscous friction. Such effects, or possibly pinning at atomic step edges, have been reported for Kr layers sliding on Au [181] and for neon layers sliding on Pb [182].

Mate and coworkers convincingly demonstrated that shearing liquid films adsorbed on a solid surface in an unconfined geometry display viscous friction while the same liquids sheared between two solid interfaces in an SFA at the same thickness and shear rates display static friction. These results demonstrate convincingly that static friction effects are greatly enhanced for films in confined geometries (Figure 27). The SFA technique, which probes the simplest type of confined geometry in thin-film systems, is described in the following sections.

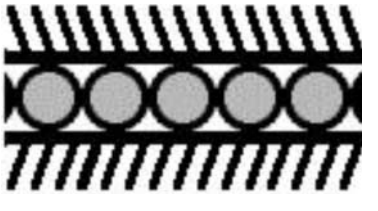

Figure 27. Sliding of an adsorbed film in a planar geometry that is confined between two solids and similar to that of a film confined within the cross-mica cylinders of an SFA.

2.4. *Thin films confined between parallel surfaces*

2.4.1. *The SFA*

The SFA is another experimental probe that is closely identified with microscopic studies of friction. It was invented close to 45 years ago and was adapted for friction measurements by Israelachvili in 1973 [21]. It has been employed to document the dependence of friction on contact area (Figure 28) and crystalline orientation and was the first technique to provide definitive evidence for the existence of wearless friction between atomically uniform surfaces. As for the case of AFM measurements, static friction and slip–stick phenomena are routinely observed in the SFA geometry. It is in this geometry that the viscous friction law, routinely applied to systems in the geometries discusses so far, begins to break down.

The SFA apparatus takes advantage of the fact that the cleavage surface of mica is molecularly smooth, with atomic-step-free areas as great as 10 cm^2 from which 1 cm^2 facets are cut. When two mica surfaces are brought into contact, an asperity-free interface is thus formed. The traditional apparatus consists of two cleaved mica surfaces glued to crossed mica cylinders. The contact area and distance between mica surfaces is determined by means of optical-beam interferometry, with a resolution in the order of 0.2 nm or better [21,217]. The mica surfaces are mounted in such a way that they can be moved horizontally or vertically, and the normal and lateral forces are measured directly from a force-mapping spring.

Although the SFA has occasionally been used for direct measurements of friction between two mica surfaces [218], its more routine use has involved lubricant layers that are squeezed between the contacting surfaces [72,219–225]. If one of the surfaces of the SFA is mounted so as to allow lateral movement along one of the axes, and then it can be used to detect the response to lateral and shearing movements. It thus allows for measurements of sliding friction between surfaces separated by molecularly thin films. This is because the squeezing action of the pressed mica cylinders brings them to within just a few molecules proximity of each other [226,227]. It should be noted that SFA and modified SFA techniques are not limited exclusively to mica surfaces [228,229] or low speeds [171].

SFA measurements have generated a wide range of results that indicate that solidification and melting of films is occurring within the confined geometry of the device [230–232]. In general, measurements are reported for increasing normal force as the mica planes are squeezed together, "force measurements", or alternatively through shear force measurements.

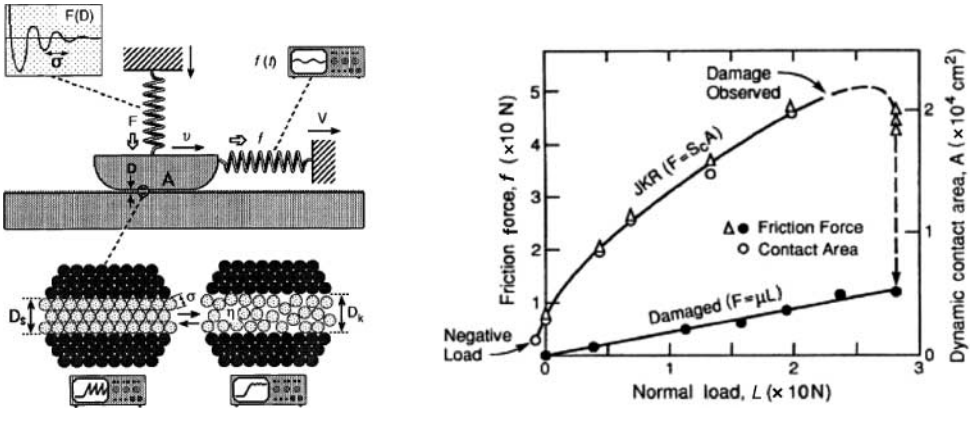

Figure 28. The SFA has been employed for direct measurements of true contact area, friction, and normal load. Left: Reprinted figure with permission from Macmillan Publishers Ltd., Nature 374, pp. 607–616, 1995 [86]. Copyright (1995). Right: Reprinted figure with permission from Israelachvili (1992) [234].

For force measurements, the surfaces are brought into progressively closer contact and the effect of the proximity of the surfaces on the structure of the initially liquid film is monitored by measuring the perpendicular forces between the surfaces. In most pure, nonaqueous liquids, the short-range interaction is a solvation force, which has been extensively studied for temperatures above the melting point T_m [233,234]. It has been regularly observed that the force oscillates between repulsive maxima and attractive minima, usually with a period close to the average molecular diameter of the material being studied. This behavior has been observed up to 10 molecular diameters in thickness for molecules that are nearly spherical, but falls off more quickly for nonspherical molecules [233,235]. The behavior is observed to persist into supercooled regimes below T_m.

If the two mica surfaces are made to slide relative to each other with a molecularly thin film between them, a viscous friction form is expected to occur for liquid-like behavior, assuming that shear is occurring within the film and not at the mica-liquid boundary. In principle, this friction force should be directly proportional to the area in contact, the viscosity, and the sliding speed, that is, very similar in form to that assumed for a sliding adsorbed layer, $F/A = \eta_2 v$.The friction force for such a system is additionally assumed to fall off linearly with the surface separation. Experiments have shown that this bulk fluid-like behavior tends to break down for mica sheets that are separated by 1–6 or more monolayers, depending on the system [210–213] (also see Sections 4.3.1 and 4.7.2) and the breakdown is frequently interpreted as a solidification or transition to glass-like behavior [236]. When the system is in such a "solid-like" state, static friction is observed to be present: a critical shear stress is required to initiate sliding. Depending on the system studied, the transition to solid-like behavior has variously been reported to be load-dependent [227], gradual [226], or abrupt [73,210,211]. The variety of results observed up to 2001 has been reviewed by a number of authors [72,73,237]. The transition to solid-like behavior is observed at temperatures *above* T_m, and recent work has revealed that model films under increasing confinement exhibit the viscosity enhancement and the nonlinear flow properties characteristic of a sheared supercooled liquid approaching its glass transition [238]. The result, in conjunction with theory [239], resolves apparent contradictions in the earlier publications.

There have been some discrepancies in the SFA literature concerning the properties of liquids confined below a few nanometer or less [240–245], but the origin of the discrepancies is now known to be contaminated by Pt nanoparticles [246,247]. In particular, Perkin *et al.* demonstrated in 2006 that when mica surfaces were prepared cleanly and with no nanoparticle contamination, the results were consistent and reproducible across a wide range of SFA laboratories worldwide. Overall, the SFA's impact on studies of confined films is expected to grow, as new X-ray related techniques emerge for probing the structure of the squeezed films within the confines of an SFA and other confined geometries [248]. Other promising techniques include combination of SFA and optical fluorescence single-molecule tracking techniques [249].

2.5. *Sliding friction of single-asperity contacts*

2.5.1. *Atomic force microscopy*

In the late 1980s, Mate *et al.* [32] adapted the newly invented scanning probe microscope for studies of atomic-scale friction. With it, they published their first observations of friction, measured atom-by-atom, in a landmark 1987 paper. An AFM consists of a sharp tip mounted at the end of a compliant cantilever (Figure 29). As the tip is scanned over a sample surface, forces that act on the tip deflect the cantilever. Various electrical and optical means (such as capacitance and interference) quantify the horizontal and vertical deflections.

Six years after its invention, a friction force microscope (FFM) was adapted to UHV conditions, for studies of sliding friction of a diamond tip on an atomically uniform diamond substrate [250]. The tip substrate contact area was estimated to be less than 20 atoms in extent, and the

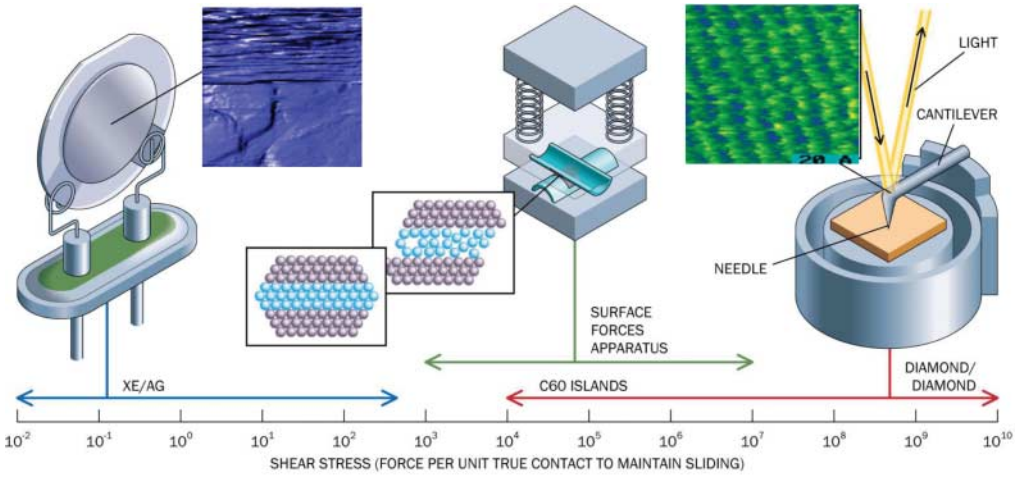

Figure 29. Shear stresses (in N m^{-2}) reported by various experimental techniques for studying nanotribology, QCM (left), SFA (center), and AFM (right). Reprinted figure with permission from J. Schneidman. The first cross-referencing of all three techniques, focusing on the effect of C60 molecules at solid–liquid interfaces was reported by Coffey in 2001 [152].

measurements were performed on both diamond (111) and (100) surfaces. Surprisingly, the data revealed no dependence of the friction force on the applied normal load. According to Amontons' law, Equation (1), this would imply that the friction coefficient is zero. But not only was friction evident, the shear stress, or force per area required to maintain the sliding was enormous: one billion Newtons per square meter, a force large enough to shear high-quality steel. As more studies emerged, it became clear that the viscous friction law, Equation (2), was also not applicable and that the shear stresses associated with the AFM geometry were on average much higher than those reported for QCM and SFA geometries (Figure 29). The elevated shear stresses are closely related to the high contact pressures at the AFM tip, whose sharpness also makes it ideal for studying friction on a truly atom-by-atom basis [77,78,251]. Accounting for such high levels of energy dissipation (which is distributed among the tip, substrate, and cantilever) at a fundamental molecular level remains to the present day a matter of great interest within the AFM community. To date, contributions to frictional energy losses from both phononic [36] and electronic [252] mechanisms have been convincingly established, demonstrating the technique's ability to probe such mechanisms. The reports are quite recent, and much progress is anticipated to occur in the near future.

2.5.2. *Friction laws for dry and lubricated AFM asperity contacts*

The earliest AFM studies revealed atomic periodicity, but not true atomic-scale resolution of defects or atomic-scale surface features [32]. The possibility of resolving such features was investigated in detail throughout the 1990s and early 2000s [253–262], and it is now generally accepted that only "noncontact mode" AFM employing frequency feedback (referred to as *frequency modulation* or *FM* technique) can reliably obtain true atomic resolution [258,259]. A significant advance in the technique was reported by Sader and Jarvis [263], who employed a frequency modulation technique to monitor changes in the resonant frequency of the AFM cantilever to monitor and detect variations between the tip interaction force with the substrate. In contrast, when data are recorded in the contact mode, the multi-atom nature of the interface obscures individual vacancies and defects and broadens the apparent width of atomic steps. The observation of an atomic lattice

in contact-mode images is now attributed to the effect of atomic lattice stick–slip motion, which is ever-present in AFM experimental studies [264] and intrinsically reflects the stiffness of the device. It also represents a major departure from the viscous friction law (Equation (2)) that governs the films adsorbed in the unconfined geometries discussed so far. Static friction and stick–slip phenomenon are ubiquitous for the AFM geometry, and in the vast majority of cases, one stick–slip event is observed per unit cell of the substrate. This is true even in cases where the atomic cell contains more than one species. Friction levels and stick–slip phenomena thus exhibit very strong dependencies on the direction that the tip moves with respect to the crystalline axes of the substrate (Figure 30). At the macroscopic scale, macroscopic contacts between solids, in general, obey Amontons law, Equation (1), and exhibit friction that is independent of velocity. For AFM contact sizes in the nanometer range, friction has been reported to increase, decrease, or be independent of sliding velocity. A logarithmic increase of friction with scanning velocity was reported, for example, [265], for polymer layers grafted on silica over a range of velocities and with four different probes. A thermally activated Eyring model was employed to analyze the data, and estimates of the interfacial shear stresses and energetic barriers to sliding were obtained. While some of the approximations that were used in the analysis lead to large variations in calculated contact areas, the fits for the shear stresses and energy barriers were consistent between the different probes. Shear stresses were found to lie mostly between 200 and 300 MPa for bare silica and between 400 and 600 MPa for the grafted layers, with barrier heights in the range $1–2 \times 10^{-19}$ J for both systems.

AFM studies of diamond, graphite, and amorphous carbon were reported to exhibit no dependence on velocity [266] so long as the scanning velocity was much lower than a characteristic slip velocity of the tip. Consequently, no velocity dependence of friction was observed for scanning speeds of up to about $10\,\mu$m s^{-1}. A logarithmic dependence was observed for higher velocities consistent with the result of Bouhacina *et al.* A different trend was reported by Bennewitz *et al.*

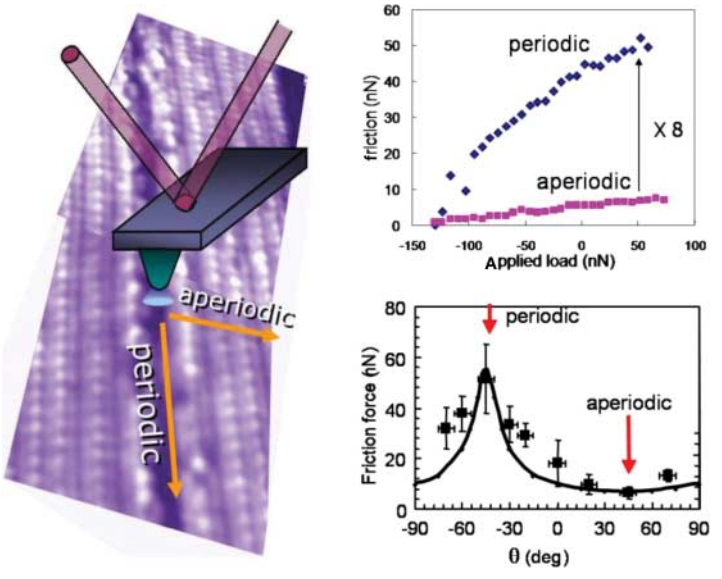

Figure 30. (color online) Friction anisotropy in decagonal quasicrystal [416]. Friction levels in periodic directions are eight times higher than in aperiodic directions. Reprinted figure with permission from J.Y. Park *et al.*, Physical Review B 74, p. 024203, 2006 [416]. Copyright (2006) by the American Physical Society.

on Cu(111) [267] and Gnecco *et al.* on NaCl(100) [268], who observed a logarithmic dependence of friction on scanning velocity for velocities less than about 1 μm s^{-1}. A thermally activated slip model and a modified Tomlinson model, respectively, were used to explain the trends observed in the data sets. A very similar model was employed by Overney and coworkers [269] to explain the logarithmic dependence of friction for *n*-hexadecane and octamethylcycloterasiloxane (OMCTS) physisorbed on silicon oxide wafers. In this case, the authors reported that interfacial liquid structuring reduced the sliding friction and that the molecular topology ultimately dictated the lubricating properties of the boundary layer. Cannara *et al.* [36] meanwhile invoked the same theory employed for phononic friction in sliding adsorbed layers to interpret AFM data recorded on surfaces of hydrogen and deuterium isotopes [37], and reinterpreted the result in terms of the spacing of the hydrogen or deuterium and not necessarily the difference in phonon frequency.

Overall, it is becoming clear that the velocity and temperature dependence is system-dependent [76], and there is a competition between thermal, adhesive, phononic, and electronic effects which ultimately determines the velocity dependence. This topic is discussed in more detail in Sections 3 and 4.

With respect to adsorbed films, in particular, Buzio *et al.* have reported a detailed study of the form of the friction laws that govern lubricated AFM contacts, particularly, those lubricated by sliding adsorbed layers of physisorbed OMCTS and squalane, which are common materials for study by alternative techniques, and may be comparable to QCM studies of physisorbed layers [270]. The studies were performed in controlled conditions, and the friction laws for nanoasperities sliding on atomically flat substrates under controlled atmosphere and liquid environment, respectively, were investigated. The group reported a power-law relation between the friction force and normal load for measurements performed in dry air, and a linear relationship, that is, Amontons' law (Equation (1)) , for junctions fully immersed in the model lubricants studied (OMCTS and squalane). They observed that the lubricated contacts display a significant reduction in friction levels, with liquid- and substrate-specific friction coefficients. They compared the results to MD simulations and found evidence that load-bearing boundary layers at the asperity junction entrance may cause the appearance of Amontons' law and impart atomic-scale character to the sliding process. Finally, they suggest a first attempt at the general criteria that may lead to nanoscale lubrication due to the presence of mobile adsorbed boundary layers.

The presence of mobile adlayers has been observed to produce Amontons' law behavior in AFM data. Mobile adlayers have also been implicated as giving rise to the atomic-scale origins of static friction [271]. As such, since mobile adlayers are present on virtually all macroscopic surfaces, their importance to date may have been underestimated in macroscopic studies.

2.5.3. *STM–QCM and related geometries*

A QCM surface electrode can easily reach speeds of cm s^{-1} to 1–2 m s^{-1}, and its amplitude of oscillation can be measured directly by means of STM [63]. The product of the oscillation amplitude with the angular frequency of the QCM yields the maximum velocity amplitude of the electrode–tip contact, and high-speed sliding friction and high strain rate studies between a single nanoasperity contact can be performed by lowering a tip into sliding contact with the QCM electrode [272].

STM–QCM has been employed to study diffusion in adsorbed monolayers, by examining the quality of the images when the oscillator is moving and stationary, and has been employed to probe whether the asperity contact regime is liquid- or solid-like, depending on the sign of the frequency shift when the tip makes contact with the surface [273]. The technique has a great potential for future studies of contact melting and/or the lubricating properties of mobile adsorbed layers in high-speed asperity contacts.

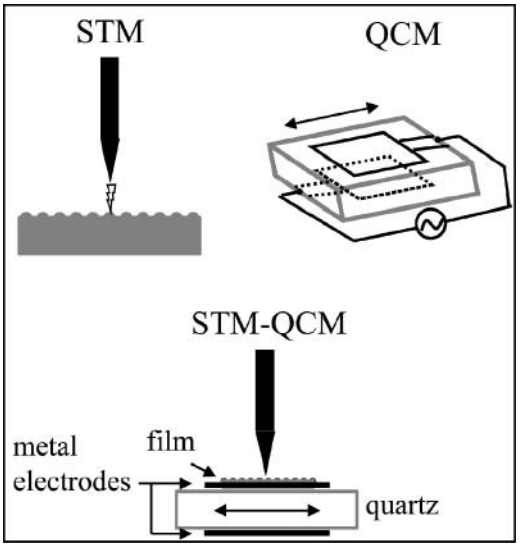

Figure 31. Schematic diagram of the STM-QCM apparatus. See also Figure 17.

Contact mechanics in a similar geometry that of a nanoindenter probe tip interacting with a QCM have also been reported [153]. This geometry allows for simultaneous measurements of normal load, displacement, and contact stiffness and changes in QCM resonant frequency. For metal–metal and glass–metal contacts in air, the QCM frequency shifts are observed to be positive and directly proportional to the contact area as inferred from the contact stiffness. Interfacial characteristics of the probe–tip contact (elasticity, contact size, and an estimate of the number of contacting asperities) can be deduced by extending a prior model of single-asperity contact to the case of multiple contacts. The tip radius is, however, quite large when a nanoindenter is employed, 0.5 mm radius of curvature tip, so it is not clear that slippage is occurring throughout the entire contact region. Nonetheless, the contact is well defined and it is possible to perform comparison studies with other QCM–probe techniques such as STM–QCM, where the sliding action of the nanoscale tip has in fact been confirmed (Figure 31).

Johannsmann [80] has reviewed the diverse variety of interactions and response of a QCM electrode in contact with a variety of counterface geometries. These include the standard thin film, a semi-infinite viscoelastic media, rough objects contacting the crystal via isolated asperities, mechanically nonlinear contacts, and dielectric films. He reports that all of the interactions can be analyzed within the small-load approximation, to provide a unified frame for interpretation and thereby opens the way for many future applications of the QCM.

2.6. *Few-asperity contact*

MEMS and NEMS devices typically have a large surface-area-to-volume ratio. As a result, a major concern in the development of such devices is friction [274]. Contact radii in MEMS and NEMS devices fall in a regime that is intermediate between the limits of single-asperity and macroscopic phenomena. The asperities that make contact in these devices may be very few in number, rendering statistical treatments inapplicable [275] (Figure 32). For example, the contacting region of an RFMEMS switch has been estimated to consist of about 10 asperities, each perhaps having 75 atoms in extent [276]. The mesoscale regime has not yet been fully explored because the majority of

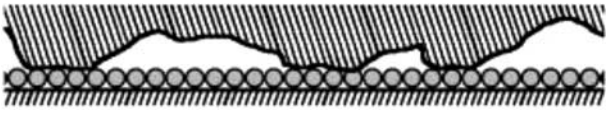

Figure 32. Few-asperity contact: a contact geometry that cannot be modeled statistically. Mesoscale investigations help bridge the gap between single-asperity and macroscopic applications and are directly applicable to MEMS and NEMS.

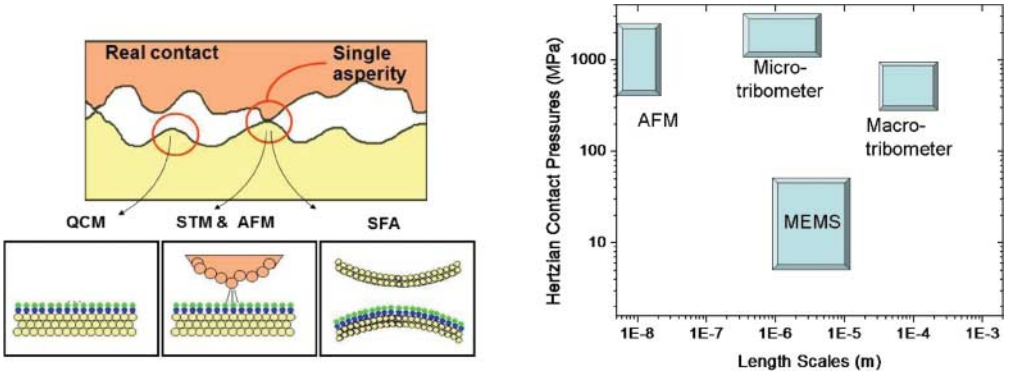

Figure 33. (color online) Length scales, contact pressures, and atomic-scale geometries associated with multiscale experimental techniques in modern tribology. Left image courtesy of M. Salmeron. Right image reprinted with permission from B.P. *et al.*, Tribology Letters. Copyright (2010) from Springer.

experimental techniques used to characterize friction do not operate in the range of forces appropriate for mesoscale studies. The pressure and length-scale regimes in which microsystems operate, moreover, is very different from other engineering applications (Figure 33), and new experimental tools are required to investigate fundamental models of friction and wear in such systems.

Two techniques suited for such studies are described in this section: the mesoscale friction tester (MFT) developed by Liechti and coworkers [277,278], and the MEMS tribometer developed by Dugger and coworkers [279,280]. These techniques, which have emerged very recently, are helping to bridge the gap between the fundamentals of single-asperity and macroscopic friction. The techniques have the potential to resolve many questions regarding friction mechanisms in the mesoscale range and also provide information of outright applicability for MEMS and NEMS applications [281,282].

2.6.1. *Mesoscale friction tester*

The MFT is a probe technique that spans AFM and SFA sliding speeds and dimensions [277]. It is capable of performing friction studies with contact radii that range from 10 nm to 10 mm and contact forces from nN to mN. Figure 34(a) shows a schematic of the MFT device. It consists of a laser diode, a beam with an attached probe as a force detector, a mirror, a polarizer, a position sensitive detector (PSD), and a sample positioning and scanning stage. All of the components are surrounded by an enclosure for environmental control. The MFT is distinguished by a force-detecting beam whose stiffness is greater than that of standard AFM beams. Commercial beads formed from a variety of materials and with diameters from a few to several hundreds of micrometers, or alternatively electrochemically etched probes with diameters from micrometers to several nanometers can be attached to the force-detecting beam to provide a wide range of contact region radii. A laser diode detects motion of the beam, in a manner similar to that of AFM.

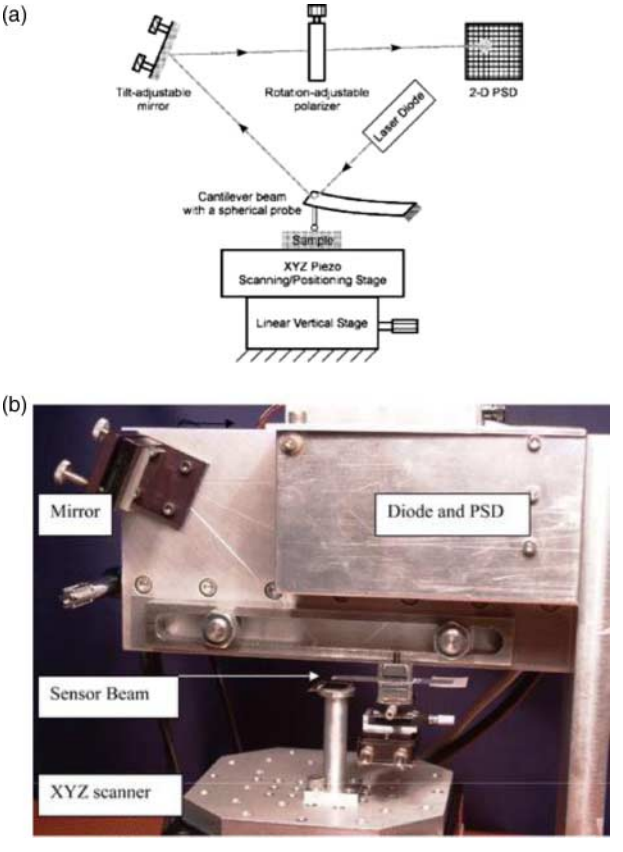

Figure 34. (color online) Schematic diagram (upper) and photograph (lower) of the MFT developed by Liechti and coworkers. Reprinted figure with permission from M. Wang *et al.*, Experimental Mechanics. Copyright (2007) from Springer.

During measurements, the sample stage, which is piezo-controlled, is moved vertically in order to bring the sample into contact with the probe until the normal contact force reaches a prescribed value. The normal force is detected by the bending deformation of the force-detecting beam. The sample stage is then scanned perpendicular to the beam axis. Friction causes the force-detecting beam to twist, and the bending and torsional deformations of the beam produce independent orthogonal movements of the laser spot on the PSD, thereby providing independent measurements of the normal contact force and the lateral friction force. Scanning speeds ranging from 0.2 to 40 mm s^{-1} have been obtained with this device, vastly expanding that available for standard AFM studies. The device has been employed for comparison studies of the sliding friction of unlubricated and lubricated contact over a wide range of sliding speeds and contact areas [278], and "quantized" friction is reported for molecularly thin films. The authors observe friction to be proportional to true contact area and stick–slip is observed to be present. The velocity dependence of friction has yet to be studied by this technique.

2.6.2. *MEMS sidewall tribometer*

Despite the major recent advances in the reliable production of MEMS devoted to fundamentals of friction [274,283,284], the majority of experimental studies of nanotribology and film sliding

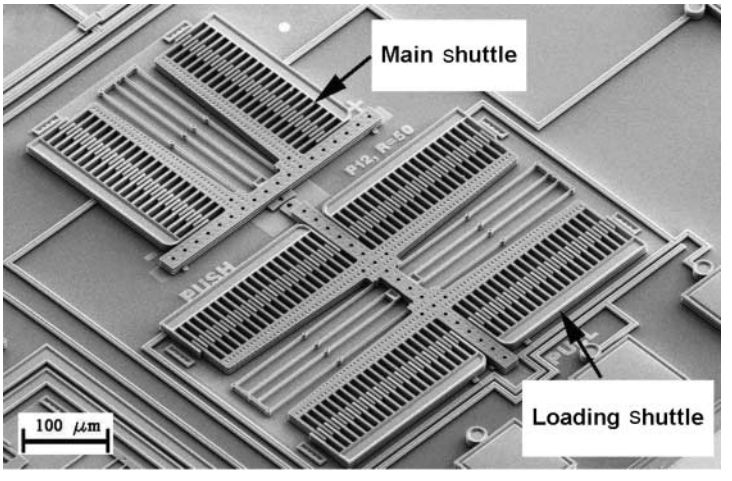

Figure 35. SEM image of an MEMS sidewall tribometer. Reprinted figure with permission from D.A. Hook *et al.*, Journal of Applied Physics 104, art#034303, 2008 [289]. Copyright (2008) by the American Institute of Physics.

to date have primarily been investigated by means of alternative techniques. This is expected to change rapidly as emerging applications in nanotechnology require studies to be performed in conditions nearly identical to the intended application [285]. To date, the vast majority of studies have been performed in engineering conditions that are not focused on fundamental understanding frictional energy dissipation mechanisms. Device preparation and cleaning procedures are, however, becoming increasingly refined, and both MEMS and NEMS devices are increasingly utilized as sensitive probes in surface science and/or UHV conditions [51,285–288].

As mentioned above, the pressure and length-scale regimes in which microsystems operate is very different from other engineering applications, and new experimental tools are required to investigate fundamental models of friction and wear in such systems. To this end, devices for quantifying friction in simplified microsystem contacts have been developed, collectively referred to as MEMS tribometers. Since the experimental apparatus are also microsystems, the surface morphology and chemistry duplicate exactly those found in more complicated systems having contacting surfaces. Unfortunately, such devices tend to fail under tribological test conditions for the same reasons that more complicated counterparts do. Nonetheless, they have generated very useful information that is key to future breakthroughs.

A typical MEMS tribometer is shown in Figure 35 [289]. The tribometer is driven using two electrostatic comb drives. One is used to pull a suspended beam into contact with a fixed semi-cylindrical post, while the other oscillates the beam back and forth along the post. Dynamic friction data for lateral motion are obtained by comparing the oscillation amplitude of the device while the post and beam are in and out of contact, respectively. Surface treatments can be evaluated in terms of friction coefficient and device lifetime. The open geometry of the MEMS tribometer allows a range of surface treatments to be pre-tested in advance of application on more complicated geometries. If unlubricated, the device lifetime is 2–3 min. Lubrication with SAMs, which are bound to the surface, increase the lifetime to hours, and in some cases days. Certain mobile layers extend the lifetime indefinitely [274,285].

2.6.2.1 *Determination of normal and frictional forces in an MEMS tribometer* The tribometer displayed in Figure 35 is fabricated by the Sandia National Laboratories Ultra-planar

Multi-level MEMS Technology 5 (SUMMiT V) fabrication process [290] and consists of a primary, or "main" shuttle for generating tangential (sliding) motion and two additional loading shuttles for applying a normal force at the sidewall surface of the main shuttle. The desired normal force at the sliding contact (Figure 35, lower) is achieved through electrostatic actuation of the loading shuttles using conventional comb drives with interdigitated fingers. Reciprocating motion is generated by individual electrically isolated banks of comb-drive actuators on each side of the shuttle. The two actuators of the main shuttle will be referred to as push and pull comb-drive actuators, while the two actuators of the loading shuttles, one close and the other remote from the contact interface, will be referred to as load and unload comb-drive actuators, respectively. The electrostatic forces generated by the main shuttle F_{m} and the loading shuttle F_{l} are given by [291]

$$F_{\mathrm{m}} = \frac{1}{2} C_{\mathrm{m}} (V_{\mathrm{push}}^2 - V_{\mathrm{pull}}^2), \tag{47}$$

$$F_{\mathrm{l}} = \frac{1}{2} C_{\mathrm{l}} (V_{\mathrm{load}}^2 - V_{\mathrm{unload}}^2), \tag{48}$$

where C_{m} ($= 6.725 \times 10^{-9}$ F m^{-1}) and C_{l} ($= 3.363 \times 10^{-9}$ F m^{-1}) are the capacitance per unit length of the comb-drive actuators of the main and loading shuttles, respectively, V_{push} and V_{pull} are the voltages applied to the push and pull actuators of the main shuttle, and V_{load} and V_{unload} are the voltages applied to the load and unload actuators of the loading shuttle, respectively. The shuttles are supported by sets of double-folded flexure suspension systems whose spring constant can be determined by a linear fit of displacement versus applied voltage squared given by

$$\frac{1}{2} C_{\mathrm{m}} (V_{\mathrm{push}}^2 - V_{\mathrm{pull}}^2) = k_{\mathrm{m}} x, \tag{49}$$

$$\frac{1}{2} C_{\mathrm{l}} (V_{\mathrm{load}}^2 - V_{\mathrm{unload}}^2) = k_{\mathrm{l}} x, \tag{50}$$

where the left-hand side components are equivalent to Equations (47) and (48), k_{m} ($= 0.384$ N m^{-1}) is the spring constant of the main shuttle's folded flexures, and k_{l} (0.128 N m^{-1}) is the spring constant of the loading shuttles' folded flexures, that is, the suspension stiffness, and x is the displacement from equilibrium.

The main shuttle possesses a long extension that allows contact with the two loading shuttle protrusions. When a voltage is applied to the comb-drive actuators of the main shuttle, the structure moves parallel to the contacting interfaces, generating the shear (friction) force. The loading shuttles apply a normal force to the sidewall interfaces. A cylindrical protrusion at the end of each loading shuttle can be brought into contact with the main shuttle by applying a suitable voltage to the comb-drive actuators of the loading shuttle.

The normal force at the contact is the sum of the mechanical restoring force of the suspension system of the loading shuttle and the electrostatic forces generated by the load and unload actuators, and the friction force is determined from a balance between the electrostatic force generated by the push and pull actuators of the main shuttle and the restoring force of the suspension springs. The normal and frictional force determinations assumed here allow for the determination of the friction coefficient if the system is governed by Amontons' law, Equation (1). An alternative approach for determining frictional forces in this system involves capacitance measurements of the response of the system to frictional damping, as described next.

2.6.2.2 *Capacitive ringdown measurement technique to measure force of friction* An additional bank of combs can be added to the standard device, whose purpose is to capacitively measure

the shuttle's amplitude of motion [285]. This allows for the measurement of the sliding friction using a ringdown technique similar to that used to measure damping in QCMs [292,293]. In this method, the sensing comb is biased by a constant voltage V_{bias}, and the main shuttle is displaced by applying a voltage to the pull actuator. A constant load is then applied to the main shuttle by the loading shuttles, and finally the voltage is dropped on the main shuttle, which releases it and allows it to oscillate at its resonant frequency. There is a direct relationship between the velocity of the oscillating shuttle and the current flowing into and out of the sensing combs given by

$$i = C_{\text{sense}} V_{\text{bias}} v, \tag{51}$$

where i is the current flowing into and out of the sense comb, V_{bias} ($= 9.515\,\text{V}$) is the constant voltage applied to the sense combs, C_{sense} ($= 3.363 \times 10^{-9}$ F m^{-1}) is the capacitance per unit length of the sense combs, and v is the velocity of the main shuttle. Therefore, a measure of the current flowing into and out of the sense combs at a constant voltage gives a measure of the velocity of the comb. A relationship between the change in the peak velocities and the force of friction is given by an analysis of the equations of motion of the main shuttle given by

$$\frac{\mathrm{d}^2x}{\mathrm{d}t^2} + \gamma \frac{\mathrm{d}x}{\mathrm{d}t} + \frac{Ff}{m} \operatorname{sgn}\left(\frac{\mathrm{d}x}{\mathrm{d}t}\right) + \omega_0^2 x = 0, \tag{52}$$

where ω_0 is the resonant frequency of the main shuttle, γ the gas damping constant, F_{f} the force of friction, m the mass of the shuttle, and $\operatorname{sgn}(\mathrm{d}x/\mathrm{d}t)$ a function that represents the friction force opposing the direction of motion ($\operatorname{sgn}(\mathrm{d}x/\mathrm{d}t) = 1$ *if* $\mathrm{d}x/\mathrm{d}t > 0$ and $\operatorname{sgn}(\mathrm{d}x/\mathrm{d}t) = -1$ *if* $(dx/dt) < 0$). The peak velocities are determined by a recursive solution to the given equation of motion

$$v_{n+1} = -v_n \, \mathrm{e}^{(\gamma/\omega_0)\pi} - (-1)^n \delta, \tag{53}$$

where v_{n} is the nth half-cycle peak velocity, ω_0 and γ are defined above, n the half-cycle number, and δ the parameter that defines the linear decrease in velocity per half-cycle due to Coulomb friction. The relationship between δ and the force of friction is given by

$$F_{\text{f}} = \frac{\delta}{2\sqrt{\omega_0^2 - \gamma^2}} \mathrm{e}^{(\gamma/\omega_0)(\pi/2 - \arctan(\gamma/\omega_0))}, \tag{54}$$

therefore the force of friction is determined by a fit to the peak values of current measured per half-cycle of oscillation.

If the measurements are performed in the presence of an ambient gas that damps the motion, then the effects of the gas damping must be taken into account. This represents a more general topic of gas damping in NEMS, and MEMS, which is somewhat beyond the scope of the present work. For more samples on this topic, the reader is referred to [294] or [295]. Craighead *et al.* examined the size- and frequency-dependent gas damping of nanobeam resonators. The authors find an optimal beam width that maximizes the quality factor at atmospheric pressure, balancing the dissipation that scales with surface-to-volume ratio and dominates at small widths, against the interaction with the underlying substrate via the air that dominates the behavior of the wider devices. Meanwhile, Ekinci *et al.* presented arguments that oscillating flow of a simple fluid in both the Newtonian and the non-Newtonian regimes can be described by a universal function of a single dimensionless scaling parameter $\omega\tau$ where ω is the oscillation (angular) frequency and τ is the fluid relaxation time; geometry and linear dimension bear no effect on the flow.

2.7. *Summary comments*

In parallel with the growing body of experimental work on atomic-scale sliding friction, a growing body of theoretical literature is emerging, with a focus on the role of phononic and electronic mechanisms of energy dissipation, and the impact of surface structure and electronic properties. The theory is illuminating basic mechanisms of energy dissipation with increasingly sophisticated approaches, as discussed in the next section.

3. Fundamental theories of sliding friction

3.1. *Overview*

As outlined in Section 1, modern study of the fundamentals of friction began at least 500 years ago, when Leonardo da Vinci recorded in unpublished notebooks the laws governing the motion of a solid block sliding over a planar surface. "Amontons' law", $F = \mu N$, Equation (1) was published in 1699 along with studies reporting that the friction force did not depend on the apparent area of contact: a third well-known law, attributed to Coulomb in 1785, states that the friction force is independent of velocity for the ordinary sliding speeds [7,296,297].

Coulomb did not have the benefit of atomic-scale knowledge of surface morphology, or even the knowledge that atoms existed. In his search for a fundamental explanation for the origins of friction, he considered whether it might arise from interlocking asperities and surface roughness (Figure 36). The friction force in this scenario is obtained by equating the work performed by the friction force to that performed against the normal load as the surfaces separate to allow asperities to slide up and over each other. This model is deeply flawed however, since the potential energy stored in the "separating" phase of the motion can, in principle, be completely recovered, so there is no net energy dissipation, and therefore no friction. Coulomb thoroughly examined this as an underlying mechanism for friction, and ultimately discounted it. The idea that increased surface roughness will increase friction persisted nonetheless well into the 1970s before being definitively discounted by surface science experiments, demonstrating that films of one-molecule thick could substantially change friction, while having minimal impact on surface roughness [14,38,39,68,298].

A significant advance occurred in the 1950s, when Bowden and Tabor documented that when two surfaces touch each other, the actual microscopic area of contact A_c is much less than the

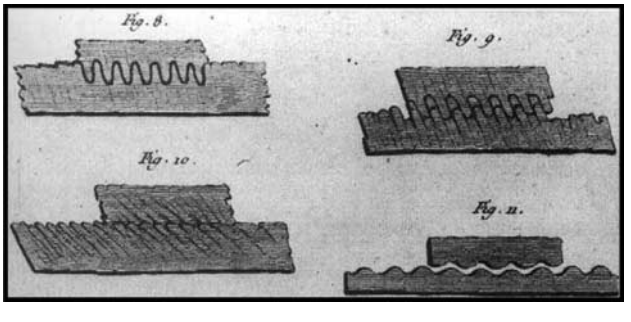

Figure 36. Coulomb's representation of rough surfaces in sliding contact, published in 1785. While establishing actual area of contact, macroscopic surface roughness was definitively ruled out as a fundamental mechanism for friction in the 1970s by the surface science experiments, demonstrating that films of one-molecule thick can substantially change friction, while having minimal impact on surface roughness. The strength and form of a periodic substrate potential at atomistic length scales does, however, have major impact on friction.

apparent macroscopic area [299]. The vast majority of surfaces are not atomically flat, and when two such surfaces touch, contact between them takes place only at their asperities. Although A_c is typically 10,000 times less than the apparent contact area, many asperities do come into contact, and locally they exhibit very high yield stresses, not unlike tiny cold-welds. The result is that friction is independent of *apparent* (macroscopic) contact area, but is proportional to *true* contact area. Their analysis went as follows.

When surfaces are forced to slide over each other, new contact regions are continuously formed, while others are severed. The shear stress needed to start and sustain sliding is called the shear strength *s*and the force to shear one contact is $A_i s$. The shear strength is a material-specific property. If the actual area of contact is constant on average, and the contacting junctions all have the same shear strength s, then the friction force is [300]

$$F_f = A_c s, \tag{55}$$

where $A_c = \Sigma A_i$ is the total real area of contact. The relations $F = A_c s$ and $F = \mu N$ can be linked, because as the normal load N increases, so does the true contact area A_c. Assuming the normal force to be collectively borne by the contact regions, the average pressure in a contact region is $P = N/A_c$, so the "adhesive" contribution to the coefficient of friction can be written as

$$\mu = \frac{F_f}{N} = \frac{A_c s}{N} = \frac{s}{P}. \tag{56}$$

The shear stress is independent of load in Equation (56), which is an implicit statement that adhesive forces are much greater than any externally applied load. Pressure dependencies are in fact quite evident for solid film lubricants such as graphite or MoS2, where the interlayer binding forces are relatively weak, resulting in a load-dependent friction coefficient. Indeed, a large body of experimental studies indicate that the shear stress s in fact rises linearly with "local" pressure N/A_c as [301]

$$s = s_0 + \frac{\alpha N}{A_c}. \tag{57}$$

Amontons' law thus applies for cases where either N/A_c is independent of load or if the local contact pressure is much greater than the adhesive contribution, that is, $N/A_c \gg s_0/a$.

In order to determine whether these conditions apply for a particular system, one must measure the contact pressure, ideally by directly measuring the true contact area as a function of normal load. A great number of methods, ranging from electrical resistance measurements to optical and acoustical methods, have attempted to perform such direct measurements [3,302] but all have shortcomings. Scientists have thus largely turned to contact mechanics modeling in order to indirectly infer true area of contact from experimental data [76], where the definition of true contact area is debated even at the atomic-scale level [303]. Nonetheless, the notion of the true contact area being linear with applied load is well grounded for a wide range of materials and surface topologies, and experimental measures of actual contact area have attained high degrees of accuracy [304–306].

Assuming this to be the case, then the coefficient, via Equation (56), may be written as $\mu = s/P$, where both s and P are properties of the contacting materials [307–311]. They are related to macroscopic materials generally by setting $s = Y/2$ and $P = 3Y$, where Y is the yield stress of the softer material [3]. Therefore, when actual material properties are considered, Equation (56) yields values for μ that lie in the range 0.17–0.2. Much larger values are routinely measured for a range of materials combinations, including ductile metals for which the theoretical estimates should be most accurate. The friction analysis of Bowden and Tabor, descriptive of the macroscopic system's response to changes in load, does not reveal the physical mechanisms that underlie frictional energy

dissipation. This information is contained in the *magnitude* of the shear stress s, the frictional force per unit area of a region of known contact.

Tabor was hard pressed to explain how friction could rise above 0.2 within the molecular-adhesion model. Jacob Israelachvili, working under Tabor's supervision, meanwhile recorded measurements of sliding of atomically uniform mica surfaces by means of the SFA technique and found significant friction levels in the complete absence of wear. New fundamental mechanisms involving wear-free friction would need to be identified to explain these results.

The fact that interlocking asperities had been discounted in the 1970s did not preclude a contribution to wearless friction arising from commensurability effects of atoms and atomic corrugation at contacting interfaces [312,313]. Improvements in UHV technology throughout the 1950s to 1970s redefined the concept of surface roughness and crystallinity, and allowed preparation of unprecedented, well-characterized crystalline surfaces, frequently covered with well-characterized films. The improvements in knowledge at the atomic scale in turn allowed theorists to make estimates of atomic-scale friction based on *ab initio* total energy calculations. Tomanek and Zhong [314], for example, reported a first principle theory of atomic-scale friction by examining a layer of Pd atoms moving across a graphite substrate using details of the interaction potentials reported in the literature. They evaluated the friction energy caused by variations of the chemical bond strength and the work against an external force (load) due to variations of the bond length along the trajectory and found only a very small dependence of the Pd–graphite interaction on the adsorption site which gives rise to a very small friction coefficient $\mu \approxeq 0.01$ for loads near 10^{-8} N. They also found μ to increase with load in agreement with experiment. The model did not include a specific mechanism for energy dissipation, but rather removed a reasonable fraction of the energy for each lattice constant of sliding motion (Figure 37(b)). As such, it did not specifically address what fundamental mechanisms were responsible for dissipating energy in the sliding system. Tabor had given this issue much thought and, by process of elimination, concluded in the late 1980s that phononic mechanisms for wear-free friction must be contributing to energy losses at nonnegligible levels [31,315]. Such mechanisms, first proposed by Prandtl in 1928 [28], occur when an atom is set into vibrational motion in response to the sliding motion of the interface. The vibrational energy is irreversibly dissipated by producing a phonon, which is ultimately manifested as friction (Figure 38).

Experimental observation of phononic friction was first reported in 1991, for QCM measurements of sliding adsorbed Kr monolayers [33–35]. At the same time. Mate and coworkers invented the FFM [32], opening up the possibility of measuring friction on an atom-by-atom basis.

The experimental breakthroughs of the early 1990s inspired much subsequent theoretical work on atomistic fundamentals of friction based on phononic energy dissipation mechanisms. Electronic excitation mechanisms for frictional energy dissipation also garnered growing interest for electrically conductive materials. Many simplifying models based on one or both of these mechanisms have been constructed in an effort to encompass the complexity of actual systems with theoretically tractable models that retain the important features of friction. Advances in computing are increasingly allowing theorists to simulate more complex systems. All such models require a description of the adsorbed–substrate interaction potential, which is overviewed briefly in the following section.

3.2. *Periodic substrate potentials*

3.2.1. *Defect-free periodic potentials*

Numerous researchers have modeled friction by applying an external force to produce horizontal motion along a substrate that is represented by a periodic substrate potential. The Lennard-Jones potential is the usual starting point for descriptions of substrate potentials, particularly where

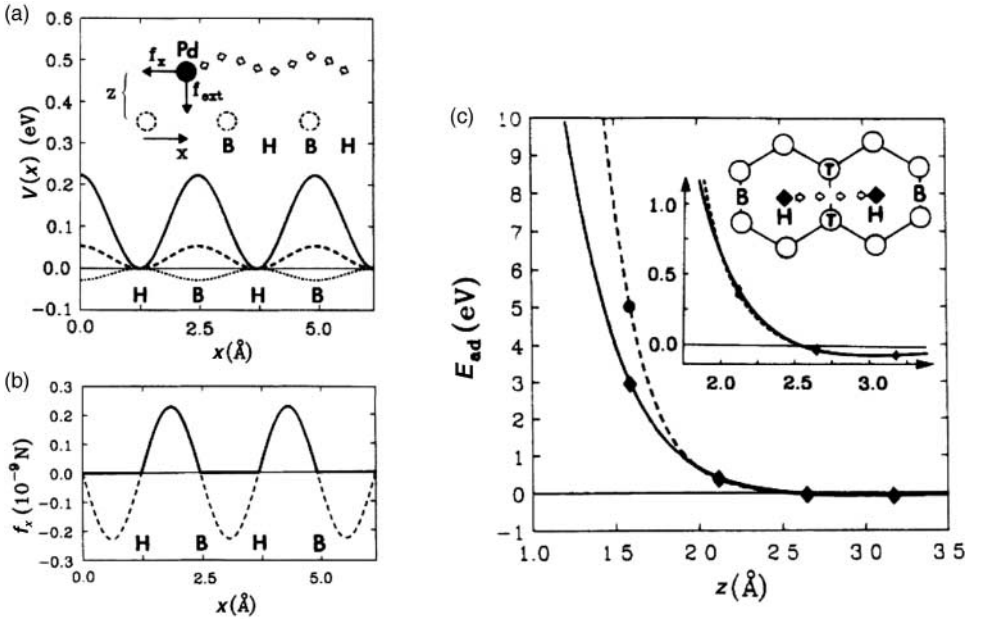

Figure 37. Tomanek's model of atomic-scale friction, a modern-day version of the Coulomb approach. Reprinted figure with permission from W. Zhong *et al.*, Physical Review Letters 64, p. 3054, 1990 [314]. Copyright (1990) by the American Physical Society. (a) Potential energy $V(x)$ of the Pd–graphite system as a function of surface position x for external forces 3 nN (dots), 6 nN (dashed), and 9 nN (solid). Inset: the adsorption geometry in top view: a possible trajectory of the Pd layer along x is shown by arrows. (b) Atomic-scale structure of the force along the surface (dashed) and the friction force (solid line) for $f_{\text{ext}} = 9$ nN. (c) Pd adsorption energy E_{ad} versus adsorption height z above the surface of hexagonal graphite for sixfold hollow (H) (solid) and the on-top (T) sites (dashed). Lower inset: an enlarged section of the graph near equilibrium adsorption, and possible side view trajectory for the Pd layer.

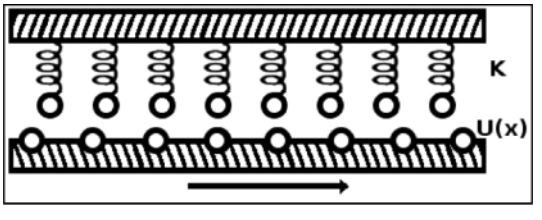

Figure 38. The Prandtl–Tomlinson, or independent oscillator model. Atoms are set into vibration when sliding over a periodic potential. The vibrational energy is irreversibly dissipated in the form of phonons (sound waves).

physically adsorbed mobile atoms are involved. It is a good approximation when describing the properties of gases, and for modeling dispersion and overlap interactions in molecular models [316]. It describes the interaction between a pair of neutral atoms or molecules as

$$V(r) = 4\varepsilon\left[\left(\frac{\sigma}{r}\right)^{12} - \left(\frac{\sigma}{r}\right)^{6}\right], \tag{58}$$

where r is the distance between particles, ε is the depth of the potential well, and σ is the separation distance at which the interparticle potential is zero. The r^{12} term reflects short-range repulsion from overlapping electron orbitals and the r^6 term reflects long-range van der Waals attractions.

Equation (58) is an approximation. The exponent in the repulsive term is chosen exclusively for ease of computation, as the square of r^6. Theoretically, it should depend exponentially on the distance. Its physical origin is related to the Pauli principle. Therefore, when the electronic clouds surrounding the atoms start to overlap, the energy of the system increases abruptly. The attractive long-range van der Waals potential does derive from physical origins, reflecting dispersion forces that arise from fluctuating dipole moments. It is especially accurate for rare-gas atoms and is a good approximation at long and short distances for neutral atoms and molecules.

Lennard-Jones interactions have been commonly used in numerical simulations of sliding friction in mobile adsorbed species of rare-gas atoms [35,117,118,318]. In general, the interactions between rare-gas atoms have been modeled by pairwise Lennard-Jones potentials, Equation (57), [318] while the interaction of the atoms with the metal substrate has been represented by a periodic potential $V_s(\boldsymbol{r},z)$ with the substrates being approximated as rigid [319]. The vector $\boldsymbol{r}$ is the position within the substrate plane and z is the distance above the first layer of the substrate. Since the compressibilites of metals are, in general, much lower than those for rare gas, deformation of the substrate is considered to be negligible.

In most cases, the analytic form chosen for the periodic substrate potential has been modeled with a formula by Steele [116], which assumes that the interaction between the atom and the substrate can be represented a sum of Lennard-Jones pairwise interactions, Equation (4) from Section 2, which is displayed here again for continuity:

$$V_s(\boldsymbol{r}, z) = V_o(z) + \sum_g V_g(z)\ \exp(i\boldsymbol{g} \cdot \boldsymbol{r}), \tag{4}$$

where V_o and $V_g$are the amplitudes of the constant and periodic components of the adsorbate–substrate potential. V_o reflects the average potential energy between the adsorbate and the substrate and V_g describes the changes in adsorbate/substrate potential with respect to the adsorbate position (surface corrugation), and $\boldsymbol{g}$ are the reciprocal lattice vectors. Equation (4) has, in some cases, been modified to include a scaling factor, f, in order to allow the effect of the corrugation of the potential to be adjusted empirically [35]. The amplitude of the surface corrugation is then $U_o = fV_g$ with $0 < f < 1$. The Steele potential represented in Equation (4) is a reasonable starting point for rare-gas solids, but far too corrugated for metal surfaces, because the delocalized conduction electrons act to smooth the potential, thus the introduction of a phenomenological scaling factor f. It moreover favors the formation of close-packed structures. The minima of $V_s(\boldsymbol{r},z)$ have historically been assumed to be located at the threefold hollow sites of these closed packed structures (Figure 39). This is a very intuitive assumption since when stacking structures at the macroscopic scale, the most stable location is expected to be in a hollow site and not directly atop of an underlying sphere. Recent experiments have revealed, however, that in many cases the most attractive adsorption sites are directly atop substrate atoms rather than in the hollows [320]. The phenomenon has been termed "anticorrugation". Newer approaches for developing accurate potentials are thus required, and in general have been obtained by using parameters derived on the basis of *ab initio* calculations and fits to data, particularly HAS data [71,103,104,321,322].

Bruch, for example, has used the energies (frequencies) of the frustrated translational phonon modes to determine the surface corrugation interaction potential for krypton on graphite and generalized the results to other adsorbate–substrate combinations by adapting the parameters to reflect the surface structure [71,115,323]. Bruch employs Equation (4) for the form of the potential and sets the sign of V_g to positive for the routine case of adsorption in threefold hollow sites and

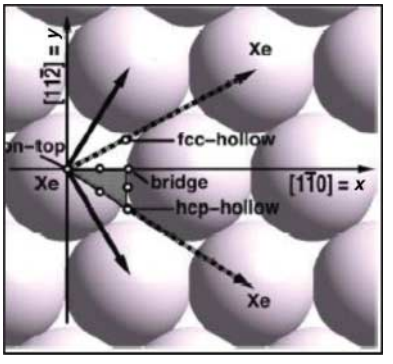

Figure 39. Top view of a Cu(111) surface, with on-top, bridge and threefold hollow sites labeled. Reprinted figure with permission from M.C. Righi *et al.*, Physical Review Letters 99, art#176101, 2007 [324]. Copyright (2007) by the American Physical Society.

negative for "anticorrugation" systems where adsorption is observed to occur on top of the substrate atoms (see Section 2.1.1). The surface corrugation, U_o, is then estimated to be $U_o = -8V_g$, for the case of anticorrugation ($V_g < 0$), and $U_o = V_g$, for "conventional" corrugation ($V_g > 0$).

The discussion in this section has so far treated perfect crystalline substrates with atoms adsorbed at equilibrium distances above the surfaces. Three selected examples are highlighted next, to demonstrate how more complicated scenarios might impact the substrate potential.

3.2.2. *Impact of an external load on a periodic potential: a case study of confined rare gases*

An external force on an adsorbed layer might be present in a strongly confined and squeezed system, or due to the presence of an external field. This case has been considered by a number of researchers. Righi and Ferrario [321,322,324], for example, proposed a model potential function to describe the interaction between rare-gas atoms and a metal surface in such circumstances with parameters derived on the basis of *ab initio* calculations. They focus on applications involving the tribology of sliding adsorbed monolayers, in particular, studying the impact of applying an external load on a sliding physisorbed monolayer. Their central result is to show that the friction of anticorrugated systems can dramatically be *decreased* by applying an external load, a behavior that is completely counterintuitive to what one would expect from the macroscopic Amontons' law. The authors attribute the results to quantum mechanical effects that induce a transformation from anticorrugation to corrugation in the near-surface region. The load-driven modifications occurring in the potential energy surface for different rare gas–metal adsorbate systems, namely Ar, Kr, Xe on Cu(111), and Xe on Ag(111), were calculated and in all cases a drop in friction, referred to as a "pressure-induced collapse", is observed. The authors argue that this is expected to occur for a wide variety of rare-gas–metal systems.

3.2.3. *Impact of coverage on periodic potentials: a case study of confined Xe/Ni(111)*

Buldum *et al*. have also analyzed the dynamics of confined xenon atoms, modeling Xe atoms at submonolayer to monolayer coverages between two Ni(110) slabs in relative motion [325–327]. They performed atomic simulations by using classical MD with realistic empirical potentials for the Xe–Ni interactions. The resistance of the xenon layer at various coverages against external loading force was examined, and the critical forces required to destroy the layer were determined. In addition, the relative motion of slabs in the lateral direction were investigated under constant

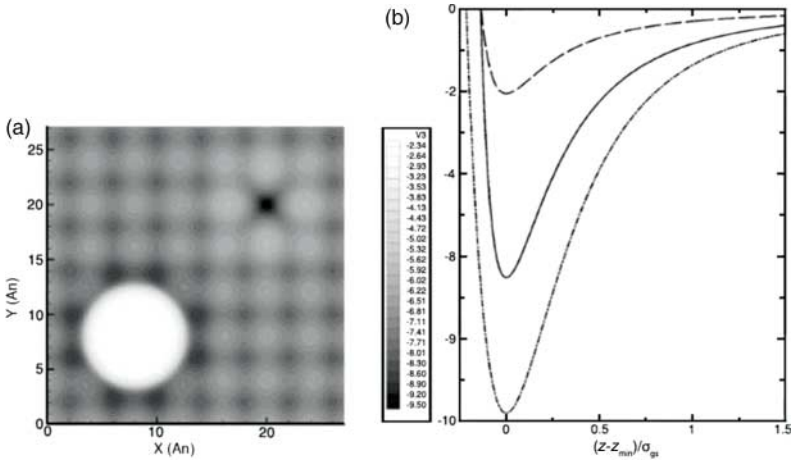

Figure 40. (Left) Potential energy $U(x, y)$ versus lateral position for one Mg adatom at $(x, y) = (8.02, 8.02\,\text{Å})$ and one missing surface atom at (20.05,20.05 Å). The scale is in units of the well depth of the gas–Mg atom pair potential (15 K). (Right) Potential energy $V(x, y, z)$ as a function of normal distance above the pit (dash-dotted), and above a surface atom in the unperturbed surface (full curve). The curves are shifted so that their minima coincide. Reprinted figure with permission from S. Curtarolo *et al.*, Physical Review E 59, p. 4402, 1999 [328]. Copyright (1999) by the American Physical Society.

normal force, for coverages ranging from zero to the monolayer xenon. The variation of potential energy, lateral force, and local hydrodynamic pressure were calculated, yielding an interesting result: the corrugation of the potential energy associated with sliding had a minimum value at submonolayer coverage, so sliding friction would be lowest at that particular coverage.

3.2.4. *Impact of defects on a periodic potential: a case study of Ne adsorption on Mg*

Cole and coworkers [328] have studied the impact of defects on the interaction potential of neon atoms with a Mg substrate. The authors assume that both Ne–Ne interactions and Mg–Ne atoms interact with a Lennard-Jones pair potentials (Equation (4) and (57). The goal of the study is not to produce strict quantitative accuracy, but rather to examine the impact on the adsorption potential of adding an extra Mg atom atop the substrate or removing one Mg atom from the substrate so as to produce a pit. Significant alterations to the potential occur in the vicinity of the defects, as is to be expected (Figure 40). The results demonstrate that atomic-scale comparisons between theory and experiment are best performed in cases where substrates are highly clean and uniform at the atomic level.

First principles models of phononic friction are now presented, including discussions of theoretical progress on the topic of incorporating defects into perfect crystalline substrates, and the use of disorder to tune and control friction. Electronic contributions to friction will be discussed in Section 3.4.

3.3. *Phononic mechanisms of friction*

"Phononic" friction occurs when atoms close to one surface are set into motion by the sliding action of atoms in the opposing surface, producing sound wave vibrations that are referred to as phonons. All vibrational energy associated with the creation of phonons is eventually dissipated as heat, and the microscopic process is manifested as friction. Phonon models of friction are most

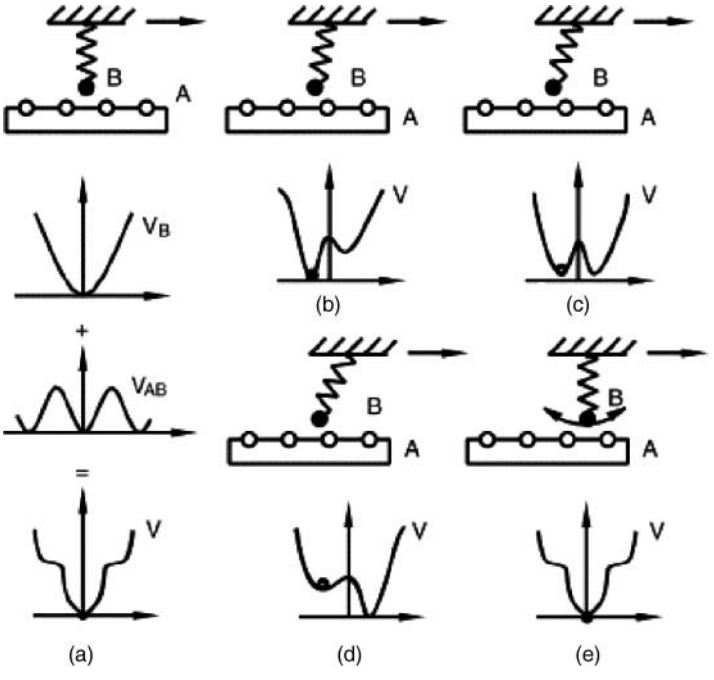

Figure 41. (a–e) Detail of motion of one atom in the independent oscillator, or Prandtl–Tomlinson model. When an atom moves to a position where the barrier between two minima (b–d) has disappeared (e), it is set into vibration and the energy is dissipated as a phonon. Reprinted figure with permission from Z. Xu and P. Huang, *Study on the Energy Dissipation Mechanism of atomic-scale friction with composite oscillator model*, Wear, 262, pp. 972–977 [343]. Copyright 2007, with permission from Elsevier.

easily constructed for solids, where there are clear and simple geometric arrangements of the constituent atoms. Prandtl and Tomlinson are credited with publishing the first model of phonon friction, which described how wear-free friction might originate at the microscale from relative motion of atomic lattices in sliding contact [28,30].

3.3.1. *Prandtl–Tomlinson, or independent oscillator model*

As mentioned in Section 1, first-principles' theory of "wearless" friction [26,27] was suggested as early as 1928 by Prandtl [28] involving phononic, or lattice vibration mechanisms. Decades later, the model came to be known as the "Tomlinson" model, based on a 1929 paper by Tomlinson paper entitled "Molecular origins of friction" that focused on adhesive contributions to friction [30]. Ironically the paper by Tomlinson in 1929 does not contain the model now known as "Tomlinson's model", but Prandtl's 1928 publication does [28]. In this review, it will be referred to as the "Prandtl–Tomlinson" model. Both papers are included here as appendices.

The independent oscillator model is a simple, pioneering model of phononic friction. In this two-dimensional model (Figures 38 and 41), two solids are held a fixed distance apart, with the upper solid being moved relative to the lower. All the atoms in the lower solid are immobile, with the sole purpose of presenting a periodic potential to the upper solid. Only the surface atoms in the upper solid are allowed to move. These atoms are connected to the remainder of the upper solid via springs that are representative of chemical bonds within the material. The atoms are unconnected to each other or any other oscillator, hence the name "independent oscillator". They are set into vibrational motion by sliding over the periodic potential of the lower surface, and energy dissipation occurs by allowing the springs to lose energy into the rest of the upper solid.

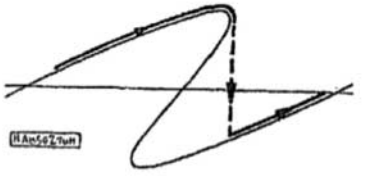

Fig. 7

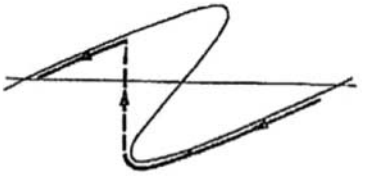

Fig. 8

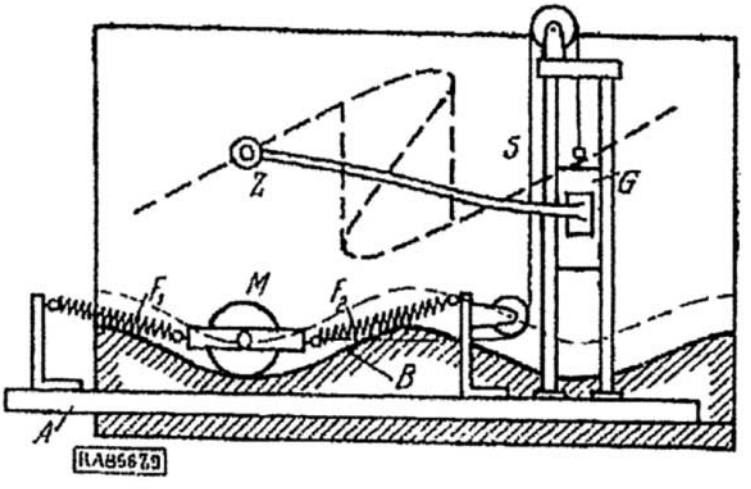

Fig. 9

Figure 42. Figures 7–9 L. Prandtl, Zeitschrift Angewandte Mathematik und Mechanik 8, 1928, p. 85 [28]. Copyright Wiley-VCH Verlag GmbH & Co. KGaA. Reproduced with permission. Depicting the mechanical analog of his model. A sliding piece G is attached to a point tracer Z. The upper end of the sliding piece is attached to a cord that is run over rollers and whose opposite end is attached to a mass M connected to two springs. For particular combinations of mass and spring strengths, there are multiple equilibrium points that result in abrupt jumps followed by mechanical vibration of the mass. The upper curves show the path traced out by the tracer (Z) in the forward and backward direction [28].

The model, which is closest in geometry to that of an AFM [329], exhibits an interesting behavior for the individual oscillators as they experience the combined effects of the spring potential and the substrate potential. Depending on the relative strengths and stiffnesses involved, oscillators will either move in a slow, smooth motion, or alternatively will exhibit instabilities and abrupt jumps from one position to another when multiple equilibrium positions are present. The abrupt jumps produce mechanical vibrations, whose energy is dissipated as friction. Figure 42 depicts Prandtl's depiction of the mechanical analog of the model.

The motion of an AFM tip sliding over an atomically uniform crystalline substrate is frequently described within the Tomlinson model framework. In the absence of thermal excitations, and under the assumption of a completely static substrate potential, the only force available to make the tip overcome the atomic potential barriers is the spring force exerted by the support via the cantilever. In this scenario, the AFM slips to the next potential minimum when the combined system of the cantilever and the tip–surface interaction becomes unstable, which is the case when it is at a location where the second derivative of the surface potential U with respect to the tip position $x$is equal to the cantilever's lateral spring constant k, $\mathrm{d}^2U/\mathrm{d}x^2 = k$. As a consequence, the tip

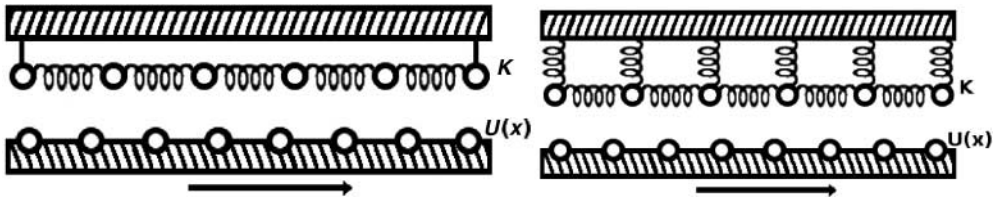

Figure 43. Schematic of the Frenkel-Kontorova (left) and Frekel–Kontorova–Tomlinson (right) models.

repeatedly slips over the atomic potential barrier with a saw-tooth-like variation in the lateral force, which is known as stick–slip motion.

There are many assumptions within the Prandtl–Tomlinson model that render it just the first step for AFM data interpretation rather than a complete treatment. These include thermal effects [330], phonon generation in substrate atoms, [36], the rate at which vibrational energy is dissipated, and the degree to which an AFM tip can be represented by an atomically sharp, rather than extended object [76]. Nonetheless, the model remains quite useful as a starting point for AFM-type geometries [329,331,332].

3.3.2. *Frenkel–Kontorova and Frenkel–Kontorova–Tomlinson models*

The Frenkel–Kontorova [333] model, like the independent oscillator model, allows only motion of surface atoms in one of the sliding solids, with the opposing solid represented by a fixed periodic potential. Similar to the independent oscillator model, the degree of commensurability between the two surfaces has a large impact on the observed friction. The atoms in the upper surface are connected with springs to their neighbors, so they are no longer independent oscillators (Figure 43, left). But springs do not connect them vertically to an upper solid as is the case for the independent oscillator model. The vertical bars connecting the atoms to the upper solid in Figure 43 represent the ability of an external force being applied to the layer of atoms to allow sliding motion.

The Frenkel–Kontorova model exhibits much richer behavior then the independent oscillator model, a direct result of the interacting nature of the sliding atoms. Aubry and collaborators have performed numerous studies for the incommensurate case [334,335] and have shown that for an irrational ratio, the layer can be shifted by an infinitesimally small force as long as the strength of the periodic potential is below a critical value. Therefore, below this critical value, there is zero static friction. The system undergoes a phase transition in the amount of frictional energy dissipated as the amplitude of the corrugation of the substrate potential increases in strength. At a critical corrugation amplitude, the static friction jumps from zero to a nonzero value. The critical strength is strongly dependent on the ratio of the atomic spacing for the surfaces. If the ratio is a simple rational number, the critical strength is small, while if the two lattices are incommensurate, the critical strength will be large. This is true only in the thermodynamic limit, that is, for the case of an infinite number of adsorbate atoms.

Numerous systems have been explored within the context of the Frenkel–Kontorova and related models [336–338]. For example, Consoli *et al.* examined the onset of sliding friction in incommensurate systems, by considering the dynamics of an incommensurate chain sliding on a periodic lattice, modeled with initial kinetic energy but without damping and driving terms [337]. They observed that the onset of friction could be attributed to a novel type of dissipative parametric resonances. Nakamura *et al.* examined the case of clusters sliding on a periodic potential. In particular, they examined the activation energy for diffusion and dynamics of nanoscale clusters of a Frenkel–Kontorova chain subject to microscopic friction and report the presence of "magic size" onset for cluster diffusion. The result is intuitive in that individual atoms are commensurate by

their nature with a substrate, but clusters will be less commensurate: not all atoms in the cluster can be located at energetically favorable locations. Their model predicts that when a cluster is pulled by a constant driving force, the critical force strength of depinning depends crucially on the cluster size, and it is smallest at the magic size. In contrast, when a cluster is pulled by a spring at a constant velocity below the critical value, clusters show a stick-and-slip motion, and the maximum force of a spring also becomes smallest at the magic size [338].

Even smaller systems have been studied with the framework of the Frenkel–Kontorova model by Bishop *et al*., who have focused on the friction associated with dimers (two atoms connected by a spring) sliding over a periodic potential [339,340]. The sliding friction of a dimer subjected to an external force was studied in the steady state for arbitrary temperatures. Nonlinear phenomena that emerge include dynamic bistability and hysteresis, and the authors were able to explain many of the observed features in terms of the resonance of a driven-damped nonlinear oscillator. MD simulations were also performed, which exhibited nonlinear behavior in the velocity. As expected, a striking variation of the friction as a function of the ratio of the length of the dimer to the substrate was observed.

In 1996, Weiss and Elmer reported an investigation of wearless friction in a model that combined a harmonic chain in a spatially periodic potential with independent oscillators connected to a sliding surface in a fixed upper potential (Figure 43, right). The frictional behavior in this combined Frenkel–Kontorova–Tomlinson model was investigated in both static and kinetic regimes. As in the Frenkel–Kontorova model, the behavior strongly depended on whether the ratio of lattice constants was commensurate or incommensurate. In the incommensurate case, Aubry's transition from zero to nonzero static friction depend, as expected, on the strength of the interaction between the sliding surfaces. The authors reported that for increasing interaction strength, they observed three characteristic thresholds for: (1) the appearance of static friction, (2) the appearance of kinetic friction in the quasistatic limit, and (3) for metastable states. The thresholds were identical only in the incommensurate case. In the commensurate case, the authors found that static friction can be nonzero even though the kinetic friction vanishes for sliding velocity tending to zero.

3.3.3. *Beyond Frenkel–Kontorova*

3.3.3.1 *Composite oscillators and hybrid models* To go much beyond the Frenkel–Kontorova model in complexity generally requires the use of numerical solutions [341] or hybrid approaches. A composite oscillator model (Figure 44, left) investigated by Xu and Huang [342,343] is an example of how the complexity of the models has increased with increased ability to obtain numerical solutions to phonon-based friction geometries.

In an alternative approach to modeling phononic friction in more complex systems, Sokoloff has employed a hybrid approach of analytic theory in combination with computer modeling. In Sokoloff's model, atoms in a sliding crystalline lattice of a solid are connected via springs, while the potential of the lower surface is assumed to be sinusoidal as a first approximation (Figure 44, right) [344–346]. The phonon modes in the upper slab are excited by the periodic potential as the block slides over it and the energy in the phonon modes is dissipated through a phenomenological damping constant ascribed to them. Sokoloff obtains a solution in the "high-velocity" limit, where the displacements of the first-layer atoms are small compared with the surface potential's wavelength. In this limit, the potential presented by the lower slab is assumed to be weak, and the speed of sliding is high enough that the atoms do not have time to relax. Sokoloff also obtains a solution for the "low-speed" limit, where he assumes that slippage occurs via the motion of edge dislocations. One of his results indicates that when the driving potential is incommensurate with the upper crystal lattice, the frictional energy is dramatically lower, of

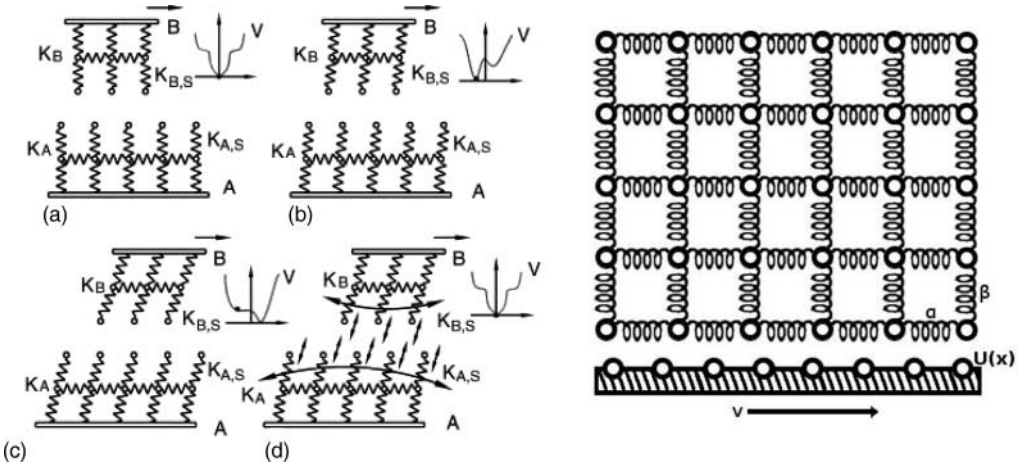

Figure 44. Numerical solutions and hybrid approaches for increasingly complex models of phonon friction have become routine, increasing the ability to both predict and control friction. Left: Reprinted figure with permission from Z. Xu and P. Huang, *Study on the Energy Dissipation Mechanism of atomic-scale friction with composite oscillator model*, Wear 262, pp. 972–977 [343], Copyright 2007, with permission from Elsevier. Right: Crystalline solid typical of that modeled by Sokoloff [345].

order 10^{13} times smaller. The result reflects the hypersensitivity of phonon friction to lattice commensurability effects. Although experimental measurements of the reduction in friction arising from commensurability effects are closer to one to two orders of magnitude, the model captures essential features of real systems.

Sokoloff also examined models whereby instead of a phenomenological damping term, the pair potentials between atoms were expanded beyond quadratic terms to include anharmonicity. Drawing upon earlier work on the spread of energy in a crystal due to anharmonicity, he showed that the ergodicity of the crystal is critically dependent on the overlap of the phonon modes, which in turn depends in large part on the size of the crystal. He used numerical calculations to solve the equations of motion and demonstrated that for small enough size crystals, there should be no phononic friction. This critical size is dependent on the speed of sliding, the atomic spacings, the phonon frequencies, and the effective damping constant [347,348]. It is also strongly dependent on the dimensionality of the model crystal. More recent work by Sokoloff and coworkers has focused on the impact of step edges and pinning effects on the sliding of adsorbed films [349–351].

3.3.3.2 *MD simulations* The MD approach to modeling phononic friction involves solving for the time evolution of a set of *N*of interacting atoms, by integrating their equations of motion at successive time steps. Simulations of this type are completely classical in nature, applying Newton's law $F = ma$ directly to each atom in a system. Starting in the early 1990s, computing power had increased to the point where the sliding of very simple systems could be modeled on a first principles atomistic basis by this method. Rare-gas monolayers sliding on a rigid corrugated substrate were ideal systems for such studies, allowing direct comparison of QCM data to numerical results. In 1994, Cieplak, Smith, and Robbins successfully employed standard MD algorithms in conjunction with analytic theory, to model QCM reports of krypton atoms sliding on a rigid gold substrate [33–35].

The gold substrate provided a fixed periodic potential that acted on the adsorbed krypton layer. The krypton–krypton interactions were modeled with a Lennard-Jones potential, Equation (57),

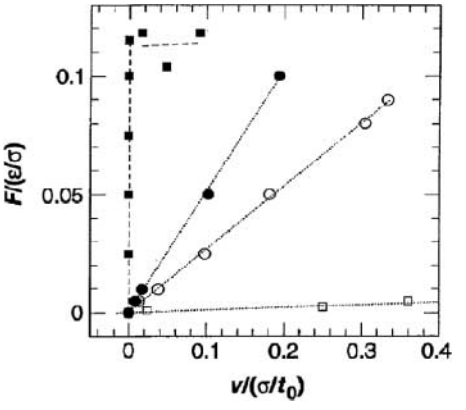

Figure 45. MD simulation results for the variation of the steady-state velocity of an adsorbed layer versus the force per atom with varying degrees of surface corrugation and commensurability. From M. Cieplak *et al.*, Science 265, p. 5176, 1994 [35]. Reprinted with permission from AAAS. Open and filled squares correspond to a commensurate layer with surface corrugation parameter $f = 0.1$ and 0.3, respectively, and temperature $k_B T = 0.385\varepsilon$. Open and closed circles correspond to an incommensurate Kr monolayer on Au(111) using $f = 1$ (no adjustment to the Steele potential, Equation (4), respectively, at $k_B T = 0.385\varepsilon$ and $k_B T = 0.8\varepsilon$ (76 and 158 K). Static friction is present only for a commensurate system above a certain threshold corrugation level, and absent for the incommensurate layers. The friction levels are observed to increase with temperature but show no dependence on the direction of sliding. $\varepsilon = 17$ meV, $\sigma = 0.357$ nm, and $t_0 = 2.5$ ps.

employing the values $\varepsilon = 17$ meV and $\sigma = 0.357$ nm as the characteristic energy and length scales for krypton, respectively. The krypton–gold interaction potential was modeled with the Steele formula, Equation (4), modified to include a scaling factor, f, in order to allow the effect of the corrugation of the potential to be adjusted empirically. The amplitude of the surface corrugation is then $U_o = fV_g$ with $0 < f < 1$, where a value less than 1 is required to reflect the fact that metals are less corrugated than rare-gas solids. Friction in this simulation was assumed to arise exclusively from vibrations (phonons) within the krypton film atoms as they slid atop the rigid gold substrate, and no energy dissipation was associated with the vibration of gold atoms in the substrate (Figure 45). With this model, the friction was determined in two ways. First, the adsorbates were oscillated with an alternating force to simulate a vibrating QCM geometry and their velocity was simultaneously monitored relative to that of the substrate. Second, a constant force was applied and the steady sliding speed attained by the adsorbed atoms was recorded (Figure 45). The friction levels were observed to increase with increased temperature and increased substrate corrugation, but exhibited little dependence on the direction of sliding for the hexagonal substrate geometry studied. The model was very close to that of the Frenkel–Kontorova model, and as such, exhibited many of the same characteristics. Like the Frenkel–Kontorova model, viscous friction was observed for incommensurate systems, but increasing the substrate corrugation within reasonable levels for Kr/Au(111) did not induce an Aubry transition from 0 to finite values of static friction. Such a transition did, however, occur for commensurate layers (open and closed squares in Figure 45), at values of the corrugation factor that fell between 0.1 and 0.3 (Figure 45).

Although the friction was higher in this model for commensurate systems, it was not dramatically higher, that is, by many orders of magnitude suggested by simple phonon models. Commensurability effects did, however, manifest themselves in an interesting and counterintuitive way: solid monolayers were observed to exhibit greater slip times (lower friction) than

liquid monolayers, a result that matched experimental observation (Figure 45) and was directly attributable to the solid phase being less flexible, and thus less commensurate, with the substrate.

Another outcome of the numerical studies concerned the dependence of the "slip time" (τ) as defined in Equation (14) on the corrugation of the potential and the lifetime of the phonons ($t_{\rm ph}$) generated:

$$\tau \sim \frac{t_{\rm ph}}{U_{\rm o}^2}. \tag{59}$$

According to Equation (59), a highly corrugated surface is predicted to have a lower slip time (higher friction) that varies as the corrugation amplitude squared, and the damping or lifetime of the phonons generated by the sliding is directly proportional to the slip time.

The simulations provided an excellent fit to the 1991 experimental QCM data published by Krim *et al*. who had reported that the solid krypton layer slipped longer on Au(111) than the liquid (Figure 46). Given the close match between their simulations and the QCM experiments, Robbins and colleagues concluded that phononic friction was the primary source of friction for the krypton on Au(111) system. The combined QCM and numerical results provided the first confirmation of the existence of phononic mechanisms for friction. Later QCM studies of the sliding friction of monolayers and bilayers of Xe on (111) substrates [352,353], along with MD simulations [354], provided further confirmation of the dominance of phonons in these simple systems, and the form of the dependence of slip time on the potential corrugation, Equation (58), was confirmed by Coffey and Krim in 2005 [355,356].

In addition to the QCM data presented in Figure 46, phononic friction mechanisms have been documented in an AFM geometry very recently by Carpick and coworkers [36]. The authors compared hydrogen- and deuterium-terminated single-crystal diamond and silicon surfaces, and in all cases the hydrogenated surface exhibited higher friction. The data were analyzed within a theoretical framework of energy transfer to an adsorbate from a moving surface rather than the more standard approach within the Tomlinson model of stick–slip motion, that is, the same model employed for QCM measurements of sliding adsorbed films.

The authors cited models of phononic friction for an adsorbate monolayer interacting with a single moving surface to interpret the AFM data and argued that changing the mass of the terminating atoms on a surface impacted the rate at which the tip's kinetic energy could be dissipated. In particular, the lower natural frequency associated with chemisorbed deuterium compared to hydrogen termination was expected to result in a reduction in the rate at which the tip's kinetic energy was dissipated, and thus lower friction. Although the geometry did not correspond exactly to that of an adsorbed layer sliding on a QCM, the authors used the model to predict qualitative behavior by assuming the AFM tip to take the place of the moving surface in models such as employed for QCM data interpretations. The hydrogen and deuterium atoms meanwhile were assumed to correspond to the adsorbates in a QCM sliding geometry, but instead chemisorbed to the diamond or Si substrate, thus having much shorter characteristic sliding times than physisorbed atoms [4,357–359]. It should be noted that Mo *et al.* [37] have re-examined the results of Cannara *et al*. with MD simulations and concluded that the experimentally observed isotope effect can be explained quantitatively by small differences in surface coverage, which are due to isotope-dependent bond stabilities. They found that a change in vibrational frequencies alone did not account for an isotope-dependent solid friction.

Nonetheless, a number of other features of phononic friction models are in evidence in AFM studies reported in the literature, particularly in terms of corrugation effects and stick–slip phenomena, as described next. It is important to point out that an AFM geometry is comprised of a number of energy dissipating constituents (tip, substrate, surface adsorbates, etc.), each of which

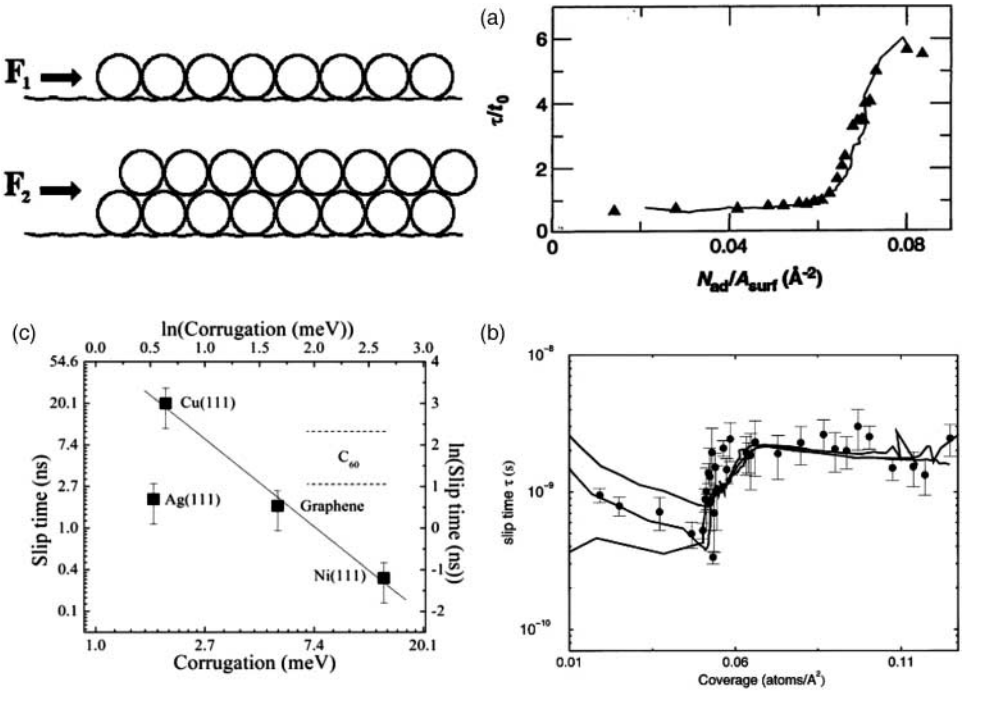

Figure 46. Reprinted figure with permission from C. Daly *et al.*, Physical Review Letters 76, p. 803, 1996 [352]. Copyright (1997) by the American Physical Society. QCM experimental confirmation of the existence of phononic friction mechanisms. Upper left: Schematic of the QCM experimental geometry. Monolayers and bilayers of adsorbed films on weakly corrugated substrates slide in response to the oscillatory motion of the substrate electrode. The external force applied to the layers (F_1 or F_2) is resisted only by friction. (a) The force to slide a one-atom-thick Kr layer as it solidifies with increasing coverage is compared to theory by plotting slip time versus coverage data for experiment (line) [33,34] and theory (triangles). From M. Cieplak *et al.*, Science 265, p. 5176, 1994 [35]. Reprinted with permission from AAAS. (b) The force required to slide a two-atom-thick film of xenon along Ag(111) is compared to that required to slide a one-atom-thick film by plotting slip time versus coverage data for experiment (points) [352,353] and theory (lines) as the film thickens from one to two layers. Reprinted figure with permission from MS. Tomassone *et al.*, Physical Review Letters 79, p. 4798, 1997 [354]. Copyright (1997) by the American Physical Society. (c) Slip time versus surface corrugation. The slope of the line fit to systems with the same lattice spacing agrees well with the -2 dependence described in Equation (58). The dashed lines around the C60 represent the uncertainty in slip time. The corrugation of Xe = C60 is unknown.

may play the dominant role in energy dissipation and bond breaking, depending on which material combination, geometry, sliding speed, and/or temperature has been studied [360]. Therefore, direction comparisons between AFM studies with theory will depend on which system constituents dissipate the most frictional energy.

3.3.4. *Commensurability/corrugation effects*

All models of phononic friction are highly sensitive to the commensurability of the lattices in sliding contact and to the degree of corrugation of the potential which they present to each other. Theoretical predictions for the drop in friction between commensurate and incommensurate states can be many orders of magnitude [345,346,361], depending on the details of the systems in contact

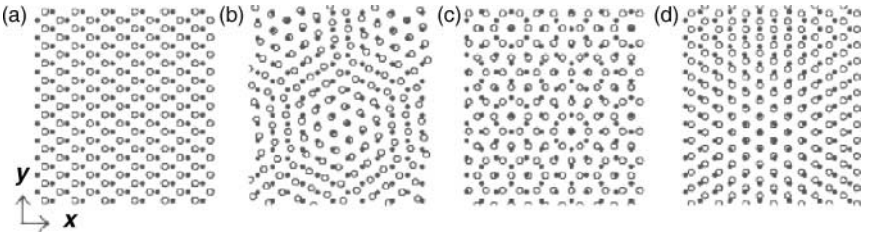

Figure 47. Projections of atoms from the bottom and top surfaces into the plane of the walls. In (a)–(c), the two walls have the same structure and lattice constant, but the top wall has been rotated by 0°, 11.6°, or 90°, respectively. In (D) the walls are aligned, but the lattice constant of the top wall has been reduced by 12/13. Atoms can only achieve perfect commensurability in case (a). From G. He *et al.*, Science 284, p. 1650, 1999 [271]. Reprinted with permission from AAAS.

[352]. Incommensurate contact is considered to be the norm for the vast majority of systems in sliding contact. It is clearly the case for a solid or adsorbed layers sliding over a substrate that have different lattice spacing. Indeed, only in special circumstances to adsorbed layers configurations exhibit commensurability with the substrate [356].

In contrast, it might seem that lattices with identical spacing, for example, self-mated materials, would routinely exhibit commensurability. A rotation of the materials with respect to each other, however, also results in incommensurability between the surfaces (Figure 47). Thus, commensurate contact is considered to be a rare occurrence.

The variation of sliding friction with rotation angle has been well documented by means of AFM experiments for the case of graphite on graphite [363,364] (Figure 48, upper left) and also SFA measurements for mica on mica [218] (Figure 48, upper right). The data for mica on mica sliding, which are not fit to any particular atomistic model of friction, exhibit a clear dependence on the rotation angle, albeit a drop in half at most, not orders of magnitude. The data for graphite on graphite compare well with a Prandtl–Tomlinson model calculation for a symmetric 96-atom graphite flake sliding over the graphite surface (solid line). They represent the average friction force recorded between a graphite surface (HOPG) and a nanoscale graphite flake at the apex of the tip of an FFM. The friction force is measured as a function of the rotation angle of the graphite sample around an axis normal to the sample surface. Two narrow peaks of high friction are observed close to 0° and 60°, respectively. Between these peaks, a wide angular range with ultra-low friction, close to the detection limit of the instrument, is found. For these intermediate orientations, the lattice of the flake is twisted so far out of registry with respect to that of the substrate that the sliding can take place almost without any energy dissipation, and thus a drop of orders of magnitude in the friction is observed. The sudden drop with rotation angle is referred to in the nanotribology community as "superlubricity".

In addition to the agreement with the Prandtl–Tomlinson model calculation, the graphite on graphite friction results are also well fit by a dislocation drag theory of friction (Figure 48, lower half), to be described in a later section. The frictional dependence on lattice rotation angle thus does not uniquely identify the underlying atomic-scale mechanisms. Studies of the dependence on temperature and sliding velocities provide additional evidence, as discussed next.

3.3.5. *Temperature and velocity dependencies*

The temperature and velocity dependencies of sliding friction are closely linked to each other, as both thermal and kinetic effects can provide sufficient thermal or kinetic energy to overcome

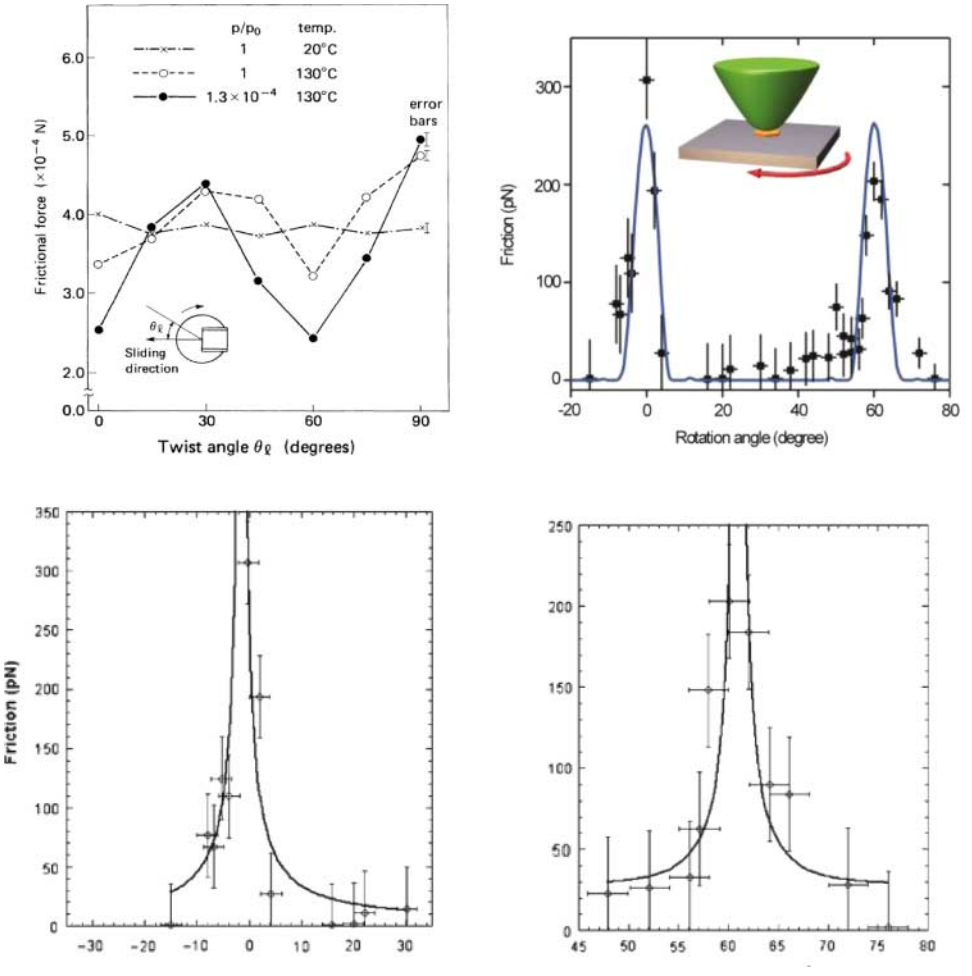

Figure 48. (color online) (top left) Reprinted figure with permission from M. Hirano *et al.*, Physical Review Letters 67, p. 2642, 1991 [218]. Copyright (1991) by the American Physical Society. Friction as a function of rotation angle for mica sliding on mica in an SFA apparatus. (right) Reprinted figure with permission from M. Dienwiebel *et al.*, Physical Review Letters 92, p. 126101, 2004 [364]. Copyright (2004) by the American Physical Society. Friction as a function of the rotation angle for a graphite flake at the tip of an AFM sliding on graphite. The solid line depicts a Tomlinson model calculation for a symmetric 96-atom graphite flake sliding over the graphite surface. Below: The same data were refit to an alternative analytic model expression for a dislocation drag theory of friction, also yielding a good fit. Reprinted with permission from A.P. Merkle *et al.*, Philosophical Magazine Letters 87, p. 527, 2007 [627]. Copyright 2007 by Taylor & Francis group, LLC.

potential barriers to sliding [365,366]. At very slow sliding speeds and constant load, the stick–slip behavior of an AFM tip is frequently viewed within a Prandtl–Tomlinson model framework, which displays stick–slip motion as an atom moves over an atomically well-defined substrate [367]. An AFM tip sliding on a NaCl(100) surface at velocities between 5 nm s^{-1} and 1 μm s^{-1}, for example, was reported to display a logarithmic dependence between the friction force and the sliding speed [268], and the dependence was attributed to thermal activation of irreversible jumps, with $F \sim \text{const}+\ln(v)$. The results were subsequently investigated in more detail by Sang *et al.*

from a theoretical point of view, to include the effects of temperature [368]. The group reported that stick–slip motion was present and that the average frictional force exhibited a logarithmic dependence on both temperature and velocity, of the form

$$F \propto \text{const} - T^{2/3} \left| \ln \frac{\upsilon}{T} \right|^{2/3}. \tag{60}$$

The results of the AFM data presented in Figure 48 were examined theoretically in more detail by Krylov *et al.* [369], who found that thermal activation could be significant even for strong surface corrugation and that regular stick–slip behavior could completely be destroyed by thermal effects. They concluded that incorporation of such "thermal lubrication", or "thermolubricity" effects provided an improved interpretation for the data in Figure 48 [363], which originally been attributed purely to mechanical effects associated with the rotation angle of the incommensurate contact. The same group has continued to examine in detail the role of temperature and velocity on friction associated with an AFM tip. Jinesh *et al.*, for example, very recently reported implementation of a set of rate equations to describe the thermal activation of a tip moving along a one-dimensional lattice, including the possibility of multiple back-and-forth jumps between neighboring potential wells [330,370]. The authors find that this theoretical approach explains many aspects of the variation in atomic friction, as measured by AFM, over a wide range of temperatures, velocities, and surface corrugations. They conclude that friction at low velocities and low surface corrugations is much lower than the weak logarithmic velocity dependence predicted earlier and that friction falls to zero in the zero-velocity limit. Although the model calculations produce excellent fits to data collected to test the predictions, the values of the fitting parameters are somewhat problematic, indicating that the underlying single-spring model may suffer from an intrinsic flaw. This may be due to either the absence of flexibility of the tip or the restriction to a one-dimensional sliding geometry, and studies are in progress to resolve this issue.

There are obvious differences between the adsorbed film geometry and the AFM geometry, that is, a planar interface versus an asperity contact, and one might conclude that the Prandtl–Tomlinson model should be used to model AFM results and the Frenkel–Kontorova model should be employed to model QCM sliding friction results. There are, however, still major unresolved questions concerning when and which phonon models dominate, and how alternative mechanisms such as defects, conduction electron, and electrostatic contributions contribute in particular systems.

The thermal lubrication concept arises from a Prandtl–Tomlinson-type single-asperity hopping model, which predicts a reduction in the friction force as temperature rises, since the probability of thermally assisted motion increases with temperature. Jansen *et al*. [332] very recently reported UHV experiments of atomic stick–slip friction on graphite in the surface temperature range of 100 and 300 K. They performed a statistical analysis of the individual stick–slip events as a function of the velocity and found that it agreed well with the thermally activated Prandtl–Tomlinson model at all temperatures. Taking into account an explicit temperature dependence of the attempt frequency, they found that all data points collapsed onto one single master curve. Multiasperity treatment within the same context results in a different temperature dependencies. Experimental measurements of temperature in such systems can be obscured, however, by gradients in temperature between the tip and the sample [371], so the comparisons with theory must be performed with great care.

Dunckle *et al.* [371], for example, employed a variable temperature, UHV AFM to characterize interfacial friction for a single-asperity diamond contact on a diamond-like carbon (DLC) substrate over a substrate temperature range 90–275 K and cautioned that large thermal gradients may exist between tips initially at room temperature in contact with substrate temperatures. For sufficiently large normal forces, they observed lateral force to be proportional to the normal force, and a friction

coefficient could be identified that varied approximately linearly with the substrate temperature, with $\mu = 0.28$ at $T = 90\,\mathrm{K}$ and $\mu = 0.38$ at $275\,\mathrm{K}$. The results were compared to other recent variable-temperature AFM friction measurements and to theoretical calculations based on the Tomlinson model. It was concluded that the comparison was largely obscured by experimentally uncontrolled temperature differences between the tip and the substrate which inevitably exist in conventional, variable-temperature AFMs. The authors presented a thermal model to quantitatively estimate these temperature differences.

Frenkel–Kontorova-style models have been employed to very successfully model sliding adsorbed layers of physisorbed monolayers (Figure 45). The phononic friction concept associated with these theories exhibit "cryolubric" trends: more phonon modes can be excited at higher temperatures resulting in higher energy dissipation and greater friction as temperature increases. Therefore, the rate of frictional energy loss for a given phonon mode also increases with temperature. Given that the Prandtl–Tomlinson thermolubricity thermal hopping effect saturates at sufficiently high temperature, it is expected that a crossover from one type of behavior should occur for sufficiently high temperature or sliding speed.

For systems more complex than that of a single-asperity AFM asperity contact or a sliding adsorbed monolayer, the modeling community has reported several cases of crossover behavior for a number of systems (Figure 49). For example, modeling studies of mechanical oscillators made of multi-walled carbon nanotubes (MWCNTs), performed within the context of creating nanomachines capable of operating in the gigahertz range [372,373], have been performed to investigate the effects of commensurability, tube length, and temperature on friction [374]. CNT oscillators can vibrate at a frequency comparable to the dominant phonon frequency at low temperature and therefore provide an ideal platform to study friction mechanism at the molecular level. The results of these MD simulations demonstrate that thermal lubrication and phononic friction can play dominant roles in different temperature ranges and lead to different temperature dependences of the friction force. For ultra-low temperatures, thermal activation can effectively reduce friction and result in lower friction force at higher temperatures. However, once the temperature exceeds a critical value at which the dominant phonon frequency is close to or higher than the vibration frequency of the oscillator, phononic friction becomes the dominant mechanisms and begins to increase monotonically (Figure 49, left).

A second example of crossover behavior is displayed on the right side of Figure 49, the result of MD simulations performed for sliding of planar α-$Al_2O_3(0001)$ surfaces under varying loads, and semi-logarithm plots of friction force versus sliding velocity for different degrees of hydroxylation. As the sliding velocity increases, a crossover from a thermal activation to viscous damping-type behavior is observed, in all cases close to $80\ \mathrm{m\ s^{-1}}$ [375]. The linear regime exhibits the same dependence as that reported by Robbins and coworkers for adsorbed rare-gas monolayers [35] (see also Figure 44). But it is certainly not the rule for nanoscale single-asperity contacts where friction has been reported to increase, decrease, or be independent of sliding velocity at speeds sufficiently high to exceed the thermal activation regime [76].

For planar contacts, linear friction governed by Equation (2) is very routinely reported in both analytic and numerical studies of sliding solids. It is certainly not the rule for macroscopic solids in sliding contact, where static friction is ever present and velocity independence is the norm at everyday sliding speeds. Bortolani *et al*. [376], for example, performed a study of the temperature dependence of static friction, as a function of temperature, between two thick solid slabs. The upper slab was formed from light particles and the substrate of heavy particles. The group examined the interaction between the phonon fields of the two blocks and on the interface corrugation contributions to the mechanisms responsible for the friction, and compared a substrate formed of fixed atoms with that of one formed of mobile atoms. In the case of the mobile substrate, a large momentum transfer from the substrate to the upper block was reported, which increased with

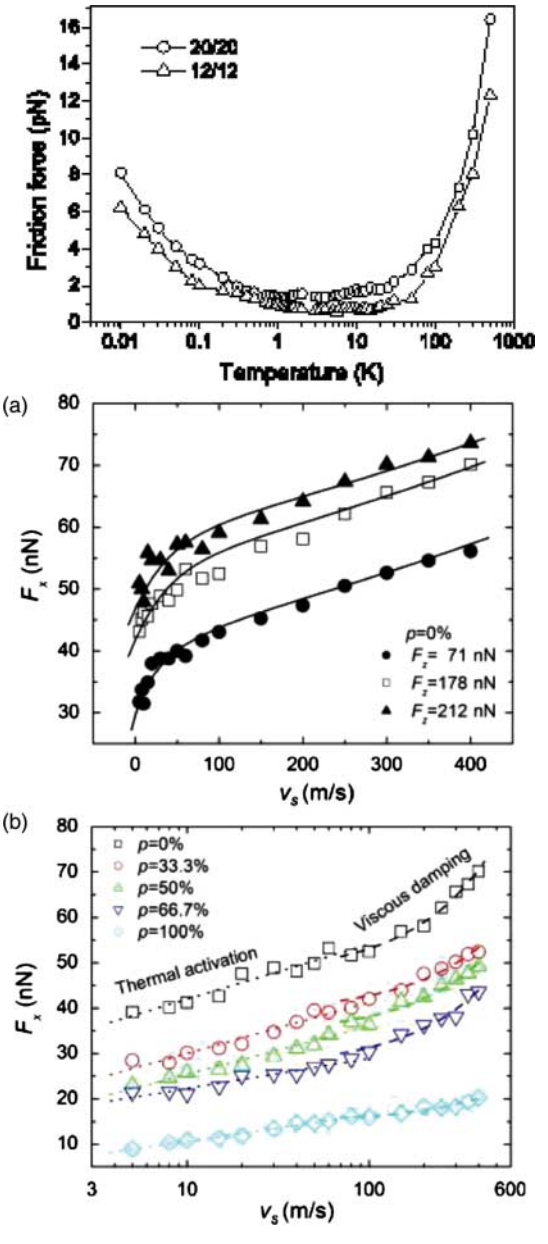

Figure 49. (color online) Top: The variation of the friction force between the inner and outer tubes versus the temperature for (4, 4)/(9, 9) DWCNTs with tube lengths of 20 layers and 12 layers of carbon atoms, respectively. The energy scale in the LJ potential is $\varepsilon = 2\varepsilon_0$. As temperature increases, the thermal jump probability saturates and the friction force becomes insensitive to temperature. Reprinted with permission from Y. Chen *et al.*, Nanotechnology 20, art#035704, 2009 [374]. Copyright (2009) by the Institute of Physics. Right: (a) Sliding velocity of the friction force F_x under various normal loads for bare Al surfaces under different normal forces. (b) Semi-logarithm plots of friction force versus sliding velocity for different degrees of hydroxylation. As the sliding velocity increases, a crossover from a thermal activation to viscous damping-type behavior is observed. Reprinted with permission from D. Wei *et al.*, Surface Science 603, L95 [375]. Copyright (2009) with permission from Elsevier.

increasing temperature and resulted in a large disorder within the upper surface. This resulted in a decrease of the static friction with respect to the case of a rigid substrate. Reducing the corrugation, the group found that with a rigid substrate the upper block becomes nearly commensurate, producing an enhancement of the static friction with respect to that of the mobile substrate.

3.3.6. *Confined films and quantized friction*

It is highly intuitive that confinement of a film should have a major impact on its tribological properties, as well as inducing quantization of the properties of the materials due to an integral number of particles allowed between the counterface materials [377]. An increasing number of theoretical efforts have treated this topic within the context of phononic friction, including the case of a confined molecule under both normal compression and shear. In the following, selected studies that have not been mentioned earlier are highlighted, to demonstrate the range and breadth of ongoing theoretical work on the topic. Recent work by Vanossi, Tosatti, and coworkers is highlighted in particular.

Buldum *et al*. reported a microscopic model of phononic energy dissipation in friction that involved the generation of a local excess phonon distribution in a nanoparticle between two sliding objects, and its damping within the objects [325,326]. The conversion of the energy stored in the nanoparticle into excess phonons and their decay rates were calculated and the authors presented a quantitative analysis of energy dissipation in sliding friction. The authors suggest that their formulism could be extended to the case of nanoparticles.

As a specific case in point, Buldum and Ciraci [327] modeled xenon atoms as a lubricant between two Ni(110) slabs in relative motion. The resistance of the xenon layer against the loading force was investigated, and the critical forces to destroy the lubricant layer at various coverages were established. They found that the corrugation of the potential energy associated with sliding reached a minimum value at submonolayer coverage. Filippov *et al*. subsequently developed a coarse-grained two-state model starting from an MD description of a molecular system under shear [378]. The model generalized the phenomenological Tomlinson model for the response of a driven system and provided a practical approach to investigate the response of sheared systems under a broad range of parameters.

Khomenko *et al*. studied melting of an ultrathin lubricant film sheared between atomically smooth surfaces within the context of a "Lorentz" (harmonic oscillator) model [379], consisting of a set of equations used for describing thermodynamic and kinetic phase transitions [380]. Additive noise associated with shear stresses, strains, and film temperature were introduced, and a phase diagram was constructed where the noise intensity of the film temperature and the temperature of rubbing surfaces defined the domains of sliding, dry, and stick–slip friction. In a follow-up study, phase diagrams were obtained for both second- and first-order transitions corresponding to melting of amorphous and crystalline lubricants, respectively [381]. For the amorphous case, a stick–slip friction domain, separating the regions of dry and sliding friction, was found. For the crystalline case, three domains of stick–slip friction arose, and characterized by the transitions between dry, metastable, and stable sliding friction. The approach provides insights into the manner in which thermal fluctuations from frictional heating as well as ambient temperature can impact and reduce friction.

Priezjev employed MD simulations to study dynamic behavior of film slip length in a fluid flow confined between atomically smooth surfaces [382]. For weak wall–fluid interactions, the slip length increased nonlinearly with the shear rate provided that the liquid/solid interface remained incommensurate. It is noted here that the first to discuss of this nonlinearity were Thompson and Troian in 1997 [198]. A gradual transition to a linear dependence was observed with increased wall–fluid interaction. Extensive simulations for a wide range of shear rates and wall–fluid interactions

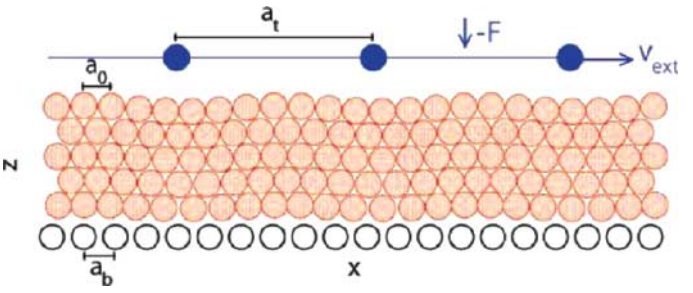

Figure 50. (color online) Three-scale model with rigid top (solid circles) and bottom (open) layers (lattice spacings a_t and a_b, respectively), the former moving at externally imposed x-velocity v_{ext}. One or more confined lubricant layers (shadowed) of rest equilibrium spacing a_0 are present. Reprinted with permission from I.E. Castelli *et al.*, Journal of Physics: Condensed Matter 20, art#354005, 2008 [391]. Copyright (2008) by the Institute of Physics.

were performed. The author found that the slip length could be well described for the wide range of conditions by a function of a single variable that in turn depended on the in-plane structure factor, contact density, and temperature of the first fluid layer near the solid wall.

Cheng *et al.* employed MD simulations to study contact between a rigid, nonadhesive, and spherical tip with radius of the order 30 nm and a flat elastic substrate covered with a fluid monolayer of adsorbed chain molecules [303,383]. Previous studies of bare surfaces had revealed that atomic-scale deviations from a sphere that are present on any tip constructed from discrete atoms could lead to significant deviations from continuum theory and dramatic variability in friction forces. The authors argued that introducing an adsorbed monolayer would lead to larger deviations from continuum theory but also decrease variations between tips with different atomic structure. They observed that fluid films remained within confined contacts and behaved qualitatively like a thin elastic coating except for certain tips at high loads. Both static and kinetic friction rose linearly with load at small loads in this study. Transitions in the state of the film lead to nonlinear behavior, however, at large loads. The friction was reported to be less clearly correlated with contact area than load.

Granot investigated frictional forces in fermionic gas that was sheared by two sliding surfaces and points out that investigations of quantum friction have revealed some very surprising effects [384]. In particular, it has been reported that two smooth dielectric surfaces moving laterally with respect to each other experience frictional forces as if the vacuum between them were a viscous fluid [385–388]. In Granot's 2007 study, roughness was introduced as a small bulge on two otherwise perfectly smooth surfaces. For extremely small bulges and when the gas was also confined in the lateral dimension, the frictional force was observed to be quantized. Specifically, the friction was observed to be described by the linear friction law $F = \eta v$, where v is the sliding velocity with respect to the lubricant gas, $\eta = 2mn_c^2h$ is the friction coefficient, h is Planck's constant, and m is an integer. The coefficient n_c depended only on the bulge's properties but not on the properties of the gas or the sliding velocity.

Vanossi, Tosatti, and coworkers have reported quantization of friction in a series of recent publications. The group has investigated the classical motion of an idealized one-dimensional solid lubricant, consisting of an interacting particle chain interposed between two periodic sliders [389] (Figure 50). Three length scales characterize this slider–lubricant–slider confined geometry [390,391], and the lattice mismatch gives rise to peculiar and robust quantized sliding regimes, characterized by a nontrivial geometrically fixed ratio, $w = v_{cm}/v_{ext}$, of the mean lubricant drift velocity to the externally imposed translational velocity. The ratio remains pinned at

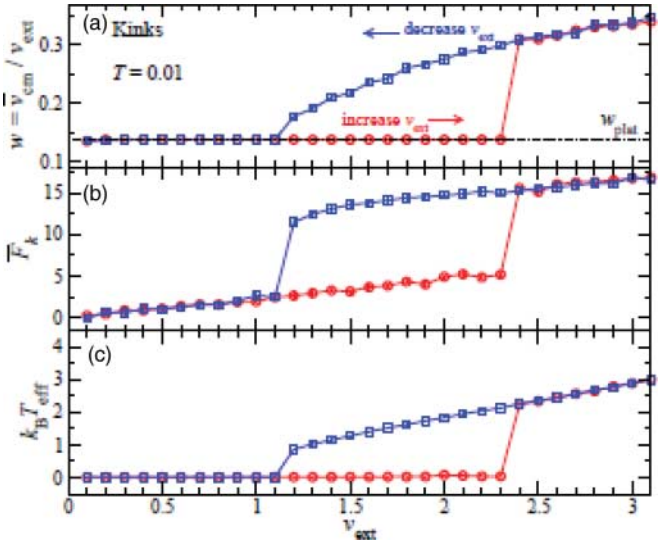

Figure 51. (color online) (a) Average drift velocity ratio $w = v_{\rm cm}/v_{\rm ext}$ of the chain as a function of its lubricant stiffness K for different commensurability ratios (r_+, r_-), with $r_\pm = a_\pm = a_0$: commensurate (3/2, 9/4), golden mean (GM) (φ, φ^2), spiral mean (SM) (σ, σ^2) ($\sigma \sim 1.3247\ldots$), and (φ^{-1}, φ). The (φ, φ^2) 1/1 plateau value is $w = 0.381966\ldots$, identical to $1 - \varphi^{-1}$ to eight decimal places. (b) The main plateau speed w as a function of r_+. (c) A sketch of the model. Reprinted figure with permission from A. Vanossi *et al.*, Physical Review Letters 97, art#056101, 2006 [389]. Copyright (2006) by the American Physical Society.

exact "plateau" values for wide ranges of parameters, including slider corrugation amplitudes, external velocity, chain stiffness, and dissipation. In addition, the ratio is strictly determined by the commensurability ratios alone (Figure 51). The plateau mechanism has been interpreted in terms of solitons, formed by the mismatch of the lubricant periodicity to that of the more commensurate substrate, being rigidly dragged by the external potential represented by the other, more mismatched, sliding surface. The quantized frictional forces associated with the drag have been evaluated and are presented in Figure 52(b).

The discovery of exact plateaus implies a kind of "dynamical incompressibility", namely identically null response to perturbations or fluctuations trying to deflect the center of mass velocity away from its quantized value. In order to probe the robustness of the plateau attractors, an additional constant force $F_{\rm ext}$, acting on all particles in the chain, was introduced. As expected, as long as $F_{\rm ext}$ remained sufficiently small, it had no effect on the velocity plateau attractor. The plateau dynamics is only abandoned above a critical force $F_{\rm c}$. The transition, occurring for increasing external driving force $F_{\rm ext}$ acting on the lubricant, displays a large hysteresis, and has the features of depinning transitions in static friction, only taking place "on the fly" [392]. Although different in nature, this phenomenon appears isomorphic to a static Aubry depinning transition [334], with the role of particles assumed by the moving solitons of the lubricant–substrate interface. A quantized sliding state of the same nature has been demonstrated by MD simulations for a substantially less idealized two-dimensional model [391], where atoms of a lubricant multilayer film were also allowed to move perpendicularly to the sliding direction and interact via Lennard-Jones potentials (Figure 50). This dynamical regime is shown to be robust against the effects of thermal fluctuations, quenched disorder in the confining substrates, and over a wide range of loading forces. By evaluating its tribological properties in terms of averaged kinetic friction $F_{\rm k}$ exerted on the top slider, the quantized sliding was found [393] to be characterized by significantly low values of $F_{\rm k}$ (Figure 52).

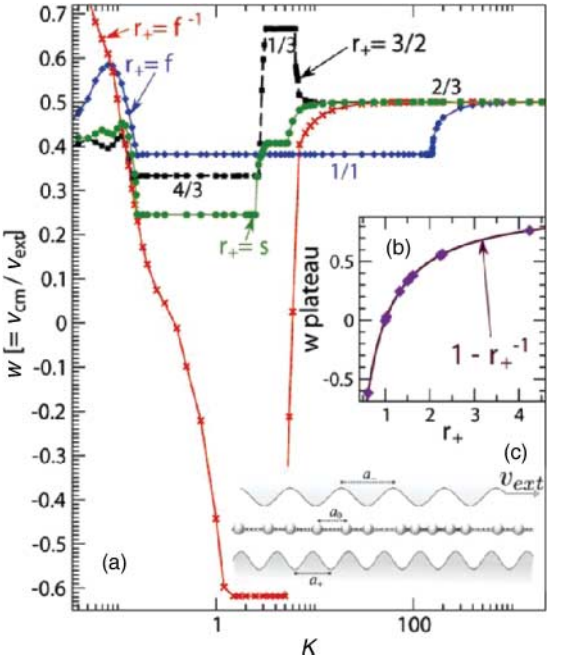

Figure 52. (color online) (a) average velocity ratio w; (b) Average friction force experienced by the top substrate; and (c) effective lubricant temperature, for top-substrate velocity v_{ext} adiabatically increased (circles) and decreased (squares). Reprinted with permission from IE. Castelli *et al.*, Journal of Chemical Physics 131, art#174711, 2009 [393]. Copyright (2009) by the American Institute of Physics.

3.3.7. *Phononic treatments of the impact of disorder, vibration, and thermal noise*

It is highly intuitive that thermal fluctuations, vibration, and/or substrate disorder should have a major impact on a film's tribological properties. The form of the applicable friction law, as well as whether static friction and pinning effects will be presented, must also be highly sensitive to disorder. An increasing number of theoretical and modeling treatments of this important topic are currently being reported [186,354,394–402]. Macroscale measurements suggest that stick–slip friction, closely related to static friction, has its origins in the formation and rupture of junctions that form between surfaces in contact [403]. When considering a one-atom- or -molecule-thick film adsorbed on a solid substrate, one might then ask whether the film will exhibit intrinsic static friction in the absence of surface disorder such as a step edge to pin the layer, or alternatively a strongly commensurate binding potential [35].

Intuitively, one might argue that the relatively weak bond strength of van der Waals interactions between the film and the surface might imply low friction parallel to the surface for such systems. The strength or weakness of perpendicular bonds do not, however, necessarily correlate with friction levels. Consider, for example, how readily one can slide two microscope slides separated by a thin film of water despite the fact that they are extremely difficult to separate in the perpendicular direction. As mentioned already in Section 1, it is intuitively clear that if a sufficiently strong shear stress is applied, any film will eventually slide. But the friction law that governs thin-film sliding has no *a priori* reason to resemble Amontons' law, $F_{\text{f}} = \mu N$. In addition, there is no *a priori* reason why static friction, which is ubiquitous at the macroscale, need be present in an adsorbed layer system. MD simulations of the kinetic friction for a monolayer of adsorbed molecules *confined* between crystalline surfaces [301] (Figure 53) show friction consistent with Amontons' laws

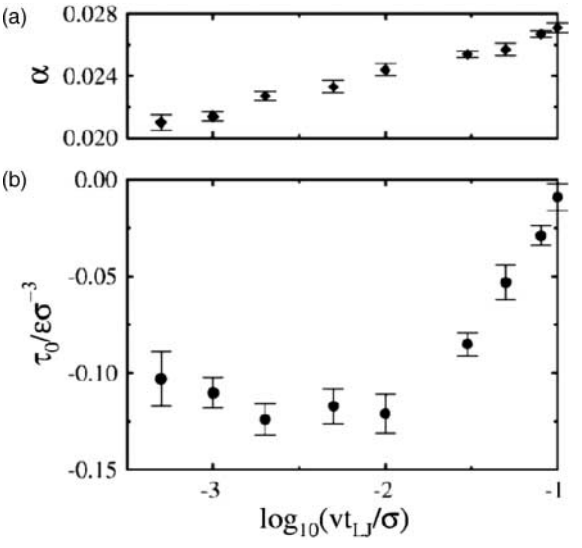

Figure 53. Plot of α and τ_0 versus sliding velocity for monolayer confined between crystalline surfaces. The friction is well described by Amontons' law written as $\mu = \alpha + \tau_0/P$. Static friction is, somewhat counterintuitively, present in this defect-free system. Reprinted with permission from G. He *et al.* [301], Tribology Letters 10 (1–2) (2001), pp. 7–14 Copyright (2001) from Springer.

that are also consistent with the Prandtl–Tomlinson model. For a thin film in an open adsorbed geometry, however, it is entirely reasonable to expect the friction law governing a thin film to be closer in the form to that of a macroscopic body moving through a viscous fluid, $F = mv/\tau$, given the absence of an opposing counterface contact in both cases. An increasing number of theoretical efforts have treated this topic within the context of phononic friction, including how friction can be controlled to provide directed transport of adsorbates. In the following, selected studies are highlighted, to demonstrate the range and breadth of ongoing theoretical work on the topic.

3.3.7.1 *Disorder* The effect of substrate step edges and pinning of adsorbed layers on a QCM was studied numerically in detail by means of numerical modeling in 1999 [186]. In particular, the effects of a step defect and a random array of point defects (such as vacancies or substitutional impurities) on the force of friction acting on a xenon monolayer film as it slid on a silver (111) substrate were studied by MD and compared with the results of lowest-order perturbation theory in the substrate corrugation potential. For the case of a step, the magnitude and velocity dependencies of the friction force were reported to be strongly dependent on the direction of sliding with respect to the step and the corrugation strength. When the applied force F was perpendicular to the step, the film was pinned for F less than a critical force F. Motion of the film along the step, however, was not pinned. Fluctuations in the sliding velocity in time provided evidence of both stick–slip motion and thermally activated creep. The critical force, however, was still much lower than the effective inertial force exerted on the film by the oscillations of the substrate in experiments done with a QCM. Nonetheless, experimental observations reveal that at sufficiently high oscillator amplitudes and monolayer coverages, the friction of adsorbed layers do slip and are well described by the linear friction, Equation (2). QCM data for sliding film friction measurement for a variety of material combinations are reviewed in Section 4.

Braiman and coworkers presented numerical and experimental evidence which demonstrated that under certain conditions, friction can be reduced by spatial disorder and/or thermal noise

[394,396]. Adsorbed films sliding on substrates exhibiting in-plane disorder [404] (in contrast to out-of-plane step edges) were cited as a case example. Possible mechanisms for the behavior were discussed, including arguments that the effect of quenched disorder could be related to a decrease in fluctuations of the center of mass motion that gives rise to friction.

Directed transport of Brownian particles is intimately linked to friction and diffusion: studies of how disorder impacts diffusion thus provide insights into the sliding friction behaviors of molecules and submonolayer films on surfaces [123,126]. Common sources of disorder include spatial disorder, vibration, and thermal noise. Luo *et al.* investigated a Brownian motor with Gaussian short-range correlated spatial disorder and time-delayed feedback [398]. The effects of disorder intensity, correlation strength, and delay time on the transport properties of an overdamped periodic ratchet were discussed for varying driving force levels. For small driving forces, the disorder intensity could induce a peak in the drift motion and a linear increasing function in diffusion motion. For large driving forces, the disorder intensity could suppress the drift motion but enhance the diffusion motion. For both small and large driving forces, the correlation strength of the spatial disorder could enhance the drift motion but suppress the diffusion motion.

3.3.7.2 *Vibration* Friction reductions through vibration have been theoretically predicted by Capozza *et al*. [405]. The effect was observed experimentally in 2006 by Socoliuc *et al.* [406] who reported sharp reductions in friction by exciting mechanical resonance of an AFM sliding system perpendicular to the contact plane, which mimics an increase in temperature in that the mechanical vibration plays the role of lubrication to overcome the stiction [407].

3.3.7.3 *Thermal noise* Ai *et al.* have published a number of reports on the topic of transport of a Brownian particle moving in a periodic potential in the presence of a symmetric unbiased external force [408–410]. The viscous medium is alternately in contact with two heat reservoirs. The group has found that the competition of the asymmetric parameter of the potential with the temperature difference leads to phenomena like current reversal and that the competition between the two driving factors is a necessary but not a sufficient condition for current reversals.

3.4. *Electronic mechanisms of friction*

In addition to phononic friction, there is another type of dissipation mechanism, electronic, that takes place in electrically conductive materials. In both electronic and phononic friction, kinetic energy associated with the sliding motion at an interface is transformed to heat. The heat is associated with temperature increases in both materials in sliding contact and is reflected in the phonon populations therein. Phononic dissipative mechanisms involve direct transfer of energy into the phonon populations. In contrast, electronic mechanisms involve energy transfer into the conduction electrons before transfer to the phonon populations. Electronic contributions to dissipation processes are manifested in many physical phenomena. These include electromigration, or "electron wind", effects [411], increased metal film resistivity in the presence of adsorbed films [412], antiabsorption peaks in infrared spectra for dipole-forbidden adsorbate vibrations [413], broadening of infrared absorption spectroscopy lines associated with the damped vibrations of surface adatoms [414,415], charge carrier level friction dependencies in semiconductors [156,157, 416,417], electron work function correlations with the elastic and frictional properties of metals [418], reports of significant increases in friction when a doped insulator becomes conducting [36], and reports of a drop in friction at superconducting transitions in both atomic- and macroscopic-scale systems [165,419–421]. Theoretical treatments of the latter phenomenon include [323,349, 351,357,422–434].

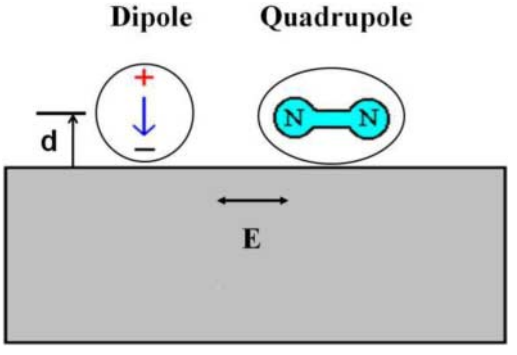

Figure 54. Schematic of conduction electron contributions to friction. Damping of adsorbate vibrations can be related to electronic effects within the bulk and at the surface of a conducting substrate.

The topic of electronic contributions to friction within the context of adsorbed molecules was pioneered by B.N.J. Persson beginning in 1978, within the context of examining how quickly molecular motion might be damped for atoms or molecules located at a distance d from the surface of a metal [435] (Figure 54). "Bulk" effects associated with the conversion of electronic currents in a metal into heat through scattering against phonons, impurities and/or other electrons had been treated in prior literature, but an additional "surface" effect associated with excitation of electron–hole pairs in the metal due to the presence of the metal surface had not been considered. Persson expected the latter mechanisms to dominate for molecules adsorbed directly on metal surfaces and proceeded to develop and refine models of electronic contribution to friction, with a particular emphasis on surface effects, including the relative proportions of surface to bulk effects.

Persson applied his theoretical framework in a landmark publication that treated the case example of a CO molecule adsorbed on Cu(100) in 1980, for a system whose vibrational properties had been experimentally probed [436] (see also [110,437]). The work was further developed in subsequent studies [438,439]. In 1991, he published another landmark work that related the change in thin-film resistance to the vibrational damping of layers adsorbed on its surface that originates in electronic effects [412]. The same year, M. Persson noted that the slip times reported for QCM measurements of sliding friction were of the same order of magnitude as the characteristic damping times generated in B.N.J. Persson's theories [119]. B.N.J. Persson further developed several applications of the surface resistivity concept and reported them in 1992, focusing on the topics of atomic-scale friction, electrochemistry, and the migration of hot adatoms [440]. Beginning in 1994, he teamed with A. Volokitin to publish a series of important papers on topics that ranged from the relation of infrared spectroscopy to adsorbate vibrations [413], electronic friction of physisorbed molecules [441], friction between small particles, and metal surface [427]. In addition, he published a number of papers that treated electronic contributions to friction in noncontact geometries [442–444]. Much of Persson's work is summarized in a book on sliding friction that he published in 1998 and updated in 2000 [4], as well as a review article coauthored with Volokitin [443]. In the following, Persson's work as well as closely related publications by other authors on electronic friction are discussed for the cases of surface resistivity, electronic contributions to rare-gas adlayers, and superconductivity dependent friction.

3.4.1. *Surface contributions to sliding friction and changes in thin-film resistivity*

In Persson's model for surface contributions to electronic friction, the presence of another surface or an adsorbate and the sliding across the metal substrate causes excitations of the conduction

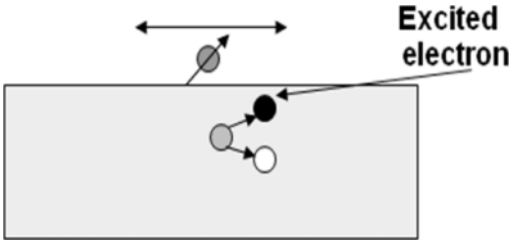

Figure 55. Schematic of sliding-induced electronic friction. Excitations of the conduction electrons near the interface generate electron–hole pairs. When the electron–hole pairs relax, the excess energy is dissipated as heat, and the temperature concomitantly rises.

electrons near the interface (Figure 55). The excitations generate electron–hole pairs which, in contrast to semiconductors, have very brief lifetimes. When the electron–hole pairs relax, the excess energy is dissipated as heat, and the temperature concomitantly rises. The mechanism is quite distinct from the forces associated with static charge buildup on insulating materials.

Persson's original relation of the electronic component of friction, μ_{eh}, to the resistivity of an adsorbate–substrate system was expressed as [412]

$$\mu_{\mathrm{eh}} = n^2 e^2 d \, \frac{\Delta\rho}{m n_{\mathrm{a}}}. \tag{10}$$

Equation (10), which is repeated here for continuity, sets n as the number of conduction electrons per unit volume, e is the electron charge, d the thickness of the metal film, $\Delta\rho$ the adsorbate-induced increase in film resistivity, m the adsorbate mass, and n_{a} the number of adsorbates per unit area in direct contact with the adsorbate (Figure 15). The expression was derived under the assumption of a viscous friction law of the form:

$$F_{\mathrm{f}} = m\mu_{\mathrm{eh}} v, \tag{61}$$

where F_{f} is the force of friction and v is the sliding speed. Extensions of Persson's resistivity formulation include thick film and semi-infinite metal formulations [445], as well as treatments of quasicrystalline films [446]. Extensive comparisons of frictional damping coefficients obtained by applying Equation (10) to surface resistivity measurements have been performed with slip times obtained by QCM (Section 4, Table 22). It should be noted that the approach, while generating values comparable in magnitude to that of the total friction as measured by QCM [447], is currently thought to require further refinement for complete determination of electronic contributions to friction in most cases.

For example, in a study of dc resistance and infrared reflectance changes induced in epitaxial Cu(100) films by adsorbed oxygen, Tobin and coworkers argued that standard surface resistivity models based on free electrons and point scatterers were inadequate, even if adsorbate-induced changes in conduction electron density are considered [448]. Electron density changes were proposed to account for the variation. Their studies revealed that the ratio for adsorbed oxygen was found to vary with the conductivity of the clean film, which differs from sample to sample. Interpreting these results within a free electron model would require that each adsorbate localizes an unreasonably large number of conduction electrons. The group thus argued that significant modification of the prevailing free-electron models, perhaps including energy-dependent scattering, would be necessary to explain the experimental results.

In 2003, Tobin and coworkers reported studies of sulfur and oxygen adsorbed on Cu(100), which have nearly identical bonding geometries and electronic structures [449]. But they observed

strikingly different trends in their scattering of conduction electrons, as reflected in the variation of the substrate's surface resistivity with adsorbate coverage. For oxygen, the surface resistivity was observed to vary linearly with coverage, as expected for noninteracting adsorbates. For sulfur, however, the coverage dependence was observed to be highly nonlinear, with the resistivity increasing strongly at low coverage and then becoming nearly constant above about 0.15 monolayers. Measurements on sputtered surfaces showed that defects and adlayer ordering were not responsible for the nonlinearity. They ultimately attributed to interactions between the adsorbed atoms that modify the electronic structure near the Fermi level so as to diminish each atom's scattering cross-section.

In 2008, they reported measurements of surface resistivity as a function of coverage for oxygen adsorbed on sulfur-predosed Cu(100) films and observed two types of interactions between sulfur and oxygen: S–O repulsion and short-range suppression of the surface resistivity change induced by oxygen adsorption [450]. The repulsive interaction was argued to cause oxygen atoms to first occupy adsorption sites far from the sulfur atoms, beyond second-nearest-neighbor sites, where the oxygen-induced surface resistivity is unaffected by sulfur. As a result, the low-coverage variation of surface resistivity with oxygen coverage was found to be indistinguishable from the linear dependence observed for oxygen on clean Cu(100). As the oxygen coverage increased, it begins to occupy sites close to sulfur. At the nearest-neighbor sites, the resistivity change due to added oxygen is completely suppressed, and the sample resistance levels off, remaining unchanged even as oxygen continues to adsorb. This resistivity suppression may involve both a reduction of oxygen's direct effect on the resistivity and an oxygen-induced reduction in the resistivity due to the already adsorbed sulfur. With increasing sulfur precoverage, both the maximum resistivity change and the oxygen coverage at which the leveling occurs decrease, because the number of sites unaffected by sulfur is reduced. Both the sulfur–oxygen repulsion and the resistivity suppression presumably arise from a through-metal coupling involving adsorbate-induced modifications of the local electronic structure.

3.4.2. *Electronic contributions to sliding friction inferred from rare-gas adlayer transitions*

3.4.2.1 *Monolayer to bilayer transitions* In 1996, Daly and Krim reported QCM measurements of the sliding friction of xenon monolayers and bilayers adsorbed on Ag(111) and compared the slip times for the same in-plane densities [352,353]. They observed that the friction per unit area required to slide the two-atom-thick film was 27% greater than that required to slide a one-atom-thick film and suggested that the ratio should be reflective of the proportion of phononic to electronic friction. Persson and Nitzan [117] (see also [451]) explored this possibility, with a model that included both phononic (μ_p) and electronic (μ_e) contributions, expressing the frictional drag coefficient in Equation (2) as the sum of phononic and electronic contributions:

$$\mu_v = \mu_e + \mu_p. \tag{62}$$

The electronic friction introduced here is purely phenomenological, and added in as the additional friction necessary to fit experimental results once the first principles' phononic contributions are accounted for. For the study [117], adsorbed Xe atoms were assumed to be moving under the influences of both an external force **F** and a stochastically fluctuating (thermal) force **f**:

$$m\frac{d^2 r_i}{dt^2} + m\mu_v \frac{dr_i}{dt} = -\frac{\partial U}{\partial r_i} - \frac{\partial V}{\partial r_i} + f_i + F, \tag{8}$$

Equation (8) (rewritten here for clarity) represents the forces on particle i, and mass m, at position **r**. The Xe–Xe interactions were modeled as a sum of Lennard-Jones pair potentials, Equation

(58). Although the substrate interaction of a xenon atom with a Ag(100) substrate rather than Ag(111) was employed, the authors argued that the general results should not be dependent on the detailed form of the potential. The form of the potential that they employed was written as (Equation (8.4) in [4])

$$U(r) = E_{\mathrm{b}}[\mathrm{e}^{-2\alpha(z-z_o)} - 2\,\mathrm{e}^{-\alpha(z-z_o)}] + U_{\mathrm{o}}[2 - \cos(kx) - \cos(ky)]\,\mathrm{e}^{-\alpha'(z-z_o)}. \tag{63}$$

Here, E_{b} is the adsorbate binding energy, $k = 2\pi/a$, with substrate lattice constant a of the substrate, $2U_{\mathrm{o}}$ is the surface corrugation or barrier height, and $\alpha$is the decay constant. Persson and Nitzan employed a barrier height of $2U_{\mathrm{o}} = 1.9$ meV, based on experimental measurements of the phonon modes for the Xe/Cu(111) system [452]. This estimate of the surface corrugation assumes that the Cu(111) substrate is not perfectly rigid, an improvement on the assumption of Cieplak *et al*. of a rigid, nondissipative substrate [35]. In addition, Persson and Nitzan used a thermostat to hold the temperature at 77.4 K. They concluded that only a very low contribution to the friction was associated with phonons and attributed almost all of the friction in the Xe/Ag(111) system to electronic friction. They interpreted the increase in friction for the second layer to be an indication that the second layer was pushing the first-layer xenon atoms closer to the silver surface, thus increasing electronic friction.

Tomassone *et al.* [354], however, reached a nearly opposite conclusion. They performed an independent simulation of the Xe/Ag(111) system and concluded that the friction was primarily arising from phononic effects. They reported that the increased number of possible dissipative vibrational modes were greater for a bilayer than for a monolayer, causing the increase in friction. They used MD simulations with a sum of Lennard-Jones pair potentials to model the Xe–Xe interaction, as did Persson and Nitzan, but they differed in that their model of the xenon atom interacting with the Ag(111) substrate was similar to that used by Cieplak *et al*. [35]. This is the potential originally derived by Steele [116] to model the interaction between a xenon atom and the silver substrate. Steele's potential is more corrugated than the actual interaction, so Tomassone and colleagues modified the Steele potential to include the electronic screening of the corrugation potentials by the conduction electrons. They state that their maximum peak-to-peak surface corrugation to be $U_{\mathrm{o}} = 2.7$ meV. As an improvement on prior models, they employed a thermostat to establish equilibrium, but turned it off while monitoring the properties of the system so as not to interfere with the frictional heating process. Using this model, which included only phononic friction, they were able to successfully fit the xenon on Ag(111) experiment of Daly and Krim and concluded that phononic mechanisms were dominant. To further support their conclusion, Tomassone *et al.* also performed simulations using the same electronic friction damping constants employed by Persson and Nitzan. With the modified Steele corrugation potential and Persson and Nitzan's model for electronic friction, they reported that 75% of the friction in the Xe/Ag(111) system was phononic in origin.

A subsequent effort by Liebsch *et al.* resulted in the conclusion that both electronic and phononic friction were required to accurately model the Xe/Ag(111) monolayer to bilayer result [453]. They concluded this based on the fact that electronic friction is not highly coverage dependent, as the experimental results of Daly and Krim suggested. They pointed out that nanotribological models are strongly dependent on knowledge of the corrugation amplitude of the Xe/Ag interaction potential, a number that has not been precisely measured. Without knowledge of the corrugation amplitude, they argued, it was not possible to predict the relative contribution of phononic versus electronic friction with any accuracy. They therefore varied both the corrugation amplitude and electronic contribution in their model according to

$$\mu_{\mathrm{v}} = \mu_{\mathrm{el}} + aU_{\mathrm{o}}^2. \tag{64}$$

Here μ_v is the total viscous friction coefficient, μ_{el} the damping due to the electronic contribution to friction, a is a constant dependent on temperature and coverage, and U_o the adsorbate/substrate interaction potential corrugation. As they varied the values of the surface corrugation, they found that if their model included a large surface corrugation, electronic friction vanished, consistent with the findings of Tomassone *et al.* But if the value for the electronic friction coefficient was large, electronic friction obviously dominated, consistent with the Persson and Nitzan result. They argued that since both the surface corrugation and the electronic friction coefficient had not been conclusively measured experimentally, it was very difficult to accurately model the friction for Xe/Ag(111).

Robbins and Muser later suggested [454,455] that a modified form for Equation (64) (repeated here for clarity):

$$\mu_v = \mu_{subs} + aU_o^2. \tag{3}$$

Here, μ_{subs} is a damping term that includes both electronic and phononic frictional dissipation within the substrate and the second term is the phononic energy dissipation occurring in the adsorbed layer. By including a contribution to the damping from phonons, the phononic frictional energy can be dissipated within the substrate rather than exclusively in the adsorbed layer. Coffey *et al.* [356] explored Equation (3) expression in detail for Xe adsorption on a series of substrates with known substrate corrugations and concluded that electronic contributions were negligible, with a best-fit value of $\eta_{sub} = 10^{-16}$ ns^{-1} and a maximum value of $\mu_{sub} = 0.08$ ns^{-1}, within experimental error for Xe/Ni(111), Xe/Cu(111), and Xe/graphene/Ni(111).

3.4.2.2 *Liquid to solid monolayer transitions* Robbins and Krim hypothesized in 1998 that electronic contribution to friction, being relatively constant with coverage, would also be reflected in the height of the jump in slippage at a liquid to solid monolayer phase transition [451]. The central results of their study are presented in Figure 56. The filled triangles represent slip time data acquired by Krim *et al.* for Kr/Au(111) [33,34]. The solid line shows the numerical model of Cieplak *et al*. [35], which fit the experimental data using only phononic friction. The dashed lines represent their numerical model with electronic friction included, and equal to 1/3, 1/2, and 9/10 of the friction at high coverage due to electronic friction, from bottom to top. Note that electronic friction serves to decrease the jump in slip time attributable to the phase transition. Coffey and Krim [355] explored this effect by documenting the size of the jump for Kr adsorbed on a series of (111) substrates and reported the ratios to fall between a maximum of 5, for adsorption on Au(111) to a minimum of 1.1, for adsorption on C60. The results were inconclusive in terms of the proportions of electronic to phononic friction.

3.4.3. *Superconductivity-dependent friction*

Arguably, the first clear experimental evidence supporting the existence of nonnegligible electronic friction levels for sliding adsorbed layers was reported in 1998 [165]. Dayo *et al.* employed a QCM to study the sliding of thin N_2 films adsorbed on a lead surface and observed the friction to drop by almost half when the substrate became superconducting (Figure 57). The changes observed at T_c were attributed to electronic mechanisms, seemingly bulk in nature since the bulk resistance drops abruptly at the superconducting transition and phononic corrugation potentials have no known dependence on superconductivity. Dayo's studies inspired much theoretical work on the topic [70,323,349,351,357,359,414,422–434,456,457] and remain open for interpretation to the present day.

Popov published one of the first theoretical formulations on the topic, treating the electrons in the metal as a hydrodynamic plasma within the two-fluid model of superconductivity

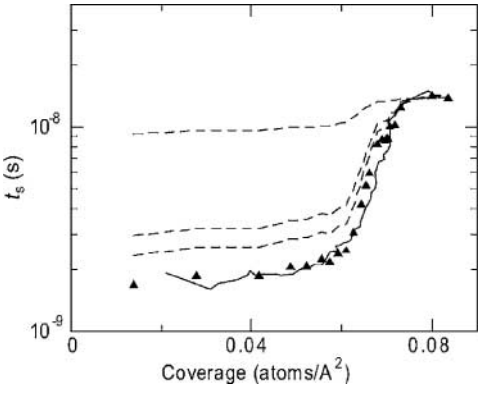

Figure 56. Slip time versus coverage for Kr/Au(111) at 77.4 K (see text) The dashed lines represent electronic friction modeled as 1/3, 1/2, and 9/10 of the friction at high coverage, from bottom to top. Note that electronic friction serves to decrease the jump in slip time attributable to the phase transition. Figure reprinted with permission from T.S. Coffey *et al.*, Physical Review B 72, art#235414, 2005 [355]. Copyright (2005) by the American Physical Society.

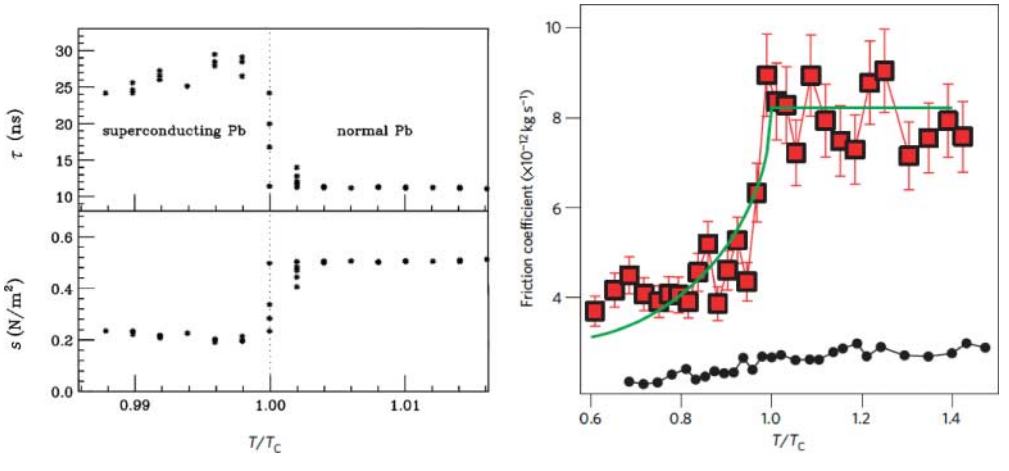

Figure 57. (color online) (Left) Slip time τ and shear stress s versus temperature for nitrogen sliding on Pb(111), above and below the Pb superconducting transition at $T_c = 7.2$ K. Reprinted figure with permission from A. Dayo *et al.*, Physical Review Letters 80, p. 1690, 1998 [165]. Copyright (1998) by the American Physical Society. (Right) Friction coefficient versus temperature for a sharp cantilever tip vibration at 5.3 kHz in close (but not contacting) proximity to a Nb surface above and below the Nb superconducting transition at 9.2 K. Phononic contributions are sufficiently small in both geometries to allow conduction electron contributions to be detected. Reprinted with permission from Macmillan Publishers Ltd: Nature Materials 10, pp. 119–122, 2011 [628], Copyright (2011).

[422,423,456,457]. In Popov's model, a drag sliding layer gives rise to a surface drag flow and to a bulk back flow of electrons. Since the dissipative properties of the back flow drop abruptly at T_c, the friction will concomitantly drop there as well. Novotný and Velický subsequently pointed out that Popov's hydrodynamic treatment was a limiting case of their own, broader, model [424] and Sokoloff *et al.* [348] in a very similar but independent treatment concluded that if the adsorbate was sufficiently charged by donating electrons to the metal, then ohmic effects could make significant contributions to friction.

Persson contested Popov's hydrodynamic model, arguing that it would not be valid for realistic metal parameters [426] in the presence of defects. He also contested Sokoloff's formulation, arguing that the amount of charge transfer to the adsorbate layer required to produce the experimentally observed effect was unrealistically high. Moreover, he derived expressions for the ratio of the surface to bulk proportions of friction, which should not be independent of each other: By his estimate the friction arising from surface effects should be a hundred to a thousand times greater than bulk contributions, so at best the drop in friction at T_c should be a fraction of a percent, and certainly not a half. Sokoloff [351] disputed Persson's contention that bulk electronic friction must necessarily be much smaller than "surface friction", in a reformulation of a treatment of bulk electronic contributions reported by Bruch in 2000 [323]. Irrespective of the details, all agree that friction levels depend critically on how much charge is being transferred between the substrate and sliding adsorbed layer, and accurate measurements of charge transfer in the systems reported on are unavailable. The matter is reminiscent of the difficulty in predicting charge transfer levels and magnitudes in rubbing contact. Electron transfer, in addition to the direct work associated with it, has been linked to material friction through changes in the elastic properties of a metal [418], and the topic of static charge transfer in sliding friction remains a matter of great interest and opportunity for future progress [64,458–460]. The detailed relation between charge transfer in a static system, for example, [461], has not been related in detail to the level of charge transfer in rubbing contact.

In an analytic treatment published in 2000, Bruch [323] investigated the result of Dayo *et al*. by considering the ohmic friction associated with a complete adsorbed monolayer, rather than individual charged particles. Assuming that the N_2molecules in the monolayer film form an ordered herringbone pattern at low temperature, he demonstrated that the field due to quadrupole moments of the ordered film can produce electronic friction which is of a comparable level to that observed experimentally. This, like all ohmic mechanisms, should vanish quickly below T_c. In Bruch's model, inert rare-gas atoms should exhibit a much smaller effect, since their quadrupole moments are considerably smaller than that of N_2. Bruch theory has been successfully compared to sliding friction measurements, at least from a qualitative point of view [420,462].

Selected theoretical treatments of superconductivity-dependent friction are now described in more detail.

3.4.3.1 *Popov's ohmic damping model* Ohmic damping models dominate the theoretical treatments of superconductivity-dependent friction on account of the abrupt drop in friction reported by Dayo *et al*. These are theories in which the only contributions to electronic friction considered are those arising from ohmic damping of image charges and currents created by a sliding adsorbate. One of the first attempts at this approach was made by Popov in 1999, with a follow-up work in 2000 and 2001 [422,423]. Popov considered the frictional force due to the dragging of conduction electrons near a metal's surface, by treating the metal's electron gas as a hydrodynamic plasma (Figure 58). As adsorbates slide along the surface of a substrate they induce a "drag current" of conduction electrons (Figure 57). During this process, the substrate must maintain charge neutrality, so a back-flow of current in the substrate also exists. Popov treated the electron gas as a hydrodynamic plasma, and the differential equation governing the motion of the gas was thus written as

$$\eta_3 \frac{\partial^2 v}{\partial y^2} - \frac{\rho v}{\tau_U} + enE = 0. \tag{65}$$

In Equation (65), v is the velocity of the electron gas, η_3 is the viscosity of the electron gas, ρ the mass density of the electron gas, τ_U is the free flight time between nonconservative collision processes, e the elementary electric charge, n the electron density, and E the electric field resultant

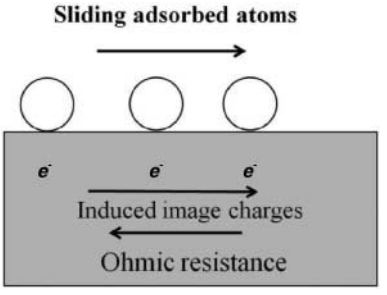

Figure 58. Schematic of bulk "ohmic" contributions to friction. Image charges induced by fluctuating dipole moments in the adsorbed atoms are pulled through the metal, encountering ohmic resistance. Popov's model includes a backflow current to achieve neutrality. Bruch's model considers a complete monolayer rather than individual atoms.

from the displacement of charge. The first two terms in Equation (65) represent the behavior of the electron gas when only the drag current is considered. The third term represents the back flow current. Popov wrote the mean free path between nonconservative collisions as

$$l = \left(\frac{\eta_3 \tau_{\mathrm{U}}}{\rho}\right)^{1/2}. \tag{66}$$

Applying these expressions to the specific case of Dayo *et al*. experiment, for a substrate thickness $d = l$, Popov employed the boundary conditions $v(0) = v_0$, and $v(d) = 0$, where v_0 is the adsorbate velocity, to solve Equation (65). For the normal state:

$$v(y) = v_0 \left(1 - \frac{4y}{d} + 3\left(\frac{y}{d}\right)^2\right). \tag{67}$$

In order to determine the frictional shear stress in the normal state, the derivative of Equation (67) was taken with respect to y, evaluated at $y = 0$, and then multiplied by the viscosity η:

$$|\sigma_{\mathrm{n}}| = \eta_3 \left|\frac{\partial v}{\partial y}\right|_{y=0} = \eta \frac{4v_0}{d}. \tag{68}$$

To solve for the shear stress in the superconducting state, Popov expressed Equation (65) as

$$\eta_3 \frac{\partial^2 v}{\partial y^2} - \frac{\rho v}{\tau_{\mathrm{U}}} = 0 \tag{69}$$

by arguing that an E field cannot be present within a superconductor. Employing the same boundary conditions, the solution to Equation (69) is then

$$v(y) = v_0 \left(1 - \frac{y}{d}\right) \tag{70}$$

and the shear stress in the superconducting state is

$$|\sigma_{\mathrm{n}}| = \eta_3 \left|\frac{\partial v}{\partial y}\right|_{y=0} = \eta_3 \frac{v_0}{d}. \tag{71}$$

Popov's model generates a factor of 4 between the shear stress in the normal and superconducting states, which is greater than the factor of 2 observed by Dayo *et al*. The model did not incorporate

the effects of phononic contributions to friction, however, which would change this ratio. As an improvement on the original work, Popov solved for the change in shear stress for the more general case of a thick film limit and obtained:

$$|\sigma_s| = \frac{\eta_3 v_0}{l} \frac{e^{d/l} + e^{d/l}}{e^{d/l} - e^{d/l}}, \tag{72}$$

$$|\sigma_n| = \frac{\eta_3 v_0}{l} \frac{(1 + d/l)e^{-d/l} - (1 - d/l)e^{d/l}}{4 - 2(e^{d/l} + e^{-d/l}) + (d/l)(e^{d/l} - e^{-d/l})}. \tag{73}$$

Popov then goes on to state that if one takes the ratio of Equations (72) and (73) measured by Dayo *et al*. ($\sigma_n/\sigma_s = 2$), this value implies $l \approx 650$ Å, a reasonable value. While Popov's model captures much of the physics of the problem, it must again be emphasized that the shear stress reported in the superconducting state by Dayo *et al*. is expected to have phononic contributions that are not reflected in Equation (72). Therefore, comparisons of the ratio alone are insufficient.

3.4.3.2 *Novotny, Velicky, and Sokoloff's ohmic damping models* Novotný and Velický subsequently pointed out that Popov's hydrodynamic treatment was a limiting case of their own, broader, model [424], and Sokoloff *et al.* [348] in a very similar but independent treatment concluded that if the adsorbate was sufficiently charged by donating electrons to the metal, then ohmic effects could make significant contributions to friction. In both studies, the authors use a classical electrodynamic approach to calculate frictional losses of a single charged dipole sliding above a metal substrate in the normal and superconducting state. The conductivity of the substrate was calculated based on a simple two-fluid model of a superconductor. The frequency-dependent conductivity can then be written as

$$\sigma(\omega) = \left(\frac{n_N e^2 \tau_s}{m}\right) + \left(\frac{i n_S e^2}{m\omega}\right). \tag{74}$$

Within in Equation (74), the first term on the right, in which n_N is the number of normal state electrons, τ the Drude relaxation time, and m the effective electron mass, represents the normal state fluid component. The second term on the right, in which n_s is the number of superconducting electrons, and ω is the drive frequency, represents the super fluid component of the conductivity. Both models then use the two-fluid conductivity to calculate the frictional force felt by an oscillating dipole due to the creation of an image charge of magnitude e within the substrates bulk. Both papers calculated a drop in friction similar in magnitude to what was reported by Dayo *et al*. Novotný *et al*. extended their model further by considering the temperature dependence of the change in friction as the substrate passes through a superconducting transition. Equation (75) describes the temperature dependence of the ratio of the superconducting and normal state coefficients of sliding friction as predicted by Novotný *et al*.:

$$\frac{\Gamma(T, \omega_d)}{\Gamma_0} = \frac{1}{1 + [4(1 - T/T_c)/\omega_d \tau]^2}. \tag{75}$$

In Equation (75), Γ is the coefficient of friction in the superconducting state, Γ_0 the normal state coefficient of sliding friction, T_c the bulk critical temperature of Pb, and ω_d the frequency of the force driving the oscillation. Equation (75) predicts a smooth rapid friction transition similar in line shape and magnitude to what has been observed. However, the transition described by Equation (75) is much more rapid in terms of temperature than any transition we have recorded. Both the models derived by Novotný *et al*. and Sokoloff *et al*. accurately describe the change in friction observed at a superconducting transition using only ohmic heating as the energy loss mechanism. It should be noted though that both theories rely on significant charging in the absorbate

layer to reproduce the Dayo *et al.* effect. As a physical justification for this assumed charging, Sokoloff *et al*. cited experiments on adsorption and a metal's work function [461] whereby the work function of the metal was lowered by the presence of gas on the surface. This would then imply the adsorbed layer is left with a residual charge. Though Sokoloff *et al*. cited a physically plausible mechanism for charge transfer, the amount of charge transferred that can be physically justified for nitrogen sliding on a Pb surface remains an open question. The charge transfer levels reported in [461] were insufficient to justify the residual charge value assumed by the models of Sokoloff *et al*. and Novotný *et al*. The detailed relation between charge transfer in a static system, moreover, has not been related in any reliable manner to the level of charge transfer in rubbing contact.

3.4.3.3 *Persson's model for surface and bulk electronic contributions* As mentioned above, Persson contested both Popov's hydrodynamic model, as well as Sokoloff's formulation, arguing that the amount of charge transfer to the adsorbate layer required to produce the experimentally observed effect was unrealistically high. Persson's theory took into account both surface scattering and bulk (ohmic damping) contributions to electronic friction [426]. He began with two classical force laws,

$$M\ddot{u} + M\mu_{\mathrm{v}}(\dot{u} - v) = F, \tag{76}$$

$$m\dot{v} - \left(\frac{n_{\mathrm{a}}}{n_{\mathrm{N}}W}\right) M\mu_{\mathrm{v}}(\dot{u} - v) + \frac{mv}{\tau} = eE. \tag{77}$$

In Equations (76) and (77), $\dot{u}$ is the velocity of the adsorbate layer relative to the substrate, v the drift velocity of the normal state electrons, M the adsorbate mass, m the effective mass of the exited electron, n_{a} the concentration of surface adsorbates, n_{N} the number density of normal state electrons, W the metal film thickness, F the driving force of the siding, τ the mean free time between collisions, and E the electric field in the substrate resulting from the displacement of charges. Persson pointed out that in the superconducting state no electric field can exist within the substrate, that is, $E = 0$, and then used this boundary condition to solve Equations (76) and (77) to yield the following coefficient of sliding friction:

$$\mu_{\mathrm{eff}} = \frac{\mu_{\mathrm{v}}}{1 + ((n_{\mathrm{a}}/n_{\mathrm{N}})W)(M/m)\eta\tau}. \tag{78}$$

Equation (78) implies that the coefficient of sliding friction would indeed be lower in the superconducting state, but the variation in η_{eff} with respect to temperature would be slow since the number of conduction electrons, n_{N} varies slowly at a superconducting transition. Persson then expands on this simple model by considering the temperature variation of η. To estimate the variation of $\eta$with temperature, Persson drew on previous work [412,439] in which adsorbed layers were considered to have permanent dipole moments that interact with the electrons in the metal film. From his previous work, Persson used the following equation for the coefficient of sliding friction associated this Coulombic interaction:

$$\mu_{\mathrm{v}} = \frac{p^2}{2M} \int \mathrm{d}qq^4 \lim_{\omega \longrightarrow 0} \left(\frac{Im\, g(q,\omega)}{\omega}\right) e^{-2qd}. \tag{79}$$

In the above equation, p is the dipole moment of the adsorbate, q is the induced charge in the substrate, and $Img\,(q,\omega)$ is the energy loss function which is proportional to the loss of power in

the metal [438,439]. By expanding $Img\,(q,\omega)$ to first order in q, Persson obtained:

$$g = \frac{\varepsilon(\omega) - 1}{\varepsilon(\omega) + 1} + A(\omega)q. \tag{80}$$

In Equation (80), ε is the Drude dielectric function given by

$$\varepsilon = 1 - \frac{\omega_{\mathrm{p}}^2}{\omega(\omega + i/\tau)}, \tag{81}$$

in which ω_{p} is the plasma frequency and τ is the bulk mean free time between scattering events. The first term on the right in Equation (80) represents scattering due to bulk impurities similar to the mechanism addressed in an earlier section. The second term on the right represents scattering due to the surface potential from the sliding layer. The short-range potential from the sliding layer causes scattering of conduction band electrons. The scattered electrons are exited and form electron–hole pairs. As the electron loses energy, it returns to its nonexcited state.

From Equations (80) and (81), Persson [426, Equations (4) and (5)] obtained surface and bulk contributions to the loss:

$$(Im\, g)_{\mathrm{bulk}} \approx 4\frac{\omega_{\mathrm{F}}}{\omega_{\mathrm{p}}}\frac{1}{k_{\mathrm{F}}l}\frac{\omega}{\omega_{\mathrm{p}}}, \tag{82}$$

$$(Im\, g)_{\mathrm{surf}} = 2\xi(q)\frac{q}{k_{\mathrm{F}}}\frac{\omega}{\omega_{\mathrm{p}}}, \tag{83}$$

where k_{F} is the Fermi wave vector, ω_{F} is Fermi frequency, l is the bulk mean free path, and $\xi(q)$ is dimensionless parameter dependent on the electron gas density, which in this case can be approximated as unity. The ratio of the surface contribution over the bulk is $\sim ql$, in this model, where $q \sim 1/d$. Persson argued that the surface contribution would dominate over the bulk contribution by a factor of $\sim l/d$, where d is the surface dipole separation, and estimated that l/d was of order 100–1000 for reasonable values for l and d. It should be noted though, that there is great uncertainty in the values: The bulk mean free path is sensitive to sample purity and morphology, while the dipole–surface separation is not precisely known.

Persson also derived the temperature dependence of the surface and bulk contributions, which revealed, as expected, that the surface contribution changed slowly at T_{c} while the bulk contribution dropped abruptly [433]. Persson found the comparison with experiment to be puzzling, and suggested that experiments be conducted on superconducting alloys, which would allow for studies of the effect of variations in the bulk mean free path l.

Persson's theory constitutes a comprehensive electrodynamics approach to the change is frictional force on a single dipole at a superconducting transition. Three additional approaches are presented next, for completeness, followed by a description of Bruch's model, which collectively treats an entire monolayer rather than the friction associated with individual adsorbed particles.

3.4.3.4 *Rekhviashvili's thermodynamic model* Rekhviashvili, in 2004, presented arguments that, below the critical temperature, the friction force must exhibit a characteristic extremum corresponding to the equality of the heat capacities of superconducting and normal phases. The derivation begins by writing the change in Gibbs free energy upon entering the superconducting state in terms of the critical field B_{c}, expressed as

$$G_{\mathrm{n}} - G_{\mathrm{s}} = \frac{VB_{\mathrm{c}}^2}{2\mu_0}, \tag{84}$$

where V is the volume of the superconductor and μ_0 is the permeability of vacuum. Rekhviashvili employs a result from bulk superconducting materials that the derivative of the change in Gibbs

free energy with respect to volume will give the change in shear stress, $\sigma_n - \sigma_s$, upon entering the superconducting state [463]. Therefore,

$$\sigma_n - \sigma_s = \frac{d}{dV}(G_n - G_s) = \frac{B_c^2}{2\mu_0} + \frac{S_s + S_n}{\alpha_T^{(V)} V}, \tag{85}$$

where the change in entropy is

$$S_s - S_n = \frac{VB_c}{\mu_0}\frac{dB_c}{dT} \tag{86}$$

and the temperature coefficient of the volume expansion of the superconductor is

$$\alpha_T^{(V)} = \frac{1}{V}\frac{dV}{dT}. \tag{87}$$

To estimate the change in shear stress at a transition, the author considered Equation (85) in the limit as $T \to 0$, which takes the form

$$\sigma_n - \sigma_s = \frac{B_0^2}{2\mu_0}, \tag{88}$$

where B_0 is the zero temperature critical field for bulk Pb. They then equate sliding friction with the force necessary to break contact for an area A_c, so multiply both sides of Equation (88) by A_c.The value derived for the change in shear stress for a single atom ($A_c = 0.01$ nm^2) and at a superconducting transition was approximately 300 N m^{-2}, substantially larger than the difference of 0.02 N m^{-2} reported experimentally. The deviation of Rekhviashvili's model from experimental observation could come from estimation made of the area an atom occupies on the substrate surface, or from the assumed value of B_0. The value for the zero temperature critical field in a thin film is not that of a bulk sample and it can in fact be much lower. A lowering of B_0 in Rekhviashvili's model would make its prediction closer to the experimental result. Rekhviashvili's model takes a unique approach to the problem and points out that the difference in entropy of the superconducting and normal states ($S_s - S_n = 0$) must be zero at $T = T_c$ and $T = 0$. Therefore, by the Nernst theorem the difference in the shear stress must exhibit an extremum corresponding to equality in the heat capacities of the normal and superconducting phases. Further experiments are suggested in the work that may allow for better comparisons with theory.

3.4.3.5 *Bruch's ohmic damping model for an adsorbed monolayer* An independent approach to ohmic damping was taken by Bruch in 2000 that constituted a significant extension of prior models that considering sliding only of single dipoles [323]. Bruch modeled instead the collective behavior of a complete sliding monolayer. His model is described as follows.

N_2 is thought to form a solid herringbone structure at low temperatures [464], which has a significant quadrupole moment that could contribute substantially to the magnitude of the ohmic damping experienced by the sliding layer (Figure 53). To incorporate the periodic structure of an adsorbed layer into a model of friction based exclusively on ohmic damping, Bruch expressed the electric field due to a periodic layer of electrostatic moments as a periodic series of field contributions expanded in terms of the monolayer reciprocal lattice vectors $\vec{g}$. The general form

of such an electric field is then

$$E_Z(\vec{r},z) = \sum_{\vec{g}} E(\vec{g},z)\exp(i\vec{g}\cdot\vec{r}), \tag{89}$$

$$\vec{E}_{\text{parallel}} = \sum_{\vec{g}} \left[\frac{\mathrm{i}\vec{g}}{g^2}\right] \exp(\mathrm{i}\vec{g}\cdot\vec{r})\frac{\partial E(\vec{g},z)}{\partial z}. \tag{90}$$

The incident field in the metal for a herringbone lattice can then be written as

$$E(\vec{g},z) = -\frac{\pi\theta}{a_{\mathrm{c}}}\exp(-g[z-z_0])\sum_{\beta=1}^{2}\exp(-i\vec{g}\cdot\rho_\beta)[\vec{g}\cdot\hat{l}_\beta]^2, \tag{91}$$

where θ is the quadrupole moment, a_{c} the area of the two-molecule unit cell, $\vec{\rho}_\beta$ the position of the molecules, and $\hat{l}_\beta$ are the unit vectors of the molecular axis. To incorporate motion into the model, Bruch added an oscillatory drive term:

$$\exp(\mathrm{i}\vec{g}\cdot\vec{r}) \rightarrow \exp[\mathrm{i}\vec{g}\cdot(\vec{r}-\vec{A}\cos\,\Omega t)], \tag{92}$$

where $\vec{A}$ is the amplitude of oscillation and Ω is the drive frequency. Bruch also derived equations similar to Equations (90)–(92) for the currents $\vec{j}$ in the substrate. With these expressions and much calculation, Bruch arrived at an expression for the loss of power due to the oscillation of an absorbed film $(\vec{j}\cdot\vec{E})$ and expressed it in terms of a decay time t_{d}, which can be interpreted as the slip time reported in QCM measurements. Bruch's expression for the slip time of an adsorbed layer with a herringbone structure is as follows:

$$\frac{1}{t_d(\hat{A})} = \frac{\theta^2 l}{6M\sigma_0(1-p)}\left(\frac{1}{a_{\mathrm{c}}}\sum_{\vec{g}}(\vec{g}\cdot\hat{A})^2\,\exp(-2gL_{\mathrm{ov}})\times\left|\sum_{\beta=1}^{2}\exp(-i\vec{g}\cdot\vec{\rho}_\beta)[\vec{g}\cdot\hat{l}_\beta]^2\right|^2\right).. \tag{93}$$

In Equation (93), L_{ov} is the distance between the sliding layer and the substrate, M is the mass of the adsorbate, σ_0 is the bulk conductivity of the metal substrate, and $(1-p)$ is the number of conduction electrons diffusely scattered at the interface. Bruch applied Equation (93) to obtain approximate slip times for the electronic contribution to friction for N_2 sliding on Pb and obtained 2–20 ns, which is in good agreement with the result of Dayo *et al*. if the electronic friction is assumed to completely vanish at T_{c}.

Bruch used the same method to calculate the ohmic damping that a triangular lattice of dipoles would experience and finds the slip time expression to be

$$\frac{1}{t_{\mathrm{d}}} = \frac{2\mu^2 l}{3Ma_{\mathrm{C}}\sigma_0(1-p)}\sum_{\vec{g}} g^4\,\exp(-2gL_{\mathrm{ov}}), \tag{94}$$

where μ is the dipole moment of an adsorbed molecule. Bruch obtained the ohmic damping term in Equation (94) for Xe sliding on Ag to be $\sim$ 200 ns. Bruch's calculation for Xe sliding on Ag indicates that the ohmic damping of the sliding layer will be much lower for layers without a quadrupole moment. If Bruch's theory accurately described superconductivity-dependent friction, the magnitude of the change in friction felt by a sliding layer at a superconducting transition would be lower for less polar sliding layers. Support for this prediction has been reported for the experimental systems of He [420] and Ne [462] sliding on Pb(111).

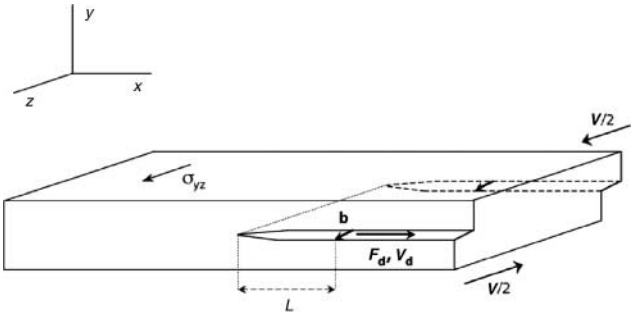

Figure 59. Force experienced by a screw dislocation resulting from an interfacial shear. Reprinted with permission from LD. Marks *et al.* [434]. Langmuir Copyright (2007) from Springer.

3.5. *A dislocation drag model of friction*

Marks and Merkle have derived an analytic expression for the friction force between solids that suggests that dislocation drag accounts for many of the observed phenomena related to solid–solid sliding. Included in this approach are strong arguments for agreement with friction dependence on temperature, velocity, orientation, and more general materials selection effects [434,465,466]. They report that their calculations of friction coefficients for sliding contacts are in good agreement with available experimental values reported from UHV experiments. Extensions of the model include solutions for common types of dislocation barriers or defects. In addition, they report that the effects of third-body solid lubricants, superplasticity, superconductivity, the Aubry transition, and supersonic dislocation motion can all be discussed within the framework of dislocation-mediated friction. This model thus begins to incorporate and merge separate phononic and electronic contributions into a more comprehensive treatment.

The model seeks to incorporate both electronic and nonelectronic sources of friction in terms of the movement of dislocations at two interfaces (Figure 59).

The absence of an atom at a dislocation can lead to regions of increased local charge density, scattering centers for phonons, and alteration of the band structure of a metal. Straining or bending a lattice can create Peierls instabilities, which cause gaps to open up in the band structure of a material and alter its conductivity [467]. The forces resisting the motion of a dislocation are written as

$$F = \sigma_{\mathrm{p}} \coth\left[\frac{b\sigma_{\mathrm{p}}}{B_{\mathrm{tot}} v_{\mathrm{d}}}\right], \tag{95}$$

where σ_{p} is the Peierls stress, b the vector defining the placement of the dislocations, v_{d} the dislocation velocity, and B_{tot} the total viscous drag term, which can be written as

$$B_{\mathrm{tot}} = B_{\mathrm{e}} + B_{\mathrm{w}} + B_{\mathrm{fl}}. \tag{96}$$

The three terms on the right-hand side of Equation (96) represent three independent contributions to the viscous drag. The pertinent term here is the electronic contribution B_{e}, which can be written as

$$B_{\mathrm{e}} \cong \frac{bN_{\mathrm{e}}\varepsilon_{\mathrm{F}}}{10 v_{\mathrm{F}}}. \tag{97}$$

In Equation (97), ε_{F} and v_{F} are the Fermi energy and the Fermi velocity, respectively, and N_{e} is the number of conduction electrons. Marks and Merkle suggest that the observations by Dayo *et al*. are consistent with the model. It should be noted that the temperature dependence of Equation (95) comes from the change in the number of conduction band electrons in Equation (97). The

number of conduction band electrons varies slowly at a superconducting transition; however, the electronic term is in the denominator of a hyperbolic cotangent function. A "coth" function has an asymptotic functional form where small changes in the argument of the function could cause large changes in the frictional force, if the function is in the correct regime. Numerical estimates of the magnitude of the change in friction and the rate at which the friction drops at a superconducting transition would be needed to definitely assess the degree to which the model agrees with experiment.

3.6. *Summary comments*

Major advances in theory are occurring rapidly in the area of fundamental theories of friction in sliding adsorbed layers. Outstanding challenges involve linking atomic-scale properties to extended length scales and moving beyond ideal contacts (single asperities, perfect crystalline substrates, etc.) to more realistic systems. In the following section, numerical and experimental results for specific material systems are reviewed.

4. Numerical and experimental results for specific material systems

In this section, measurements of the sliding friction of adsorbed molecular and monolayers are reviewed, with a focus on systems studied in unconfined geometries as probed by QCM and related techniques. A selection of notable and closely related experimental and theoretical literature reports are also included. Results in this section are presented according to the adsorbate studied, followed by discussion of categories of materials systems. These include superconducting substrates, semiconducting substrates, fullerenes, systems of interest for MEMS devices, and adsorbed films exhibiting solid–liquid, commensurate incommensurate phase transitions. Table A.1 presents slip time data categorized according to substrate, for adsorbed films ranging in thickness between 0.2 and 5 monolayers.

It is clear that atomic-scale surface defects and disorder must be taken into consideration when discussing experimental measures of sliding friction (Figure 60) [468–472]. "Substrate types" listed in the tables are categorized as "textured", "terraced", and "fractal" (Figure 60). "Amorphous" substrates are flat but disordered, while "fractal" substrates are both disordered and exhibit substantial out-of-plane roughness plus self-affine fractal scaling. Such surfaces arise from deposition of metal upon a substrate that is already rough, and/or by ion-beam bombardment of an initially crystalline surface [470]. A more quantitative description of submicron roughness may be found in [473].

While theoretical treatments of crystalline surfaces are straightforward, preparation of uniform crystalline substrates for studies of sliding friction in monolayers involve painstaking procedures. Bruschi *et al*. [182] have succeeded to prepare atomically uniform "terraced" Pb(111) films (Figure 60(b)) by e-beam evaporating 150 nm thick, high-purity Pb films in UHV conditions onto polished blank QCM at 155 K that had been prebaked and outgassed at 520 K. The morphology of the sample was characterized *in situ* by means of STM after annealing the sample to room temperature, and typical platelet sizes as large as 90 nm in extent, with a peak in the size distribution near 20 nm.

The gold film depicted in Figure 60(a) was prepared by thermal evaporation of 65 nm of high-purity Au at room temperature onto a polished blank QCM in UHV conditions after extensive outgassing of the sample [34]. Samples such as these, as well as the Pb(111) films utilized by Highland *et al*. [420], are characterized *in situ* through the degree of verticality of Xe adsorption isotherm steps, which allows terrace size to be estimated [474,475] (see also Figure 63). Typical terrace sizes estimated in this manner are in the order of 10 nm. X-ray diffraction scans performed

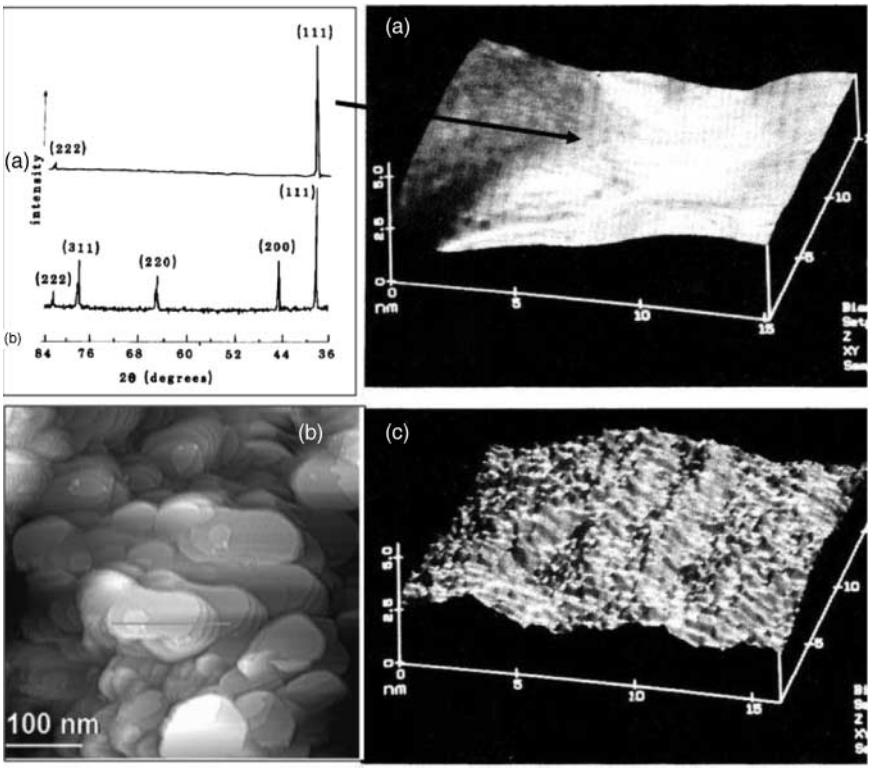

Figure 60. Examples of substrate types employed as electrodes prepared on the surfaces of QCMs for measurements of slip time: (a) Reprinted figure with permission from J. Krim *et al.*, Physical Review Letters 66, p. 181, 1991 [34]. Copyright (1991) by the American Physical Society. STM image of Au(111) fiber "textured" substrate along with X-ray diffraction data for the film compared to Au powder. Reprinted with permission from J. Krim, Thin Solid Films 137, pp. 297–303 [147]. Copyright (1986) with permission from Elsevier. (b) STM image of "terraced" Pb(111) substrate. Reprinted figure with permission from L. Bruschi *et al.*, Physical Review Letters 96, p. 216101, 2006 [182]. Copyright (2006) by the American Physical Society. (c) STM image of a "fractal" Ag film surface, Substrate types listed as "amorphous" are flat but not ordered with the surface plane. Reprinted figure with permission from J. Krim *et al.*, Physical Review Letters 66, p. 181, 1991 [34]. Copyright (1991) by the American Physical Society.

on the samples reveal a strong (111) texture that becomes stronger upon annealing the sample to 100°C [147]. Such samples are therefore referred to as "textured" given the documented fiber texture, but not "terraced", as step edges have not been resolved in the STM images.

Single-crystal graphite substrates are also referred to as "terraced" in the tables that follow. QCM slip times reported for adsorption on graphite have been obtained by Suzuki and co-workers [476] by attaching a graphite flake to an existing Au QCM electrode. The flake was obtained by dissolving a natural mineral, "Franklin Marble", in hydrochloric acid, then immersing it in a reaction mixture of sulfuric and nitric acid for 16 h to cause exfoliation. After neutralizing and drying, it was expanded by flash heating to 1050°C for 15 s, then heated in vacuum at 900°C for 4 h. In order to attach the flake to the QCM electrode, 100 nm Ag films were evaporated onto both the flake and the existing gold QCM electrode, the flake was pressed to the electrode in an atmosphere of hydrogen gas for 30 min at 290°C, and finally any excess graphite was removed. Sample uniformity was characterized by AFM, Laue photographs, and the verticality of adsorption

Table 2. QCM slip time data for ^{4}He films.

Substrate	Substrate type	T (K)	Reference	τ (ns) $\Theta = 1$	$\Theta = 2$	$\Theta = 4 - 5$
Ag	Textured		[479]		>0	
Au	Porous	0.5–2	[480]	>0		
Graphite	Terraced	0.45	[486]	20	7,80	
Graphite	Terraced	1.00	[486]	20	8,80	
Graphite	Terraced	1.25	[486]	20	8.5,70	
Graphite	Terraced	1.50	[486]		9, 60	
Hectorite	Porous	0.5–2.0	[490]	>0		
Hectorite	Porous	0.15–4	[490]		>0	
Hectorite	Porous	0.15–4	[490]		>0	
Hectorite	Porous	0.5–2.5	[481]	>0		
Pb(111): $T > T_c$	Textured	7.20	[420]	No magnet		76
Pb(111): $T < T_c$	Textured	7.20	[420]	No magnet		196
Pb(111)	Textured	7.20	[420]	No magnet		126(E)
Pb(111): $T > T_c$	Textured	7.20	[420]		Magnet	87
Pb(111): $T < T_c$	Textured	7.20	[420]		Magnet	1540
Pb(111)	Textured	7.20	[420]		Magnet	92(E)
Air-exposed Pb(111): $T < T_c$	Textured	4.20	[166]	20	10	18

isotherms, and large regions of uniformity in the order of 100 nm were reported. The ability to observe two-dimensional phase transitions is an indicator of very high substrate uniformity, for example, the Kr C–IC transition in the case of graphite substrates, and the liquid–solid monolayer transition for the case of metal substrates [33,34,355]. Very recently, the structure of Kr films adsorbed on very uniform Au film QCM electrode substrates have been resolved by means of HAS [174].

4.1. *Adsorbed rare-gas atoms*

4.1.1. *Helium films*

QCM slip time data for ^{4}He films are summarized in Table 2. When two values are present for the bilayer coverage, individual slip times for the first and second layers, respectively, are listed.

Early QCM reports of sliding in adsorbed helium films were published in 1972, for superfluid helium films adsorbed onto optically polished Au and Al electrodes, with and without pre-adsorbed neon layers. The measurements were performed at relatively low velocity amplitudes that did not exceed 0.8 mm s^{-1} [477]. In these studies, Chester and Yang compared the response of a transverse shear-mode QCM to helium films in the normal and superfluid state, and reported that only the normal fraction remains rigidly coupled to the substrate motion. Adsorption isotherms of He-4 measured by means of QCM showed clear departures from conventional behavior and the effect was attributed to the onset and presence of superfluidity in the film. In subsequent studies, the same authors reported that only the nonsuperfluid component of the helium film adsorbed on QCMs was producing a frequency shift response [478]. From this, they obtained detailed curves of the superfluid content in helium films below the superfluid transition. Given that they were focused on superfluid behavior and frequency shift data, but not quality factor shifts in the QCM, they did not detect that the normal components of the films were also slipping, albeit at only small levels compared to the superfluid constituents. More than 30 years later, it was firmly established that the normal phase component of He-4 also exhibits slippage on Ag [479], Au [480], hectorite [481], Pb(111) [420], and graphite [482–486] substrates.

Hieda *et al*. measured the decoupling of He-4 films adsorbed on Grafoil attached to Ag QCM electrodes [484,485]. They reported that nonsuperfluid He-4 films decoupled from the oscillating substrate, and that the degree of decoupling depended on the oscillating amplitude and the temperature. Based on the amplitude dependence of the decoupling data, the authors concluded that the friction was not proportional to the sliding velocity. Also, they reported that the temperature dependence of the sliding friction exhibited a decrease below a certain temperature, that is, at low temperatures the film falls into a low-friction state. The same authors also reported measurements of sliding friction of [484,485] nonsuperfluid He-4 films adsorbed on a porous gold substrate. Their gold substrate was reported to have a highly uniform porous structure, with a surface area effectively 20 times larger than that of a flat substrate. It was found that the degree of slippage between He-4 films and the substrate increases below a certain onset temperature, as in the case of grafoil and that the onset temperature decreased with increasing He-4 areal density. The increase depended strongly on the oscillating amplitude of the quartz crystal.

Hosomi and coworkers have performed extensive studies of multilayer He-4 films adsorbed on graphite [486–488] and have found the system to be very rich in structure. In one investigation [487], they observed that in a low-temperature regime, the sliding friction of an adsorbed He layer remained metastable after switching off the oscillation amplitude before relaxing to a constant value which was determined by the amplitude. They also reported that the relaxation characteristics of the friction were qualitatively different for decreasing and increasing amplitudes. In the former case, the relaxation depended strongly on temperature with a quasi-exponential time dependence, while for the latter they observed a quasi-logarithmic dependence. They interpreted the results in terms of relaxation by a model of a small low-friction domain, which is created or annihilated by overcoming a potential barrier.

In 2008, they reported an analysis of changes in the resonance frequency and Q value using a multilayer model and obtained the sliding friction of the boundary between the atomic layers in the film, in addition to the boundary between the film and the substrate. The sliding friction of the boundary of the first and second atomic layers was reported to be much smaller than that of the boundary between the film and the substrate [486] (Figure 61, left). The slip time values in Table 2 reflect this by listing two separate values for the two-layer-thick film. The first is the slip time for the first layer sliding on the substrate, while the second is the slip time of the second layer sliding over the first. More recently, Hosomi *et al*. reported that the solid atomic layers underneath the superfluid layer stop slipping from the oscillating substrate when the superfluid density grows to a certain magnitude (Figure 61, top) [488]. They explained the observation by a mechanism in which the mass transport caused by the motion of edge dislocations in solid atomic layers is canceled by counter flow of the superfluid overlayer.

The sliding behavior of helium films has also been studied on lead films both above and below the superconducting transition temperature at 7.2 K. Highland and Krim [420] studied sliding friction levels for four-atom-thick "superheated" He films adsorbed on Pb(111) substrates driven in and out of the superconducting state by an external magnetic field. Reductions in friction upon entry into the superconducting state were very small, but still detectable, consistent with Bruch's theory that linked electronic friction to adsorbate polarizability [115,323]. The work curiously revealed that repetitive cycling of an externally applied magnetic field also impacted the friction levels. Both values are reported in Table 2.

Slippage of nonsuperfluid He-3 films has also been documented in the literature. Casey *et al*. [489] employed a high-precision torsional oscillator to study He-3 films on silver of thickness from 100 to 350 nm, in the temperature range $5 < T < 200$ mK. The films were reported to decouple from the motion of the oscillator below 60 mK, and the data were interpreted in terms of an interfacial sliding friction model. The thicknesses studied were much smaller than the viscous penetration depth, and also much smaller than the low-temperature inelastic mean-free path of

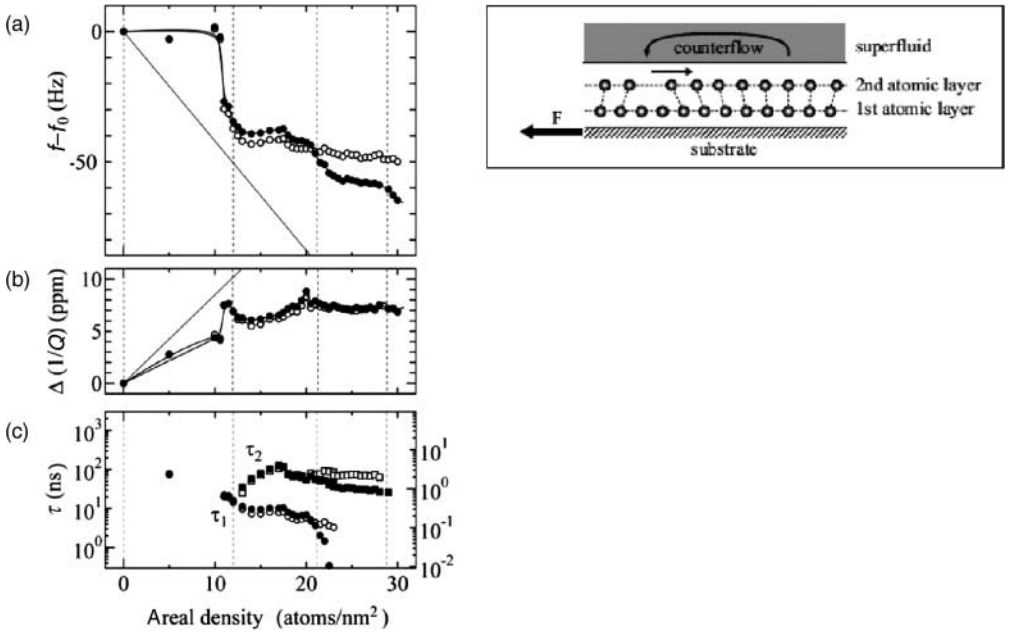

Figure 61. (upper right) Schematic of mass cancellation due to superfluid counterflow: the solid atoms underneath the superfluid layer stop slipping when the superfluid density attains a critical magnitude. (Left): Areal density dependence of the changes in (a) the resonance frequency and (b) Q value for 1.0 (closed) and 0.45 K (open). The solid line in (a) corresponds to the estimated mass loading of 4.2 Hz/(atoms nm^{-2}), while for (b) it is the possible maximum value, which takes place under the condition that the decrease in resonance frequency is half of the maximum decrease. (c) Calculated slip time for 1.0 K (closed) and 0.45 K (open) using the multilayer model. τ is for the boundary between the film and substrate, and τ is for the boundary between the first and second atomic layers. Reprinted figure with permission from N. Hosomi *et al.*, Physical Review B 79, p. 172503, 2009 [488]. Copyright (2009) by the American Physical Society.

He-3 quasiparticles. QCM reports of slippage of nonsuperfluid He-3 films have also been reported for hectorite substrates [490].

4.1.2. *Neon films*

QCM slip time data for Ne films are summarized in Table 3, the vast majority of which have been reported by the group of Bruschi, Mistura, and coworkers. This group has obtained very homogeneous and atomically uniform lead electrodes by depositing the lead at 150 K and then annealing at room temperature, as described earlier in this section [182,184]. The substrate type is listed as "terraced" given the "stacked platelet" nature of the films clearly present in STM images of the atomically uniform substrates. In measurements reported in 2006, a very pronounced and reproducible depinning transition between the low coverage region, where the layer is locked to the oscillating electrode, and a higher coverage regime characterized by slippage of the adsorbed film (Figure 62). The data were interpreted as a structural depinning of the Ne layer when it becomes incommensurate with the lead substrate, consistent with MD simulations. The result is the first observation of sliding friction changes in a commensurate to incommensurate transition for a physisorbed layer [182].

In 2010, they reported two more studies of sliding friction of neon on Pb(111). Given that neon slides readily at 7 K, the group was able to perform measurements of the sliding friction of

Table 3. QCM slip time data for neon films.

Preplate	Substrate	Substrate type	T (K)	Reference	τ (ns) $\Theta = 0.2$	$\Theta = 0.4$	$\Theta = 0.8$	$\Theta = 1$	$\Theta = 9$
	Pb(111): $T < T_c$	Terraced	5.4	[182]	0	0	0.15		
	Pb(111): $T < T_c$	Terraced	6.5	[182]	0	0	0.45		
	Pb(111): $T < T_c$	Terraced	6.5	[491]	0	0.7	2.5	3	
1–4 Kr monolayers	Pb(111): $T < T_c$	Terraced	6.5	[491]	0	0.7	7	8	
1–3 Xe monolayers	Pb(111): $T < T_c$	Terraced	6.5	[491]	1	4	7	8	
	Pb(111): $T > T_c$	Terraced	7.2	[462]			2.5	<5	
	Pb(111): $T < T_c$	Terraced	7.2	[462]			2.5	<5	
Brief air exposure	Pb(111): $T < T_c$	Textured	5.75	[166]					>>50

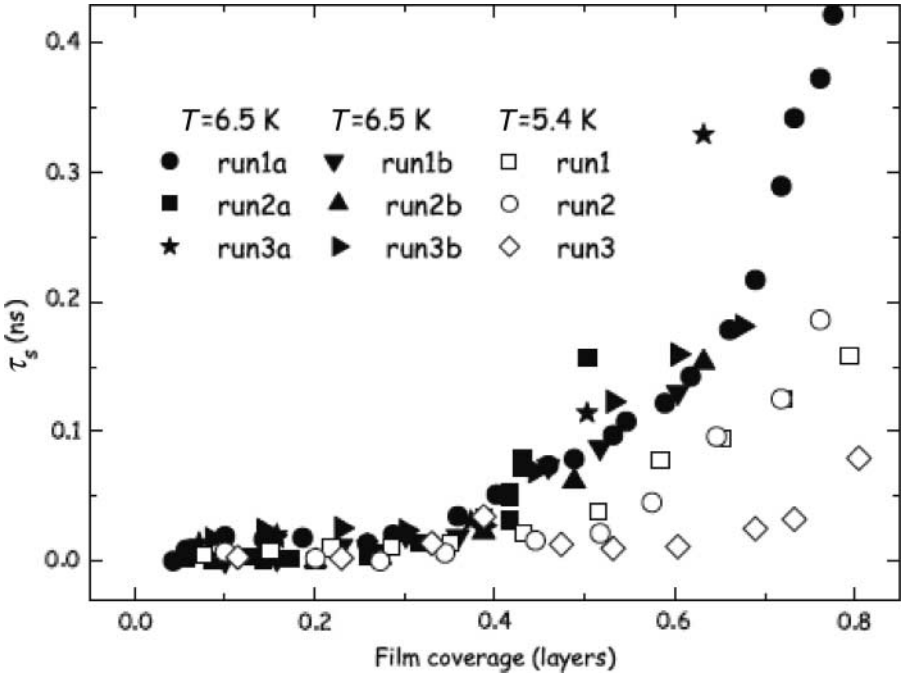

Figure 62. Normalized slip times for neon sliding on the Pb(111) substrates depicted in Figure 59 on successive days. A depinning transition is observed between 5.4 and 6.5 K above 0.3 monolayers. Reprinted figure with permission from L. Bruschi *et al.*, Physical Review Letters 96, art#216101, 2006 [182]. Copyright (2006) by the American Physical Society.

submonolayer films above and below the superconducting transition at 7.2 K [462]. They observed no change in friction, within experimental error, documenting that electronic contributions are very small for this system, as expected theoretically.

In a separate study in 2010, they measured the slip times of nanofriction of Ne monolayers at temperatures below 6.5 K and in UHV conditions deposited on metallic surfaces plated with heavy rare-gas multilayers. Overall, the slip times measured were an order of magnitude larger than those reported in the 2006 study, presumably due to the fact that slip times are exceptionally sensitive to surface structure. Covering the electrode with one layer of Kr or Xe increased the slippage of a Ne monolayer by a factor close to 3. Such a behavior has been observed with these smooth

Table 4. QCM slip time data for argon films.

Preplate	Substrate	Substrate type	T (K)	Reference	τ (ns) $\Theta = 0.2$	$\Theta = 0.5$	$\Theta = 1.0$
	Ag(111)	Terraced	77.4	[87,473]			1.5
Xe bilayer	Ag(111)	Textured	77.4	[87,473]			4
Xe monolayer	Ag(111)	Textured	77.4	[87,473]			4
	Pb(111)	Terraced	10–15	[493]	0	0	0

lead electrodes, as well as in a number of alternative experimental systems. The lubrication effect did not increase with thicker overlayers. Given that the electronic could not account for the large difference, the authors explained the effect in terms of changes in the substrate corrugation [491]. Dayo [166] also reported extensive slippage of neon films, for (111) fiber-textured Pb films that had very briefly been exposed to air before transfer to UHV conditions. The estimated film thickness was nine monolayers, however the slippage was so great that the error bars were very large.

4.1.3. *Argon films*

QCM slip time data for Ar films are summarized in Table 4. Relatively few studies have been performed for adsorbed argon films. The data that do exist, however, reinforce results that have been reported for alternative systems. In particular, the lubricating effect that occurs when a preplated monolayer is present [87,473], which completely concurs with the [491] observation. Also, the fact that argon films become pinned at low temperatures on Pb(111) films is completely consistent with the regular reports of pinning in similar systems [419,492,493].

In addition to the experimental results listed in Table 4, theoretical investigations of load-driven modifications occurring in the potential energy surface for Ar/Cu(111) has been performed, and the friction was found to dramatically *decrease* with load. As described in more detail in Sections 3.2.1 and 3.2.2, the behavior is argued to arise from quantum mechanical effects that induce a transformation from anticorrugation to corrugation in the near-surface region [321,322].

4.1.4. *Krypton films*

QCM slip time data for Kr films are summarized in Table 5. Slip times followed by (IC) denote incommensurate solid phase, while (C) denotes commensurate. When two values are present for the bilayer coverage, individual slip times for the first and second layers, respectively, are listed.

Numerous studies of sliding friction have been performed on Kr films, including the development of QCM as a technique itself for studies of sliding friction in the late 1980s [147,148,176,494]. The first sliding friction measurements on an atomically uniform substrate were reported in 1991 for krypton monolayers sliding on Au(111) [33,34]. The Au(111) surfaces were prepared in UHV, and the measurement of krypton adsorption were performed *in situ* to ensure surface quality and carried out at 77.4 K by submerging the adsorption chamber in a liquid nitrogen bath and allowing it to come to equilibrium. At 77.4 K, Kr condenses as a liquid and then solidifies as pressure is increased. Solid Kr monolayers sliding on Au(111) exhibited five times longer slip times (lower friction) than liquid monolayers of Kr. In other words, the surface was "slippery when dry". Measurements of the increase in slip time at the liquid–solid transition have also been reported by Coffey and Krim for Ag(111), C60, Ni(111), and Cu(111) substrates [355]. The 1991 results provided the first definite evidence for the existence of phononic mechanisms for friction [35] (see also Figure 45).

Table 5. QCM slip time data for krypton films.

					τ (ns)				
Preplate	Substrate	Substrate type	T(K)	Reference	$\Theta = 0.2$	$\Theta = 0.5$	$\Theta = 1$ (liquid)	$\Theta = 1$ (solid)	$\Theta = 2$
	Au	Amorphous	77.4	[404]			4	50	100
	Ag	Fractal	77.4	[33,34]			1.5		
	Au	Terraced	85	[181]	0&7	0&2	0&1		0
	Au	Terraced	85	[185]	0&1.5	0&1	0.1		0.2
	Ag(111)	Textured	77.4	[355]			2.1	2.7	
C60 fixed bilayer	Ag(111)	Textured	77.4	[355]			3.1	3.3	
C60 monolayer	Ag(111)	Textured	77.4	[355]			1.6	2.7	
	Au(111)	Textured	77.4	[355]			1	5	
	Au(111)	Textured	77.4	[33,34]		1.5	2	10	
	Au(111)	Textured	77.4	[173]			1	5	
	Au(111)	Textured	77.4	[404]				1	5
	Au(111)	Textured	77.4	[176]			1.5		4
C60 fixed monolayer	Ag(111)	Textured	77.4	[539]	10	4	3		
C60 fixed bilayer	Ag(111)	Textured	77.4	[539]	10	4	3		
	Cu(111)	Textured	77.4	[355]			7	11	
C60 fixed monolayer	Cu(111)	Textured	77.4	[539]	10	4	3		
C60 fixed bilayer	Cu(111)	Textured	77.4	[539]	10	4	3		
	Graphite	Terraced	85.8	[476]		0&60(C)		10(IC)	8, 300
	Graphite	Terraced	85.8	[476]		0&60(C)		0&60(C)	
	Ni(111)	Textured	77.4	[355]			0.26	0.78	
	Pb(111): $T < T_c$	Terraced	6.5	[491]	0	0		0	0
	Pb(111): $T > T_c$	Terraced	10–15	[493]	0	0		0	0

Studies of sliding friction of Kr monolayers on disordered (within the plane) Au substrates have also been performed, revealing a "disorder-induced lubrication" effect [394,404]. The gold substrates on which the measurements were performed were prepared by depositing gold films onto polished quartz substrates held at 80 and 300 K, the 80 K samples being the more disordered of the two. The fact that lower friction levels were observed for more disordered systems was possibly explained by the inhibition of phonon excitations in these systems [495].

Mak *et al.* [173] also employed QCM to measure the vibrational amplitude dependence of quality factor shifts for Kr adsorbed on gold electrodes. Assuming that the friction force was proportional to some power of the sliding velocity of the film relative to its substrate, they could infer whether or not the friction force law was linear in form by performing measurements at varying oscillator amplitude (Figure 19). The linear friction law was reported to be valid for a full monolayer of both liquid and solid krypton, for sliding speeds estimated to be in the range 3–8 cm s^{-1}. The form of the friction law at lower coverages appeared to be nonlinear, but the nonlinearity might have been associated with changes in submonolayer island sizes forming at differing QCM amplitudes.

In 2002, Bruschi and coworkers employed QCM to measure the sliding friction of krypton films physisorbed on gold [181]. By slowly increasing the amplitude of the substrate oscillations, they observed a sharp transition from a film locked to the substrate to a sliding one, thus two values are reported for the slip time in Table 5, corresponding to the pinned and sliding state. The transition was characterized by hysteresis in both the dissipation and inertial mass as the amplitude

was raised and lowered, and they examined the dependence of this transition on film coverage in detail. The group subsequently performed further studies of the sliding of atomically thin Kr films adsorbed on gold [181] and observed sharp pinning transitions separating a low-coverage region, characterized by slippage at the surface, from a high-coverage region where the film is locked to the oscillating electrodes. In addition, they could induce sliding of the film by slowly increasing the amplitude of the substrate oscillations. The depinning transition was characterized by a hysteresis as the amplitude was decreased back to zero. The results were reproducible with two different quartz plates, although a quantitative comparison among the different experimental runs indicated that the location of the dynamical transitions was strongly dependent on the state of the substrate surface.

Kobyashi *et al.* very recently extended the depinning studies of Kr for films adsorbed on exfoliated graphite taken from a single crystal and then attached to the surface electrode of a QCM [476]. Kr/graphite is an ideal system given the well-documented nature of its two-dimensional phase diagram [103,104,496,497]. They investigated both the coverage dependence of the sliding friction and the depinning transition up to coverages of two monolayers. A pinned commensurate plus mobile fluid (C + F) phase was observed for submonolayer coverages. Increasing the surface coverage resulted in a commensurate (C) phase, then a C–IC transition to an incommensurate (IC) phase. They reported that at submonolayer coverages, parts of the film were pinned and analyzed the data in terms of pinned plus sliding components rather than one uniformly sliding layer. The portions of the commensurate layer that were sliding exhibited a slip time of 60 ns within this model. Close to, and slightly above, monolayer completion, the film (incommensurate at this coverage) was observed to slide uniformly without pinning and its slip time was close to 10 ns. Slippage of commensurate monolayers has also been reported for Xe/Cu(111) [356] and in numerical simulations for adsorbed Kr monolayers [35]. For the bilayer film, the experimental data were reasonably explained by a model in which the slip occurred at the boundary between the first and second atomic layers, as well as the film and the substrate. The authors thus report separate slip time τ_1 and τ_2 for the first and second layers, as they have earlier for helium films. For the oscillation amplitude sweep at a constant coverage, a rapid change in frequency was observed for the monolayer and bilayer films, which was attributed to the depinning transition. This magnitude takes the minimum value around the layer completion.

The presence of static friction between two solid bodies implies that they are interlocked. In the absence of adsorbed contaminants, the interlocking can result from a competition between elastic and interfacial interactions. Reguzzoni *et al*. [53] examined this effect numerically by studying size dependence of pinning in Kr clusters adsorbed on Cu(111) and Si substrates.

Reguzzoni [61] numerically examined the size dependence of pinning in Kr clusters adsorbed on Cu(111) and Si substrates. When the size of the contact was reduced below a critical value, they observed domains to coalesce and the interfaces to become commensurate (Figure 7). They first considered monolayer islands of krypton on Cu(111) and reported agreement with QCM experiments. They next examined Kr clusters on silicon and found similar results. Given the fact that macroscopic contacts are comprised of many small contacts, they concluded that macroscopic contacts are much more commensurate than may be initially suspected.

In addition to the experimental results listed in Table 5, theoretical investigations of load-driven modifications occurring in the potential energy surface for Kr/Cu(111) has been performed, and the friction was found to dramatically *decrease* with load. The behavior is argued to arise from quantum mechanical effects that induce a transformation from anticorrugation to corrugation in the near-surface region [321,322]. Frictional heating effects have also been studied experimentally for Kr monolayers sliding on graphene/Ni(111) substrates [498]. Finally, adsorbed Kr films have been studied extensively at very low temperatures and found to be pinned at all coverages studied, up to 5 layers thick in the temperature range 10–15 K [493].

Table 6. Slip time data for Xe films.

						τ (ns)				
Preplate	Substrate	Substrate type	Technique	T (K)	Reference	$\Theta = 0.2$	$\Theta = 0.5$	$\Theta = 1$ (liquid)	$\Theta = 1$ (solid)	$\Theta = 2$
	Ag(111)		Theory		[115,323]				200(E)	
C60 fixed bilayer	Ag(111)	Textured	QCM	77.4	[356]				5.5	
	Ag(111)	Textured	QCM	77.4	[356]				2	
	Ag(111)	Textured	QCM	77.4	[352]	2.3	1.2		1.1	1.8
	Ag(111)	Textured/rough	QCM	77.4	[353]	2.3	1.2		1.1	1.8
	Ag(111)	Textured	QCM	77.4	[164]		0.25		0.8	1
	Ag(111)	Textured	Resistivity	77.4	[164]		3.3(E)		4(E)	6(E)
	Ag(111)	Textured	Resistivity	10	[447]		3(E)			
	Au(111)	Textured	QCM	110	[508]	1.7	1.1	0.7		
	Au(111)	Textured	QCM	80	[33]				1.2	4
	Au(111)	Textured	QCM	113.6	[33]		1	2		5
	Cu(111)	Textured	QCM	77.4	[356]				15.5	30
	Cu(111)	Textured	QCM	77.4	[356]				>12.5(E)	
Graphene	Ni(111)	Textured	QCM	77.4	[356]		2		1.7	
Graphene	Ni(111)	Textured	QCM	77.4	[356]				>12.5(E)	
	Ni(111)	Textured	QCM	77.4	[356]		0.4		0.47	0.2
	Ni(111)	Textured	QCM	77.4	[356]				>12.5(E)	
	Pb(111)	Terraced	QCM	10–15	[493]	0	0		0	0
	Pb(111)	Textured/rough	QCM	77.4	[625]				0.7	

4.1.5. *Xe films*

QCM slip time data for Xe films are summarized in Table 6. Slip times followed by (E) denote electronic contributions only. Xe/Cu(111) is commensurate, while all other systems are incommensurate.

The first reports of sliding friction measurements of adsorbed Xe films occurred in 1996, in a comparison study of the sliding friction of xenon monolayers and bilayers on Ag(111) [352,353, 499]. Slip times were reported under the assumption that the second layer slides in unison with the first, which is supported by numerical simulations [354]. The Ag(111) films were prepared in UHV, and the xenon adsorption was conducted *in situ*, to ensure surface quality. At 77.4 K, xenon forms an incommensurate triangular solid monolayer film with a nearest-neighbor spacing of 0.452 nm (5.624 atoms nm^{-2}). With increasing xenon adsorption, the monolayer film allows more atoms by compressing until it reaches a nearest-neighbor spacing of 0.439 nm (5.97 atoms nm^{-2}). This spacing is the same as bulk solid Xe(111). As more xenon is adsorbed, the second layer forms on top of the monolayer and is commensurate with the compressed monolayer. Daly and Krim reported that the friction force per unit area required to slide the two-layer-thick Xe film was 27% greater than that required to slide the monolayer film [352]. In a follow-up study, they compared slip time measurements for Ag(111) substrates that exhibited small, but nonnegligible out-of-plane roughness, and found no significant impact on the form of the slip time with coverage [353].

As discussed extensively in Section 3.2.3, dominance of phononic friction for this system, as well as for adsorbed xenon films, in general, has been suggested by most theoretical and experimental studies of the system. Tomassone [354], for example, performed molecular dynamic simulations for a Xe film sliding on Ag(111) from the submonolayer through the bilayer regime, which, when compared to both friction and surface resistivity measurements, demonstrated that the friction in this system was dominated by phonon excitations. Slip times were obtained both through direct calculation of the decay of the center-of-mass velocity, as well as from the decay of

the velocity correlation function. The agreement of the slip times from the two methods supported the occurrence of a friction force that is linear in velocity over a wide velocity range.

Bruch [115,323] added additional support for the dominance of phononic friction for the system Xe/Ag(111) by performing theoretical estimates of electronic contributions to friction. He utilized the fact that the electrostatic moments on the atoms or molecules of a monolayer solid are the source of an electric field with spatial variation determined by the reciprocal-lattice vectors of the monolayer. Center-of-mass oscillations of the monolayer then generate an oscillating electric field in a metallic substrate. The contribution of the resulting "ohmic" loss to the damping of the oscillation was evaluated for adsorption dipole moments, resulting in very small levels of electronic friction, and slip times due to electronic effects in the order of 200 ns.

Schumacher *et al*. [447] inferred electronic friction coefficients for Xe/Ag(111) on Ag(111) from resistivity measurements. The resistivity of a Ag(111) film was observed to increase monotonically with the adsorption of the Xe, up to coverages of one monolayer. Above one monolayer, the resistivity increased only very slightly. The resistivity results were reproduced in 1998 by Dayo *et al*. [164], and both groups concluded that the electronic contribution would be at most 30% of the total for this system, under the assumption that resistivity measurements accurately reflect electronic friction. The values obtained were nonetheless substantially large than those obtained theoretically by Bruch.

Goncalves [500] performed MD simulations of a Xe monolayer sliding on Ag(001) and Ag(111) in order to ascertain the proportions of electronic and phononic friction and concluded that they were of similar magnitude. For several values of the electronic contribution to the friction of individual Xe atoms, the intra-overlayer phonon dissipation was calculated as a function of the corrugation amplitude of the substrate potential. Within the accuracy of the numerical results and the uncertainty with which the values of the relevant parameters are known at present, they concluded that electronic and phononic dissipation channels are of similar importance. While phonon friction gives rise to the rapid variation with coverage, the electronic friction provides a roughly coverage-independent contribution to the overall sliding friction.

Fois [493] reported that xenon adsorbed on Pb(111) below 15 K failed to exhibit sliding, a result which may be due to an intrinsic inability to slide over the potential corrugation, or alternatively due to pinning at step edges.

Tomassone and Sokoloff performed numerical simulations to examine the effects of a step defect and a random array of point defects (such as vacancies or substitutional impurities) on the force of friction acting on a xenon monolayer film adsorbed on Ag (111) [186]. In particular, they studied by MD simulations and compared with the results of lowest-order perturbation theory in the substrate corrugation potential. For the case of a step, the magnitude and velocity dependencies of the friction force were reported to be strongly dependent on the direction of sliding with respect to the step and the corrugation strength. When the applied force F was directed perpendicular to the step, the film was pinned for F less than a critical force F. Motion of the film along the step, however, was not pinned. Simulations performed on a substrate containing a 5% concentration of random point defects for various directions of the applied force show that the film was pinned for the force below a critical value.

Xe slip times for monolayers adsorbed on a variety of substrates other than Ag(111) were reported in 2005 for adsorption at 77 K on Cu(111), Ni(111), graphene/Ni(111), and C_{60} substrates [355,356]. Coffey and Krim recorded a set of QCM sliding friction measurements of Xe monolayers adsorbed to electrodes formed from a variety of metals in systems whose corrugation potentials had been determined independently, allowing a direct comparison of theory and experiment in an environment free of adjustable parameters [35] had predicted a strong dependence of phononic friction coefficient (η) on surface corrugation in systems with similar lattice spacing, but data had been unavailable on account of a lack of substrates with identical lattice spacings.

Measurements for xenon monolayers at 77.4 K sliding on Cu(111), Ni(111), graphene/Ni(111) (which have similar substrate lattice spacings), and C_{60} substrates provided direct experimental evidence that the sliding friction coefficient is proportional to the square of the surface corrugation U_o^2 for systems with comparable lattice spacing. It was also argued that the results provided convincing evidence that phononic dissipation mechanisms dominate electronic mechanisms in these systems by at least an order of magnitude.

Buldum *et al*. analyzed the dynamics of xenon atoms as lubricant between two Ni(110) slabs in relative motion [327]. They performed atomic simulations by using classical MD with realistic empirical potentials for the Xe–Ni interactions. The resistance of the xenon layer at various coverages against external loading force was examined and critical forces were determined that would destroy it. In addition, the relative motion of slabs in the lateral direction was investigated under constant normal force, for coverages ranging from zero to the monolayer xenon. The variation of potential energy, lateral force, and local hydrodynamic pressure was calculated, yielding an interesting prediction: the corrugation of the potential energy associated with sliding has a minimum value at submonolayer coverage. A phononic energy dissipation mechanism was employed to interpret the results.

In a manner similar to argon, and described earlier in Section 3.2, Ferrario *et al.* performed theoretical investigations of load-driven modifications occurring in the potential energy surface for Xe on Cu(111) and Ag(111), and the friction was found to dramatically *decrease* with load. The behavior is associated with quantum mechanical effects that induce a transformation from anticorrugation to corrugation in the near-surface region [321,322].

Finally, Bortolani *et al.* [501] performed an MD study of the slip time and static friction for a slab of Xe deposited on a slab of Cu. In order to model the role played by the phonons in the two blocks, they compared results obtained with a substrate formed by fixed atoms with the one formed by mobile atoms. In the latter case, the scattering between Xe and Cu mobile atoms is inelastic and there is an exchange of momentum and energy between the two blocks. This in turn produces disorder in the interface plane, which favors a decrease of the static friction and a consequent increase of the slip time. The authors describe the interaction between Xe and Cu with a phenomenological multi-ion potential which gives rise to anticorrugation of the charge distribution and reproduces very well the ab initio density functional calculations. Since the model potential is a linear superposition of a corrugating potential and an anti-corrugating one, the authors could probe how static friction by passing from an anticorrugated to a fully corrugated system.

4.2. *Adsorbed diatomic molecules*

4.2.1. *Hydrogen and deuterium films*

Deuterium and hydrogen remain as intact molecules when physisorbed at low temperatures, and generally disassociate and form chemisorbed layers at higher temperatures. Very few reports of slippage or slip times have been reported for these systems, one via QCM [493] and one via resistivity measurements [447]. Fois *et al.* [493] employing QCM, reported that deuterium D_2, monolayers slide readily on Pb(111) substrates at low temperatures in the range 10–15 K, but that the data exhibited a poor signal to noise ratio on account of the low resolution of the film. Quantitative slip time data were therefore not reported for either H_2 or D_2 sliding as physisorbed phases at very low temperatures. The electronic contribution of hydrogen on Ni was reported to be 0.001 ns, inferred from resistivity measurements [447].

Despite the small number of slip time measurements, the presence of hydrogen has been documented by means of AFM, as well as theory, to have major impact on the friction levels measured that technique. Three representative examples include [36,502,503].

Cannara *et al*. [36] performed AFM measurements on surfaces by changing the mass of the terminating atoms on a surface, and thus their vibrational frequencies, to explore how this impacted friction. In particular, they compared hydrogen- and deuterium-terminated single-crystal diamond and silicon surfaces, and in all cases the hydrogenated surface exhibited higher friction. They concluded that the lower natural frequency of chemisorbed deuterium reduced the rate at which the tip's kinetic energy is dissipated and argued that the result was consistent with a model describing energy transfer to adsorbates from a moving surface. As mentioned in Section 3, Mo *et al.* [37] later modeled the Cannara *et al*. results with MD simulations and concluded that a change in vibrational frequencies alone did not account for an isotope-dependent solid friction for the modeling parameters that they employed.

Chen *et al.* [502] showed that the friction force, as measured by AFM, varies with the sliding velocity in a manner that depends on the chemical nature of the interface. Surfaces terminated with hydrogen acceptor and donor moieties capable of forming H-bond networks exhibited a friction that decreased with sliding velocity, a behavior that is opposite to that of surfaces where no such networks can form. The results were explained by a model that assumed the domains of glassy H-bond networks to be disrupted at a critical applied stress, leading to slippage at that point.

Diamond and DLC films exhibit a wide range of sometimes contradictory tribological behavior, with hydrogen adatoms thought to have a major impact on the variability [504–507]. Experimentally, isolating the influences of factors such as film structure, testing conditions, and environmental effects has proved to be difficult. Ciraci *et al*. [503], employing numerical techniques, found that the strong attractive interaction between two clean diamond (001) slabs turns repulsive upon the hydrogenation of surfaces. The repulsion effectively acted as a type of "boundary lubricant" by preventing close contact of the sliding surfaces, even under high normal forces. As a result, calculated lateral force variation generated during sliding had a small magnitude under high constant loading forces. The results were argued to explain how experimental reports of superlow friction between DLC-coated surfaces can be understood: steady repulsive interaction between sliding surfaces is present, as well as strong and stiff carbon–carbon and carbon–hydrogen bonds which do not favor energy dissipation. The authors noted, however, that in ambient conditions, the steady repulsive interaction would be destroyed by oxygen atoms which chemically modify the stiffness of the surface bonds.

Schall *et al*. performed MD simulations to examine the effects of film structure, passivation, adhesion, tribochemistry, and load on the tribology of self-mated DLC contacts in the presence and absence of hydrogen [507]. Addition of hydrogen to the DLC film caused a large decrease in the unsaturated carbon bonds at the *interface* of the film when compared to both bulk and nonhydrogenated films. The unsaturated carbon atoms served as initiation points for the formation of covalent bonds between the counterface and the film, which caused an increase in friction during sliding (Figure 64). The formation and breaking of the covalent bonds during sliding also resulted in the formation of a transfer film. The simulations revealed that reducing unsaturated atoms, both sp- and sp^2-hybridized carbon, at the *sliding interface* reduces the number of adhesive interactions, alters the transfer film formed, and reduced friction. In addition, the simulations supported and elucidated the passivation hypothesis for DLC friction.

4.2.2. *Physisorbed nitrogen films*

QCM and resistivity slip time data for N_2 films are summarized in Table 7. Slip times followed by (E) denote electronic contributions only.

Measurements performed on liquid films adsorbed at 77 K focused primarily on the development of QCM as a technique itself for studies of sliding friction [176] and for initial comparisons

with other systems, such as water [508]. Resistivity measurements of the impact of nitrogen uptake on Ni surfaces have yielded typical ps values for the system, typical of a chemisorbed system.

In 1998, Dayo *et al.* [164] performed QCM and electrical resistivity measurements on nitrogen films adsorbed on Pb(111) that had been prepared identically alongside each other to explore the relative contributions of electronic and phonon dissipative mechanisms. They found the electronic contributions to be nonnegligible based on the resistivity measurements. Much clearer evidence supporting the existence of nonnegligible electronic friction levels was reported later in 1998 by Dayo *et al*. [165]. Dayo *et al*. employed a QCM to study the sliding of thin N_2 films adsorbed on a Pb(111) surface that had briefly been exposed to air, and observed the friction to drop by almost half when the substrate became superconducting. Given that superconducting systems exhibit a significant change in electronic properties over a narrow temperature range where changes in phononic behavior are assumed to be minimal, the changes observed at T_c were attributed to electronic mechanisms.

The studies of Dayo *et al.* inspired a surge of subsequent theoretical and experimental investigations of the effect. An effort to reproduce the result by Renner *et al*. resulted in N_2 films that failed to slip at all at the superconducting temperature of 7.2 K [509,510]. Three subsequent experimental studies were performed on samples that were prepared exclusively in UHV conditions [419,420,493]. Fois *et al.* performed the measurements on atomically uniform terraced substrates (Figure 63) and observed the nitrogen films to be always pinned at 7.2 K. Mason [419] and Highland [420] reported frequent pinning of the nitrogen at 7.2 K in about 50% of the samples

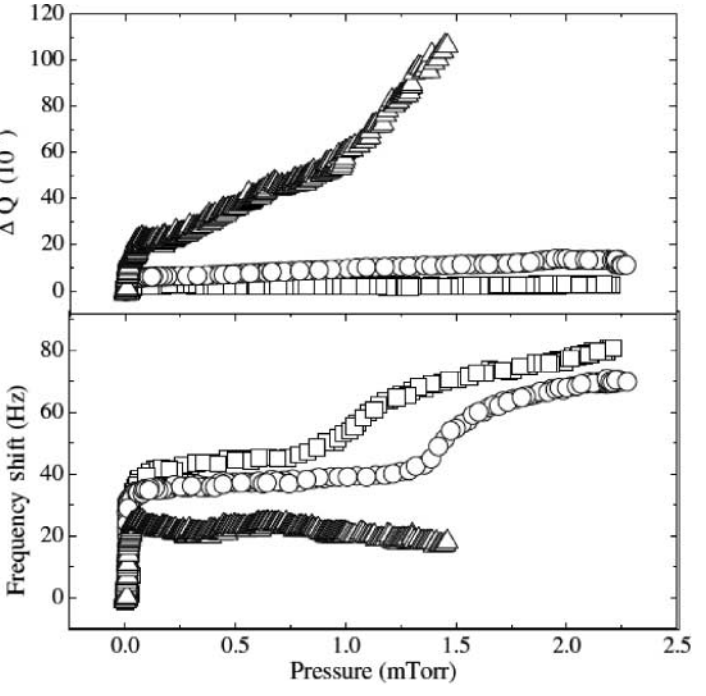

Figure 63. Xenon mass uptake and quality factor shift (raw data) for Cu(111) (triangles), Ni(111) (squares), and grapheme/Ni(111) (circles). High slippage (low friction) of Xe layers sliding on Cu(111) cause a reduced frequency shift, irrespective of the fact that the system is commensurate. Reprinted figure with permission from T.S. Coffey *et al.*, Physical Review Letters 95, art#076101, 2005 [356]. Copyright (2005) by the American Physical Society.

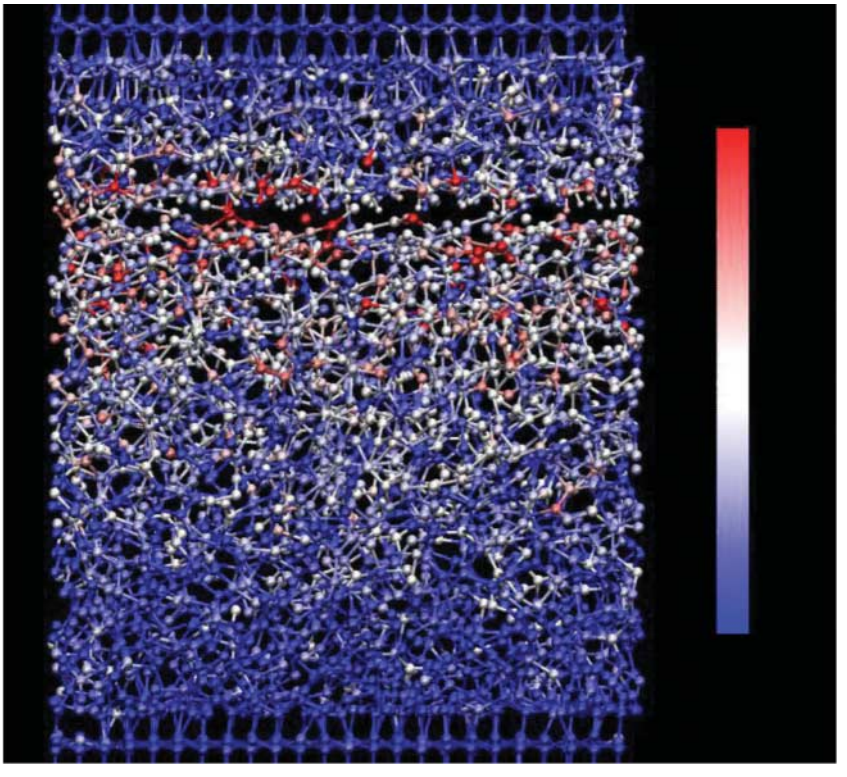

Figure 64. Snapshot of a hydrogen-terminated DLC tip in sliding contact with a hydrogen-free DLC film subjected to a 60 nN load. Atoms are colored by relative temperature with red atoms having the highest temperature and blue atoms having the lowest temperature. Blue atoms are at 300 K. Average temperature in the interface region is in excess of 800 K. Carbon and hydrogen atoms are represented by large and small spheres, respectively. Sliding causes the formation of bonds across the sliding interface. Image courtesy of J.A. Harrison.

studied. Both reported slightly longer slip times for the pristine Pb(111) substrates compared to those of the air-exposed samples. Reductions in friction upon entry into the superconducting state were greater for N_2 than He, consistent with a theory by Bruch that linked electronic friction to adsorbate polarizability. The work curiously revealed that repetitive cycling of an externally applied magnetic field may impact friction, and therefore a second set of values are listed [420]. Regarding the cleanliness of the surface, Mason reported the effect to gradually weaken and be almost indiscernible for samples left in vacuum for 3 days. It is becoming increasingly evident that nitrogen films pin more readily on the terraced surfaces and that there an intrinsic effect associated with uniform surfaces that is the opposite of "disorder-induced lubrication" [394,404,476]. In short, electronic effects at superconducting transitions have only been observed when phononic friction background levels are very low.

The topic of superconductivity-dependent friction in nitrogen films has inspired much theoretical work [348,422–424,426]. They are discussed in detail in Section 3.4.

4.2.3. *Oxygen and carbon monoxide films*

QCM and resistivity slip time data for O_2 and CO films are summarized in Table 8. Slip times followed by (E) denote electronic contributions only. The majority of the systems reported in the

Table 7. Slip time data for N2 films.

					τ (ns)				
Substrate	Substrate type	Technique	T (K)	Reference	$\Theta = 0.5$	$\Theta = 1$ (liquid)	$\Theta = 1$ (solid)	$\Theta = 2$	$\Theta = 4 - 5$
Au(111)	Textured	QCM	77.4	[508]	3	4		8	
Au(111)	Textured	QCM	77.4	[176]		4		7	
Pb(111)	Textured	QCM	77.4	[166]		1.5		1.2	2
Pb(111)	Textured	Resistivity	7.2	[164]	1.3(E)				
Air-exposed Pb(111): $T > T_c$	Textured	QCM	7.2	[165]				12	
Air-exposed Pb(111): $T < T_c$	Textured	QCM	7.2	[165]				29	
Air-exposed Pb(111)	Textured	QCM	7.2	[165]				21(E)	
Pb	Textured	QCM	7.2	[510]			0		
Pb(111): $T < T_c$	Textured	QCM	7.2	[419]		0 & τ(SC) > τ(N) > 20 ns			
Pb(111): $T > T_c$	Textured	QCM	12	[419]			0	0	
Pb(111): $T > T_c$	Textured	QCM	7.2	[420]				19	
Pb(111): $T < T_c$	Textured	QCM	7.2	[420]				40	
Pb(111)	Textured	QCM	7.2	[420]				36(E)	
Pb(111): $T > T_c$	Textured	QCM	7.2	[420]				140	
Pb(111): $T < T_c$	Textured	QCM	7.2	[420]				1190	
Pb(111)	Textured	QCM	7.2	[420]				160(E)	
Pb(111)	Terraced	QCM	9	[493]			0		
Pb(111)	Terraced	QCM	15	[493]			0		
Pb(111)	Terraced	QCM	19	[493]	0		0.05	0.12	
Pb(111)	Single crystal	Theory		[115,323]			2–20(E)		
Ni	Terraced	Resistivity		[447]	0.046(E)				

Table 8. Slip time data for O_2 and CO films.

						τ (ns)			
Adsorbate	Preplate	Substrate	Technique	T (K)	Reference	$\Theta = 0.2$	$\Theta = 0.5$	$\Theta = 1$ (solid)	$\Theta = 2$
O_2	TCP	Cr	QCM	573	[514]	0	0	0	0
O_2	TCP	Fe	QCM	573	[514]	~0.001	~0.001	~0.001	~0.001
O_2		Ag(111)	QCM	300	[511]	0	0	0	0
CO		Ag(111)	Resistivity		[447]		0.36(E)		
O_2		Pb(111): $T > T_c$	QCM	7.2	[492]		0 & τ(SC) > τ(N) > 0		
CO		Pb(111)	QCM	7.2	[492]	0	0	0	
O_2		Cu	Resistivity		[447]		0.007(E)		
CO		Cu	Resistivity		[447]		0.039(E)		
CO		Ni	Resistivity		[447]		0.014(E)		

literature are for chemisorbed layers of these materials. At sufficiently low temperatures, however, oxygen and CO fail to disassociate and are physically adsorbed on the substrates.

Oxidation is of interest for tribological considerations on account of its common occurrence, particularly in sliding contacts, under ambient conditions. The exact mechanism of the friction reduction observed is a matter of great interest, including the relative contributions of phononic and electronic dissipation mechanisms. The impact of oxidation on sliding friction has been probed by means of QCM, AFM, and surface resistivity measurements.

In 1994, Krim and co-worker Mak [511] employed QCM to measure characteristic slip times for ethane and ethylene monolayers adsorbed on silver and chemisorbed oxygen/silver surfaces. They reported no slippage whatsoever of the oxygen layer itself upon the Ag(111) substrate. The presence of oxygen did, however, reduce friction relative to slippage on bare Ag(111).

In a similar study of the impact of oxidation on surface friction, Perry and coworkers employed AFM with standard surface analytical methods to investigate the frictional properties of a potential hard-coating material, vanadium carbide (VC), as a function of surface oxidation [512,513]. In this study, a single-crystal VC sample was prepared under UHV conditions by sputtering and annealing, then characterized by LEED and Auger electron spectroscopy. The surface was found to be free of oxygen and to exhibit good crystallographic order with atomically flat terraces similar to 100–200 Åin width. The coefficient of friction between a silicon nitride probe tip and the clean VC surface was measured as 0.52 ± 0.04. Chemical modification of this surface was accomplished by exposure to molecular oxygen which produced a saturation coverage of chemisorbed atomic oxygen. The coefficient of friction between the same silicon nitride tip and the "oxidized" VC surface in the wearless regime was measured as 0.32 ± 0.05, a 40% reduction in friction. The authors associated the reduction in friction with the density of metal d electrons nearest the Fermi level which occurs upon oxygen adsorption. The changes were argued to provide evidence for the contribution of an electronic mechanism of energy dissipation at the sliding interface of a solid–solid point contact.

Highland [492] reported high levels of slippage for physisorbed oxygen films adsorbed on Pb(111) substrates. The work curiously revealed that repetitive cycling of an externally applied magnetic field caused the film to become pinned. The latter result is in the opposite direction as that observed for nitrogen layers. Further measurements would be required to document the nature of this result, if reproducible. Highland additionally reported pinning of CO films on Pb(111) at low temperature.

Abdelmaksoud *et al.* [514] reported no slippage whatsoever for oxygen uptake on tricresylphosphate (TCP) layers preadsorbed at elevated temperatures on chrome substrates, and trace (ps) levels of slippage on TCP layers preadsorbed on iron. The trace levels of slippage were linked to substantive differences in macroscopic effectiveness as a lubricant.

Tobin and coworkers have performed extensive measurements of the change in surface resistivity of metal surfaces upon uptake of oxygen, and the information that can be inferred about electronic contributions to energy dissipation of vibrating adatoms [66,449,450,515]. The characteristic friction coefficients for vibrating atoms have been reported to be comparable in magnitude to those of sliding adatoms of for similar materials, as listed in Table 8 [447]. Tobin's values are not explicitly listed in Table 8, as Tobin's work has revealed inadequacies in the theory.

For example, in a study of dc resistance and infrared reflectance changes induced in epitaxial Cu(100) films by adsorbed oxygen, the Tobin group showed that standard surface resistivity models based on free electrons and point scatterers were inadequate, even if adsorbate-induced changes in conduction electron density are considered [448]. Electron density changes were proposed to account for the variation. Their studies revealed that the ratio for adsorbed oxygen was found to vary with the conductivity of the clean film, which differs from sample to sample. Interpreting these results within a free electron model would require that each adsorbate localize an unreasonably large number of conduction electrons. The group thus argued that significant modification of the prevailing free-electron models, perhaps including energy-dependent scattering, would be necessary to explain the experimental results.

In 2003, Tobin and coworkers reported studies of sulfur and oxygen adsorbed on Cu(100), which have nearly identical bonding geometries and electronic structures [449]. But they observed strikingly different trends in their scattering of conduction electrons, as reflected in the variation of the substrate's surface resistivity with adsorbate coverage. For oxygen, the surface resistivity

was observed to vary linearly with coverage, as expected for noninteracting adsorbates. For sulfur, however, the coverage dependence was observed to be highly nonlinear, with the resistivity increasing strongly at low coverage and then becoming nearly constant above about 0.15 ML. Measurements on sputtered surfaces showed that defects and adlayer ordering were not responsible for the nonlinearity. They ultimately attributed to interactions between the adsorbed atoms that modify the electronic structure near the Fermi level so as to diminish each atom's scattering cross-section.

In 2008, they reported measurements of surface resistivity as a function of coverage for oxygen adsorbed on sulfur-pre-dosed Cu(100) films and observed two types of interactions between sulfur and oxygen: S–O repulsion and short-range suppression of the surface resistivity change induced by oxygen adsorption [450]. The repulsive interaction was argued to cause oxygen atoms to first occupy adsorption sites far from the sulfur atoms, beyond second-nearest-neighbor sites, where the oxygen-induced surface resistivity is unaffected by sulfur. As a result, the low-coverage variation of surface resistivity with oxygen coverage was found to be indistinguishable from the linear dependence observed for oxygen on clean Cu(100). As the oxygen coverage increased, it begins to occupy sites close to sulfur. At the nearest-neighbor sites, the resistivity change due to added oxygen is completely suppressed, and the sample resistance levels off, remaining unchanged even as oxygen continues to adsorb. This resistivity suppression may involve both a reduction of oxygen's direct effect on the resistivity and an oxygen-induced reduction in the resistivity due to the already adsorbed sulfur. With increasing sulfur precoverage, both the maximum resistivity change and the oxygen coverage at which the leveling occurs decrease, because the number of sites unaffected by sulfur is reduced. Both the sulfur–oxygen repulsion and the resistivity suppression presumably arise from a through-metal coupling involving adsorbate-induced modifications of the local electronic structure.

4.3. *Other adsorbed species*

4.3.1. *Water films*

QCM and resistivity slip time data for H_2O films are summarized in Table 9. Slip times followed by (E) denote electronic contributions only. Although very few explicit studies of slip time have been performed of sliding water layers, a wide variety of studies have been performed on closely related topics by means of QCM, AFM, and SFA [201,202,516–527].

As described earlier in Section 2, Barrat and Bocquet and coworkers [199–202] have demonstrated that although it is well known that, at a macroscopic level, the boundary condition for a viscous fluid at a solid wall is one of "no slip" (i.e. the liquid velocity field vanishes at a fixed solid boundary), in the case of a liquid that partially wets the solid (i.e. Figure 21(b) and (c)) the no-slip condition may break down. The authors performed extensive MD simulations and showed that for sufficiently large contact angle, the boundary condition varied dramatically at the microscopic scale from that of the no-slip boundary condition. In particular, they have reported

Table 9. Slip time data for H_2O films.

					τ (ns)				
Substrate	Substrate type	Technique	T (K)	Reference	$\Theta = 0.2$	$\Theta = 0.5$	$\Theta = 1$ (liquid)	$\Theta = 1$ (solid)	$\Theta = 2$
Pb(111)	Textured	QCM	7.2	[420]			$\tau(\mathrm{SC}) > \tau(\mathrm{N})$		
Ag(111)	Textured	QCM	300	[508]	7	3	4		8
Ag(111)	Textured	QCM	300	[87,473]			4		
Ag(111)	Textured	Resistivity	300	[87,473]		0.1(E)			

water slip lengths as a function of contact angle for various surfaces. Their MD simulations of an atomistic water model allowed studies of hydrodynamic slippage of water adsorbed on both inorganic (diamond-like and Lennard-Jones models) and organic (silane monolayers). Slippage, quantified by a slip length, was found to exhibit a "quasi-universal" dependence on the macroscopic contact angle characterizing the surface wettability. Slippage was observed to be larger for more hydrophobic surfaces, which the authors explained by means of a scaling description of molecular friction occurring at the water–solid interface (see Figure 23 in Section 2). An excellent description of experimental efforts to explore these predictions may be found in [229] and references therein. Cottin-Bizonne *et al.* performed dynamic SFA studies of the slip length of water confined between surfaces with varying degrees of hydrophobicity and report the boundary slip to be in good agreement with numerical simulations. In particular, no slip is reported for confined films that exhibit complete wetting on atomically flat surfaces, and discrepancies in the experimental literature are attributed to potential contamination by hydrophobic particles and/or gas pockets or films trapped closed to rough surfaces.

Jinesh and Frenken have recently reported atomic-scale friction force measurements that strongly suggest that the capillary condensation of water [528] between a tungsten tip and a graphite surface leads to the formation of ice at room temperature [516]. This phenomenon increases the friction force, introduces a short-term memory in the form of an elastic response against shearing, and even allows them to "write" a temporary line of ice on a hydrophobic surface. Rearrangements of the condensate are shown to take place on a surprisingly slow time scale of seconds. The water is thus shown to behave like a glue.

Brigo *et al*. [517] report a micro-particle imaging velocimetry recording system that allows fluid velocity measurements in a wide range of flow conditions both inside microchannels and at liquid–solid interfaces to be performed by using epifluorescence and total internal reflection fluorescence excitation. To demonstrate the technique, the authors studied the slippage of water over flat surfaces characterized by different degrees of hydrophobicity and the effects that a grooved surface has on the fluid flow inside a microchannel. Preliminary measurements of the slip length of water past various flat surfaces showed no significant dependence on the contact angle.

Choi *et al*. [518] report the ability to distinguish between a supercooled dew and frost below 0°C by means of a QCM technique monitoring slip of the layer. The slip phenomenon occurring at an interface between the water droplet and the surface of the quartz crystal resonator of the QCM sensor was argued to reflect in a simple and accurate manner a highly accurate measurement of the dew or the frost point without misreading in the dew-point sensor at temperatures below 0°C.

Lee *et al*. have performed MD simulations of how contact angle correlates with slip length [529], and for a Lennard-Jones fluid in Couette flow between graphite-like hexagonal-lattice walls. The fluid–wall interaction is varied by modulating the interfacial energy parameter and the particle size parameter to achieve hydrophobicity (solvophobicity) or hydrophilicity (solvophilicity). The authors report that the slip length grows rapidly with a high shear rate, as wall velocity increases three decades from 100 to $10^5\,\mathrm{m\,s^{-1}}$. The authors conclude that fluid–solid interfaces with low interfacial energy and high particle size should be chosen to increase slip and are prime candidates for drag reduction.

Li *et al*. have studied the viscoelastic dynamics of nanoconfined wetting liquids by means of AFM (Figure 65) [399,418]. They observe a nonlinear viscoelastic behavior similar to that widely observed in metastable complex fluids. By measuring the viscoelastic modulus at different frequencies and strains, they found that the intrinsic relaxation time of nanoconfined water is in the range 0.1–0.0001 s, orders of magnitude longer than that of bulk water, and comparable to the dielectric relaxation time measured in supercooled water at 170–210 K (Figure 66). Note the nonoscillatory character of the viscosity and diffusion curves. Indeed, oscillatory variations of

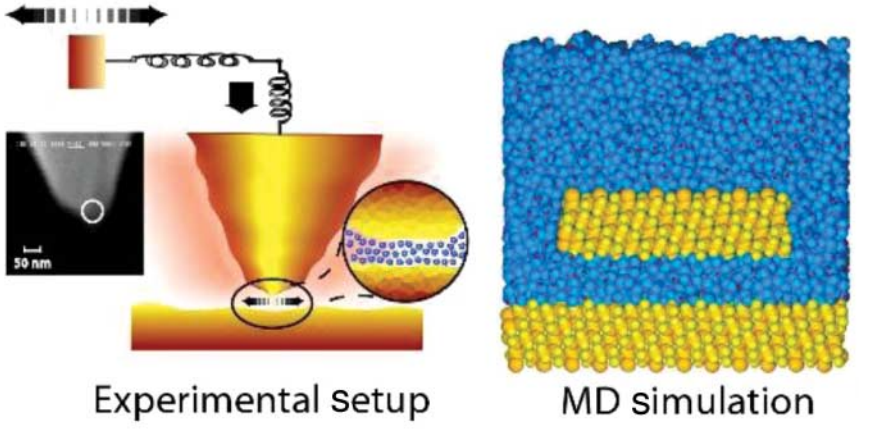

Figure 65. Left: Li *et al.* employed an AFM to measure the normal and lateral forces between a nanosize untreated silicon tip and three different flat solid surfaces in de-ionized water. In this figure, a scanning electron microscopy SEM image of the tip apex is also depicted. Right: an atomic configuration illustrating the MD simulation model. The water (oxygen in blue and hydrogen in red) and the quartz substrate (oxygen in yellow and silicon in dark yellow) are extended with the use of periodic boundary conditions in the *x*–*y*-plane normal to the page. The tip is fully immersed in water. Reprinted figure with permission from T.D. Li *et al.*, Physical Review B 75, p. 115415, 2007 [418]. Copyright (2007) by the American Physical Society.

these quantities are found only when density layering in the gap is accompanied by the development of intralayer order which is not observed for this system.

Fukama and colleagues also employed AFM [530] to probe a tip–water–mica interface and probe the structure of water at a mica–water interface with atomic-scale resolution. Their goal was to examine whether the interface was more solid- or liquid-like [531]: They found evidence for a combination of both, thus possibly reconciling varying reports in the literature.

The fluidity of molecularly thin water films and the concept of hydration lubrication have also been reported on extensively in the SFA literature (see, e.g. [519–522]) along with important theoretical advances in understanding the results of these studies [523,524].

Raviv [520], for example, studied the viscosity of water versus film thickness in the confined SFA geometry, and found it to be within a factor of 3 of its bulk value for films down to molecular dimensions, in contrast to organic solvents, whose viscosity increased starting at 5–8 molecular layers. The lack of promotion of solidification in the case of water was attributed to suppression of the highly directional hydrogen-bond networks associated with formation of ice. Raviv and Klein [521] also studied the shear forces of aqueous salt solutions and found fluidity characteristic of the bulk liquid for films as thin as 1 nm. The fluidity was attributed to ready exchange of water molecules with the rubbing hydration layers. Leng and Cummings have studied this effect theoretically by means of MD simulations [523,524]. For water confined between two mica surfaces, they observe persistent fluidity and high degrees of diffusion for films as thin as two monolayers. For thinner films, they observe that confinement can ultimately lead to a transition to a bilayer ice layer whose density is much less than the bulk value.

The lubricating properties of biomimetic surfaces immersed in water films have also been studied by means of SFA [519,522,532,533]. In general, very low friction is observed in cases where the mica surfaces are coated by an anchored phospholipid film. The studies are of potential impact in the area of biomedical applications, as the systems mimic those in actual biological systems. See also the discussion in Section 4.7.2.

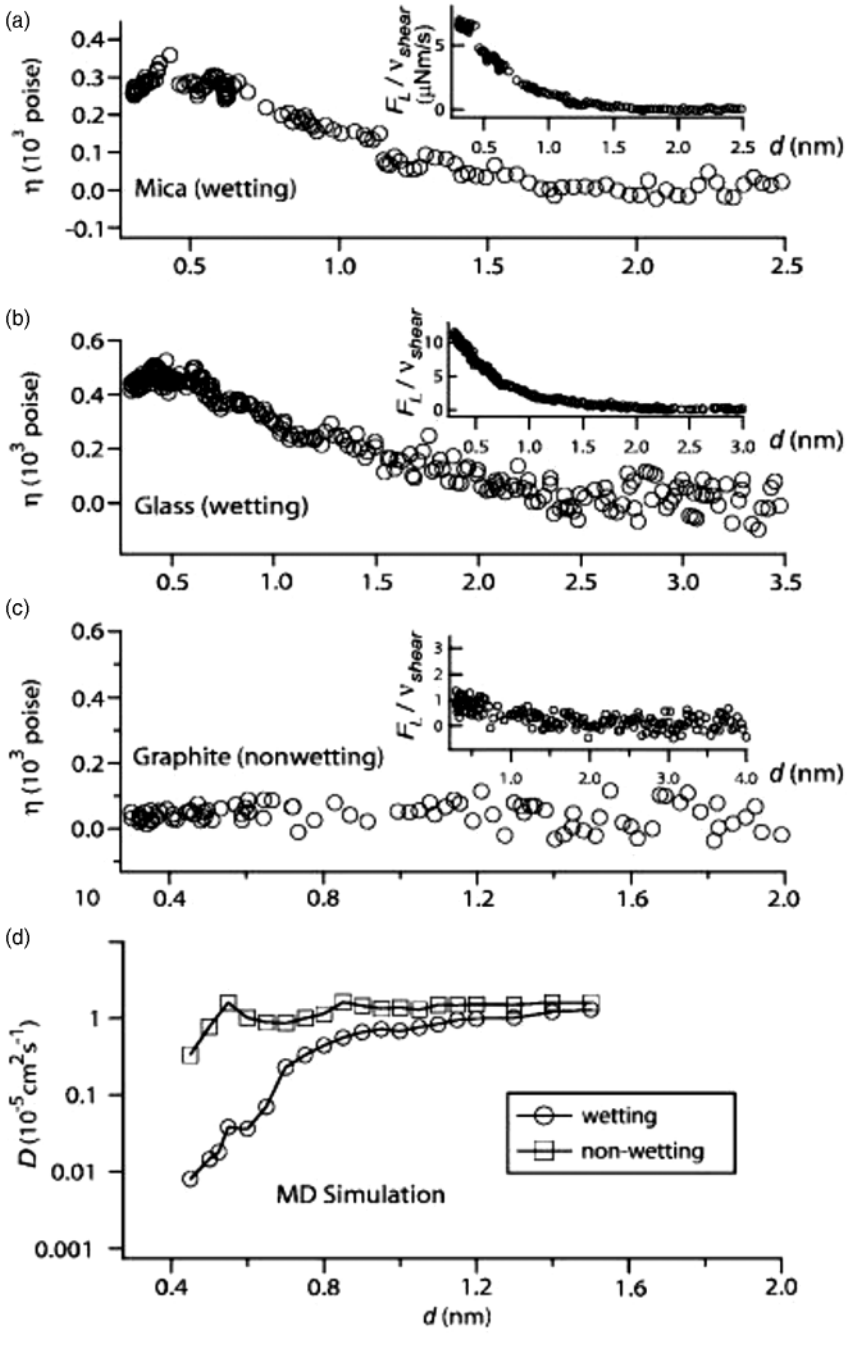

Figure 66. Experimentally measured viscosity η versus d for (a) mica, (b) glass, and (c) HOPG. F_L/v_{shear} versus d is depicted in the insets. (d) Simulated D versus d in water films confined by wetting and nonwetting interfaces. Only molecules remaining in the confinement during 150 ps are selected for computing the displacements. Reprinted figure with permission from T.D. Li *et al.*, Physical Review B 75, p. 115415, 2007 [418]. Copyright (2007) by the American Physical Society.

Table 10. Slip time data for hydrocarbon and closely related films.

Adsorbate	Preplate	Substrate	Technique	T (K)	Reference	τ (ns) $\Theta = 0.2$	$\Theta = 0.5$	$\Theta = 1$	$\Theta = 2$
C_2H_{12} (cyclohexane)		Ag(111)	QCM	300	[508]		0	2	
C_2H_{12} (cyclohexane)		Ag(111)	Resistivity		[447]		1.7(E)		
C_2H_4 (ethylene)		Ag(111)	QCM	77.4	[511]		15	5	
C_2H_4 (ethylene)	Oxygen	Ag(111)	QCM	77.4	[511]		26	16	
C_2H_4 (ethylene)		Ag(111)	Resistivity		[447]		0.72(E)		
C_2H_5 (ethanol)		Al	QCM	300	[536]		1	0.5	0
C_2H_5 (ethanol)	PFTS	Al	QCM	300	[536]		2	4	
C_2H_5 (ethanol)		Si	QCM	300	[536]		4	8.5	
CF_3CH_2OH (TFE)		Si	QCM	300	[536]		1	3.5	15
CF_3CH_2OH (TFE)		Al	QCM	300	[536]		0	0	
CF_3CH_2OH (TFE)	PFTS	Al	QCM	300	[536]		0	0	0
C_2H_6 (ethane)		Ag(111)	QCM	77.4	[511]		15	9	8
C_2H_6 (ethane)	Oxygen	Ag(111)	QCM	77.4	[511]		30	18	6
C_2H_6 (ethane)		Ag(111)	Resistivity		[447]		3.6(E)		
C_5H_{12} (pentanol)		Si	QCM	300	[536]		4	6	5
C_5H_{12} (pentanol)	PFTS	Al	QCM	300	[536]		0.5	6	0.8
C_5H_{12} (pentanol)		Al	QCM	300	[536]		0	0	0.9
C_6H_6 (benzene)		Cu(111)	STM-QCM	300	[272]			>0	1.5
C_6H_6 (benzene)		Graphite	HeSE	140	[128]		0.00045		2
C_6H_6 (benzene)		Ag(111)	Resistivity	50	[447]		1.4E		
C_6H_5I (iodobenzene)	Cu(111)	STM-QCM	300		[272]	0	0		
C_7H_8 (toluene)		Ag(111)	QCM	300	[537]			10	
C_7H_8 (toluene)	C60 rotating bilayer	Ag(111)	QCM	300	[537]			0.1	
C_8H_{18} (n-octane)		Cu(111)	QCM	300	[623]		1.5	0.9	
C_8H_{18} (n-octane)		Pb(111)	QCM	300	[623]			0.6	1
CH_3OH (methanol)	C60 monolayer	Cu(111)	QCM	300	[539]	10	7	3.6	4
CH_3OH (methanol)	C60 rotating bilayer	Ag(111)	QCM	300	[539]	3	4	1.9	9
CH_3OH (methanol)	C60 monolayer	Ag(111)	QCM	300	[539]	10	7	3.6	
CH_3OH (methanol)	C60 rotating bilayer	Cu(111)	QCM	300	[539]	3	4	1.9	0

4.3.2. *Hydrocarbons, triflouroethanol, and iodobenzene*

Slip time data for hydrocarbon and closely related films are summarized in Table 10. Slip times followed by (E) denote electronic contributions only. Studies of slip times in hydrocarbons have a wide ranging interest. Alkanes and alchohols allow controlled variation of molecular size for careful comparison studies of sliding friction [534,535] and have thus received much attention in the AFM community [76]. Their tribology, including tribochemisty, can numerically be modeled with a high degree of accuracy [507]. Hydrocarbons are known lubricants in many cases at the macroscale [298], and recent breakthroughs in MEMS lubrication and links to atomic-scale mobility have been reported for gas-phase lubrication with pentanol and ethanol [274,285,536]. Comparison studies of alcohols with closely related systems (iodobenzene and benzene, trifluoroethanol (TFE) with ethanol, etc.) also provide valuable insights into the chemical impact on sliding friction. For example, ethanol slides readily on many substrates, even at very low coverages, while TFE is readily pinned [536].

The first studies of slip times for hydrocarbons were reported in 1994, for ethane and ethylene monolayers adsorbed on silver and chemisorbed oxygen/silver surfaces [511]. No slippage of the oxygen layer upon the Ag(111) substrate was reported, therefore the slippage was entirely

attributed to the ethane or ethylene layers. The work was motivated by reports of resistivity measurement data of electronic slip times for the films adsorbed on Ag(111) [447]. The systems were therefore thought to be model systems for studies of the relative contributions of electronic and phonon processes towards frictional energy losses. Slip times for the chemisorbed oxygen/silver surfaces were observed to be longer than those for silver. It was therefore argued that electronic contributions to friction should be considered whenever conducting surfaces are involved, and were likely to be lower when oxide films were present. The friction inferred by the resistivity measurements was, however, *higher* than that inferred by the QCM, which revealed an inconsistency in the comparisons: the electronic contribution to friction, as inferred from resistivity, cannot be higher than the sum of the phononic and electronic contributions as measured by QCM.

In 2001, Coffey [152,537] investigated the changes in interfacial friction of toluene on mica and Ag(111) both in the presence and in the absence of interfacial C-60 layers employing AFM and QCM techniques. The LFMs fail to detect C-60 at the toluene/mica interface, presumably because the C-60 is dislodged by the slow-moving probe tip. In contrast, QCM measurements of interfacial friction and slippage for toluene/Ag(111) was sensitive to the presence of interfacial C-60 and was reported to be approximately double when C-60 is present.

Abdelmaksoud *et al.* observed that when mobile adsorbed films of benzene, TCP, and tertiarybutyl phenyl phosphate are present on the surface electrode of a QCM, oscillation of the QCM produces clearer STM images of the electrode surface [272]. This was in contrast to an immobile overlayer of iodobenzene, where identical images are observed whether or not the QCM is oscillating. The observation was attributed to a "windshield wiper effect", where at MHz frequencies the tip motion maintains a region of the surface where the absorbate concentration is reduced, which leads to a clearer image. The interpretation was backed up by modeling efforts led by the group of Brenner *et al*. [538], who developed straightforward model providing guidelines for effective lubrication of contacts operating at MHz frequencies.

Also in 2006, Coffey *et al.* inspired by suggestions of C_{60} "nanobearings" measured sliding friction of methanol monolayers sliding on fixed and rotating C_{60} layers to explore whether a lubricating effect was present. The measurements constituted the first direct link of friction to a documented molecular rotation state [539] (Figure 67). Friction was observed to be *higher* for rotating layers, in defiance of the ball-bearing analogy. Thus, no direct mapping of macro- to nanoscale attributed was established. Indeed, the opposite effects were observed.

Hedgeland *et al*. have recently combined helium and neutron spin-echo techniques to obtain friction coefficients for the Brownian motion of benzene molecules adsorbed on graphite.

The spin-echo techniques, which track motion in both atomic-scale time (ps) and length (nm) scales, revealed the motion directly through the time dependence of structural correlations on the surface [128]. The measurements constitute the highest precision measurements of slip time at sub-ps time scale reported to date.

From Table 10, it appears to be an overall trend of shorter slip times, thus higher sliding friction for large hydrocarbon molecules. However, a systematic study of this, normalized for differences in substrates and temperatures, has not been reported.

4.3.3. *Large molecular lubricants: t-butylphenyl phosphate, TCP, and perfluoropolyether*

Slip time data for three large molecular lubricants (TCO, TBBP, and PFPE) are summarized in Table 11. All are known to provide macroscopic lubrication as molecularly thin films in some cases [168,540,541], all of which are characterized by nonzero, but very short, (ps) slip times. Overall, the slip times reported for these systems are very short.

In 2002 and 2004, Abselmaksoud *et al*. reported QCM measurements of the nanoscale tribological properties of TCP reaction films formed at elevated temperatures in UHV conditions on

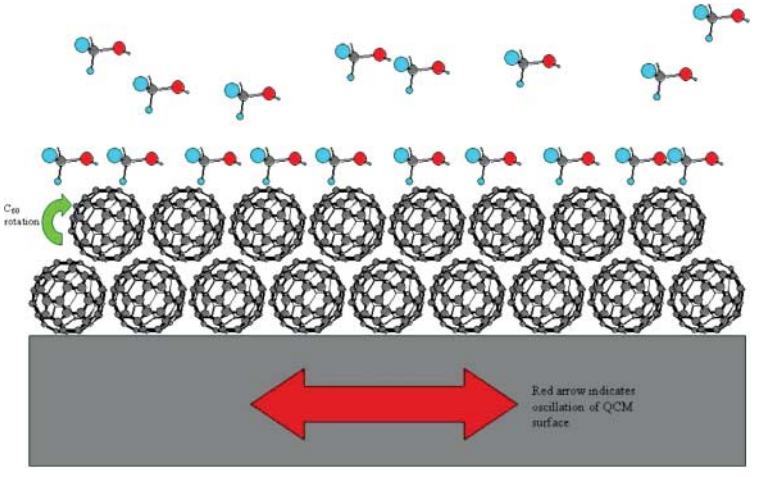

Figure 67. (color online) Schematic of measurements of sliding friction of methanol on rotating C60. Rotation caused friction to increase, not decrease in this case. Image courtesy of T.S. Coffey.

Table 11. Slip time data for large molecular lubricants.

						τ (ns)					
Adsorbate	Preplate	Substrate	Technique	T (K)	Reference	$\Theta = 0.2$	$\Theta = 0.5$	$\Theta = 1$ (liquid)	$\Theta = 1$ (solid)	$\Theta = 2$	$\Theta = 4 - 5$
TCP		Cr	QCM	300	[155]		1	0.9		0.9	
TCP		Cr	QCM	573	[155]	>0	>0	>0		>0	
TCP		Cr	QCM	673	[155]	0	0		0	0	0
TCP	O_2	Cr	QCM	573	[514]	0	0		0	0	0
TCP		Cr	QCM	673	[514]	0	0		0	0	0
TCP		Fe	QCM	300	[155]	2	1.75	1.75		1.5	
TCP		Fe	QCM	380–450	[155]	>0	>0	>0		>0	
TCP		Fe	QCM	500–673	[155]	0	0	0		0	0
TCP		Fe	QCM	673	[514]	0	0		0	0	0
TCP		Fe	QCM	573	[514]	0	0		0	0	0
TCP	O_2	Fe	QCM	573	[514]	~0.001	~0.001		~0.001	~0.001	~0.001
TCP	O_2	Fe	QCM	673	[514]	~0.001	~0.001		~0.001	~0.001	~0.001
TCP	OTS	Si-amorph	QCM	300	[615]	0.05					0.48
TCP		Si-amorph	QCM	300	[615]	0	0	0.1		0.9	0.9
TCP		Si-poly	QCM	300	[615]	0	0	0.1		0.12	0.14
PFPE		SiO_x/Si	Blowoff	300	[216]			0.0004			
TBBP	OTS	Si-amorph	QCM	300	[615]	0.1					0.24
TBBP		Si-amorph	QCM	300	[615]	0	0.05	0.1		0.3	0.3
TBBP		Si-poly	QCM	300	[615]	0	0	0.2		0.25	

high-purity iron, chromium, iron oxide, and chromium oxide surfaces. The data revealed interfacial slippage and/or viscoelastic effects for reaction films formed in systems that TCP was known to effectively lubricate at the macroscopic scale, namely iron oxide, but not iron in the absence of oxygen. The slippage detected was extremely small, in the order of ps. Nonetheless, it mapped directly to macroscopic properties. In contrast, rigidly attached TCP reaction films were observed to form on systems that TCP does not effectively lubricate at the macroscopic scale, such as chrome. The results thus revealed a link between the nanodynamical behavior of a tribological

film and its performance at the macroscale and as such are a step toward bridging the gap between macro- and nanotribology.

In 2000, Mate and coworkers constructing a "blowoff apparatus" (Figure 26) to measure the shear response of molecularly thin liquid films on solid substrates subjected to an applied air stress [214]. Unlike the SFA, where the sheared film is confined between two solid surfaces, the film in the blowoff apparatus is confined by a single solid surface, resulting in a dramatically different rheological behavior that is virtually identical to that of the QCM. Having atoms and molecules slide against a single solid surface makes the blowoff technique similar to the QCM technique, but with four orders of magnitude slower sliding speeds ($10\,\mathrm{mm\,s^{-1}}$ versus $1\,\mathrm{cm\,s^{-1}}$). The group investigated whether the films would be pinned at slow sliding speeds, and exhibit static friction effects similar to the pinning at atomic step edges, that have subsequently been reported for Kr layers sliding on Au [181] and for Neon layers sliding on Pb [182,542]. The group observed no pinning for the thin perfluoropolyether (PFPE) polymer films on silicon wafers that they studied.

In a follow-up study, Scarpulla *et al*. [216] employed the blowoff apparatus technique to study wind-driven movement of thin PFPE polymer films on silicon wafers and CN_x, comparing PFPE films with varying end groups and from different manufacturers. The ease with which a liquid polymer film moves across a surface when sheared was described in terms of a "shear mobility" parameter, and slip time, interpreted both in terms of continuum flow and in terms of wind-driven diffusion. They observed, in general, that the movement of PFPE films could be described as a flow process with an effective viscosity, even when the film thickness was smaller than the polymer's diameter of gyration. Table 11 lists a slip time characteristic of the range of materials that were reported on. Notably, the slip time is of sub-ps magnitude, but the viscous behavior is analogous to that reported for rare-gas systems [14,68].

In 2001, Johannsmann and coworkers employed a QCM to study PFPE films coated onto the surface of the QCM when it came into rubbing contact with a ceramic sphere. For a lubricant thickness of up to 1.1 nm, the quality factor of the QCM dropped, attributed to dissipation occurring during intermittent contact between the substrate and the sphere. For film thicknesses greater than 2.5 nm, the sphere discontinuously jumped into contact, after which the movements of the sphere and the quartz were reported to be locked together [542].

Spreading behavior of highly viscous poly(dimethyl)siloxane oils was reported in 1999 by means of reflection and attenuation of a Rayleigh surface acoustic wave from a small stripe of viscous fluid spreading across the acoustic path [543]. As the stripe spread across the acoustic path, with an accompanying decrease in stripe height to conserve volume, the reflected and attenuated acoustic signals exhibited a distinct pattern of resonances that allowed the authors to infer physical spreading propertied of the molecularly thin layers.

4.4. *Adsorbed metal clusters*

The diffusive and frictional behavior of clusters of particles can vary dramatically with size [54,125]. Sliding friction values may drop for clusters of atoms, for example, because the formation of an island generally requires that some or all of the atoms in the layer becomes incommensurate with the substrate. Gold islands of 250 atoms have been routinely observed to diffuse on graphite substrates with surprisingly large diffusion coefficients [158] ($D = 1000\,\mathrm{cm^2\,s^{-1}}$ and $E_\mathrm{d} = 0.5\,\mathrm{eV}$ compared to single atom values [159] of $D = 0.002\,\mathrm{cm^2\,s^{-1}}$ and $E_\mathrm{d} = 0.08\,\mathrm{eV}$). Similar behavior has been reported both experimentally and numerically for other metal clusters as well [160,544–546]. Diffusion of metal clusters on rare-gas substrates has also been reported on, with the interpretation of the results still a matter of debate [547,548].

In 2003, Antonov *et al.* studied aggregation and the size distribution of Au nanostructures as a function of the substrate composition (Xe, Kr, and Ar) and thickness. The measurements were performed using transmission electron microscopy to image them after buffer desorption and delivery to amorphous carbon substrates [547]. Desorption of the rare-gas buffer was argued to cause the clusters to aggregate in a process known as "buffer-layer-assisted growth". For small Au nanostructures less than 5 nm in mean radius, the diffusivity varied strongly with size and was observed to increase with size in a certain size range. The enhanced diffusion was attributed to self-heating during coalescence. The authors found the diffusivity to scale as the inverse of the contact area, in agreement with MD simulations of fast slip diffusion of nanocrystals on incommensurate surfaces [503].

Marchenko and Neklyudov suggested an alternative interpretation of the experiments [548]. In a numerical simulation study of the migration of Cu clusters on Xe(111), the diffusion coefficients of stable clusters were obtained for temperatures of 30–70 K and it was found that copper clusters of four, six, and seven atoms became embedded in the substrate, displacing an Xe atom, in less than 3 ns. The latter effect had not been accounted for in the original interpretation of the experimental data.

4.5. *Metal substrates*

4.5.1. *Ag(111) substrates (Table 12)*

Slip time data for adsorption on Ag substrates are summarized in Table 12. Slip times followed by (E) denote electronic contributions only. Overall, there is a distinct trend towards longer slip times as adsorbed layers become less chemically bonded. Chemisorbed oxygen is not observed to slip, while physisorbed layers exhibit slip times of the order of 1–10 ns.

Slip time studies performed on Ag(111) substrates were originally motivated by the fact that the potential corrugation is extremely low ($U_o = 0.7$–2.7 meV), thus allowing studies of highly ideal two-dimensional systems [355,356]. This, and the fact that many resistivity measurements have been performed on Ag(111), provided an incentive for early QCM studies of sliding friction. Ag(111) additionally provides a convenient substrate for studies of C60 layers, as C60 readily bonds to both Ag(111) and Cu(111) [549]. Nonetheless, the actual corrugation level of Ag(111) remains poorly documented, motivating sliding friction measurements to be performed on better characterized systems such as Cu(111) and Ni(111) [355,356].

Comparison of resistivity data with QCM data for total friction inferred by the resistivity again reveals some inconsistencies, especially for water films: electronic contribution to friction, as inferred from resistivity, cannot be higher than the sum of the phononic and electronic contributions as measured by QCM. Meanwhile, Bruch's theoretical estimate of electronic friction for Xe/Ag(111) of 200 ns is very different from that inferred from resistivity data. The difference cannot be attributed to differences in the sample morphology, and resistivity measurements obtained by Dayo and Krim [164] are in very close agreement with those reported by Schumacher [447]. The resistivity measurements were performed on identical substrates as the QCM slip time measurements [164].

4.5.2. *Au(111) substrates (Table 13)*

Slip time data for adsorption on gold substrates are summarized in Table 13. Measurements have been performed by independent groups on gold substrates, and on a number of different surface morphologies. It is evident that the lowest friction is reported for amorphous substrates, consistent with lower phononic dissipation effects [394,404]. Pinning is moreover observed for low-amplitude oscillation on the terraced (111) substrates employed by Carlin [185] and

Table 12. Slip time data for adsorption on Ag substrates.

					τ (ns)				
Adsorbate	Substrate type	Technique	T (K)	Reference	$\Theta = 0.2$	$\Theta = 0.5$	$\Theta = 1$ (liquid)	$\Theta = 1$ (solid)	$\Theta = 2$
^{4}He(helium)	Amorphous	QCM		[479]		10			
Ag	(111) textured	Resistivity		[447]		0.1(E)			
H2O (water)	(111) textured	Resistivity	300	[87,473]		0.1(E)			
CO(carbon monoxide)	(111) textured	Resistivity		[447]		0.36(E)			
C2H4 (ethylene)	(111) textured	Resistivity	50	[447]		0.72(E)			
C6H6 (benzene)	(111) textured	Resistivity	50	[447]		1.4(E)			
C2H12 (cyclohexane)	(111) textured	Resistivity		[447]		1.7(E)			
Xe (xenon)	(111) textured	Resistivity	10	[447]		3(E)			
Xe (xenon)	(111) textured	Resistivity	77.4	[164]		3.3(E)		4(E)	6(E)
C2H6 (ethane)	(111) textured	Resistivity	50	[447]		3.6(E)			
Xe (xenon)	(111) textured	Theory		[115,323]				200(E)	
C2H12 (cyclohexane)	(111) textured	QCM	300	[508]		0	2		1.5
O2 (oxygen)	(111) textured	QCM	300	[511]	0	0		0	0
Xe (xenon)	(111) textured	QCM	77.4	[164]		0.25		0.8	1
Xe (xenon)	(111) textured	QCM	77.4	[352]	2.3	1.2		1.1	1.8
Xe (xenon)	(111) textured	QCM	77.4	[353]	2.3	1.2		1.1	1.8
Xe (xenon)	(111) textured	QCM	77.4	[356]				2	
Ar (argon)	(111) textured	QCM	77.4	[87,473]			1.5		
Kr (krypton)	Fractal	QCM	77.4	[33,34]			1.5		
Kr (krypton)	(111) textured	QCM	77.4	[355]			2.1	2.7	
H_2O (water)	(111) textured	QCM	300	[508]	7	3	4		8
H_2O (water)	(111) textured	QCM	300	[87,473]			4		
C_2H_4 (ethylene)	(111) textured	QCM	77.4	[511]		15	5		
C_2H_6 (ethane)	(111) textured	QCM	77.4	[511]		15	9		
C_7H_8 (toluene)	(111) textured	QCM	300	[537]			10		15

Table 13. QCM slip time data for Au substrates.

				τ (ns)				
Adsorbate	Substrate type	T (K)	Reference	$\Theta = 0.2$	$\Theta = 0.5$	$\Theta = 1$ (liquid)	$\Theta = 1$ (solid)	$\Theta = 2$
^{4}He(helium)	Amorphous	0.5–2	[480]				>0	
Kr (krypton)	(111) terraced	85	[185]	0&1.5	0&1	0.1		0.2
Kr (krypton)	(111) terraced	85	[181]	0&7	0&2	0&1		0
Kr (krypton)	(111) textured	77.4	[355]			1	5	
Kr (krypton)	(111) textured	77.4	[173]			1	5	
Kr (krypton)	(111) textured	77.4	[176]			1.5		4
Kr (krypton)	(111) textured	77.4	[33,34]		1.5	2	10	
Kr (krypton)	Amorphous	77.4	[404]			4	50	100
Xe (xenon)	(111) textured	80	[33]				1.2	4
Xe (xenon)	(111) textured	113.6	[33]		1	2		5
Xe (xenon)	(111) textured	110	[508]	1.7	1.1	0.7		
N_2(nitrogen)	(111) textured	77.4	[508]		3	4		8
N_2(nitrogen)	(111) textured	77.4	[176]			4		7

Bruschi [181]. Bruschi and coworker observed that by slowly increasing the amplitude of the substrate oscillations, they could induce a sharp transition from a film locked to the substrate to a sliding one, thus two values are reported for the slip time in Table 13, corresponding to the pinned and sliding state. The group also observed sharp pinning transitions separating a low-coverage region, characterized by slippage at the surface, from a high-coverage region where the film is locked to the oscillating electrodes. The role of the step edges in the pinning remains a matter of

Table 14. Slip time data for fiber textured Cu(111) and Ni(111) substrates.

					τ (ns)				
Adsorbate	Substrate	Technique	T (K)	Reference	$\Theta = 0.2$	$\Theta = 0.5$	$\Theta = 1$ (liquid)	$\Theta = 1$ (solid)	$\Theta = 2$
H(hydrogen)	Ni	Resistivity		[447]		0.001(E)			
O_2 (oxygen)	Cu	Resistivity		[447]		0.007(E)			
CO(carbon monoxide)	Ni	Resistivity		[447]		0.014(E)			
CO(carbon monoxide)	Cu	Resistivity		[447]		0.039(E)			
N_2(nitrogen)	Ni	Resistivity		[447]		0.046(E)			
C_6H_5I (iodobenzene)	Cu(111)	STM-QCM	300	[272]	0	0		0	0
C_6H_6 (benzene)	Cu(111)	STM-QCM	300	[272]			>0	>0	
Xe (xenon)	Ni(111)	QCM	77.4	[356]		0.4		0.47	0.2
Kr (krypton)	Ni(111)	QCM	77.4	[355]			0.26	0.78	
C_8H_{18}(n-octane)	Cu(111)	QCM	300	[623]		1.5	0.9		0.8
Kr (krypton)	Cu(111)	QCM	77.4	[355]			7	11	
Xe (xenon)	Cu(111)	QCM	77.4	[356]				15.5	30

great interest, as it must be accounted for in all realistic treatments of sliding friction. Liquid films appear much less susceptible to variations in slip time attributable to pinning.

4.5.3. *Cu(111) and Ni(111) substrates (Table 14)*

Slip time data for adsorption on Cu(111) and Ni (111) substrates are summarized in Table 14.

Slip times followed by (E) denote electronic contributions only. Cu(111) and Ni(111) are very close in lattice spacing (0.4414 and 0.0441 nm, respectively), but have very different potential corrugations ($U_o = 1.9$ and 14 meV, respectively). The systems have received attention on account of the fact that their binding potential energies have been reported in the literature [355,356] and also for the numerous resistivity measurements that have been reported for adsorbates on these substrates [447]. Resistivity measurements indicate very high levels of electronic friction, and QCM measurements show relatively high levels of friction, and low slip times for the majority of systems studied. The exception is Xe/Cu(111): although the system is commensurate, the potential corrugation is evidently too low to pin the layer [356]. This result was predicted numerically by Cieplak *et al*. [35], who reported a lack of static friction in commensurate systems with low potential corrugation amplitudes. Reguzzoni [61] have very recently examined the size dependence of pinning in Kr clusters adsorbed on Cu(111) and Si substrates by numerical methods, as described above . When the size of the contact was reduced below a critical value, they observed domains to coalesce and the interfaces to become commensurate (Figure 7). The behavior is interpreted in terms of the competing effects of interfacial and elastic interactions.

To explore this effect in more detail, Bortolani *et al.* performed an MD study of the slip time and static friction for a slab of Xe deposited on a slab of Cu [163,501]. In order to model the role played by the phonons in the two blocks, they compared results obtained with a substrate formed by fixed atoms with one formed by mobile atoms. In the latter case, the scattering between Xe and Cu mobile atoms was found to be inelastic and there was an exchange of momentum and energy between the two blocks. This in turn produced disorder in the interface plane, which acted to decrease the static friction also increase the slip time. The authors describe the interaction between Xe and Cu with a phenomenological multi-ion potential which gave rise to anticorrugation of the charge distribution and reproduced their *ab initio* density functional calculations. Since the model

Table 15. QCM slip times on Pb(111) above and below $T_c = 7.2$ K compared to selected slip times on Ag(111).

System	Substrate type	T(K)	Reference	Θ (monolayers)	$t_{ph} = \tau$ (SC) (ns)	$\tau_{total} = \tau$ (N) (ns)	τ_e (ns)
He/Pb(111)	Textured	7.20	[420]	4	196	76	126
He/Pb(111)	Air-exposed, textured	4.20	[166]	4	18		
Ne/Pb(111)	Terraced	6.50	[182]	0.8	0.45		
Ne/Pb(111)	Terraced	6.50	[491]	0.8	2.5		
Ne/Pb(111)	Terraced	7.20	[462]	0.8	2.5	2.5	$\tau_e > 2.5$
Ne/Pb(111)	Air-exposed, textured	5.75	[166]	9	>>50		
N2/Pb(111)	Air-exposed, textured	7.20	[165]	1.7	29	12	21
N2/Pb(111)	Textured	7.20	[420]	1.7	40	19	36
N2/Pb(111)	Terraced	7.20	[493]	1	0	0	0
N2/Pb(111)			[115,323]	1			$2 < \tau_e < 20$
Xe/Ag(111)			[115,323]	1			200
Xe/Pb(111)	Textured	77.4	[625]	1		0.7	
Xe/Ag(111)	Textured	77.4	[164]			0.8	
Xe/Ag(111)	Textured	77.4	[352]			1.1	
He/Pb(111)	Textured (magnet)	7.20	[420]	4	1538	87	92
N2/Pb(111)	Textured (magnet)	7.20	[420]	1.7	1190	140	160

potential is a linear superposition of a corrugating potential and an anticorrugating one, the authors could probe how static friction evolves by passing from an anticorrugated to a fully corrugated system.

4.5.4. *Pb(111) substrates (normal and superconducting) (Table 15)*

Slip time data for films adsorbed on Pb(111) substrates above and below T_c are summarized in Table 15. Slip times followed by (E) denote electronic contributions only. Although much attention has been devoted already in earlier sections to the topic of superconductivity-dependent friction, a number of experimental details become more evident by comparing all adsorbates and experimental results alongside each other, beginning with reports of which systems are pinned, and which exhibit sliding. Also included in Table 15 are data for selected slip times on Ag(111), as substrate with slip times comparable to Pb(111) for Xe at 77.4 K.

Both Fois [493] and Highland [492] reported that argon adsorbed on Pb(111) at temperatures below 15 K failed to exhibit sliding. Fois [493] reported that krypton and xenon adsorbed on Pb(111) below 15 K failed to exhibit sliding, while Highland [492] reported that CO adsorbed on Pb(111) at 7 K failed to exhibit sliding. Both Fois [493] and Dayo [166] report that neon films slide readily on Pb(111) at low temperatures in the range 5–8 K. Renner and coworkers reported pinning of N_2 at low temperatures [509,510].

The picture emerging at this time is that solid films are pinned more readily on the terraced substrates with step edges. Given that amorphous substrates have been associated with lower levels of phononic friction and that partial pinning is quite possible in solid systems [583]. The best comparisons between systems will likely occur in liquid adsorbed systems. For the case of neon on Pb(111), no difference in the slip time was detected by Pierno *et al*. [462]. However, the electronic slip time contributions reported by Highland and Krim [420] of order 100 ns for much thicker helium layer would have been below the detection limit in the setup [472]. Work continues

in this fascinating area to explain the experiments with theory, with a focus on surface topology, step edges, and/or charge transfer effects for a full explanation of the data.

Bortolani *et al*., for example, have performed an MD study of static friction of a nitrogen block sliding on Pb(111), as a function of the temperature [550]. They report that lattice vibrations and structural disorder are responsible for the behavior of the static friction as a function of the temperature. In particular, they report that a large momentum transfer from the Pb atoms to the N_2 molecules displaces the nitrogen planes in the proximity of the interface, and around $T = 20$ K this effect produces the formation of an hcp stacking at the interface. By increasing the temperature, the hcp stacking propagates into the slab, toward the surface. Above $T = 25$ K, they observe a sharp, rapid drop of more than three orders of magnitude in the static friction force, with subsequent melting of the nitrogen at $T = 50$ K. The temperature behavior of the calculated static friction is in good agreement with the QCM results of Fois *et al*. [493]. A difference in surface defect and step edge morphology therefore is the likely explanation for the fact that the nitrogen films studied by Highland [420] and Mason [419] are pinned only in a half of the data sets. Changes in friction at T_c are observed in those cases where the films remain unpinned at 7.2 K, when sliding occurs [165,419,420] (Figure 68).

In addition to sliding friction already measured on Pb surfaces, an emerging area of quantum effects [385] and quantum control of friction in lead has developed in recent years, whereby friction levels of sliding films are expected to depend on the thickness and quantum nature of the lead film itself. Atomically flat, ultrathin Pb films grown on semiconductor substrates form quasi-two-dimensional (2D) electronic systems. As such, they offer the opportunity to explore novel properties induced by quantum size effects (QSEs) [551]. In these systems, the motion of electrons in the film plane is essentially free, however, in the film normal direction it is confined, which leads to the quantized electronic states, that is, quantum well states (QWSs). The formation of QWSs induces the redistribution of electrons and changes the electronic structure of the metal films and thus modifies their properties. By controlling the film thickness, the width of the confinement potential well, the QWSs, together with the physical and chemical properties of the films can be engineered. Jia has summarized a variety of studies for the Pb/Si(111) system and discussed the perspectives in this area. Although not yet probed, friction is expected to be one of the material properties impacted.

Dong *et al*., for example, have employed UHV AFM to measure the adhesive force of atomically flat (111) oriented Pb island on Si(111) surface at low temperature (similar to 60 K) [552]. The experimental results indicate that for the same (111) surface the adhesive force changes and oscillates with the island thickness. This phenomenon is shown to have originated from the electron structure modulation by strong QSEs along the island surface normal direction, which modifies surface energy and leads to the observed oscillatory adhesive forces.

Quantum restructuring of surface morphology is not limited to lead: It has also been reported for boron-doped nanocrystalline diamond, with a large impact on submicron surface structure [553].

4.5.5. *$YBa_2Cu_3O_7$ substrates*

To date, studies of sliding friction of adsorbed films on superconducting substrates have been limited to Pb(111) substrates. However, the work has inspired studies of friction at the superconducting transition of $YBa_2Cu_3O_7$ (YBCO) thin films, at both the macro- and nanoscale [64,421].

In 2001, Ding and coworkers performed a study of YBCO thin films and polysilicon films, to investigate macroscopic sliding friction properties with a conventional ball-on-flat tribometer [629]. Measurements were performed for when samples in contact with either sapphire or steel balls. or a steel ball in ambient environment. They reported the friction (at room temperature) of YBCO to be lower than for silicon for contact with sapphire, and about the same for contact

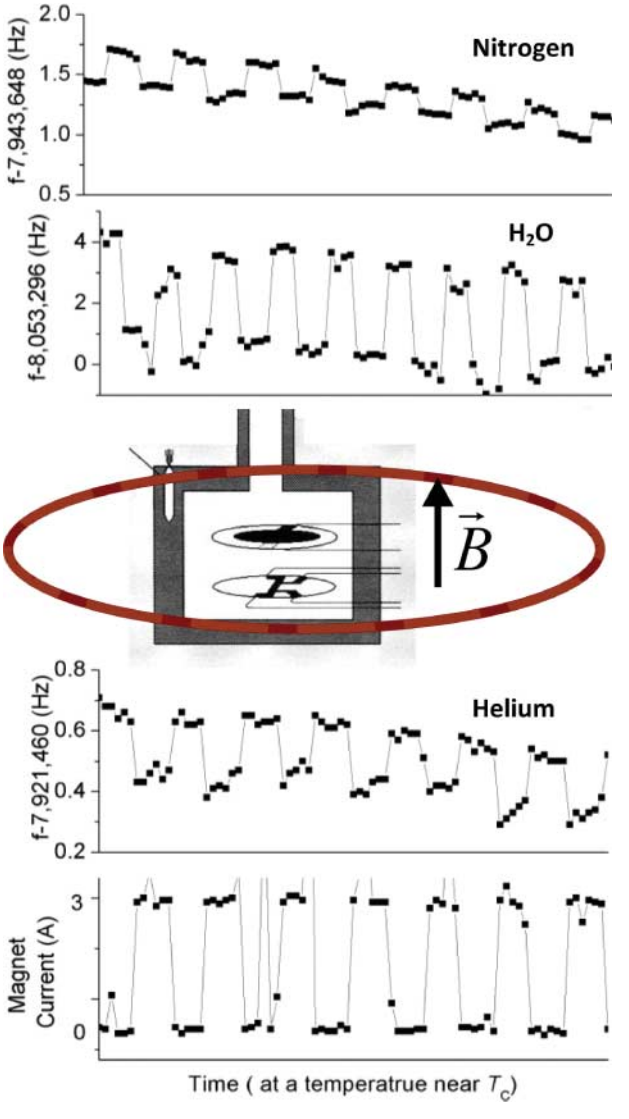

Figure 68. (color online) Schematic of apparatus and frequency response of H_2O, He, and N_2 to the presence of a magnetic field at temperatures slightly below T_c as the system is repeatedly driven into and out of the superconducting phase by an externally imposed magnetic field. Reprinted figure with permission from M. Highland *et al.*, Physical Review Letters 96, art#226107, 2006 [420]. Copyright (2006) by the American Physical Society.

with steel, and that YBCO substrates exhibited desirable wear properties in terms of stick–slip phenomena. The group subsequently extended their capabilities to vacuum and low temperature, to allow studies of friction of YBCO in the superconducting state. Curiously, they observed a major drop from 0.4 to 0.15 in the friction coefficient with cooling, and presumed it to be at the superconducting transition T_c, for contact with a steel tip [431].

Altfeder *et al*. subsequently examined whether the same effect might also be present at the atomic scale [64]. In particular, magnetic probe microscopy was employed to examine levitation

and friction for YBCO ($T_c = 90$ K) between 65 and 293 K. While levitation effects were observed exclusively below T_c, the friction coefficient dropped from 0.35 to 0.19 completely in advance of cooling to T_c, with no abrupt drop at T_c itself. The results were interpreted as electronic in nature, with electrostatic, rather than mobile, charge likely contributing to the effect (Figure 8).

4.6. *Graphite-, graphene-, and carbon-based substrates (Table 16)*

4.6.1. *Carbon/diamond/graphite/graphene/nanotubes*

Slip time data for graphite and graphene substrates are summarized in Table 16. Measurements performed on these substrates have the advantage of a long historical background of surface science studies performed on single crystalline graphite [14,68,554–557]. The well-documented character of graphite, along with the well-documented nature of two-dimensional films adsorbed on graphite [496,558], have thus made it a popular substrate to perform nanotribological studies on by means of both QCM and AFM. The fact that graphite is also a macroscopic lubricant has also driven studies in this area. Adsorption isotherms performed on graphite attached to a QCM electrode reveal close association with known two-dimensional phase diagrams of adsorbed systems. Inspection of Table 16 reveals frequent pinning effects for monolayers coverages of Kr, with the commensurate layer having *lower* friction than the incommensurate layer, in cases where it is not pinned. Two layer helium films are also notable by nature of the fact that the second layer is reported to slide relative to the first, rather than being locked together with the first layer. Frictional heating effects have also been studied experimentally for Kr monolayers sliding on graphene/Ni(111) substrates [498].

Measurements performed on graphene are too few in number at this point in time to be directly comparable to those performed on graphite. The fact that graphene can have a variable lattice spacing allows for a myriad of interesting future studies in an ever growing area of graphene and graphene related materials. Selected non-QCM nanotribological studies are now highlighted, to demonstrate the range of studies performed on these materials that include a focus on friction.

In 2001, Brune *et al.* reported AFM friction measurements on laser-deposited amorphous carbon and carbon nitride (CNx) thin films in 2001 [559]. They studied the friction in relation to the structure and surface morphology resulting from the applied deposition parameters and found

Table 16. Slip time data for graphite and graphene/Ni(111).

						τ (ns)			
Adsorbate	Substrate	Substrate type	Technique	T (K)	Reference	$\Theta = 0.5$	$\Theta = 1$ (liquid)	$\Theta = 1$ (solid)	$\Theta = 2$
^{4}He (helium)	Graphite	Terraced	QCM	0.45	[486]			20	7,80
^{4}He (helium)	Graphite	Terraced	QCM	1.0	[486]			20	8,80
^{4}He (helium)	Graphite	Terraced	QCM	1.25	[486]			20	8.5,70
^{4}He (helium)	Graphite	Terraced	QCM	1.5	[486]				9, 60
^{4}He (helium)	Graphite	Terraced	QCM	0.75	[488]		Inifinite		
He-4 (helium)	Graphite	Terraced	QCM	<4K	[484,485]		>0		
C_6H_6 (benzene)	Graphite	Terraced	HeSE	140	[128]	0.00045			
Kr (krypton)	Graphite	Terraced	QCM	85.8	[476]	0&60(C)		0&20 (IC)	10,300
Kr (krypton)	Graphite	Terraced	QCM	85.8	[476]	0&60(C)		0&60(C)	
Kr (krypton)	C60 monolayer/ Cu(111)	Textured	QCM	77.4	[539]	4	3		
Xe (xenon)	graphene/ Ni(111)	Textured	QCM	77.4	[356]	2		1.7	

high nanoscopic friction for amorphous carbon thin films, medium friction for CN_x and very low friction for graphite.

In 2004, Dienwiebel *et al*. reported what they termed "superlubricity of graphite" recorded on a home-built friction force instrument capable of measuring force of friction down to 15 pN. The group captured a graphite flake at the end of a tungsten tip, and slid it along a crystalline graphite substrate while measuring the friction. The contact area of the flake was estimated to be in the order of a hundred atoms and the measurements were performed versus rotation angle along the surface. The flake was thus brought in an out-of-perfect commensurability with rotation, as theoretically expected, but never reported before in the experimental literature in such a dramatic manner, high friction levels in the commensurate positions were present and incommensurate sliding was characterized by friction lower than the resolution of the apparatus. The authors suggest that the low friction levels observed may account for the lubricity of graphite at the macroscopic scale. While their work in no way proves this, it does provide a convincing case for Tomlinson-type mechanical vibrations as a fundamental source of friction that may well be manifested at the macroscopic scale.

In 1999, Falvo *et al*. reported AFM measurements of the ability to manipulate, slide, and roll CNTs along graphite [44]. Buldum *et al*. subsequently reported MD studies of atomic-scale sliding and rolling of CNTs in 1999 with a focus on the motion of nanotubes on a graphite surface [45,326,327]. They reported that sliding and rolling nanotubes had different characters and that the potential energy barriers fur sliding nanotubes were higher than that for perfect rolling.

In 2009, Lucas *et al.* presented a combined theoretical and experimental study of the frictional forces encountered by a nanosize tip sliding on top of a supported MWCNT along a direction parallel or transverse to the CNT axis [560]. Counterintuitively, they found a higher friction coefficient in the transverse direction compared with the parallel direction. The effect was through numerical simulations which revealed that transverse friction elicits a soft 'hindered rolling' of the tube and a frictional dissipation that is largely absent for chiral CNTs, when the tip slides parallel to the CNT axis. The author's findings contribute to developing enhanced strategies for large-scale CNT handling (both assembly and sorting) on a surface. A second example of the emerging area of friction and nanomachines was reported by Nagapriya [561] who performed an experimental study of stick–slip in WS_2 nanotubes. The authors observed torsional stick–slip behavior between the inner and outer walls when an external torque was applied and surpassed a threshold value. The results were interpreted in terms of a balance between in plane shear stiffness and the interwall friction.

Also in 2009, Hedgeland *et al*. reported using helium and neutron spin-echo techniques to obtain friction coefficients for the Brownian motion of benzene molecules adsorbed on graphite.

The spin-echo techniques, which track motion in both atomic-scale time (ps) and length (nm) scales, revealed the motion directly through the time dependence of structural correlations on the surface [128]. The data represent the shortest time scales (sub-ps) resolved to date for measurements of frictional slip times.

In 2008, Carpick and coworkers performed AFM measurements of diamond substrates. The work was motivated by the well-documented and impressively low friction and wear of diamond in humid environments, whose origin is actively debated. They found ultralow friction and wear for ultrananocrystalline diamond surfaces even in dry environments, and also observed negligible rehybridization except for a modest, submonolayer amount under the most severe conditions (high load, low humidity). The work supported a passivation hypothesis for lubricity of diamond [562]. In 2010, the same group used AFM to compare nanoscale frictional characteristics of atomically thin sheets of graphene, molybdenum disulfide (MoS_2), niobium diselenide, and hexagonal boron nitride exfoliated onto a weakly adherent substrate (silicon oxide) to those of their bulk counterparts [563]. Measurements down to single atomic sheets revealed that friction monotonically

increased as the number of layers decreased for all four materials. The generality of the result indicated that it could be a universal property of nanoscale friction for atomically thin materials weakly bound to substrates.

4.6.2. *Rotating and fixed fullerenes and related materials*

QCM slip time data for films adsorbed on fullerenes are summarized in Table 17.

Since their discovery, fullerene-based materials have been of great interest to surface science community [564], with a particular interest in the friction reducing potential for the spherically shaped molecules [565,566]. In 1996, Campbell *et al*. [567], employing an SFA, reported a large increase in interfacial slip when C60 was dissolved in toluene squeezed between two atomically uniform mica sheets. C60 was thus established as an additive for macroscopic lubricants based on the high interfacial slip levels observed for C60 dissolved in toluene [418]. performed direct MD simulations molecular "ball bearings" composed of fullerene molecules (C60 and C20) and MWCNTs. The comparison of friction levels indicated that fullerene ball bearings had extremely low friction in certain cases. Other nanotribological measurements have indicated, however, that interfacial slippage of model lubricant films does not reduce friction or that C60 rotation does not provide an additional energy dissipation channel in the friction process.

Liang [568] and Li [569], for example, studied the nanotribological properties of C60 single crystal (111) and (100) surfaces around the orientational order-disorder phase transition temperature, by AFM/FFM in high vacuum. Results show that for both surfaces across the phase transition

Table 17. QCM slip time data for adsorbed films on fullerenes.

					τ (ns)				
Adsorbate	Preplate	Substrate	T (K)	Reference	$\Theta = 0.2$	$\Theta = 0.5$	$\Theta = 1$ (liquid)	$\Theta = 1$ (solid)	$\Theta = 2$
Kr (krypton)		Ag(111)	77.4	[355]			2.1	2.7	
Kr (krypton)	C60 fixed bilayer	Ag(111)	77.4	[355]			3.1	3.3	
Kr (krypton)	C60 monolayer	Ag(111)	77.4	[355]			1.6	2.7	
Kr (krypton)	C60 fixed monolayer	Ag(111)	77.4	[539]	10	4	3		
Kr (krypton)	C60 fixed bilayer	Ag(111)	77.4	[539]	10	4	3		
Kr (krypton)		Cu(111)	77.4	[355]			7	11	
Kr (krypton)	C60 fixed monolayer	Cu(111)	77.4	[539]	10	4	3		
Kr (krypton)	C60 fixed bilayer	Cu(111)	77.4	[539]	10	4	3		
Xe (xenon)	C60 fixed bilayer	Ag(111)	77.4	[356]				5.5	
Xe (xenon)		Ag(111)	77.4	[356]				2	
C_7H_8 (toluene)		Ag(111)	300	[537]			10		15
C_7H_8 (toluene)	C60 rotating bilayer	Ag(111)	300	[537]			0.1		5
CH_3OH (methanol)	C60 monolayer	Ag(111)	300	[539]	10	7	3.6		
CH_3OH (methanol)	C60 monolayer	Cu(111)	300	[539]	10	7	3.6		
CH_3OH (methanol)	C60 rotating bilayer	Ag(111)	300	[539]	3	4	1.9		
CH_3OH (methanol)	C60 rotating bilayer	Cu(111)	300	[539]	3	4	1.9		

temperature, the friction force, and the adhesive force between a C-60 coated AFM tip and the C-60 crystal surfaces exhibit discontinuous behavior. The friction force within the applied external load range in the low-temperature phase was significantly larger than that in the high temperature phase, with no obvious change in the slope of the friction force curves (the friction coefficient) in the low- and high-temperature phases. The abrupt change in friction was found to be caused mainly by the abrupt change in adhesion, which, in turn, can be qualitatively understood through changes in the van der Waals interaction and the short-range Coulomb interaction associated with the structural changes across the phase transition. Compared to most other degrees of freedom, the rotation of C-60 molecules was found to have little effect on friction and is an ineffective energy dissipation channel.

Coffey *et al*. [152,537] in a study more comparable to that of Campbell *et al*. [567] investigated the changes in interfacial friction of toluene on mica and Ag(111) both in the presence and in the absence of interfacial C60 layers employing AFM and QCM techniques. The LFMs fail to detect C60 at the toluene/mica interface, presumably because the C-60 was dislodged by the slow-moving probe tip. In contrast, QCM measurements of interfacial friction and slippage for toluene/Ag(111) are sensitive to the presence of interfacial C60, but the friction *doubled* when the C60 was present.

In a follow-up experiment, inspired by suggestions of C60 "nanobearings", Coffey and Krim [45] measured sliding friction of methanol layers on fixed and rotating C60 layers prepared on Ag(111) and Cu(111) substrates [539,549] to explore whether any lubricating effect was present. They referred to this general phenomenon as "nanomapping", whereby macroscopic attributes are mapped in a one-on-one fashion to nanoscale entities. The measurements were the first to document friction in a known nanoscale molecular rotation state. Once again, however, the friction was observed to be *higher* for rotating layers, in defiance of the ball bearing analogy.

4.7. *Silicon-, semiconductor-, SAM-, and MEMS-related materials (Table 18)*

Slip time data for adsorbed films on silicon- and SAM-coated silicon are presented in Table 18.

Silicon substrates are frequently the focus of nanotribological studies [570]. Single-crystal silicon wafers are exceptionally flat, allowing ellipsometry to detect molecularly thin films, for blowoff device measurements performed by Mate and coworkers [214,216]. They are able to be doped so as to control their conductivity for studies of electronic friction [156,157,252,416,417]. In addition, they form the primary constituent in the majority of MEMS device systems, which are currently limited by tribological considerations [571,572]. Studies of self-assembled-monolayers and other adsorbed layers on both silicon and silicon with a SAM precoat [573] are at the focus of the increasingly successful area of vapor phase lubrication of MEMS [89,161,274,285,536,574–576].

4.7.1. *Doped silicon substrates*

Salmeron and coworkers have succeed to control and vary the electronic properties in semiconducting materials. Through a series of AFM studies, they have proved this to be a viable means for detection of electronic phenomena in nanotribological studies (Figure 69). They first employed the technique in 2006 to document a dependence of the friction force on carrier concentration in n-doped silicon substrates [252]. The samples consisted of intrinsic n-type Si(100) wafers patterned with 2-μm-wide stripes of highly B-doped p-type material. The AFM tip was coated with conductive titanium nitride and the local carrier concentration was controlled through application of forward or reverse bias voltages between the tip and the sample in the p and the n regions. Charge depletion or accumulation resulted in substantial differences in friction force, providing very convincing evidence of a capability to electronically control friction in doped semiconductor

Table 18. Slip time data at 300 K for Si substrates, SAMS preplates, and candidate materials for MEMS lubrication.

					τ (ns)					
Adsorbate	SAMS layer	Substrate	Technique	Reference	$\Theta = 0.2$	$\Theta = 0.5$	$\Theta = 1$ (liquid)	$\Theta = 1$ (solid)	$\Theta = 2$	$\Theta = 4 - 5$
C_5H_{12} (pentanol)		Al	QCM	[536]	0	0	0		0	
CF_3CH_2OH (TFE)	PFTS	Al	QCM	[536]	0	0	0			
CF_3CH_2OH (TFE)		Al	QCM	[536]	0	0	0		0	
PFPE		SiOx/Si	Blowoff	[216]			0.0004			
$(CH_3C_6H_4) \cdot 3PO_4$ (TCP)		Si-amorph	QCM	[615]	0	0	0.1		0.9	0.9
TBBP		Si-amorph	QCM	[615]	0	0.05	0.1		0.3	0.3
$(CH_3C_6H_4) \cdot 3PO_4$ (TCP)		Si-poly	QCM	[615]	0	0	0.1		0.12	0.14
TBBP		Si-poly	QCM	[615]	0	0	0.2		0.25	
C_2H_5 (ethanol)		Al	QCM	[536]		1	0.5		1	
CF_3CH_2OH (TFE)		Si	QCM	[536]		1	3.5		2	
C_2H_5 (ethanol)	PFTS	Al	QCM	[536]		2	4		4	
C5H12 (pentanol)	PFTS	Al	QCM	[536]		0.5	6		6	
C5H12 (pentanol)		Si	QCM	[536]		4	6		8	
C_2H_5 (ethanol)		Si	QCM	[536]		4	8.5		9	
$(CH_3C_6H_4) \cdot 3PO_4$ (TCP)	OTS	Si-amorph	QCM	[615]	0.05					0.48
TBBP	OTS	Si-amorph	QCM	[615]	0.1					0.24

devices. The result extended the range of materials systems in which electronic contributions had been established to semi conductors, thus opening the door to a wide range of new applications in the area of nanoscale machines with parts in moving contact.

In 2007, the same group presented experimental results on similar samples that also showed a significant dependence of the properties of the friction force on charge carrier concentration in a Si semiconductor sample containing p- and n-type regions [156,157]. The carrier concentration was controlled through application of forward or reverse bias voltages in the p and n regions that caused surface band bending in opposite directions. Excess friction was observed only in the highly doped p regions when in strong accumulation. The excess friction was observed to increase with tip-sample voltage, contact strain, and velocity and was not in any way associated with wear or damage of the surface.

In 2008, Salmeron's group reported observations of the electronic contribution to friction at GaAs semiconductor surfaces, using a Pt-coated tip with 50 nm radius in an AFM sliding against an n-type GaAs(100) substrate [416]. The GaAs surface was covered by an approximately 1 nm thick oxide layer. Charge accumulation or depletion was induced by the application of forward or reverse bias voltages. Again they observed a substantial increase in friction force in accumulation (forward bias) with respect to depletion (reverse bias). The authors considered many possible sources for the levels of electronic friction that they measured, including electron–hole pair creation, electron wind effects, charge carrier drag, and fluctuating electron fields. In all cases, the contributions

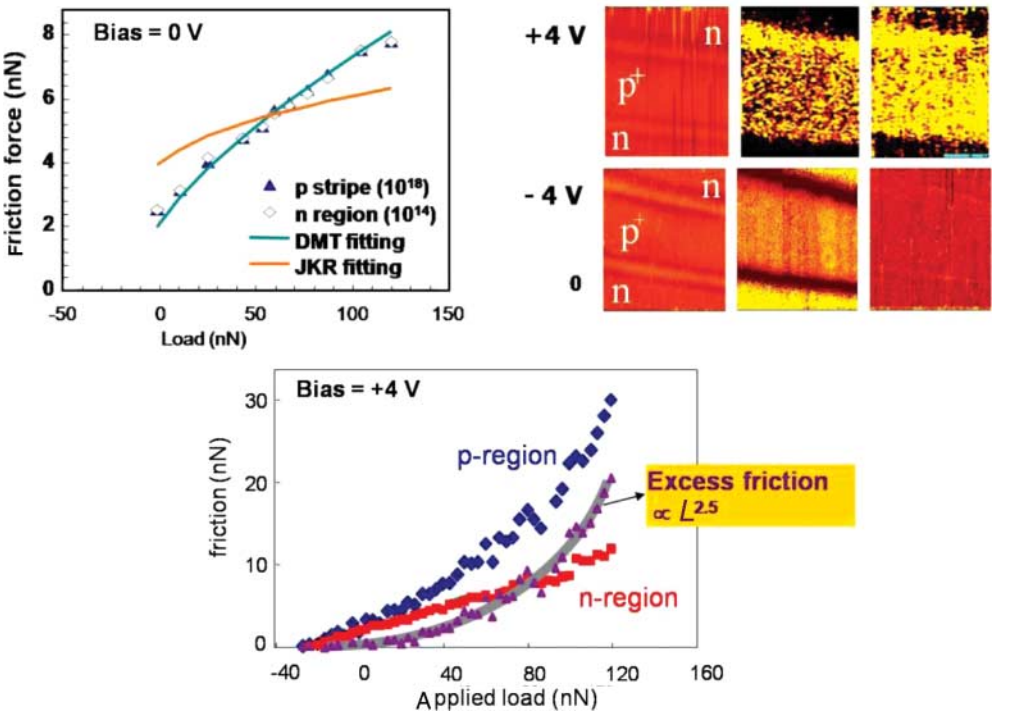

Figure 69. (color online) Friction during accumulation and depletion. Reprinted figure with permission from Park *et al.*, Physical Review B 76, art#064108 (2007) [157]. Copyright (2007) by the American Physical Society.

from conduction electron effects, as discussed in detail in Section 2, were too small by many orders of magnitude to account for the observed dissipation levels, which were in the order of 10^{-5} N s m^{-1}. In the end, Qi *et al.* obtained quantitative agreement only by assuming the charges were trapped at the surface and that the forces were electrostatic in nature: They concluded that as the tip moves across the surface, it leaves a "trail" of trapped charge, causing electrostatic attraction that is manifested as friction [417]. Studies of electrostatic effects are quite challenging, yet increasingly important, if all contributions to atomic-scale friction are to be accounted for. They represent an area ripe for future studies in the area of nanotribology.

4.7.2. *SAM-coated surfaces*

SAM layers on silicon and other surfaces have been widely studied by the nanotribological community, both for their MEMS applications and also as model lubricants [577–580]. Tribological studies of SAMs were preceded by friction measurements of Langmuir–Blodgett films on mica [581] and metal substrates [582] in the early 1980s. A SAM consists of a chain molecule with a head group that binds to a surface and a tail group that delivers desirable chemical qualities to the exposed interface. The majority of the nanotribological studies have been performed on hydrocarbon SAM layers [93,94,584–593]. Barrena, for example, demonstrated that energy losses during friction of alkylsilane SAMs with sharp AFM tips could be correlated to molecular events occurring at specific threshold loads [589,594] (Figure 70). Under these loads, discrete molecular tilts occurred, which were dictated by the geometrical requirements of the close packing of molecules. The barriers overcome during these tilt events gave rise to discrete changes in the frictional forces.

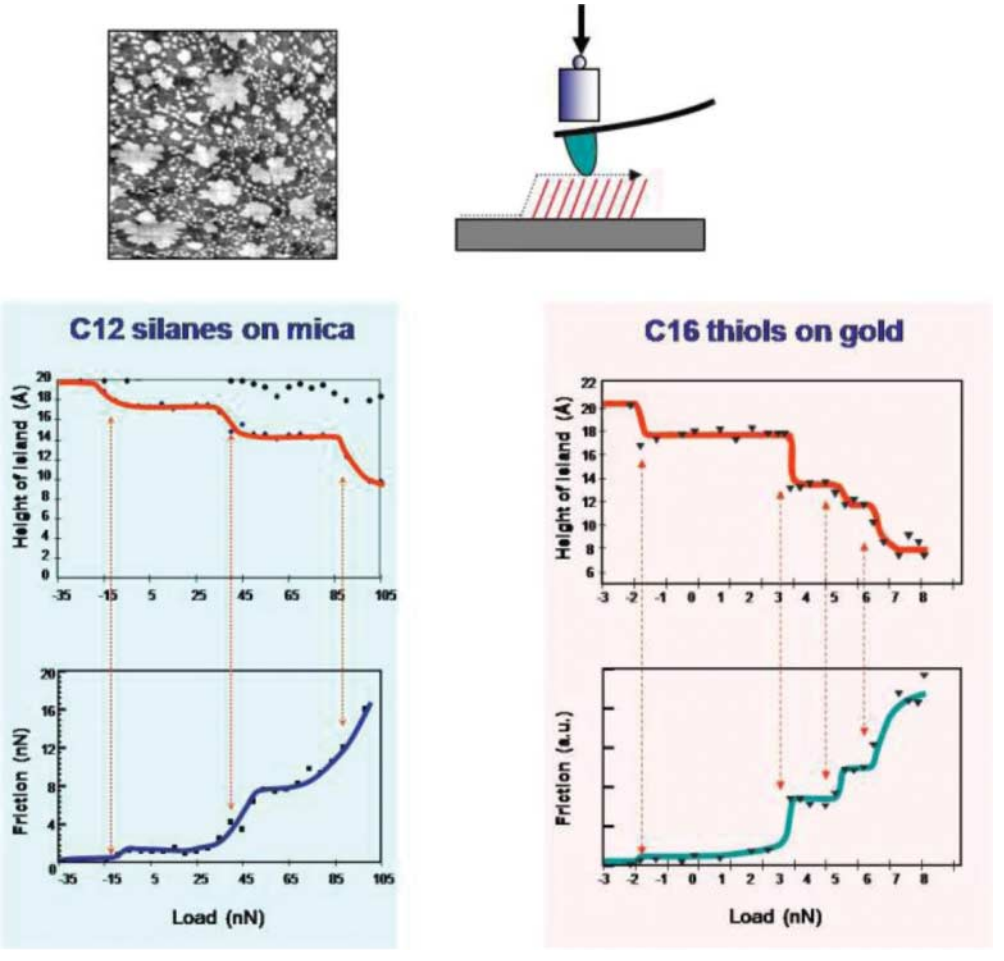

Figure 70. (color online) Friction and structure of alkane-chain SAMs under pressure. Image courtesy of M. Salmeron.

For further discussions of AFM studies of SAM layers, the reader is referred to [595–600] and extensive literature reviews by Carpick and Szulfarska [76–78].

Studies involving SFA geometries have also demonstrated important new experimental and theoretical understandings of the impact of a SAM coating on friction, for both charged and neutral molecules [74]. Selected significant studies include [601–612].

Witten [601] reported some of the earliest studies, consisting of numerical results that revealed interpenetration of lamellar copolymers to be significantly inhibited when opposing interfaces were pressed into contact. The authors also found that the sliding stress grew exponentially as a fractional power of the molecular weight because of the very small levels of interpenetration. The results thus provided a theoretical framework for experimental studies of friction. Kreer [606] later performed MD simulations of friction between polymer brushes in nonsteady-state conditions. In particular, they studied systems where the sliding was intermittently stopped and started, to examine in particular sliding at a steady speed compared to oscillatory motion. They concluded that dissipation mechanisms for oscillatory shear are similar to those for constant velocity sliding

if the drive amplitude exceeded a certain threshold value. Below this value, enhanced losses were observed that were not necessarily associated with the onset of stick–slip behavior.

Notable experimental studies include [602], which employed a modified SFA for studies of the friction and rheology of confined polymer melts, with a focus on how the bulk properties compared and contrasted with the molecularly confined films. At low shear rates, thick films were observed to exhibit bulk-like properties, while thin films (<20–200 nm) became distinct from the bulk, but still liquid-like. Below 30 nm, the films exhibited nonlinear behavior, transitioning to glassy and solid-like states. Schorr [604] also studied the thickness dependence of reported an SFA study of the shear forces between tethered polymers as a function of compression, velocity, and solvent quality, mapping out a wide range of behaviors ranging from linear viscous behaviors to a sublinear response for high shear velocities and higher degrees of compression, in agreement with simulations reported for these effects.

Raviv *et al*. [605] reported a study of lubrication of charged polymers, one of only a very few studies that have systematically examined the role of static charge effects on frictional at the molecular layer [605,607,611]. In contrast to studies reported in AFM geometries, where electrostatic charges generated by contact electrification increase friction [64,156,157], charging of polymers was observed to decrease friction. This was attributed to a decrease in interpenetration as a result of electrostatic repulsion [609,610]. Studied the effect theoretically, and confirmed that ultra-low friction between two polyelectrolyte polymer brush-coated surfaces could indeed result from the lack of entanglement: the osmotic pressure due to the counterions in the opposing surfaces was sufficient to support a realistic load and hold the brushes sufficiently far apart so as to prevent entanglement.

Hartung [608] employed SFA and macroscopic tribological tests to study the lubricity of SAM layers in the presence and absence of a surrounding aqueous medium. They reported that the SAM plus water combination was to varying extent, more lubricious than water alone. This is not an isolated occurrence: bound plus mobile film combinations are known to be especially effective in lubrication of MEMS devices [285,613,614].

Chandross and colleagues have reported a number of MD studies of the adhesion and friction of ordered SAMS in both SFA [603] and AFM [612] geometries. A large range of conditions were studied for the SFA geometry, and stick–slip was observed in all cases. At high pressure, the friction was observed to be independent of chain length, while at low contact pressures a weak dependence of friction on shear velocity was observed. For the AFM asperity geometry, they also found relatively little dependence of the friction on the chain length. Significantly, they reported that even at low loads of about 10 nN, shearing of the tip caused damage and removal of the SAM. Their results are consistent with the recent studies reported within the context of SAMs for MEMS applications [289] (Figure 71).

Hook *et al*. reported that a SAM alone cannot prevent tribological degradation of an MEMS device [289]. The topic of mobile-adsorbed films atop a SAM layer has thus received growing attention on account of the recent success of alcohol vapor-phase lubrication to prevent failure of MEMS [285,574,575,614]. Vapor-phase lubrication had been considered one of the most likely means of lubricating MEMS devices with replenishable for close to a decade [88,89,161]. The gas-phase replenishment occurs both directly from the vapor phase, through sideways mobility of the adsorbed films, and through trapping of mobile-adsorbed phases in defects and from voids in the SAM [285,613].

Neeyakorn performed QCM measurements of the uptake and nanotribology of organophosphate (TCP and *t*-butylphenylphosphate (TBPP)) layers adsorbed from the vapor phase onto amorphous and polycrystalline silicon and octadecyltrichlorosilane (OTS)-treated silicon substrates [615]. Three to five monolayer-thick organophosphate films were observed to form readily on both silicon and OTS-treated silicon. The coatings moreover exhibited mobility in the form of

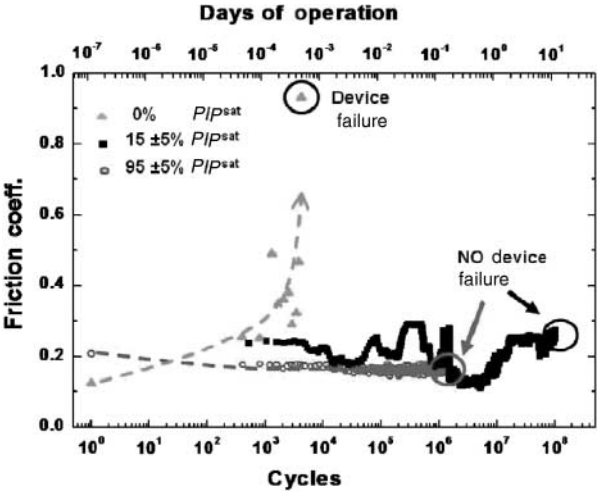

Figure 71. (color online) MEMS friction test device lifetime in partial pressures of pentanol vapor. Reprinted with permission from D.B. Asay *et al.*, Langmuir, **24**, p. 155, 2008 [574]. Copyright (2008) by American Chemical Society.

interfacial slippage or viscoelasticity in response to the oscillatory motion of the QCM, implying that enhanced tribological performance could be expected in MEMS applications. Although mobile as adsorbates, these organophosphates have yet to be proved effective on MEMS due to the difficulty of delivering them in the gas phase for room-temperature operations.

Miller and Krim subsequently reported QCM slip times for ethanol, TFE, and pentanol films adsorbed on silicon, aluminum, and perfluorodecyl-trichlorosilane (PFTS)-treated substrates [536]. The measurements yield experimental parameters that allow estimates of the spreading diffusion rates and island diffusion coefficients for these systems. The diffusion coefficients were in addition related to the ability of these materials to effectively lubricate asperity contacts through sideways replenishment of areas that have been scraped free of the adsorbed layer. Ethanol and pentanol showed particular promise as lubricants. Hook and coworkers subsequently reported that trace levels of adsorbed ethanol on actual MEMS devices resulted in unprecedented reductions in friction and wear were discovered. The devices remained operational for indefinitely long time periods in the presence of very low levels of surrounding gas and for very long residual periods after the surrounding gas was removed. The presence of a SAM enhanced this residual effect, evidently acting as a reservoir for the lubricant. The success of the lubrication was linked to atomic-scale mobility in the adsorbed layers [538,613].

4.8. *Frictional anisotropy, commensurate incommensurate, and solid–liquid transitions*

4.8.1. *Commensurate incommensurate transitions*

There has been much work done on commensurate and incommensurate frictional properties of materials, as well as on friction anisotropy. When two surfaces are commensurate, their lattices match in perfect registry. As discussed earlier in detail, it has been shown theoretically, that commensurate systems can have as much as 14 orders of magnitude higher friction than a corresponding incommensurate system. The lower friction levels for incommensurate systems are due to the random positions of atoms with respect to each other on the mismatched lattices. Interfacial forces tend to cancel in this case, resulting in very low friction.

In addition to the graphite on graphite results discussed in earlier sections [363], wide range of experiments and simulations have revealed the effect of incommensurability on friction. Fuhrmann [616] reported a study of the damping (energy relaxation) of low-frequency adsorbate vibrational modes via one-phonon emission and showed that the phononic friction vanishes for incommensurate layers sliding on solid surfaces. Hu *et al.* performed detailed atomic-scale friction studies of SAMs surfaces on Au(111) by means of MD simulations, tracking, in particular, the mechanism of energy dissipation [617]. They observed that the shear stress and chain angle on commensurate SAMs exhibit a clean periodic pattern and atomic stick–slip friction was manifested as a gradual storage and sudden release of energy. Energy was built up during the stick, followed by a sudden separation as the equilibrium becomes unstable, with most energy being dissipated at the time of slip. The simulations revealed that more energy was stored and released in commensurate sliding, thus much higher friction resulted than for incommensurate cases.

Sheehan and Lieber employed AFM to study the sliding of MoO_3 nanocrystals on single-crystal MoS_2 surfaces and reported highly anisotropic friction, and the nanocrystals would only slide along certain preferred directions of the substrate. The anisotropy was exploited to demonstrate that reversibly interlocking structures could be fabricated, and the authors argue that such devices could potentially serve as the basis for mechanical logic gates [618].

Lucas *et al.* performed a combined theoretical and experimental study of the frictional forces encountered by a nanosize tip sliding on top of a supported MWCNT along a direction parallel or transverse to the CNT axis and found a higher friction coefficient in the transverse direction compared with the parallel direction [560].

Hirano and colleagues employed STM in UHV to study the sliding of a tungsten wire tip surface on a planar silicon surface. Much like an AFM, they rastered the tungsten tip across the silicon surface, and used a displacement sensor to measure the bending of the tungsten wire caused by the friction between the two surfaces. Employing Hooke's law to extract the frictional force from the displacement of the tungsten tip, they found that the frictional force of the two surfaces in commensurate contact was 8×10^{-8} N. The friction vanished when the surfaces were in incommensurate contact, within their resolution (the resolution of their instrument was 3×10^{-9} N) [218,619]. Friction anisotropy has also been convincingly demonstrated in AFM measurements on quasicrystalline surfaces [416] (Figure 72).

Not all frictional anisotropy, however, can be related to surface commensurability. In some experiments, frictional anisotropy disappears at low loads when the surfaces are in elastic contact and is only present at high loads when the surfaces are in plastic contact. An experiment by Ko and Gellman [298,620,621] explored the friction between nickel(100) surfaces in UHV with and without adsorbed surface coatings of sulfur and ethanol. The adsorbed coatings modified the surface lattice from the bare nickel: the sulfur surface was well ordered with lattice vectors rotated 45°with respect to the bulk nickel, and the adsorbed ethanol was not ordered. The friction in this study was anisotropic and related to the bulk lattice structure of the nickel. The static friction coefficient was found to be minimized (lower by a factor of 3–4) at a bulk lattice mismatch of 45°, regardless of the modifications to the surface by monolayers of atomic sulfur and up to four monolayers of adsorbed ethanol. These results suggest that in some systems in plastic contact the frictional anisotropy is related to deformation of the bulk material and not simply incommensurability. Similar results were observed for two Pd(100) surface in contact. Friction anisotropy was reported at the macroscopic scale for two Pd(100) single-crystal surfaces sliding in an UHV environment, and systematically measured with varying levels of octane. The anisotropy persisted up to 20 monolayers of octane [622].

Slip time data for literature reports of slip times for commensurate systems are summarized in Table 19.

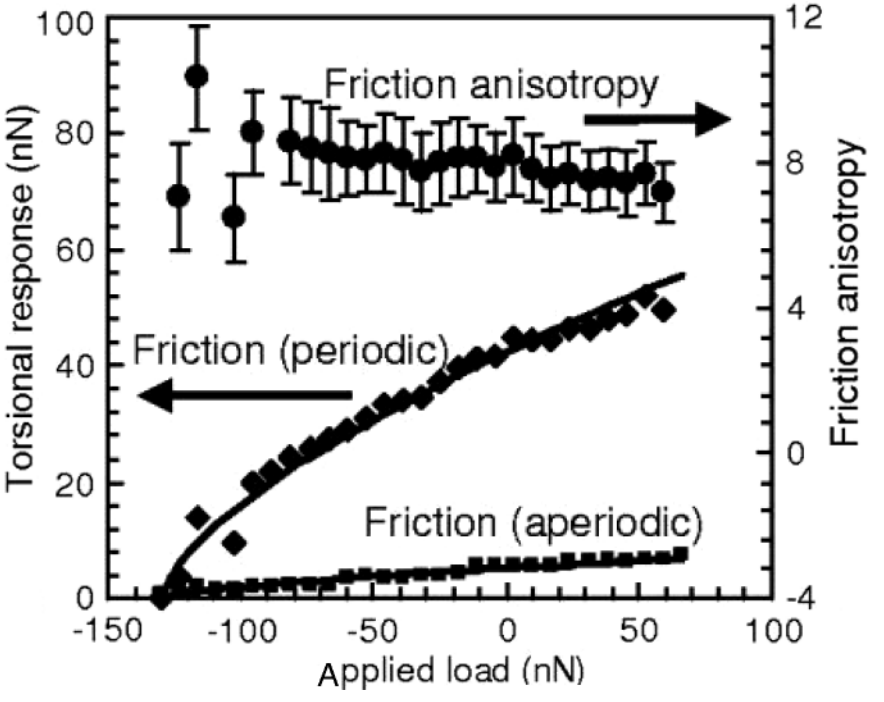

Figure 72. Results from a friction force measurement on a clean, structurally anisotropic surface of a quasicrystal. The surface is the twofold face of decagonal Al–Ni–Co, which has both periodic and quasiperiodic surface directions. The torsional response of an AFM cantilever, as a function of applied load, along these two directions is shown in the bottom two curves. The torsional response reveals that the friction force is eight times higher in the periodic direction than in the quasiperiodic direction, that is, the friction anisotropy is 8. The adhesion force is 130 nN. The lines are fits to the DMT model for contact shear stresses of 690 and 85 MPa. The AFM tip is modified with an alkanethiol layer to prevent irreversible adhesion. Reprinted figure with permission from J.Y. Park *et al.*, Physical Review B 74, p. 024203, 2006 [416]. Copyright (2006) by the American Physical Society.

Table 19. QCM slip time data for structural transitions in solid films.

					τ (ns)		
Adsorbate	Substrate	Substrate type	T (K)	Reference	$\Theta = 0.2$	$\Theta = 0.5$	$\Theta = 1$ (solid)
Kr (krypton)	Graphite	Terraced	85.8	[476]		0&60(C)	10(IC)
Kr (krypton)	Graphite	Terraced	85.8	[476]		0&60(C)	0&60(C)
Ne (neon)	Pb(111)	Terraced	5.4	[182]	0(C)	0(C)	
Ne (neon)	Pb(111)	Terraced	6.5	[182]	0(IC)	0.08(IC)	0.3(IC)
Xe (xenon)	Cu(111)	Textured	77.4	[356]			15.5(C)

Note: C, commensurate; IC, incommensurate.

It is immediately apparent that not all commensurate adsorbed layers are pinned, with 0 slip time, and commensurate films that do slide can have low friction. In the case of Kr/graphite, the friction while sliding is lower than reported for the incommensurate layers. The result is consistent with Cieplak [35] for low surface corrugation systems. It should be noted, however,

Table 20. Slip time data for solid and liquid Krypton monolayers.

Preplate	Substrate	Substrate type	T (K)	Reference	τ_l (ns): liquid	τ_s (ns): solid	τ_s/τ_l
	Au	Amorphous	77.4	[404]	4	50	12.5
	Ag(111)	(111) textured	77.4	[355]	2.1	2.7	1.29
C60 fixed bilayer	Ag(111)	(111) textured	77.4	[355]	3.1	3.3	1.06
C60 fixed monolayer	Ag(111)	(111) textured	77.4	[355]	1.6	2.7	1.69
	Au(111)	(111) textured	77.4	[355]	1	5	5.0
	Au(111)	(111) textured	77.4	[33,34]	2	10	5.0
	Cu(111)	(111) textured	77.4	[355]	7	11	1.6
	Ni(111)	(111) textured	77.4	[355]	0.26	0.78	3.0

that commensurate layers are more likely to be pinned, as in the case of Ne/Pb. The fact that friction anisotropy is exceptionally widespread in alternative geometries is likely related to the fact that confined systems or bulk systems pressed together into contact are more sensitive to surface corrugation effects: adsorbed layers have in principle the option of out-of-plane motion that allows sliding when otherwise might be inhibited.

4.8.2. *Liquid–solid monolayer phase transitions*

Slip time data for literature reports of slip times for literature reports of liquid to solid phase transitions are summarized in Table 20. To date, all have been performed on Kr monolayers sliding on metal or C60 surfaces at 77.4 K. The solid phase exhibits lower friction, a fact explained well by the numerical simulations of Robbins and coworkers [35,451], by noting that liquid monolayers are more deformable, and thus are "more commensurate" than their solid counterparts. The modeling results also showed that the decrease in friction was about a factor of 5 upon solidification [35], but if electronic friction was present, the increase would be less. Inspection of Table 20 shows the increase to range between a factor of 1 and 5 for (111) substrates. The conclusions of this result remain unclear, however, with respect to electronic effects in these systems [355].

4.9. ***Preplated systems***

Slip time data for surfaces preplated with monolayers of a pinned material are listed in Table 21.

Slip time data for the second layer of helium sliding on the first layer is also included for comparison [486].

The first of such studies occurred in 1994, when Krim and coworkers Mak [511] employed QCM to measure characteristic slip times for ethane and ethylene monolayers adsorbed on silver and chemisorbed oxygen/silver surfaces. They reported no slippage whatsoever of the oxygen layer itself upon the Ag(111) substrates. The systems had been suggested as model systems for studies of the relative contributions of electronic and phonon processes towards frictional energy losses. Slip times for the chemisorbed oxygen/silver surfaces were observed to be longer than those for silver. Based on this observation, it was argued that electronic contributions to friction should be considered whenever conducting surfaces are involved and were likely to be lower when oxide films were present. Similar studies were performed by a group of Perry and coworkers, by using AFM, who arrived at similar conclusions [512].

It has since become apparent, however, that slip times on preplated substrates are virtually always significantly longer than on bare substrates [87,473,486,491,511], with the exception of highly corrugated preplate materials such as OTS [615] or C60 [355,356]. Alternative explanations

Table 21. Slip time data for preplated substrates.

Adsorbate	Preplate	Substrate	Technique	T (K)	Reference	τ (ns) $\Theta = 0.2$	$\Theta = 0.5$	$\Theta = 1$ (liquid)	$\Theta = 1$ (solid)	$\Theta = 2$
Ne (neon)	1–3 Xe monolayers	Pb(111)	QCM	6.5	[491]	1	5		8	
Ne (neon)	1–4 Kr monolayers	Pb(111)	QCM	6.5	[491]	0	1		7	
Ne (neon)		Pb(111)	QCM	6.5	[491]	0	1		3	
Ar (argon)	Xe bilayer	Ag(111)	QCM	77.4	[87,473]			4		
Ar (argon)	Xe monolayer	Ag(111)	QCM	77.4	[87,473]			4		
Ar (argon)		Ag(111)	QCM	77.4	[87,473]			1.5		
C_7H_8 (toluene)	C60 rotating bilayer	Ag(111)	QCM	300	[537]			0.1		5
C_7H_8 (toluene)		Ag(111)	QCM	300	[537]			10		15
Kr (krypton)	C60 fixed bilayer	Ag(111)	QCM	77.4	[355]			3.1	3.3	
Kr (krypton)	C60 monolayer	Ag(111)	QCM	77.4	[355]			1.6	2.7	
Kr (krypton)		Ag(111)	QCM	77.4	[355]			2.1	2.7	
^{4}He(helium)		Graphite	QCM	0.45	[486]				20	7,80
^{4}He(helium)		Graphite	QCM	1.0	[486]				20	8,80
^{4}He(helium)		Graphite	QCM	1.25	[486]				20	8.5,70
^{4}He(helium)		Graphite	QCM	1.5	[486]					9,60
C_2H_4 (ethylene)	Oxygen	Ag(111)	QCM	77.4	[511]		26	16		
C_2H_4 (ethylene)		Ag(111)	QCM	77.4	[511]		15	5		
C_2H_6 (ethane)	Oxygen	Ag(111)	QCM	77.4	[511]		30	18		
C_2H_6 (ethane)		Ag(111)	QCM	77.4	[511]		15	9		
O_2 (oxygen)		Ag(111)	QCM	300	[511]	0	0		0	0

include changes in the potential corrugation levels [491], as well as passivation of surface defects and step edges in the first layers. Electronic effects should be reduced in the second layer, since it is farther from the substrate. However, the presence of the second layer can also press the first layer closer to the substrate, which would increase the electronic contributions to friction [117]. Altogether, the preplating effect of reducing friction is a very robust result, and likely the combination of all of the aforementioned effects acting in unison.

4.10. *Comparison of electronic and total slip time values*

Slip time data for systems where both the total friction and electronic component have been reported are summarized in Table 22. Slip times followed by (E) denote electronic contributions only. Electronic contributions have been determined theoretically, via resistivity measurements, or by the change in the slip time at the superconducting transition, in the case of Pb(111). Given that the relation between the total friction and the electronic and phononic contributions is written as Equation (62), $\eta = \eta_e + \eta_p$ where $\eta = \tau^{-1}$, the electronic slip time must be greater than the total slip time if the two values are consistent. Inspection of the data in the table reveals that inconsistencies are present for the cases of water, ethylene, and ethane. These data, along with work by the group of Tobin and coworkers, reveal that further refinements in the theory of how resistivity measurements relate to sliding friction are required.

Table 22. QCM slip time data for total friction compared to estimates of electronic friction.

					τ (ns)		
Adsorbate	Substrate	Technique	T (K)	Reference	$\Theta = 0.5$	$\Theta = 1$ (liquid)	$\Theta = 1$ (solid)
C_2H_{12}(cyclohexane)	Ag(111)	QCM	300	[508]	0	2	
C_2H_{12}(cyclohexane)	Ag(111)	Resistivity		[447]	1.7(E)		
C_2H_4(ethylene)	Ag(111)	QCM	77.4	[511]	15	5	
C_2H_4(ethylene)	Ag(111)	Resistivity	50	[447]	0.72(E)		
C_2H_6(ethane)	Ag(111)	QCM	77.4	[511]	15	9	
C_2H_6(ethane)	Ag(111)	Resistivity	50	[447]	3.6(E)		
H_2O (water)	Ag(111)	QCM	300	[508]	3	4	
H_2O (water)	Ag(111)	Resistivity	300	[87,473]	0.1(E)		
N_2(nitrogen)	Pb(111)	QCM	7.2n	[420]			19
N_2(nitrogen)	Pb(111)	Theory		[115,323]			2–20(E)
N_2(nitrogen)	Pb(111)	QCM	7.2	[420]			36(E)
Xe (xenon)	Ag(111)	QCM	77.4	[353]	1.2		1.1
Xe (xenon)	Ag(111)	Theory		[115,323]			200(E)
Xe (xenon)	Ag(111)	QCM	77.4	[356]			>12.5(E)
Xe (xenon)	Ag(111)	Resistivity	77.4	[164]	3.3(E)		4(E)
Xe (xenon)	Ag(111)	Resistivity	10	[447]	3(E)		

Acknowledgements

This work was supported in part by NSF DMR #DMR0805204 and the Extreme Friction MURI program, AFOSR Grant No. FA9550-04-1-0381. J. Pike and H. Kancharlapalli are acknowledged for aid in manuscript preparation. Numerous authors are heartily thanked for contributing figures and captions, including J.L. Barratt, D. Brenner, L.W. Bruch, M. W. Cole, M.T. Dugger, J.A. Harrison, K. Leicthi, E. Reido M.O. Robbins, M. Salmeron, Seong Kim, P. Taborek, P. Thiel and E. Tosatti.

References

[1] H.P. Jost, *Tribology: Origin and future*, Wear 136(1) (1990), pp. 1–17.
[2] V. Panella, R. Chiarello, and J. Krim, *Adequacy of the Lifshitz theory for certain thin absorbed films*, Phys. Rev. Lett. 76(19) (1996), pp. 3606–3609.
[3] K.C. Ludema, *Friction, Wear, Lubrication: A Textbook in Tribology*, CRC Press, Boca Raton, FL, 1996.
[4] B.N.J. Persson, *Sliding Friction: Physical Principles and Applications*, 2nd ed., Springer, Berlin, 2000.
[5] C.M. Mate, *Tribology on the Small Scale: A Bottom Up Approach to Friction, Lubrication, and Wear*, Oxford University Press, Oxford, 2007.
[6] V.L. Popov, *The Prandtl–Tomilson Model for Dry Friction in Contact Mechanics and Friction*, Springer, Berlin, Heidelberg, 2010.
[7] D. Dowson, *History of Tribology*, Longman, London, 1979.
[8] M.D. Drory and M.O. Robbins (eds.), *Tribology on the 300th Anniversary of Amontons' Law*, MRS, Warrendale, 1999.
[9] J. Heyman, *Coulomb's Memoir on Statics: An Essay in the History of Civil Engineering*, Bilingual edition, World Scientific, Singapore, 1998.
[10] T.E. Madey, *Early applications of vacuum, from Aristotle to Langmuir*, J. Vac. Sci. Tech. A 2 (1984), pp. 110–117.
[11] T.E. Madey and W.C. Brown (eds.), *Otto von Guericke's account of the Magdeburg hemispheres experiment*, in *History of Vacuum Science and Technology*, R. Sherman, trans., American Institute of Physics, New York, 1984.

[12] G.M. McClelland and J.N. Glosli, *Friction at the Atomic Scale*, in *Fundamentals of Friction: Macroscopic and Microscopic Processes*, I.L. Singer and H.M. Pollack, eds., Kluwer Academic Publishers, Dordrecht, the Netherlands, 1992, p. 405.
[13] D.H. Buckley, *Surface Effects in Adhesion, Friction, Wear and Lubrication*, Elsevier, Amsterdam, the Netherlands, 1981.
[14] J. Krim, *Surface science and the atomic-scale origins of friction: What once was old is new again*, Surf. Sci. 500 (2002), pp. 741–758.
[15] L.A. Harris, *Analysis of materials by electron-excited Auger electrons*, J. Appl. Phys. 39(3) (1968), pp. 1419–1427.
[16] F. Hofmann and J.P. Toennies, *High-resolution helium atom time-of-flight spectroscopy of low-frequency vibrations of adsorbates*, Chem. Rev. 96(4) (1996), pp. 1307–1326.
[17] P.W. Palmberg and W.T. Peria, *Low energy electron diffraction studies on Ge and Na-covered Ge*, Surf. Sci. 6(1) (1967), pp. 57–97.
[18] R.E. Weber and W.T. Peria, *Use of LEED apparatus for detection and identification of surface contaminants*, J. Appl. Phys. 38(11) (1967), pp. 4355–4358.
[19] D. Tabor and R.H.S. Winterton, *Surface forces: Direct measurement of normal and retarded van der Waals forces*, Nature 219 (1968), pp. 1120–1121.
[20] J.N. Israelachvili, Y. Min, M. Akbulut, A. Alig, G. Carver, W. Greene, K. Kristiansen, E. Meyer, N. Pesika, K. Rosenberg, and H. Zeng, *Recent advances in the surface forces apparatus (SFA) technique*, Rep. Prog. Phys. 73(2010), art#036601.
[21] J.N. Israelachvili, *Thin-film studies using multiple-beam interferometry*, J. Colloid Interface Sci. 44(2) (1973), pp. 259–272.
[22] H. Yoshizawa, Y.-L. Chen, and J. Israelachvili, *Fundamental mechanisms of interfacial friction. 1. Relation between adhesion and friction*, J. Phys. Chem. 97 (1993), pp. 4128–4140.
[23] J.N. Israelachvili and D. Tabor, *Shear properties of molecular films*, Nat. Phys. Sci. 241 (1973), pp. 148–149.
[24] H. Yoshizawa, Y.L. Chen, and J.N. Israelachvili, *Recent advances in molecular understanding of adhesion, friction and lubrication*, Wear 168(1–2) (1993), pp. 161–166.
[25] H. Yoshizawa and J. Israelachvili, *Fundamental mechanisms of interfacial friction. 2. Stick–slip friction of spherical and chain molecules*, J. Phys. Chem. 97 (1993b), pp. 11300–11313.
[26] A.M. Homola, J.N. Israelachvili, P.M. McGuiggan, and M.L. Gee, *Fundamental experimental studies in tribology – The transition from interfacial friction of undamaged molecular smooth surfaces to normal friction with wear*, Wear 136(1) (1990), pp. 65–83.
[27] S. Kopta and M. Salmeron, *The atomic scale origin of wear on mica and its contribution to friction*, J. Chern. Phys. 113(18) (2000), pp. 8249–8252.
[28] L. Prandtl, *Ein Gedanken Modell zur kluctishen Theorie fester Korper* [*A Conceptual Model to the Kinetic Theoy of Solid Bodies*], Z. Angew. Math. Mech. 8 (1928), p. 85; see English translation in [29].
[29] V.L. Popov and J.A.T. Gray, *Prandtl–Tomlinson model: History and applications in friction, plasticity, and nanotechnologies*, Z. Angew. Math. Mech. (2012), DOI 10.1002/zamm.201200097.
[30] G.A. Tomlinson, *A molecular theory of friction*, Philos. Mag. 7(7) (1929), pp. 905–939.
[31] D. Tabor, *Tribology – The last 25 years – A personal view*, Tribol. Int. 28(1) (1995), pp. 7–10.
[32] C.M. Mate, G.M. McClelland, R. Erlandsson, and S. Chang, *Atomic-scale friction of a tungsten tip on a graphite surface*, Phys. Rev. Lett. 59(17) (1987), pp. 1942–1945.
[33] J. Krim and R. Chiarello, *Sliding friction measurements of molecularly thin films*, J. Vac. Sci. Technol. A 9 (1991), pp. 2566–2569.
[34] J. Krim, D.H. Solina, and R. Chiarello, *Nanotribology of a Kr monolayer: A quartz crystal microbalance study of atomic-scale friction*, Phys. Rev. Lett. 66 (1991), pp. 181–184.
[35] M. Cieplak, E.D. Smith, and M.O. Robbins, *Molecular origins of friction: The force on adsorbed layers*, Science 265(5176) (1994), pp. 1209–1212.
[36] R.J. Cannara, M.J. Brukman, K. Cimatu, A.V. Sumant, S. Baldelli, and R.W. Carpick, *Nanoscale friction varied by isotopic shifting of surface vibrational frequencies*, Science 318(5851) (2007), pp. 780–783.

[37] Y. Mo, M.H. Muser, and I. Szlufarska, *Origin of the isotope effect on solid friction*, Phys. Rev. B 80 (2009), art#155438.
[38] J. Krim, *Atomic-scale origins of friction*, Langmuir 12 (1996), pp. 4564–4566.
[39] J. Krim, *Friction at the atomic scale*, Sci. Am. 275 (1996), pp. 74–80.
[40] L.L. Singer and H.M. Pollock, *Adhesion, friction and lubrication of molecularly smooth surfaces*, in *Fundamentals of Friction*, J.N. Israelachvili, ed., Kluwer Academic Publishers, Dordrecht, the Netherlands, 1992, pp. 351–385.
[41] L.L. Singer and H.M. Pollack (eds.), *Fundamentals of Friction: Macroscopic and Microscopic Processes*, Kluwer Academic Publishers, Dordrecht, the Netherlands, 1992.
[42] R. Superfine, Private communication, 2001.
[43] M.R. Falvo, J. Steele, R.M. Taylor, and R. Superfine, *Gearlike rolling motion mediated by commensurate contact: Carbon nanotubes on HOPG*, Phys. Rev. B 62(16) (2000), pp. R10665–R10667.
[44] M.R. Falvo, R.M. Taylor II, A. Helser, V. Chi, F.P. Brooks Jr., S. Washburn, and R. Superfine, *Nanometer-scale rolling and sliding of carbon nanotubes*, Nature (London) 397(6716) (1999), pp. 236–238.
[45] A. Buldum and J.P. Lu, *Atomic scale sliding and rolling of carbon nanotubes*, Phys. Rev. Lett. 83 (1999), pp. 5050–5053.
[46] J.D. Schall and D.W. Brenner, *Molecular dynamics simulations of carbon nanotube rolling and sliding on graphite*, Mol. Simul. 25 (2000), pp. 73–79.
[47] M. Porto, M. Urbakh, and J. Klafter, *Atomic scale engines: Cars and wheels*, Phys. Rev. Lett. 84(26) (2000), pp. 6058–6061.
[48] M. Porto, M. Urbakh, and J. Klafter, *Molecular motor that never steps backwards*, Phys. Rev. Lett. 84(26) (2000), pp. 6058–6061.
[49] M. Porto, M. Urbakh, and J. Klafter, *Motors on the molecular scale*, J. Lumin. 94 (2001), pp. 137–142.
[50] D. Fleishman, J. Klafter, M. Porto, and M. Urbakh, *Mesoscale engines by nonlinear friction*, Nano Lett. 7(3) (2007), pp. 837–842.
[51] Y.T. Yang, C. Callegari, X.L. Feng, and M.L. Roukes, *Surface adsorbate fluctuations and noise in nanoelectromechanical systems*, Nano Lett. 11(4) (2011), pp. 1753–1759.
[52] R.D. Astumian and M. Bier, *Fluctuation driven ratchets: Molecular motors*, Phys. Rev. Lett. 72 (1994), pp. 1766–1769.
[53] P. Reimann, *Brownian motors: Noisy transport far from equilibrium*, Phys. Rep. 361 (2002), pp. 57–265.
[54] D. Wu, S. Zhu, and X. Luo, *Coupled Brownian motors with two different kinds of time delays*, Phys. Stat. Mech. Appl. 391(4) (2012), pp. 1032–1037.
[55] M.H. Muser, M. Urbakh, and M.O. Robbins, *Statistical mechanics of static and low-velocity kinetic friction*, Adv. Chem. Phys. 126 (2003), pp. 187–272.
[56] B.Y. Derjaguin, Y.M. Muller, and Yu.P. Toporov, *Effect of contact deformations on the adhesion of particles*, J. Colloid Interface Sci. 53(2) (1975), pp. 314–326.
[57] M.H. Muser, L. Wenning, and M.O. Robbins, *Simple microscopic theory of Amontons' laws for static friction*, Phys. Rev. Lett. 86(7) (2001), pp. 1295–1298.
[58] S. Akarapu, T. Sharp, and M.O. Robbins, *Stiffness of contacts between rough surfaces*, Phys. Rev. Lett. 106(20) (2011), art#204301.
[59] M.H. Muser, *Structural lubricity: Role of dimension and symmetry*, Europhys. Lett. 66 (2004), pp. 97–103.
[60] M.H. Muser and M.O. Robbins, *Atomistic computer simulations of friction between solids*, in *Springer Handbook of Nanotechnology*, B. Bhushan, ed., Springer, Berlin, 2004, pp. 717–738.
[61] M. Reguzzoni and M.C. Righi, *Size dependence of static friction between clusters and adsorbates*, Phys. Rev. B 85 (2012), art#201412.
[62] S.H.J. Idziak, C.R. Safinya, R.S. Hill, K.E. Kraiser, M. Ruths, H.E. Warriner, S. Steinberg, K.S. Liang, and J.N. Israelachvili, *The X-ray surface forces apparatus: Structure of a thin smectic liquid crystal film under confinement*, Science 264 (1994), pp. 1915–1918.

[63] B. Borovsky, B.L. Mason, and J. Krim, *Scanning tunneling microscope measurements of the amplitude of vibration of a quartz crystal oscillator*, J. Appl. Phys. 88(7) (2000), pp. 4017–4021.
[64] I.B. Altfeder and J. Krim, *Temperature dependence of nanoscale friction for Fe on YBCO*, J. Appl. Phys. 111(2012), art#094916.
[65] Y.J. Chabal, P. Dumas, M.K. Weldon, and G.P. Williams, *Molecules at surfaces and interfaces studied using vibrational spectroscopies and related techniques*, Surf. Rev. Lett. 6(2) (1999), pp. 225–255.
[66] R.G. Tobin, *Mechanisms of adsorbate-induced surface resistivity – Experimental and theoretical developments*, Surf. Sci. 502 (2002), pp. 374–387.
[67] J.V. Barth, *Transport of adsorbates at metal surfaces: From thermal migration to hot precursors*, Surf. Sci. Rep. 40(3–5) (2000), pp. 75–149.
[68] J. Krim, *Friction at macroscopic and microscopic length scales*, Am. J. Phys. 70 (2002), pp. 890–897 [Resource Letter].
[69] O.M. Braun and A.G. Naumovets, *Nanotribology: Microscopic mechanisms of friction*, Surf. Sci. Rep. 60(6–7) (2006), pp. 79–158.
[70] G.V. Dedkov, *Experimental and theoretical aspects of modern nanotribology*, Phys. Stat. Sol. A 179(1) (2000), pp. 3–75.
[71] L.W. Bruch, R.D. Diehl, and J.A. Venables, *Progress in the measurement and modeling of physisorbed layers*, Rev. Mod. Phys. 79 (2007), pp. 1381–1454.
[72] H.K. Christenson, *Confinement effects on freezing and melting*, J. Phys. Condens. Matter 13 (2001), pp. R95–R133.
[73] E. Kumacheva, *Interfacial friction measurement in surface force apparatus*, Prog. Surf. Sci. 58(2) (1998), pp. 75–120.
[74] M.K. Chaudhury, *Adhesion and friction of self-assembled organic monolayers*, Curr. Opin. Colloid Interface Sci. 2 (1997), pp. 65–69.
[75] F. Schreiber, *Structure and growth of self-assembling monolayers*, Prog. Surf. Sci. 65 (2000), pp. 151–256.
[76] I. Szlufarska, M. Chandross, and R.W. Carpick, *Recent advances in single-asperity nanotribology*, J. Phys. D: Appl. Phys. 41(12) (2008), art#123001.
[77] R.W. Carpick, D.F. Ogletree, and M. Salmeron, *Lateral stiffness: A new nanomechanical measurement for the determination of shear strengths with friction force microscopy*, Appl. Phys. Lett. 70(12) (1997), pp. 1548–1550.
[78] R.W. Carpick and M. Salmeron, *Scratching the surface: Fundamental investigations of tribology with atomic force microscopy*, Chem. Rev. 97(4) (1997), pp. 1163–1194.
[79] J.Y. Park and P. Thiel, *Atomic scale friction and adhesion properties of quasicrystal surfaces*, J. Phys.: Condens. Matt. 20(31) (2008), art#314012.
[80] D. Johannsmann, *Viscoelastic, mechanical, and dielectric measurements on complex samples with the quartz crystal microbalance*, Phys. Chem. Chem. Phys. 10(31) (2008), pp. 4516–4534.
[81] L.D. Marks, O.L. Warren, A.M. Minor, and A.P. Merkle, *Tribology in full view*, MRS Bull. 33(12) (2008), pp. 1168–1173.
[82] E. Lauga, M.P. Brenner, and H.A. Stone, *Micro?uidics: The no-slip boundary condition*, in *Handbook of Experimental Fluid Dynamics*, J. Foss, C. Tropea and A. Yarin, eds., Springer, New York, 2007.
[83] J.S. Ellis and M. Thompson, *Slip and coupling phenomena at the liquid–solid interface*, Phys. Chem. Chem. Phys. 6(21) (2004), pp. 4928–4938.
[84] L. Bocquet and E. Charlaix, *Nanofluidics, from bulk to interfaces*, Chem. Soc. Rev. 39 (2010), pp. 1073–1095.
[85] E. Bonaccurso, H.J. Butt, V.S.J. Craig, D.R. Evans, and C. Neto, *Boundary slip in Newtonian liquids: A review of experimental studies*, Rep. Progr. Phys. 68(12) (2005), pp. 2859–2897.
[86] B. Bhushan, J.N. Israelachvili, and U. Landman, *Nanotribology: Friction, wear and lubrication at the atomic scale*, Nature 374 (1995), pp. 607–616.
[87] J. Krim, *Progress in nanotribology: Experimental probes of atomic scale friction*, Comm. Condens. Matter Phys. 17 (1995), pp. 263–280.
[88] J. Krim (guest ed.), *Fundamentals of friction*, MRS Bull. 23(6) (1998), pp. 20–51.

[89] J. Krim and M. Abdelmaksoud, *Nanotribology of vapor-phase lubricants*, in *Tribology Issues and Opportunities in MEMS*, B. Bhushan, ed., Kluwer Academic Publishers, Dordrecht, the Netherlands, 1998, pp. 273–284.
[90] G. Hahner and N. Spencer, *Rubbing and scrubbing*, Phys. Today 51 (1998), pp. 22–27.
[91] S. Granick, *Soft matter in a tight spot*, Phys. Today 52(7) (1999), pp. 26–31.
[92] S. Granick, Y.X. Zhu, and H. Lee, *Slippery questions about complex fluids flowing past solids*, Nat. Mater. 2 (2003), pp. 221–227.
[93] S.S. Perry (guest ed.), *Progress in the pursuit of the fundamentals of tribology*, Tribol. Lett. 10(1–2) (2001), pp. 1–132.
[94] S.S. Perry, S. Lee, Y.S. Shon, R. Colorado, and T.R. Lee, *The relationships between interfacial friction and the conformational order of organic thin films*, Tribol. Lett. 10 (2001), pp. 81–87.
[95] S.S. Perry and W.T. Tysoe, *Frontiers of fundamental tribological research*, Tribol. Lett. 19(3) (2005), pp. 151–161.
[96] M. Urbakh and E. Meyer, *Nanotribology: The renaissance of friction*, Nat. Mater. 9 (2010), pp. 8–10.
[97] W.N. Unertl and M. Grunze, *Physical and chemical mechanisms of tribology*, Langmuir 12(19) (1996), pp. 4481–4610.
[98] J.N. Israelachvili, *Intermolecular and Surface Forces*, 3rd revised ed., Academic Press, New York, 2011.
[99] A.P. Graham and J.P. Toennies, *Determination of the lateral potential energy surface of single adsorbed atoms and molecules on single crystal surfaces using helium atom scattering*, Surf. Sci. 427–428 (1999), pp. 1–10.
[100] C. Woll, *Low energy vibrations of molecular species adsorbed on metal surfaces*, in *Physics of Sliding Friction*, B.N.J. Persson and E. Tosatti, eds., Kluwer Academic Publishers, Dordrecht, the Netherlands, 1996, 231 pp.
[101] G. Witte, *Low frequency vibrational modes of adsorbates*, Surf. Sci. 502 (2002), pp. 405–416.
[102] J. Braun, D. Fuhrmann, A. Siber, B. Gumhalter, and C. Woll, *Observation of a zone-center gap in the longitudinal mode of an adsorbate overlayer: Xenon on Cu(111)*, Phys. Rev. Lett. 80(1) (1998), pp. 125–128.
[103] L.W. Bruch, M.W. Cole, and E. Zaremba, *Physical Adsorption: Forces and Phenomenon*, Oxford University Press, Oxford, UK, 1997. Corrected and reprinted by Dover Publications, Mineola, NY, 2007.
[104] L.W. Bruch and F.Y. Hansen, *Mode damping in a commensurate monolayer solid*, Phys. Rev. B 55(3) (1997), pp. 1782–1792.
[105] W. Press, *Single Particle Rotations in Molecular Crystals*, Springer, Heidelberg, 1981.
[106] F.Y. Hansen, V.L.P. Frank, H. Taub, L.W. Bruch, H.J. Lauter, and J.R. Dennison, *Corrugation in the nitrogen–graphite potential probed by inelastic neutron scattering*, Phys. Rev. Lett. 64 (1990), pp. 764–767.
[107] A.M. Lahee, J.P. Toennies, and C. Woll, *Low energy adsorbate vibrational modes observed with inelastic helium atom scattering*, Surf. Sci. 177 (1986), pp. 371–388.
[108] J.P. Toennies, in *Surface Phonons*, W. Kress and F. de Wette, eds., Springer Series in Surface Science 21, Springer, Heidelberg, 1991.
[109] B. Voigtlander, D. Bruchmann, S. Lehwald, and H. Ibach, *Structure and adsorbate–adsorbate interactions of the compressed Ni(100)-(2*1) CO structure*, Surf. Sci. 225 (1990), pp. 151–161.
[110] C.J. Hirschmugl, G.P. Williams, F.M. Hoffmann, and Y.J. Chabal, *Adsorbate–substrate resonant interactions observed for CO on Cu(100) in the far infrared*, Phys. Rev. Lett. 65 (1990), pp. 480–483.
[111] A.P. Graham, W. Silvestri, and J.P. Toennies, in *Surface Diffusion: Atomistic and Collective Processes*, M.C. Tringides, ed., Plenum Press, New York, 1997, 565 pp.
[112] J.W.M. Frenken and B.J. Hinch, in *Helium Atom Scattering from Surfaces*, E. Hulpke, ed., Springer, Berlin, 1992, 287 pp.
[113] F. Hofmann, W. Schöllkopf, and J.P. Toennies, in *Chemical dynamics of transient species*, Proceedings of the 38th Welch Foundation Symposium, 1994, 197 pp.

[114] A.C. Levi, R. Spadacini, and G.E. Tommei, *Quantum-theory of atom surface scattering – Incommensurate and fluid adsorbates*, Surf. Sci. 121(3) (1982), pp. 504–518.
[115] L.W. Bruch, A.P. Graham, and J.P. Toennies, *The dispersion curves of the three phonon modes of xenon, krypton, and argon monolayers on the Pt(111) surface*, J. Chem. Phys. 112(7) (2000), pp. 3314–3332.
[116] W.A. Steele, *Physical interaction of gases with crystalline solids. 1. Gas–solid energies and properties of isolated adsorbed atoms*, Surf. Sci. 36(1) (1973), pp. 317–352.
[117] B.N.J. Persson and A. Nitzan, *Linear sliding friction: On the origin of the microscopic friction for Xe on silver*, Surf. Sci. 367(3) (1996), pp. 261–275.
[118] B.N.J. Persson and E. Tosatti (eds.), *Physics of Sliding Friction*, Kluwer Academic Publishers, Dordrecht, the Netherlands, 1996.
[119] M. Persson, *Possible electronic mechanism behind nanotribology of a rare gas monolayer*, Solid State Commun. 80 (1991), pp. 917–918.
[120] D. Schumacher, *Surface Scattering Experiments with Conduction Electrons*, Springer Tracts Modern Physics, Springer, Berlin, Sections 4.2–4.3, 1993.
[121] C.L. Hsu, E.F. McCullen, and R.G. Tobin, *Evidence for an adsorbate-dependent mechanism for surface resistivity: Formic acid, oxygen and CO on Cu(100)*, Chem. Phys. Lett. 316(5–6) (2000), pp. 336–342.
[122] A. Einstein, *The theory of the Brownian Motion*, Ann. der Physik 19(2) (1906), pp. 371–381.
[123] S. Pisov, E. Tosatti, U. Tartaglino, and A. Vanossi, *Gold clusters sliding on graphite: A possible quartz crystal microbalance experiment?* J. Phys. Condens. Matter 19 (2007), art#303015.
[124] D. Tabor, *Gases*, *Liquids and Solids and Other States of Matter*, Cambridge University Press, Cambridge, 1991.
[125] R. Guerra, U. Tartaglino, A. Vanossi, and E. Tosatti, *Ballistic nanofriction*, Nat. Mater. 9 (2010), pp. 634–637.
[126] A. Widom, and J. Krim, *Spreading diffusion and its relation to sliding friction in molecularly thin adsorbed films*, Phys. Rev. B 49 (1994), pp. 4154–4156.
[127] A.P. Jardine, J. Ellis, and W. Allison, *Quasi-elastic helium-atom scattering from surfaces: Experiment and interpretation*, J. Phys.: Condens. Matter 14 (2002), pp. 6173–6190.
[128] H. Hedgeland, P. Fouquet, A.P. Jardine, G. Alexandrowicz, W. Allison, and J. Ellis, *Measurement of single-molecule frictional dissipation in a prototypical nanoscale system*, Nat. Phys. 5 (2009), pp. 561–564.
[129] R. Gomer, *Diffusion of adsorbates at metal surfaces*, Rep. Progr. Phys. 53 (1990), pp. 917–1002.
[130] E.W. Muller, *Das Feldionenmikroskop*, Z. Phys. 131(1) (1951), pp. 136–142.
[131] G. Ehrlich and F.G. Hudda, *Atomic view of surface self-diffusion – Tungsten on tungsten*, J. Chem. Phys. 44(3) (1966), pp. 1039–1049.
[132] D.W. Bassett, *Surface Mobilities on Solid Materials*, V.T. Binh, ed., Plenum Press, New York, 1983, 63 pp.
[133] G. Ehrlich, *Diffusion of individual adatoms*, Surf. Sci. 299(1–3) (1994), pp. 628–642.
[134] R. Viswanathan, D.R. Burgess, P.C. Stair, E. Weitz, *Laser flash description of CO from clean copper surfaces*, J. Vac. Sci. Technol. 20(3) (1982), pp. 605–606.
[135] E.G. Seebauer and L.D. Schmidt, *Surface-diffusion of hydrogen on Pt(111) – laser-induced thermal-desorption studies*, Chem. Phys. Lett. 123(102) (1986), pp. 129–133.
[136] S.M. George, A.M. Desantolo, and R.B. Hall, *Surface-diffusion of hydrogen on Ni(100) studied using laser-induced thermal-desorption*, Surf. Sci. 159(1) (1985), pp. L425–L432.
[137] G. Binnig, C.F. Quate, and C.H. Gerber, *Atomic force microscope*, Phys. Rev. Lett. 56(9) (1986), pp. 930–933.
[138] G. Binnig, H. Fuchs, and E. Stoll, *Surface-diffusion of oxygen-atoms individually observed by STM*, Surf. Sci. 169(2–3) (1986), pp. L295–L300.
[139] M.C. Tringides, M. Gupalo, Q. Li, and X. Wang, *Equilibrium versus non-equilibrium surface diffusion measurements* in *Anomalous Diffusion, from Basis to Applications*, A. Pekalski, and K. Sznajd-Weron, eds., Springer, Berlin, 1999, 389 pp.
[140] R.C.L. Bosworth, *The mobility of potassium on tungsten*, Proc. R. Soc. A 154(A881) (1936), pp. 112–123.

[141] A. Lee, X.D. Zhu, A. Wong, L. Deng, and U. Linke, *Observation of diffusion of H and D on Ni(111) from over-barrier hopping to nonactivated tunneling*, Phys. Rev. B 48(15) (1993), pp. 11256–11259.
[142] A. Wong, A. Lee, and X.D. Zhu, *Coverage dependence of quantum tunneling diffusion of hydrogen and deuterium on Ni(111)*, Phys. Rev. B 51(7) (1995), pp. 4418–4425.
[143] X.D. Zhu and G.X. Gao, *Surface Diffusion: Atomistic and Collective Processes*, M.C. Tringides, ed., Plenum Press, New York, 1997, 607 pp.
[144] G.X. Cao, E. Nabighian, and X.D. Zhu, *Diffusion of hydrogen on Ni(111) over a wide range of temperature: Exploring quantum diffusion on metals*, Phys. Rev. Lett. 79(19) (1997), pp. 3696–3699.
[145] J.W.M. Frenken, J.P. Toennies, and C. Woll, *Self-diffusion at a melting surface observed by He scattering*, Phys. Rev. Lett. 60(17) (1988), pp. 1727–1730.
[146] P. Fourquet, H. Hedgeland, and A.P. Jardine, *Surface diffusion studies using neutron and helium spin-echo spectroscopy*, Phys. Chem. Chem. Phys. 224 (2010), pp. 61–81.
[147] J. Krim, *Fiber texture and surface composition of evaporated gold films on quartz*, Thin Solid Films 137 (1986), pp. 297–303.
[148] J. Krim and A. Widom, *Damping of a crystal oscillator by an adsorbed monolayer and its relation to interfacial viscosity*, Phys. Rev. B 38(17) (1988), pp. 12184–12189.
[149] G. Sauerbrey, *Verwendung von Schwingquarzen zur Wagung Dunner Schichten und zur Mikrowagung*, Zeitschrift fur Physik 155(2) (1959), pp. 206–222.
[150] S. Berg, M. Ruths, and D. Johannsmann, *High frequency measurements of interfacial friction using quartz crystal resonators integrated into a surface forces apparatus*, Phys. Rev. E 65 (2002), 026119026119-9.
[151] B. Borovsky, M. Abdelmaksoud, and J. Krim, *STM-QCM studies of vapor phase lubricants*, in *Nanotribology: Critical Assessment and Research Needs*, S.M. Hsu and Z.C. Ying, eds., Kluwer Academic Publishers, Boston, MA, 2002, pp. 361–375.
[152] T.S. Coffey, M. Abdelmaksoud, B. Borovsky, and J. Krim, *Viewing a moving contact: A scanning probe and quartz crystal microbalance study of TCP and C60*, in *Fundamentals of Tribology and Bridging the Gap Between the Macro-and Micro/nanoscales*, B. Bhushan, ed., Kluwer Academic Publishers, Dordrecht, the Netherlands, 2001, pp. 171–176.
[153] B. Borovsky, J. Krim, S.A. Syed Asif, and K.J. Wahl, *Measuring nanomechanical properties of a dynamic contact using an indenter probe and quartz crystal microbalance*, J. Appl. Phys. 90(12) (2001), pp. 6391–6396.
[154] F.N. Dultsev, V.P. Ostanin, and D. Klenerman, *Hearing bond breakage measurement of bond rupture forces using a quartz crystal microbalance*, Langmuir 16 (2000), pp. 5036–5040.
[155] M. Abdelmaksoud, J.W. Bender, and J. Krim, *Nanotribology of a vapor-phase lubricant: A quartz crystal microbalance study of tricresylphosphate (TCP) uptake on iron and chromium*, Tribol. Lett. 13(3) (2002), pp. 179–186.
[156] J.Y. Park, Y. Seo, and I. Yu, *N-2 adsorption study on quartz, silver, and carbon nanotube by inductive pulse quartz crystal microbalance*, J. Appl. Phys. 101(5) (2007), art#053521.
[157] J.Y. Park, Y.B. Qi, D.F. Ogletree, P.A. Thiel, and M. Salmeron, *Influence of carrier density on the friction properties of silicon PN junctions*, Phys. Rev. B 76(6) (2007), art#064108.
[158] L. Bardotti, P. Jensen, A. Hoareau, M. Treilleux, B. Cabaud, A. Perez, and F. Cadete Santos Aires, *Diffusion and aggregation of large antimony and gold clusters deposited on graphite*, Surf. Sci. 367(3) (1996), pp. 276–292.
[159] C.D. VanSiclen, *Single jump mechanism for large cluster diffusion on metal-surfaces*, Phy. Rev. Lett. 75(8) (1995), pp. 1574–1577.
[160] S.C. Wang and G. Ehrlich, *Diffusion of large surface clusters: Direct observations on Ir(111)*, Phy. Rev. Lett. 79(21) (1999), pp. 4234–4237.
[161] A.J. Gellman, *Vapor lubricant transport in MEMS devices*, Tribol. Lett. 17 (2004), pp. 455–461.
[162] O.Y. Fajardo and J.J. Mazo, *Effects of surface disorder and temperature on atomic friction*, Phys. Rev. B 82 (2010), art#035435.
[163] A. Franchini, V. Bortolani, G. Santoro, and K. Xheka, *Effects of the commensurability and disorder on friction for the system Xe/Cu*, J. Phys. Condens. Matter 23 (2011), art#484004.

[164] A. Dayo and J. Krim, *Atomic-scale friction in Xe/Ag and N-2/Pb*, Int. J. Thermophys. 19 (1998), pp. 827–834.
[165] A. Dayo, W. Allnassallah, and J. Krim, *Superconductivity-dependent sliding friction*, Phys. Rev. Lett. 80(8) (1998), pp. 1690–1693.
[166] A. Dayo, *Quartz crystal microbalance measurements of electronic contributions to sliding friction*, Ph.D. diss., Northeastern University, Boston, MA, 1998.
[167] A. Laschitsch and D. Johannsmann, *High frequency tribologica1 investigations on quartz resonator surfaces*, J. Appl. Phys. 85(7) (1999), pp. 3759–3765.
[168] B. Zhang, H. Chiba, A. Nakajima, *Blow-off of nano PFPE liquid film at hard disk surfaces*, Tribol. Lett. 39 (2010), pp. 193–199.
[169] J. Klein, D. Perahia, and S. Warburg, *Forces between polymer-bearing surfaces undergoing shear*, Nature, 352 (1991), pp. 143–145.
[170] E. Eiser and J. Klein, *The effect of mobile polymers on the normal and shear forces between polymer brushes*, Macromolecules 40 (2007), pp. 8455–8463.
[171] D.D. Lowrey, K. Tasaka, J.H. Kindt, X. Banquy, N. Belman, Y. Min, N.S. Pesika, G. Mordukhovich, and J.N. Israelachvili, *High-speed friction measurements using a modified surface forces apparatus*, Tribol. Lett. 42 (2011), pp. 117–127.
[172] M. Zach, J. Vanicek, and M. Heuberger, *The extended surface forces apparatus. Part III. High-speed interferometric distance measurement*, Rev. Sci. Instrum. 74(1) (2003), pp. 260–266.
[173] C. Mak and J. Krim, *Quartz-crystal microbalance studies of the velocity dependence of interfacial friction*, Phys. Rev. B 58(9) (1998), pp. 5157–5159.
[174] M.F. Danisman and B. Ozkan, *Simultaneous detection of surface coverage and structure of krypton films on gold by helium atom diffraction and quartz crystal microbalance techniques*, Rev. Sci. Instrum. 82 (2011), art#115104.
[175] C.D. Stockbridge, *Vacuum Microbalance Techniques*, Vol. 5, Plenum Press, New York, 1966.
[176] E.T. Watts, J. Krim, and A. Widom, *Experimental observation of interfacial slippage at the boundary of molecularly thin films with gold substrates*, Phys. Rev. B. 41 (1990), pp. 3466–3472.
[177] M. Rodahl and B. Kasemo, *On the measurement of thin liquid overlayers with the quartz crystal microbalance*, Sens. Actuators A 54 (1996), pp. 448–456.
[178] M. Rodahl and B. Kasemo, *A simple setup to simultaneously measure the resonant frequency and absolute dissipation factor of a quartz crystal microbalance*, Rev. Sci. Instrum. 67 (1996), pp. 3238–3241.
[179] L. Bruschi, G. Delfitto, and G. Mistura, *Inexpensive but accurate driving circuits for quartz crystal microbalances*, Rev. Sci. Instrum. 70(1) (1999), pp. 153–157.
[180] M.E. Frerking, *Crystal Oscillator Design and Temperature Compensation*, Van Nostrand, New York, 1978, 240 pp.
[181] L. Bruschi, A. Carlin, and G. Mistura, *Depinning of atomically thin Kr films on gold*, Phys. Rev. Lett. 88(4) (2002), art#046105.
[182] L. Bruschi, G. Fois, A. Pontarollo, G. Mistura, B. Torre, F.B. de Mongeot, C. Boragno, R. Buzio, and U. Valbusa, *Structure depinning of Ne monolayers on Pb at $T < 6.5\,K$*, Phys. Rev. Lett. 96(21) (2006), art#216101.
[183] L. Bruschi and G. Mistura, *Measurement of the friction of thin films by means of a quartz crystal microbalance in the presence of a finite vapor pressure*, Phys. Rev. B 63 (2001), art#235411.
[184] L. Bruschi, A. Carlin, F.B. de Mongeot, F. dalla Longa, L. Stringher, and G. Mistura, *Ultrahigh vacuum apparatus for quartz crystal microbalance measurements in the temperature range 4–400 K*, Rev. Sci. Instrum. 76 (2005), art#023904.
[185] A. Carlin, L. Bruschi, M. Ferrari, and G. Mistura, *Observation of depinning phenomena in the sliding friction of Kr films on gold*, Phys. Rev. B 68(4) (2003), art#045420.
[186] M.S. Tomassone and J.B. Sokoloff, *Effects of defects on friction for a Xe film sliding on Ag(111)*, Phys. Rev. B 60 (1999), pp. 4005–4017.
[187] P.G. Degennes, *Wetting – statics and dynamics*, Rev. Modern Phys. 57(3) (1995), pp. 827–863.
[188] J.G. Dash, *Clustering and percolation transition in helium and other thin-films*, Phy. Rev. B 15(6) (1977), pp. 3136–3146.

[189] E. Ruckenstein and P. Rajora, *On the no-slip boundary condition of hydrodynamics*, J. Colloid Interf. Sci. 96 (1983), pp. 488–493.
[190] D.C. Tretheway and C.D. Meinhart, *Apparent fluid slip at hydrophobic microchannel walls*, Phys. Fluids 14 (2002), pp. L9–L12.
[191] H.R. Brown, M.K. Chaudhury, and B.M. Newby, *Relation between slip and energy dissipation in viscoelastic adhesives*, Adv. Fracture Res. 1–6 (1997), pp. 3037–30430.
[192] V.S.J. Craig, C. Neto, and D.R.M. Williams, *Shear-dependent boundary slip in an aqueous Newtonian liquid*, Phys. Rev. Lett. 87 (2001), pp. 4404–4507.
[193] E. Lauga and T.M. Squires, *Brownian motion near a partial slip boundary: A local probe of the no-slip condition*, Phys. Fluids 17 (2005), art#103012.
[194] B.M.Z. Newby and M.K. Chaudhury, *Effect of interfacial slippage on viscoelastic adhesion*, Langmuir 13 (1997), pp. 1805–1809.
[195] H. Spikes and S. Granick, *Equation for slip of simple liquids at smooth solid surfaces*, Langmuir 19 (2003), pp. 5065–5071.
[196] P.A. Thompson and M.O. Robbins, *Simulations of contact-line motion-slip and the dynamic contact angle*, Phys. Rev. Lett. 63 (1989), pp. 766–769.
[197] P.A. Thompson, G.S. Grest, and M.O. Robbins, *Phase-transitions and universal dynamics in confined films*, Phys. Rev. Lett. 68 (1992), pp. 3448–3451.
[198] P.A. Thompson and S.M. Troian, *A general boundary condition for liquid flow at solid surfaces*, Nature 389 (1997), pp. 360–362.
[199] J.L. Barrat and L. Bocquet, *Large slip effect at a nonwetting fluid–solid interface*, Phys. Rev. Lett. 82 (1999), pp. 4671–4674.
[200] J.L. Barrat and L. Bocquet, *Influence of wetting properties on hydrodynamic boundary conditions at a fluid/solid interface*, Faraday Discuss. 112 (1999), pp. 119–127.
[201] D.M. Huang, C. Sendner, D. Horinek, R.R. Netz, and L. Bocquet, *Water slippage versus contact angle: A quasiuniversal relationship*, Phys. Rev. Lett. 101(22) (2008), art#226101.
[202] L. Bocquet and J.L. Barrat, *Flow boundary conditions from nano- to microscales*, Soft Mat. 3 (2007), pp. 685–693.
[203] G.S. Smith, J. Majewski, T. Kuhl, J. Israelachvili, and J. Wong, *Neutron reflectivity studies of model biomembranes at solid-liquid interfaces*, Biophys. J. 80 (2001), pp. 14A–14A.
[204] J.A. Cowen, R. Lucklum, G. McHale, and M.I. Newton, *Influence of viscoelasticity and interfacial slip on acoustic wave sensors*, J. Appl. Phys. 88(12) (2000), pp. 7304–7312.
[205] J.S. Ellis and G.L. Hayward, *Interfacial slip on a transverse-shear mode acoustic wave device*, J. Appl. Phys. 94(12) (2003), pp. 7856–7867.
[206] J.S. Ellis and M. Thompson, *Hydrodynamics and slip at the liquid-solid interface*, in *Advances in Chemical Physics*, Vol. 131, ed. S.A. Rice, John Wiley & Sons Inc., New York, 2007, pp. 61–84.
[207] B.Y. Du, E. Goubaidoulline, and D. Johannsmann, *Effects of laterally heterogeneous slip on the resonance properties of quartz crystals immersed in liquids*, Langmuir 20(24) (2004), pp. 10617–10624.
[208] M. Jonson, B. Kasemo, and M.V. Voinova, *On dissipation of quartz crystal microbalance as a mechanical spectroscopy tool*, Spectrosc. Int. J. 18(4) (2004), pp. 537–544.
[209] N.J. Cho, J.N. D'Amour, C.W. Frank, K. Kanazawa, W. Knoll, and J. Stalgren, *Quartz resonator signatures under Newtonian liquid loading for initial instrument check*, J. Colloid Interf. Sci. 315(1) (2007), pp. 248–254.
[210] J. Klein and E. Kumacheva, *Confinement-induced phase-transitions in simple liquids*, Science 269(5225) (1995), pp. 816–819.
[211] J. Klein and E. Kumacheva, *Simple liquids confined to molecularly thin layers. I. Confinement-induced liquid-to-solid phase transitions*, J. Chem. Phys. 108(16) (1998), pp. 6996–7009.
[212] S.T. Cui, P.T. Cummings, and H.D. Cochran, *Molecular simulation of the transition from liquidlike to solidlike behavior in complex fluids confined to nanoscale gaps*, J. Chem. Phys. 114(16) (2001), pp. 7189–7195.
[213] H. Docherty and P.T. Cummings, *Direct evidence for fluid–solid transition of nanoconfined fluids*, Soft Matter 6(8) (2010), pp. 1640–1643.

[214] C.M. Mate and B. Marchon, *Shear response of molecularly thin liquid films to an applied air stress*, Phys. Rev. Lett. 85(18) (2000), art#390223905.
[215] C.M. Mate, *On the road to an atomic- and molecular- level understanding of friction*, MRS Bull. (2002), pp. 967–971.
[216] M.A. Scarpulla, C.M. Mate, and M.D. Carter, *Air shear driven flow of thin perfluoropolyether polymer films*, J. Chem. Phys. 118(7) (2003), pp. 3368–3375.
[217] R.G. Horn, J.N. Israelachvili, and F. Pribac, *Measurements of the deformation and adhesion of solids in contact*, J. Colloid Interf. Sci. 115(2) (1987), pp. 480–492.
[218] M. Hirano, K. Shinjo, and Y. Murata, *Anisotropy of frictional fores in muscovite mica*, Phys. Rev. Lett. 67(19) (1991), pp. 2642–2645.
[219] J.N. Israelachvili and G.E. Adams, *Measurement of forces between 2 mica surfaces in aqueous–electrolyte solutions in range 0–100 nm*, J. Chem. Soc. Faraday Trans. I 74 (1978), pp. 975–1001.
[220] J.N. Israelachvili, P.M. McGuiggan, and A.M. Homola, *Dynamic properties of molecularly thin liquid-films*, Science 240(4849) (1988), pp. 189–191.
[221] H. Yoshizawa and J. Israelachvili, *Relation between adhesion and friction forces across thin-films*, Thin Solid Films 246(1–2) (1994), pp. 71–76.
[222] J. Klein, *Forces between mica surfaces bearing adsorbed macromolecules in liquid-media*, J. Chem. Soc. Faraday Trans. I 79 (1983), pp. 99–118.
[223] J.L. Parker, H.K. Christenson, and B.W. Ninham, *Device for measuring the force and separation between 2 surfaces down to molecular separations*, Rev. Sci. Instrum. 60(10) (1989), pp. 3135–3138.
[224] H.K. Christenson, *Non-DLVO forces between surfaces – Solvation, hydration and capillary effects*, J. Dispersion Sci. Technol. 9(2) (1988), pp. 171–206.
[225] H.K. Christenson and V.V. Yaminsky, *Adhesion and solvation forces between surfaces in liquids studied by vapor-phase experiments*, Langmuir 9(9) (1993), pp. 2448–2454.
[226] M.L. Gee, P.M. McGuiggan, J.N. Israelachvili, and A.M. Homola, *Liquid to solid-like transitions of molecularly thin-films under shear*, J. Chem. Phys. 93 (1990), pp. 1895–1906.
[227] J. Van Alsten and S. Granick, *Molecular tribometry of ultrathin liquid-films*, Phys. Rev. Lett.61(22) (1988), pp. 2570–2573.
[228] J.M. Georges, S. Millot, J.L. Loubet, and A. Tonck, *Drainage of thin liquid-films between relatively smooth surfaces*, J. Chem. Phys. 98 (1993), pp. 7345–7360.
[229] C. Cottin-Bizonne, B. Cross, A. Steinberger, and E. Charlaix, *Boundary slip on smooth hydrophobic surfaces: Intrinsic effects and possible artifacts*, Phys. Rev. Lett. 94 (2005), art#056102.
[230] A.L. Demirel and S. Granick, *Friction fluctuations and friction memory in stick–slip motion*, Phys. Rev. Lett. 77(21) (1996), pp. 4330–4333.
[231] A. Dhinojwala, S.C. Bae, and S. Granick, *Shear-induced dilation of confined liquid films*, Tribol. Lett. 9(1–2) (2000), pp. 55–62.
[232] J.P. Gao, W.D. Luedtke, and U. Landman, *Layering transitions and dynamics of confined liquid films*, Phys. Rev. Lett. 79(4) (1997), art#7055708.
[233] H.K. Christenson, D.W.R. Gruen, R.G. Horn, and J.N. Israelachvili, *Structuring in liquid alkanes between solid-surfaces – Force measurements and mean-field theory*, J. Chem. Phys. 87(3) (1987), pp. 1834–1841.
[234] J.N. Israelachvili, K.L. Johnson, M.O. Robbins, U. Landman, B.R. Lawn, H.M. Pollock, R.S. Polizzotti, I.L. Singer, and E. Rabinowicz, *Adhesion, friction and lubrication of molecularly smooth surfaces*, in *Fundamentals of Friction: Macroscopic and Microscopic Processes*, I.L. Singer and H.M. Pollock, eds., NATO Advanced Science Institutes Series E, Applied Sciences, Vol. 220, 1992, pp. 351–385.
[235] H.K. Christenson and J.N. Israelachvili, *Temperature dependence of solvation forces*, J. Chem. Phys. 80(9) (1984), pp. 4566–4567.
[236] F. Mugele and M. Salmeron, *Dynamics of layering transitions in confined liquids*, Phys. Rev. Lett. 84 (2000), pp. 5796–5799.
[237] Y.Z. Hu and S. Granick, *Microscopic study of thin film lubrication and its contributions to macroscopic tribology*, Tribol. Lett. 5(I) (1988), pp. 81–88.
[238] L. Bureau, *Nonlinear rheology of a nanoconfined simple fluid*, Phys. Rev. Lett. 104(2010), art#218302.

[239] T. Becker and F. Mugele, *Nanofluidics: Viscous dissipation in layered liquid systems*, Phys. Rev. Lett. 91 (2003), art#166104.
[240] Y.X. Zhu and S. Granick, *Reassessment of solidification in fluids confined between mica sheets*, Langmuir 19 (2003), pp. 8148–8151.
[241] J. Israelachvili, N. Maeda, and M. Akbulut, *Comment on reassessment of solidification in fluids confined between mica sheets*, Langmuir 22 (2006), pp. 2397–2398.
[242] S. Granick, Y.X. Zhu, Z. Lin, S.C. Bae, J.S. Wong, and J. Turner, *Reply to comment on reassessment of solidification in fluids confined between mica sheets*, Langmuir 22 (2006), pp. 2399–2401.
[243] Y.X. Zhu and S. Granick, *Superlubricity: A paradox about confined fluids resolved*, Phys. Rev. Lett. 93 (2004), art#096101.
[244] D. Gourdon and J. Israelachvili, *Comment on superlubricity: A paradox about confined fluids resolved*, Phys. Rev. Lett. 96 (2006), art#099601.
[245] J.S. Wong, S.C. Bae, S. Anthony, Y.X. Zhu, and S. Granick, *Reply to comment on superlubricity: A paradox about confined fluids resolved*, Phys. Rev. Lett. 96 (2006), art#099602.
[246] Z.Q. Lin and S. Granick, *Platinum nanoparticles at mica surfaces*, Langmuir 19(17) (2003), pp. 7061–7070.
[247] S. Perkin, L. Chai, N. Kampf, U. Raviv, W. Briscoe, I. Dunlop, S. Titmuss, M. Seo, E. Kumacheva, and J. Klein, *Forces between mica surfaces, prepared in different ways, across aqueous and nonaqueous liquids confined to molecularly thin films*, Langmuir 22(14) (2006), pp. 6142–6152.
[248] Y. Golan, Y.A. Martin-Herranz, Y. Li, C.R. Safinya, and J. Israelachvili, *Direct observation of shear-induced orientational phase coexistence in a lyotropic system using a modified X-ray surface forces apparatus*, Phys. Rev. Lett. 86(7) (2001), pp. 1263–1266.
[249] S. Granick, S.C. Bae, B. Wang, S. Kumar, J. Guan, C. Yu, K. Chen, and J. Kuo, *Single-molecule methods in polymer science*, J. Polym. Sci. 48(24) (2010), pp. 2542–2543.
[250] G.J. Germann, S.R. Cohen, G. Neubauer, G.M. Mcclelland, H. Seki, and D. Coulman, *Atomic scale friction of a diamond tip on diamond (100)-surface and (111)-surface*, J. Appl. Phys. 73 (1993), pp. 163–167.
[251] R.W. Carpick, N. Agrait, D.F. Ogletree, and M. Salmeron, *Variation of the interfacial shear strength and adhesion of a nanometer-sized contact*, Langmuir 12(13) (1996), pp. 3334–3340.
[252] D.F. Ogletree, J.Y. Park, M. Salmeron, and P.A. Thiel, *Electronic control of friction in silicon pn junctions*, Science 313(5784) (2006), p. 186.
[253] N. Sasaki, K. Kobayashi, and M. Tsukada, *Atomic-scale friction image of graphite in atomic-force microscopy*, Phys. Rev. B 54 (1996), pp. 2138–2148.
[254] E. Meyer, R. Luthi, L. Howald, M. Bammerlin, M. Guggisberg, and H.J. Guntherodt, *Site-specific friction force spectroscopy*, J. Vac. Sci. Technol. B 14(2) (1996), pp. 1285–1288.
[255] M.A. Lantz, S.J. Oshea, M.E. Welland, and K.L. Johnson, *Atomic-force-microscope study of contact area and friction on $NbSe_2$*, Phys. Rev. B 55(16) (1997), pp. 10776–10785.
[256] R. Perez, I. Stich, M.C. Payne, and K. Terakura, *Surface–tip interactions in noncontact atomic-force microscopy on reactive surfaces: Si(111)*, Phys. Rev. B 58 (1998), art#10835.
[257] V. Koutsos, *Atomic-force microscopy and real atomic-resolution – Simple computer simulations*, Europhys. Lett. 26 (1994), pp. 103–107.
[258] A. Abdurixit, A. Baratoff, and E. Meyer, *Molecular dynamics simulations of dynamic force microscopy: Applications to the $Si(111) - 7 \times 7$ surface*, Appl. Surf. Sci. 157 (2000), pp. 355–360.
[259] R. Bennewitz, A.S. Foster, L.N. Kantorovich, M. Bammerlin, C. Loppacher, S. Schar, M. Guggisberg, E. Meyer, and A.L. Shluger, *Atomically resolved edges and kinks of NaCl islands on Cu(111): Experiment and theory*, Phys. Rev. B 62 (2000), pp. 2074–2084.
[260] A.S. Foster, C. Barth, A.L. Shluger, and M. Reichling, *Unambiguous interpretation of atomically resolved force microscopy images of an insulator*, Phys. Rev. Lett. 86 (2001), pp. 2373–2376.
[261] E. Gnecco, R. Bennewitz, A. Socoliuc, and E. Meyer, *Friction and wear on the atomic scale*, Wear 254 (2003), pp. 859–862.
[262] A.S. Foster, A.L. Shluger, and R.M. Nieminen, *Realistic model tips in simulations of nc-AFM*, Nanotechnology 15 (2004), pp. S60–S64.

[263] J.E. Sader and S.P. Jarvis, *Accurate formulas for interaction force and energy in frequency modulation force spectroscopy*, Appl. Phys. Lett. 84(10) (2004), pp. 1801–1804.
[264] S.N. Medyanik, W.K. Liu, I.-H. Sung, and R.W. Carpick, *Predictions and observations of multiple slip modes in atomic-scale friction*, Phys. Rev. Lett. 97(13) (2006), art#136106.
[265] T. Bouhacina, J.P. Aimé, S. Gauthier, D. Michel, and V. Heroguez, *Tribological behaviour of a polymer grafted in silanized silica probed with a nanotip*, Phys. Rev. B: Condens. Matter 56 (1997), pp.7694–7703.
[266] O. Zwörner, H. Holscher, U.D. Schwarz, and R. Wiesendanger, *The velocity dependence of frictional forces in point-contact friction*, Appl. Phys. A: Mater. Sci. Process. 66 (1998), pp. S263–S267.
[267] R. Bennewitz, T. Gyalog, M. Guggisberg, M. Bammerlin, E. Meyer, and H.J. Gntherodt, *Atomic-scale stick–slip processes on Cu(111)*, Phys. Rev. B 60 (1999), pp. R11301–R11304.
[268] E. Gnecco, R. Bennewitz, T. Gyalog, C. Loppacher, M. Bammerlin, E. Meyer, and H.J. Guntherodt, *Velocity dependence of atomic friction*, Phys. Rev. Lett. 84 (2000), pp. 1172–1175.
[269] M.Y. He, A.S. Blum, G. Overney, and R.M. Overney, *Effect of interfacial liquid structuring on the coherence length in nanolubrication*, Phys. Rev. Lett. 88 (2002), art#154302.
[270] R. Buzio, C. Boragno, and U. Valbusa, *Friction laws for lubricated nanocontacts*, J. Chem. Phys. 125 (2006), art#094708.
[271] G. He, M.M. Muser, and M.O. Robbins, *Adsorbed layers and the origin of static friction*, Science 284(5420) (1999), pp. 1650–1652.
[272] M. Abdelmaksoud, S.M. Lee, C.W. Padgett, D.L. Irving, D.W. Brener, and J. Krim, *STM, QCM, and the windshield wiper effect: A joint theoretical–experimental study of absorbate mobility and lubrication at high sliding rates*, Langmuir 22(23) (2006), pp. 9606–9609.
[273] B.D. Dawson, S.M. Lee, and J. Krim, *Tribo-induced melting transition at a sliding asperity contact*, Phys. Rev. Lett. 103 (2009), art#205502.
[274] S.H. Kim, D.B. Asay, and M.T. Dugger, *Nanotribology and MEMS*, Nano Today 2 (2007), pp. 22–29.
[275] D.J. Dickrell III, M.T. Dugger, M.A. Hamilton, and W.G. Sawyer, *Direct contact-area computation for MEMS using real topographic surface data*, J. Micro. Electro. Mech. Syst. 16 (2007), pp. 1263–1268.
[276] S. Majumder, N.E. McGruer, G.G. Adams, P.M. Zavracky, R.H. Morrison, and J. Krim, *Study of contact in an electrostatically actuated microswitch*, Sens. Actuators A- Physical 93 (2001), pp. 19–26.
[277] M. Wang, D. Xu, K. Ravi-Chandar, and K.M. Liechti, *On the development of a mesoscale friction tester*, Exp. Mech. 47 (2007), pp. 123–131.
[278] D.W. Xu, K.A. Liechti, and K. Ravi-Chandar, *On scale dependence in friction: Transition from intimate to monolayer-lubricated contact*, J. Colloid Interf. Sci. 318(2) (2008), pp. 507–519.
[279] A.D. Romig, M.T. Dugger, and P. McWhorter, *Materials issues in microelectromechanical devices: Science, engineering, manufacturability and reliability*, J. Acta Mater. 51 (2003), pp. 5837–5866.
[280] D.C. Senft and M.T. Dugger, *Friction and wear in surface micromachined tribological test devices*, Proceedings of the SPIE –The International Society for Optical Engineering, Vol. 3224, 1997, p. 31.
[281] J.A. Williams and H.R. Le, *Tribology and MEMS*, J. Phys. D: Appl. Phys. 39 (2006), pp. R201–R214.
[282] S.J. Timpe and K. Komvopoulos, *An experimental study of sidewall adhesion in microelectromechanical systems*, J. Micro. Electro. Mech. Syst. 14 (2005), pp. 1356–1363.
[283] W.M. van Spengen and J.W.M. Frenken, *The Leiden MEMS tribometer: Real time dynamic friction loop measurements with an on-chip tribometer*, Tribol. Lett. 28 (2007), pp. 149–156.
[284] W.M. van Spengen, V. Turq, and J.W.M. Frenken, *The description of friction of silicon MEMS with surface roughness: Virtues and limitations of a stochastic Prandtl–Tomlinson model and the simulation of vibration-induced friction reduction*, Beilstein J. Nanotechnol. 1 (2010), pp. 163–171.
[285] D.A. Hook, B.P. Miller, B.M. Vlastakis, M.T. Dugger, and J. Krim, *Vapor-phase lubrication and SAMS reservoir effect at low partial pressures of ethanol*, Langmuir, submitted for publication.
[286] Z. Wang, J. Wei, P. Morse, J.G. Dash, O.E. Vilches, and D.H. Cobden, *Phase transitions of adsorbed atoms on the surface of a carbon nanotube*, Science 327 (2010), pp. 552–555.
[287] M. Walker, C. Nordquist, D. Czaplewski, G. Patrizi, N. McGruer, and J. Krim, *Impact of in situ oxygen plasma cleaning on the resistance of Ru and Au-Ru based rf microelectromechanical system contacts in vacuum*, J. Appl. Phys. 107 (2010), art#084509.

[288] D. Berman, M.J. Walker, M. Nordquist, and J. Krim, *Impact of adsorbed organic monolayers on vacuum electron tunneling contributions to electrical resistance at an asperity contact*, J. Appl. Phys. 110 (2011), art#114307.
[289] D.A. Hook, S.J. Timpe, M.T. Dugger, and J. Krim, *Tribological degradation of fluorocarbon coated silicon microdevice surfaces in normal and sliding contact*, J. Appl. Phys. 104(3) (2008), art#034303.
[290] J.J. Sniegowski and M.P. de Boer, *IC-compatible polysilicon surface micromachining*, Annu. Rev. Mater. Sci., 30 (2000), pp. 299–333.
[291] W.C. Tang, Electrostatic comb drive for resonant sensor and actuator applications, Ph.D. diss., University of California, Berkeley, CA, 1990.
[292] JE. Rutledge, Private communication, 2009.
[293] M. Rodahl, F. Höök, A. Krozer, P. Brzezinski, and B. Kasemo, *Quartz crystal microbalance setup for frequency and Q-factor measurements in gaseous and liquid environments*, Rev. Sci. Instrum. 66(7) (1995), pp. 3294–3930.
[294] H.G. Craighead, R. Ilic, J.M. Parpia, and S.S. Verbridge, *Size and frequency dependent gas damping of nanomechanical resonators*, Appl. Phys. Lett. 93(1) (2008), art#013101.
[295] K.L. Ekinci, D.M. Karabacak, and V. Yakhot, *Universality in oscillating flows*, Phys. Rev. Lett. 101(26) (2008), art#264501.
[296] G. Amontons, *De la Resistance Caus'ee dan les Machines*, Memoires de l'Academie Royale A, Chez Gerard Kuyper, Amsterdam, 1706, pp. 257–282.
[297] C.A. Coulomb, *Theorie des machines simples*, Mem. Math. Phys. Acad. Sci. 10(1785), pp. 161–331; see also J. Heyman, *Coulomb's Memoir on Statics: An Essay in the History of Civil Engineering*, Bilingual edition, World Scientific, Singapore, 1998.
[298] A.J. Gellman and J.S. Ko, *The current status of tribological surface science*, Tribol. Lett. 10(1–2) (2001), pp. 39–44.
[299] F.P. Bowden and D. Tabor, *Friction and lubrication of solids*, 2 Vols., Oxford University Press, Oxford, 1964.
[300] M. Enachescu, R.J.A. van der Oetelaai, and R.W. Carpick, *Observation of proportionality between friction and contact area at the nanometer scale*, Tribol. Lett. 7(2–3) (1999), pp. 73–78.
[301] G. He and M. Robbins, *Simulations of the kinetic friction due to adsorbed surface layers*, Tribol. Lett. 10(1–2) (2001), pp. 7–14.
[302] J.H. Dieterich and B.D. Kilgore, *Imaging surface contacts: Power law contact distributions and contact stresses in quartz, calcite, glass and acrylic plastic*, Tectonophysics 256 (1996), pp. 219–239.
[303] S.F. Cheng and M.O. Robbins, *Defining contact at the atomic scale*, Tribol. Lett. 39 (2010), pp. 329–348.
[304] S.M. Rubinstein, G. Cohen, and J. Fineberg, *Contact area measurements reveal loading-history dependence of static friction*, Phys. Rev. Lett. 96 (2006), art#256103.
[305] O. Ben-David, G. Cohen, and J. Fineberg, *The dynamics of the onset of frictional slip*, Science 330 (2010), pp. 211–214.
[306] O. Ben-David, S.M. Rubinstein, and J. Fineberg, *Stick–slip and the evolution of frictional strength*, Nature 463 (2010), pp. 76–79.
[307] L. Pope, L. Fehrenbacher, and W. Winer (eds.), *New Materials Approaches to Tribology: Theory and Applications*, MRS, Pittsburgh, PA, 1989.
[308] K.L. Johnson, *Contact Mechanics*, Cambridge University Press, Cambridge, 1985.
[309] K.L. Johnson, K. Kendall, and A.D. Roberts, *Surface energy and the contact of elastic solids*, Proc. R. Soc. Lond. Ser. A 324(1558) (1971), pp. 301–313.
[310] L.M. Hutchings, *Tribology: Friction and Wear of Engineering Materials*, CRC Press, Boca Raton, FL, 1992.
[311] J.A. Greenwood and J.B. Williams, *Contact of nominally flat surfaces*, Proc. R. Soc. Lond. Ser. A 295(1442) (1966), pp. 300–319.
[312] K.N.G. Fuller and D. Tabor, *The effect of surface roughness on the adhesion of elastic solids*, Proc. R. Soc. Lond. Ser. A 345(1642) (1975), pp. 327–342.
[313] N. Gane and F.P. Bowden, *Microdeformation of solids*, J. Appl. Phys. 39(3) (1968), pp. 1432–1435.
[314] W. Zhong and D. Tomanek, *First principle theory of atomic scale friction*, Phys. Rev. Lett. 64(25) (1990), pp. 3054–3057.

[315] D. Tabor, *Friction as a dissipative process*, in *Fundamentals of Friction: Macroscopic and Microscopic Processes*, I.L. Singer and H.M. Pollack, eds., Vol. 3, Kluwer Academic Publishers, Dordrecht, the Netherlands, 1992.
[316] J.E. Lennard-Jones, *On the determination of molecular fields. II. From the equation of state of a gas*, Proc. R. Soc. A106 (1924), pp. 463–477.
[317] E.D. Smith, M.O. Robbins, and M. Cieplak, *Friction on adsorbed monolayers*, Phys. Rev. B 54 (1996), pp. 8252–8260.
[318] S. Rauber, J.R. Klein, and M.W. Cole, *Substrate-mediated dispersion interaction between adsorbed atoms and molecules*, Surf. Sci. 123 (1982), pp. 173–178.
[319] R.A. Trasca, M.W. Cole, and R.D. Diehl, *Systematic model behavior of adsorption on flat surfaces*, Phys. Rev. E 68 (2003), art#041605.
[320] R.D. Diehl, T. Seyller, M. Caragiu, G.S. Leatherman, N. Ferralis, K. Pussi, P. Kaukasoina, and M. Lindroos, *The adsorption sites of rare gases on metallic surfaces: A review*, J. Phys. Condens. Matter 16 (2004), pp. S2839–S2862.
[321] M. Ferrario and M.C. Righi, *Potential energy surface for rare gases adsorbed on Cu(111): Parameterization of the gas/metal interaction potential*, J. Phys.: Condens. Matt. 19(30) (2007), art#305008.
[322] M. Ferrario and M.C. Righi, *Pressure induced friction collapse of rare gas boundary layers sliding over metal surfaces*, Phys. Rev. Lett. 99(17) (2007), art#176101.
[323] L.W. Bruch, *Ohmic damping of center-of-mass oscillations of a molecular monolayer*, Phys. Rev. B 61(23) (2000), pp. 16201–16206.
[324] M.C. Righi and M. Ferrario, *Pressure induced friction collapse of rare gas boundary layers sliding over metal surfaces*, Phys. Rev. Lett. 99 (2007), art#176101.
[325] A. Buldum and S. Ciraci, *Atomic-scale of dry sliding friction*, Phys. Rev. B 55 (1997), pp. 2606–2611.
[326] A. Buldum, S. Ciraci, and D.M. Leitner, *Model for phononic energy dissipation in friction*, Phys. Rev. B 59(24) (1999), pp. 16042–16046.
[327] A. Buldum and S. Ciraci, *Theoretical study of boundary lubrication*, Phys. Rev. B 60(3) (1999), pp. 1982–1988.
[328] S. Curtarolo, G. Stan, M.W. Cole, M.J. Bojan, and W.A. Steele, *Computer simulations of the wetting properties of Ne on heterogeneous surfaces*, Phys. Rev. E 59 (1999), pp. 4402–4407.
[329] T. Gyalog and H. Thomas, *Atomic friction*, Z. fuer Physik B: Condens. Matter 104 (1997), pp. 669–674.
[330] K.B. Jinesh, S. Yu, H. Valk, M. Dienwiebel, and J.W.M. Frenken, *Thermolubricity in atomic-scale friction*, Phys. Rev. B 78 (2008), art#155440.
[331] I. Barel, M. Urbakh, L. Jansen, and A. Schirmeisen, *Multibond dynamics of nanoscale friction: The role of temperature*, Phys. Rev. Lett. 104 (2010), art#066104.
[332] L. Jansen, H. Holscher, H. Fuchs, and A. Schirmeisen, *Temperature dependence of atomic-scale stick–slip friction*, Phys. Rev. Lett. 104 (2010), art#256101.
[333] O.M. Braun and Y.S. Kivshar, *The Frenkel-Kontorova Model: Concepts, Methods, and Applications*, Springer-Verlag, Berlin, Germany, 2004, 472pp.
[334] M. Peyrard and S. Aubry, *Critical behaviour at the transition by breaking of analyticity in the discrete Frenkel–Kontorova model*, J. Phys. C: Solid State Phys. 16 (1983), pp. 1593–1608.
[335] S. Aubry, *The new concept of transitions by breaking of analyticity in a crystallographic model*, in *Solitons and Condensed Matter Physics*, A.R. Bishop and T. Schneider, eds., Springer, New York, 1978.
[336] T. Gyalog and H. Thomas, *Friction between atomically flat surfaces*, Europhys. Lett. 37 (1997), pp. 195–200.
[337] L. Consoli, A. Fasolino, and H.J.F. Knops, *Onset of sliding friction in incommensurate systems*, Phys. Rev. Lett. 85(2) (2000), pp. 302–305.
[338] J. Nakamura, A. Natori, T. Nitta, and K. Ohno, *Atomic scale friction of nanoscale clusters*, J. Vacuum Sci. Technol. B 22(4) (2004), pp. 2026–2029.
[339] A.R. Bishop, S. Goncalves, and V.M. Kenkre, *Nonlinear friction of a damped dimer sliding on a periodic substrate*, Phys. Rev. B 70(19) (2004), art#195415.
[340] A.R. Bishop, C. Fusco, S. Goncalves, and V.M. Kenkre, *Bistability and hysteresis in the sliding friction of a dimer*, Phys. Rev. B 72(19) (2005), art#195418.

[341] T. Kawaguchi and H. Matsukawa, *Dynamical frictional phenomena in an incommensurate two-chain model*, Phys. Rev. B 56 (1997), pp. 13932–13942.
[342] Z. Xu and P. Huang, *Composite oscillator model for the energy dissipation mechanism of friction*, Acta Phys. Sinica 55 (2006), pp. 2427–2432.
[343] Z. Xu and P. Huang, *Study on the energy dissipation mechanism of atomic-scale friction with composite oscillator model*, Wear 262 (2007), pp. 972–977.
[344] J.B. Sokoloff, J.E. Sacco, and J.F. Weisz, *Undamped lattice-vibrations in systems with 2 incommensurate periodicities*, Phys. Rev. Lett. 41(22) (1978), pp. 1561–1564.
[345] J.B. Sokoloff, *Theory of energy-dissipation in sliding crystal-surfaces*, Phys. Rev. B 42(I) (1990), pp. 760–765; correction 42, 674556745.
[346] J.B. Sokoloff, *Theory of atomic level sliding friction*, in *Fundamentals of Friction: Macroscopic and Microscopic Processes*, I.L. Singer and H.M. Pollack, eds., Kluwer Academic Publishers, Dordrecht, the Netherlands, 1992.
[347] J.B. Sokoloff, J. Krim, and A. Widom, *Determination of an atomic-scale frictional force law through quartz-crystal microbalance measurements*, Phys. Rev. B 48(12) (1993), pp. 9134–1937.
[348] J.B. Sokoloff, *Possible nearly frictionless sliding for mesoscopic solids*, Phys. Rev. Lett. 71(21) (1993), pp. 3450–3453.
[349] J.B. Sokoloff, M.S. Tomassone, and A. Widom, *Strongly temperature dependent sliding friction for a superconducting interface*, Phys. Rev. Lett. 84(3) (2000), pp. 515–517.
[350] J.B. Sokoloff, *Static friction between elastic solids due to random asperities*, Phys. Rev. Lett. 86(IS) (2001), pp. 3312–3315.
[351] J.B. Sokoloff, *Kinetic friction due to Ohm's law heating*, J. Phys.: Condens. Matt. 14(21) (2002), pp. 5277–5287.
[352] C. Daly and J. Krim, *Sliding friction of xenon monolayers and bilayers on Ag(lll)*, Phys. Rev. Lett. 76(5) (1996), pp. 803–806.
[353] C. Daly and J. Krim, *Friction and damping of Xe/Ag(111)*, Surf. Sci. 368 (1996), pp. 49–54.
[354] M.S. Tomassone, J.B. Sokoloff, A. Widom, and J. Krim, *Dominance of phonon friction for a xenon film on a silver (III) surface*, Phys. Rev. Lett. 79(24) (1997), pp. 4798–4801.
[355] T.S. Coffey and J. Krim, *Quartz-crystal microbalance studies of the slippage of solid and liquid krypton monolayers on metal(111) and C-60 surfaces*, Phys. Rev. B 72 (2005), art#235414.
[356] T.S. Coffey and J. Krim, *Impact of substrate corrugation on the sliding friction levels of adsorbed films*, Phys. Rev. Lett. 95(7) (2005), art#076101.
[357] B.N.J. Persson and Z.Y. Zhang, *Theory of friction: Coulomb drag between two closely spaced solids*, Phys. Rev. B 57(12) (1998), pp. 7327–7334.
[358] B.N.J. Persson and J.W. Gadzuk, *Comments on vibrational dynamics of low-frequency*, Surf. Sci. 410(2–3) (1998), pp. L779–L782.
[359] B.N.J. Persson and E. Tosatti, *The puzzling collapse of electronic sliding friction on a super-conductor surface*, Surf. Sci. 411 (1998), pp. L855–L857.
[360] A.E. Filippov, J. Klafter, and M. Urbakh, *Friction through dynamical formation and rupture of molecular bonds*, Phys. Rev. Lett 92 (2004), art#135503.
[361] J.E. Sacco and J.B. Sokoloff, *Free sliding in lattices with 2 incommensurate periodicities*, Phys. Rev. B 18(12) (1978), pp. 6549–6559.
[362] S. Goncalves, M. Kiwi, C. Scherer, and E.S. Torres, *Nanoscale sliding friction versus commensuration ratio: Molecular dynamics simulations*, Phys. Rev. B 73(3) (2006), art#035434.
[363] M. Dienwiebel, G.S. Verhoeven, N. Pradeep, J.W.M. Frenken, J.A. Heimberg, and H.W. Zandbergen, *Superlubricity of graphite*, Phys. Rev. Lett. 92(12) (2004), art#126101.
[364] M. Dienwiebel, N. Pradeep, G.S. Verhoeven, H.W. Zandbergen, and J.W.M. Frenken, *Model experiments of superlubricity of graphite*, Surf. Sci. 576(1–3) (2005), pp. 197–211.
[365] H.E. Johnson, J.F. Douglas, and S. Granick, *Topological influences on polymer adsorption and desorption dynamics*, Phys. Rev. Lett. 70 (1993), pp. 3267–3270.
[366] A. Socoliuc, R. Bennewitz, E. Gnecco, and E. Meyer, *Transition from stick–slip to continuous sliding in atomic friction: Entering a new regime of ultralow friction*, Phys. Rev. Lett. 92 (2004), art#134301.

[367] M.H. Muser, *Velocity dependence of kinetic friction in the Prandtl–Tomlinson model*, Phys. Rev. B 84(12) (2011), art#125419.
[368] Y. Sang, M. Dube, and M. Grant, *Thermal effects on atomic friction*, Phys. Rev. Lett. 87 (2001), art#174301.
[369] S.Y. Krylov, K.B. Jinesh, H. Valk, M. Dienwiebel, and J.W.M. Frenken, *Thermally-induced suppression of friction at the atomic scale*, Phys. Rev. E 71 (2005), art#065101.
[370] S.Y. Krylov and J.W.M. Frenken, *The crucial role of temperature in atomic-scale friction*, J. Phys. Condens. Matter 20 (2008), art#354003.
[371] C.G. Dunckle, I.B. Altfeder, A.A. Voevodin, J. Jones, J. Krim, and P. Taborek, *Temperature dependence of single asperity friction for a diamond on diamond-like carbon interface*, J. Appl. Phys. 107 (2010), art#114903.
[372] J. Cumings and A. Zettl, *Low-friction nanoscale linear bearing realized from multiwall carbon nanotubes*, Science 289 (2000), pp. 602–604.
[373] Q. Zheng and Q. Jiang, *Multiwalled carbon nanotubes as gigahertz oscillators*, Phys. Rev. Lett. 88 (2002), art#045503.
[374] Y. Chen, J. Yang, X. Wang, Z. Ni, and D. Li, *Temperature dependence of frictional force in carbon nanotube oscillators*, Nanotechnology 20 (2009), art#035704.
[375] D. Wei and Y. Zhang, *Friction between α-Al_2O_3(0001) surfaces and the effects of surface hydroxylation*, Surf. Sci. 603 (2009), pp. L95–L98.
[376] V. Bortolani, M. Brigazzi, A. Franchini, and G. Santoro, *Theory of static friction: Temperature and corrugation effects*, J. Phys.: Condens. Matter 20(22) (2008), art#224019.
[377] S. Morita, S. Fujisawa, and Y. Sugawara, *Spatially quantized friction with lattice periodicity*, Surf. Sci. Rep. 23 (1996), pp. 1–41.
[378] A.E. Filippov, J. Klafter, and M. Urbakh, *Confined molecules under shear: From a microscopic description to phenomenology*, Phys. Rev. Lett. 87 (2001), art#275506.
[379] H. Haken, *Synergetics: An Introduction*, Vol. 177, Springer/Mir, Berlin/Moscow, 1980.
[380] A.V. Khomenko and I.A. Lyashenko, *Stochastic theory of ultrathin lubricant film melting in the stick–slip regime*, Tech. Phys. 50(11) (2005), pp. 1408–1416.
[381] A.V. Khomenko and I.A. Lyachenko, *Phase dynamics and kinetics of thin lubricant film driven by correlated temperature fluctuations*, Fluctuations Noise Lett. 7(2) (2007), pp. L111–L133.
[382] N.V. Priezjev, *Rate-dependent slip boundary conditions for simple fluids*, Phys. Rev. E 75(5) (2007), art#051605.
[383] S.F. Cheng, B.Q. Luan, and M.O. Robbins, *Contact and friction of nanoasperities: Effects of adsorbed monolayers*, Phys. Rev. E 81 (2010), art#016102.
[384] E. Granot, *Shearing a fermionic gas and quantized friction*, Europhys. Lett. 77(3) (2007), art#36002.
[385] J.B. Pendry, *Shearing the vacuum-quantum friction*, J. Phys.: Condens. Matter 9(47) (1997), pp. 10301–10320.
[386] J.B. Pendry, *Quantum friction-fact or fiction*? New J. Phys. 12 (2010), art#033028.
[387] A. Volokitin and B.N.J. Persson, *Theory of friction: The contribution from a fluctuating electromagnetic field*, Phys. Cond. Matt. 11 (1999), pp. 345–359.
[388] A.I. Volokitin and B.N.J. Persson, *Quantum friction*, Phys. Rev. Lett. 106 (2011), art#094502.
[389] A. Vanossi, N. Manini, G. Divitini, G.E. Santoro, and E. Tosatto, *Exactly quantized dynamics of classical incommensurate sliders*, Phys. Rev. Lett. 97 (2006), art#056101.
[390] O.M. Braun, A. Vanossi, and E. Tosatti, *Incommensurability of a confined system under shear*, Phys. Rev. Lett. 95 (2005), art#026102.
[391] I.E. Castelli, R. Manini, R. Capozza, A. Vanossi, G.E. Santoro, and E. Tosatti, *Role of transverse displacements for a quantized-velocity state of a lubricant*, J. Phys. Condens. Matter 20 (2008), art#354005.
[392] A. Vanossi, N. Manini, F. Caruso, G.E. Santoro, and E. Tosatti, *Static friction on the fly: Velocity depinning transitions of lubricants in motion*, Phys. Rev. Lett. 99 (2007), art#206101.
[393] I.E. Castelli, R. Capozza, A. Vanossi, G.E. Santoro, R. Manini, and E. Tosatti, *Tribology of the lubricant quantized state*, J. Chem. Phys. 131 (2009), art#174711.

[394] Y. Braiman, H.G.E. Hentschel, F. Family, C. Mak, and J. Krim, *Tuning friction with noise and disorder*, Phys. Rev. E 59(5) (1999), pp. R4737–R4740.
[395] T.S. Van Erp, A. Fasolino, O. Radulescu, and T. Janssen, *Pinning and phonon localization in Frenkel–Kontorova models on quasiperiodic substrates*, Phys. Rev. B 60 (1999), pp. 6522–6528.
[396] F. Family, H.G.E. Hentschel, and Y. Braiman, *Friction at the nanoscale*, J. Phys. Chem. B 104 (16) (2000), pp. 3984–3987.
[397] M.N. Popescu, C.M. Arizmendi, A.L. Salas-Brito, and F. Family, *Disorder induced diffusive transport in ratchets*, Phys. Rev. Lett. 85(15) (2000), pp. 3321–3324.
[398] X.Q. Luo, D. Wu, and S.Q. Zhu, *Transport in a ratchet with spatial disorder and time-delayed feedback*, Phys. Lett. A 372(12) (2008), pp. 2002–2009.
[399] Q.Y. Li and K.S. Kim, *Micromechanics of friction: Effects of nanometer-scale roughness*, Proc. R. Soc. A Math. Phys. Eng. Sci. 464 (2008), pp. 1319–1343.
[400] H. Holscher, D. Ebeling, and U.D. Schwarz, *Friction at atomic-scale surface steps: Experiment and theory*, Phys. Rev. Lett. 101 (2008), art#246105.
[401] C.V. Achim, J.A.P. Ramos, M. Karttunen, K.R. Elder, E. Granato, T. Ala-Nissila, and S.C. Ying, *Nonlinear driven response of a phase-field crystal in a periodic pinning potential*, Phys. Rev. E 79 (2009), art#011606.
[402] J.A.P. Ramos, E. Granato, S.C. Ying, C.V. Achim, K.R. Elder, and T. Ala-Nissila, *Dynamical transitions and sliding friction of the phase-field crystal model with pinning*, Phys. Rev. E 81 (2010), art# 011121.
[403] R. Budakian and S.J. Putterman, *Time scales for cold welding and the origins of stick–slip friction*, Phys. Rev. B 65(23) (2002), art#235429.
[404] C. Mak and J. Krim, *Quartz crystal microbalance of disorder-induced lubrication*, Faraday Discussions 107(107) (1997), pp. 389–397.
[405] R. Capozza, A. Vanossi, A. Vezzani, and S. Zapperi, *Suppression of friction by mechanical vibrations*, Phys. Rev. Lett. 103 (2009), art#085502.
[406] A. Socoliuc, E. Gnecco, S. Maier, O. Pfeiffer, A. Baratoff, R. Bennewitz, and E. Meyer, *Atomic-scale control of friction by actuation of nanometer-sized contacts*, Science 313 (2006), pp. 207–210.
[407] S.G.K. Tennakoon and R.P. Behringer, *Vertical and horizontal vibration of granular materials: Coulomb friction and a novel switching state*, Phys. Rev. Lett. 81(4) (1998), pp. 794–797.
[408] B.Q. Ai, L.G. Liu, and L.Q. Wang, *Transport reversal in a thermal ratchet*, Phys. Rev. B 72(3) (2005), art#031101.
[409] B.Q. Ai, L.G. Lin, and L.Q. Wang, *Brownian micro-engines and refrigerators in a spatially periodic temperature field: Heat flow and performances*, Phys. Lett. A 352(4–5) (2006), pp. 286–290.
[410] B.Q. Ai, H.Y. Liao, L.G. Lin, and H.Z. Xie, *Efficiency in a temporally asymmetric Brownian motor with stochastic potentials*, J. Stat. Mech.: Theory Exp. (2006), art#P09016.
[411] J.R. Lloyd and J.J. Clement, *Electromigration in copper conductors*, Thin Solid Films 262 (1995), pp. 135–141.
[412] B.N.J. Persson, *Surface resistivity and vibrational damping in adsorbed layers*, Phys. Rev. B 44(7) (1991), pp. 3277–3296.
[413] B.N.J. Persson and A.I. Volokitin, *Infrared reflection–adsorption spectroscopy of dipole-forbidden adsorbate vibrations*, Surf. Sci. 310(1–3) (1994), pp. 314–336.
[414] B.N.J. Persson, E. Tosatti, E. Fuhrmann, G. White, and C. Woll, *Low-frequency adsorbate vibrational relaxation and sliding friction*, Phys. Rev. B 59 (1999), pp. 11777–11791.
[415] G. Witte, K. Weiss, J. Jakob, J. Braun, K.L. Kostov, and C. Woll, *Damping of molecular motion on a solid substrate: Evidence for electron–hole pair creation*, Phys. Rev. Lett. 80 (1998), pp. 121–124.
[416] J.Y. Park, D.F. Ogletree, M. Salmeron, R.A. Ribeiro, P.C. Canfield, C.J. Jenks, and P.A. Thiel, *Tribological properties of quasicrystals: Effect of aperiodic vs. periodic surface order*, Phys. Rev. B 74 (2006), art#024203.
[417] Y.B. Qi, J.Y. Park, B.L.M. Hendriksen, D.F. Ogletree, and M. Salmeron, *Electronic contribution to friction on gas: An atomic force microscope study*, Phys. Rev. B 77(18) (2008), art#184105.
[418] D.Y. Li and Y.P. Li, *Prediction of elastic-contact friction of transition metals under light loads based on their electron work functions*, J. Phys. D: Appl. Phys. 40(19) (2007), pp. 5980–5983.

[419] B.L. Mason, S.M. Winder, and J. Krim, *On the current status of quartz crystal microbalance studies of superconductivity-dependent sliding friction*, Tribol. Lett. 10(1–2) (2001), pp. 59–65.
[420] M. Highland and J. Krim, *Superconductivity dependent friction of water, nitrogen, and superheated He films absorbed on Pb(111)*, Phys. Rev. Lett. 96 (2006), art#226107.
[421] Q.D. Ding, C. Li, L. Dong, M. Wang, Y. Peng, and X. Yan, *Preparation and properties of $YBa_2Cu_3O_{7-\delta}$/Ag self-lubricating composites*, Wear 265 (2008), pp. 1136–1141.
[422] V.L. Popov, *Electronic contribution to sliding friction in normal and superconducting states*, JETP Lett. 69(7) (1999), pp. 558–561.
[423] V.L. Popov, *Superslipperiness at low temperatures: Quantum mechanical aspects of solid state friction*, Phys. Rev. Lett. 83 (1999), pp. 1632–1635.
[424] T. Novotny and B. Velicky, *Electronic sliding friction of atoms physisorbed at superconductor surface*, Phys. Rev. Lett. 83(20) (1999), pp. 4112–4115.
[425] D.C. Langreth and M. Plihal, *Electronic friction in the presence of strong intra-atomic correlations for atoms moving near metal surfaces*, Phys. Rev. B 60(8) (1999), pp. 5969–5980.
[426] B.N.J. Persson, *Electronic friction on a superconducter surface*, Solid State Commun. 115(3) (2000), pp. 145–148.
[427] B.N.J. Persson and A.I. Volokitin, *Dissipative van der Waals interaction between a small particle and a metal surface*, Phys. Rev. B 65(11) (2002), art#115419.
[428] G.V. Dedkov and A.A. Kyasov, *Fluctuation-induced electromagnetic interaction of a moving particle with a plane surface*, Phys. Solid State 43(1) (2001), pp. 176–184.
[429] G.V. Dedkov and A.A. Kyasov, *Nonrelativistic theory of electromagnetic forces on particles and nanoprobes moving near a surface*, Phys. Low-Dimensional Struct. 1–2 (2003), pp. 1–86.
[430] G.V. Dedkov and A.A. Kyasov, *Vacuum attraction, friction and heating of nanoparticles moving nearby a heated surface*, J. Phys.: Condens. Matt. 20(35) (2008), art#354006.
[431] G.V. Dedkov and A.A. Kyasov, *Fluctuation–electromagnetic interaction of a moving neutral particle with a condensed-medium surface: Relativistic approach*, Phys. Solid State 51(1) (2009), pp. 1–26.
[432] J.E. Hirsch, *Superconductors as giant atoms predicted by the theory of hole superconductivity*, Phys. Lett. A 309(5–6) (2003), pp. 457–464.
[433] S.S. Rekhviashvili, *The phenomenon of decrease in the friction force upon transition to the superconducting state*, Tech. Phys. Lett. 30(1) (2004), pp. 4–5.
[434] L.D. Marks and A.P. Merkle, *A predictive analytical friction model from basic theories of interfaces, contacts and dislocations*, Tribol. Lett. 26(1) (2007), pp. 73–84.
[435] B.N.J. Persson, *Theory of damping of excited molecules located above a metal-surface*, J. Phys. C Solid State 11(20) (1978), pp. 4251–4269.
[436] B.N.J. Persson and M. Persson, *Vibrational lifetime for CO adsorbed on Cu(100)*, Solid State Commun. 36(2) (1980), pp. 175–179.
[437] W. Akemann and A. Otto, *Vibrational-modes of CO adsorbed on disordered copper-films*, J. Raman Spect. 22(12) (1991), pp. 797–803.
[438] B.N.J. Persson and R. Ryberg, *Brownian-motion and vibrational phase relaxation at surfaces – CO on Ni(111)*, Phys. Rev. B 32(6) (1985), pp. 3586–3596.
[439] B.N.J. Persson and E. Zaremba, *Electron–hole pair production at metal-surfaces*, Phys. Rev. B 31 (1985), pp. 1863–1872.
[440] B.N.J. Persson, *Applications of surface resistivity to atomic scale friction, to the migration of hot adatoms, and to electrochemistry*, J. Chem. Phys. 98(2) (1992), pp. 1659–1672.
[441] B.N.J. Persson and A.I. Volokitin, *Electronic friction of physisorbed molecules*, J. Chem. Phys. 103(19) (1995), pp. 8679–8683.
[442] A.I. Volokitin and B.N.J. Persson, *Near-field radiative heat transfer and noncontact friction*, Rev. Modern Phys. 79(4) (2007), pp. 1291–1329.
[443] A.I. Volokitin and B.N.J. Persson, *Radiative heat transfer and noncontact friction between nanostructures*, PHYSICS-USPEKHI 50(9) (2007), pp. 879–906.
[444] A.I. Volokitin and B.N.J. Persson, *Theory of the interaction forces and the radiative heat transfer between moving bodies*, Phy. Rev. B 78(15) (2008), art#155437.

[445] H. Ishida, *Semiclassical derivation of the surface-resistivity formula*, Phys. Rev. B 60(7) (1999), pp. 4532–4534.
[446] T. Janssen and C.V. Landauro, *Study of the conductivity of thin quasicrystalline films and its relation with the electronic friction*, Physica B: Condens. Matt. 348(1–4) (2004), pp. 459–464.
[447] D. Schumacher, *Probing the electronic friction via surface resistivity measurements*, in *Physics of Sliding Friction*, NATO ASI Series E: Applied Sciences Vol. 311, B.N.J. Persson and E. Tosatti, eds., Kluwer Academic Publishers, Dordrecht, the Netherlands, 1996, pp. 203–216.
[448] C.L. Hsu, E.F. McCullen, and R.G. Tobin, *Electron density changes and the surface resistivity of thin metal films: Oxygen on Cu(100)*, Surf. Sci. 481(1–3) (2001), pp. 198–204.
[449] R.G. Tobin, *Intralayer interaction effects on surface resistivity: Sulfur and oxygen on Cu(100)*, Surf. Sci. 524(1–3) (2003), pp. 183–190.
[450] C. Liu and R.G. Tobin, *Effects of interadsorbate interactions on surface resistivity: Oxygen on sulfur-predosed Cu(100)*, J. Chem. Phys. 128(24) (2008), art#244702.
[451] M.O. Robbins and J. Krim, *Energy dissipation in interfacial friction*, MRS Bull. 23 (1998), pp. 23–26.
[452] J. Braun, D. Fuhrmann, M. Bertino, A.P. Graham, J.P. Toennies, Ch. Wöll, A. Bilić, and B. Gumhalter, *Multiphonon He atom scattering from Xeoverlayers on Cu(111) and Cu(001) surfaces*, J. Chem. Phys. 106(23) (1997), pp. 9922–9929.
[453] A. Liebsch, S. Goncalves, and M. Kiwi, *Electronic versus phononic friction of xenon on silver*, Phys. Rev. B 60(7) (1999), pp. 5034–5043.
[454] M.O. Robbins and M.H. Muser, *CRC Handbook of Modern Tribology*, B. Bhushan, ed., CRC Press, Boca Raton, FL, 2000.
[455] M.O. Robbins and M.H. Muser, *Computer simulations of friction, lubrication and wear*, in *The Handbook of Modern Technology*, B. Bhushan, ed., CRC Press, Boca Raton, FL, 2010.
[456] V.L. Popov, *Electron and phonon mechanisms of friction in crystalline solids in atomically close contact at low temperatures*, Tech. Phys. 45(5) (2000), pp. 574–583.
[457] V.L. Popov, *Electronic and phononic friction of solids at low temperatures*, Tribol. Int. 34(4) (2001), pp. 277–286.
[458] R. Budakian, K. Weninger, R.A. Hiller, and S. Putterman, *Picosecond discharges and stick–slip friction at a moving meniscus of mercury on glass*, Nature (London) 391 (1998), pp. 266–268.
[459] R. Budakian and S.J. Putterman, *Correlation between charge transfer and stick–slip friction at a metal–insulator interface*, Phys. Rev. Lett. 85 (2000), pp. 1000–1003.
[460] C.G. Camara, J.V. Escobar, J.R. Hird, and S.J. Putterman, *Correlation between nanosecond X-ray flashes and stick–slip friction in peeling tape*, Nature 455 (2008), pp. 1089–U7.
[461] C. Wang and R. Gomer, *Adsorption and coadsorption with oxygen of xenon on the (110) and (100) planes of tungsten*, Surf. Sci. 91(2–3) (1980), pp. 533–550.
[462] M. Pierno, L. Bruschi, G. Fois, G. Mistura, C. Boragno, F. Buatier de Mongeot, and U. Valbusa, *Nanofriction of neon films on superconducting lead*, Phys. Rev. Lett. 105 (2010), art#016102.
[463] E. Lynton, *Superconductivity*, Methuen, London, 1969; Mir, Moscow, 1971.
[464] L.W. Bruch and F.Y. Hansen, *Monolayer solid of N_2/Ag(111)*, Phys. Rev. B 57(15) (1998), pp. 9285–9292.
[465] Y. Liao and L.D. Marks, *Modeling of thermal-assisted dislocation friction*, Tribol. Lett. 37 (2010), pp. 283–288.
[466] A.P. Merkle and L.D. Marks, *A predictive analytical friction model from basic theories of interfaces, contacts and dislocations*, Tribol. Lett. 26 (2007a), pp. 73–84.
[467] A. Gerber and G. Deutscher, *Upper critical-field of superconducting Pb films above and below the percolation-threshold*, Phys. Rev. Lett. 63 (1989), pp. 1184–1186.
[468] V. Andrea, B.R. Alan, and B. Virginio, *Role of substrate geometry in sliding friction*, Nanotechnology 15 (2004), pp. 790–794.
[469] J.E. Hunter, W.P. Reinhardt, and C. Seagraves, *Frictional effects in the simulation of polymers pulled around smooth and corrugated posts*, J. Chem. Phys. 110(12) (1999), pp. 6066–6078.
[470] J. Krim, I. Heyvaert, C. Van Haesendonck, and Y. Brunseraede, *Scanning tunneling microscopy observation of self-affine fractal roughness in ion-bombarded film surfaces*, Phys. Rev. Lett. 70 (1993), pp. 57–61.

[471] S.M. Lee and J. Krim, *Scanning tunneling microscopy characterization of the surface morphology of copper films grown on mica and quartz*, Thin Solid Films 489(1–2) (2005), pp. 325–329.
[472] M. Reguzzoni, M. Ferrario, S. Zapperi, and M.C. Righi, *Onset of frictional slip by domain nucleation in adsorbed monolayers*, Proc. Natl. Acad. USA 107 (2010), pp. 1311–1316.
[473] J. Krim and G. Palasantzas, *Experimental observations of self-affine scaling and kinetic roughening at sub-micron lengthscales*, Int. J. Mod. Phys. B 9 (1995), pp. 599–632.
[474] Y. Larher, *The critical exponent β associated with the two-dimensional condensation in the second adlayer of argon on the cleavage face of cadmium chloride*, Mol. Phys. 38 (1979), pp. 789–795.
[475] J. Krim, J.G. Dash, and J. Suzanne, *Triple-point wetting of light molecular gases on Au(111) surfaces*, Phys. Rev. Lett. 52(8) (1984), pp. 640–643.
[476] H. Kobayashi, J. Taniguchi, M. Suzuki, K. Miura, and I. Arakawa, *Sliding friction of Kr films adsorbed on graphite*, J. Phys. Soc. Jpn. 79 (2010), art#014602.
[477] M. Chester, J.B. Stephens, and L.C. Yang, *Quartz microbalance studies of an adsorbed helium film*, Phys. Rev. Lett. 29(4) (1972), pp. 211–214.
[478] M. Chester and L.C. Yang, *Superfluid fraction in thin helium films*, Phys. Rev. Lett. 31(23) (1973), pp. 1377–1380.
[479] T. Koike, M. Hieda, and M. Suzuki, *Slippage of nonsuperfluid He-4 films on Ag*, J. Low Temp. Phys. 126 (2002), pp. 391–396.
[480] K. Wataru, J. Taniguchi, M. Hieda, and M. Suzuki, *Slippage of He-4 adsorbed on porous gold*, J. Phys. Chem. Solids 66 (2005), pp. 1535–1538.
[481] N. Wada, T. Matsushita, M. Hieda, and R. Toda, *Fluid state of helium adsorbed in nanopores*, J. Low Temp. Phys. 157 (2009), pp. 324–351.
[482] T. Ogura, N. Hosomi, M. Hieda, and M. Suzuki, *QCM studies of 4He films adsorbed on grafoil*, Physica B 329–333 (2003), pp. 256–257.
[483] M. Suzuki, N. Hosomi, A. Tanabe, and M. Hieda, *Slippage of nonsuperfluid 4He films adsorbed on grafoil*, J. Phys. Chem. Solids 66 (2005), pp. 1527–1531.
[484] M. Hieda, M. Suzuki, J. Taniguchi, and K. Wataru, *Slippage of He-4 films adsorbed on porous gold*, J. Phys. Chem. Solids 66(8–9) (2005), pp. 1535–1538.
[485] M. Hieda, N. Hosomi, M. Suzuki, and A. Tanabe, *Slippage of nonsuperfluid He-4 films adsorbed on grafoil*, J. Phys. Chem. Solids 66(8–9) (2005), pp. 1527–1531.
[486] N. Hosomi and M. Suzuki, *Sliding friction of multilayer He-4 films absorbed on graphite*, Phys. Rev. B 77(2) (2008), art#024501.
[487] N. Hosomi, A. Tanabe, M. Suzuki, and M. Hieda, *Sliding friction of helium films in the metastable state and its relaxation*, Phys. Rev. B 75(6) (2007), art#064513.
[488] N. Hosomi, T. Minoguchi, M. Suzuki, and J. Taniguchi, *Dynamical sticking of a solid He-4 film with superfluid overlayer*, Phys. Rev. B 79(17) (2009), art#172503.
[489] A. Casey, B. Cowan, J. Parpia, J. Saunders, and R. Schanen, *Interfacial friction of thin He-3 slabs in the Knudsen limit*, Phys. Rev. Lett. 92(25) (2004), art#255301.
[490] M. Hieda, T. Nishino, M. Suzuki, N. Wada, and K. Torii, *Slippage of nonsuperfluid helium films*, Phys. Rev. Lett. 85 (2000), pp. 5142–5145.
[491] L. Bruschi, M. Pierno, G. Fois, F. Ancilotto, G. Mistura, C. Boragno, F.B. de Mongeot, and U. Valbusa, *Friction reduction of Ne monolayers on preplated metal surfaces*, Phys. Rev. B 81 (2010), art#115419.
[492] M. Highland, *Superconductivity dependent sliding friction*, Ph.D. diss., North Carolina State University, Raleigh, NC, 2005.
[493] G. Fois, L. Bruschi, L. d'Apolito, G. Mistura, B. Torre, F.B. de Mongeot, C. Boragno, R. Buzio, and U. Valbusa, *Low-temperature static friction of N-2 monolayers on Pb(111)*, J. Phys.: Condens. Matt. 19(30) (2007), art#305013.
[494] A. Widom and J. Krim, *Q-factors of quartz oscillator modes as a probe of submonolayer film dynamics*, Phys. Rev. B Rapid Commun. 34 (1986), pp. R3–R6.
[495] E. Granato and S.C. Ying, *Nonlinear sliding friction of adsorbed overlayers on disordered substrates*, Phys. Rev. B 69 (2004), art#125403.
[496] A. Thomy and X. Duval, *Stepwise isotherms and phase transitions in physisorbed films*, Surf. Sci. 299/300 (1994), pp. 415–425.

[497] M. Bienfait, *Two-dimensional melting and polymorphism in adsorbed phases*, Surf. Sci. 89 (1979), pp. 13–27.
[498] M. Walker, C. Jaye, J. Krim, and M.W. Cole, *Frictional temperature rise in a sliding physisorbed monolayer of Kr/graphene*, J. Phys.: Condensed Matter, in press.
[499] C. Daly and J. Krim, *Sliding friction of compressing Xe monolayers*, in *Micro/Nanotribology and Its Applications*, B. Bhushan, ed., Kluwer Academic Publishers, Dordrecht, the Netherlands, 1997, p. 311.
[500] S. Goncalves, M. Kiwi, and A. Liebsch, *Electronic versus phononic friction of xenon on silver*, Phys. Rev. B 60(7) (1999), pp. 5034–5043.
[501] V. Bortolani, M. Brigazzi, A. Franchini, and G. Santoro, *Theoretical investigation of the anticorrugation effects on the tribological properties of the Xe/Cu interface*, J. Phys.: Condens. Matt. 21(26) (2009), art#264008.
[502] J. Chen, I. Ratera, J.Y. Park, and M. Salmeron, *Velocity dependence of friction and hydrogen bonding effects*, Phys. Rev. Lett. 96(23) (2006), art#236102.
[503] S. Ciraci and S. Dag, *Atomic scale study of superlow friction between hydrogenated diamond surfaces*, Phys. Rev. B 70(24) (2004), art#241401.
[504] J.A. Harrison, C.T. White, R.J. Colton, and D.W. Brenner, *Investigation of the atomic-scale friction and energy dissipation in diamond using molecular dynamics*, Thin Solid Films 260 (1995), pp. 205–211.
[505] J.A. Harrison, S.J. Stuart, and M.D. Perry, *The tribology of hydrocarbon surfaces investigated using molecular dynamics*, in *Tribology Issues and Opportunities in MEMS*, B. Bhushen, ed., Kluwer Academic Publishers, Dordrecht, the Netherlands, 1998, pp. 285–300, in Ref. [17].
[506] A.B. Tutein, S.J. Stuart, and J.A. Harrison, *Role of defects in compression and friction of anchored hydrocarbon chains on diamond*, Langmuir 16(2) (2000), pp. 291–296.
[507] J.D. Schall, G. Gao, and J.A. Harrison, *The effects of adhesion and transfer film formation on the tribology of self-mated DLC contacts*, J. Phys. Chem. C 114 (2010), pp. 5321–5330.
[508] J. Krim, E.T. Watts, and J. Digel, *Slippage of simple liquid-films absorbed on silver and gold substrates*, J. Vac. Sci. Technol. 8(4) (1990), pp. 3417–3420.
[509] R.L. Renner, J.E. Rutledge, and P. Taborek, *Quartz microbalance studies of superconductivity-dependent sliding friction*, Phys. Rev. Lett. 83(6) (1999), pp. 1261–1261.
[510] R.L. Renner, P. Taborek, and J.E. Rutledge, *Friction and pinning of nitrogen films on lead substrates near the superconducting transition*, Phys. Rev. B 63(23) (2001), art#233405.
[511] C. Mak, C. Daly, and J. Krim, *Atomic-scale friction measurements on silver and chemisorbed oxygen surfaces*, Thin Solid Films 253(1–2) (1994), pp. 190–193.
[512] P.B. Merrill and S.S. Perry, *Fundamental measurements of the friction of clean and oxygen-covered VC(100) with ultrahigh vacuum atomic force microscopy: Evidence for electronic contributions to interfacial friction*, Surf. Sci. 418 (1998), pp. 342–351.
[513] P. Frantz, S.Y. Didzuilis, P.B. Merrill, and S.S. Perry, *Spectroscopic and scanning probe studies of oxygen and water on metal carbide surfaces*, Tribol. Lett. 4(2) (1998), pp. 141–148.
[514] M. Abdelmaksoud, J.W. Bender, and J. Krim, *Bridging the gap between macro- and nanotribology: A quartz crystal microbalance study of the tricresylphosphate uptake on metal and oxide surfaces*, Phys. Rev. Lett. 92 (2004), art#176101.
[515] C. Liu and R.G. Tobin, *Bonding-site dependence of surface resistivity: CO on epitaxial Cu(100) films*, J. Chem. Phys. 126(12) (2007), art#124705.
[516] K.B. Jinesh and J.W.M. Frenken, *Capillary condensation in atomic scale friction: How water acts like a glue*, Phys. Rev. Lett. 96 (2006), art#166103.
[517] L. Brigo, M. Natali, M. Pierno, F. Mammano, C. Sada, G. Fois, A. Pozzato, S. dal Zilio, M. Tormen, and G. Misture, *Water slip and friction at a solid surface*, J. Phys. Condens. Matter 20(35) (2008), art#354016.
[518] B.I. Choi, J.C. Kim, and S.Y. Kwon, *Recognition of supercooled dew in a quartz crystal microbalance dew-point sensor by slip phenomena*, Metrologia 44(5) (2007), pp. L37–L40.
[519] A.M. Trunfio-Sfarghiu, Y. Berthier, M.H. Meurisse, and J.P. Rieu, *Role of nanomechanical properties in the tribological performance of phospholipid biomimetic surfaces*, Langmuir, 24 (2008), pp. 8765–8771.

[520] U. Raviv, P. Laurat, and J. Klein, *Fluidity of water confined to sub-nanometre films*, Nature 413 (2001), pp. 51–54.
[521] U. Raviv and J. Klein, *Fluidity of bound hydration water*, Science 297 (2002), pp. 1540–1543.
[522] W.H. Briscoe, S. Titmuss, F. Tiberg, R.K. Thomas, D.J. McGillivray, and J. Klein, *Boundary lubrication under water*, Nature 444 (2006), pp. 191–194.
[523] Y. Leng and P.T. Cummings, *Fluidity of hydration layers nanoconfined between mica surfaces*, Phys. Rev. Lett. 94 (2005), art#026101.
[524] Y. Leng and P.T. Cummings, Hydration structure of water confined between mica *Surfaces*, J. Chem. Phys, 124 (2006), art#074711.
[525] T.D. Li, J. Gao, R. Szoszkiewicz, U. Landman, and E. Riedo, *Structured and viscous water in subnanometer gaps*, Phys. Rev. B 75 (2007), art#115415.
[526] T.D. Li and E. Riedo, *Nonlinear viscoelastic dynamics of nanoconfined wetting liquids*, Phys. Rev. Lett. 100 (2008), art#106102.
[527] O.I. Vinogradova, *Slippage of water over hydrophobic surfaces*, Int. J. Miner. Process 56 (1999), pp. 31–60.
[528] M. Binggeli and C.M. Mate, *Influence of capillary condensation of water on nanotribology studied by force microscopy*, Appl. Phys. Lett. 65(4) (1994), pp. 415–417.
[529] L.L. Lee, D.V. Papavassiliou, and R.S. Voronov, *Boundary slip and wetting properties of interfaces: Correlation of the contact angle with the slip length*, J. Chem. Phys. 124(20) (2006), art#204701.
[530] T. Fukuma, Y. Ueda, S. Yoshioka, and H. Asakawa, *Scale distribution of water molecules at the mica–water interface visualized by three-dimensional scanning force microscopy*, Phys. Rev. Lett. 104 (2010), art#016101.
[531] J.W.M. Frenken and T.H. Oosterkamp, *When mica and water meet*, Nature 464 (2010), pp. 38–39.
[532] M. Chen, W.H. Briscoe, S.P. Armes, and J. Klein, *Lubrication at physiological pressures by polyzwitterionic brushes*, Science 323 (2009), pp. 1698–1701.
[533] R. Goldberg, A. Schroeder, G. Silbert, K. Turjeman, Y. Barenholz, and J. Klein, *Boundary lubricants with exceptionally low friction coefficients based on 2D close-packed phosphatidylcholine liposomes*, Adv. Mater. 23 (2011), pp. 3517–3521.
[534] R. Pit, H. Hervet, and L. Leger, *Direct experimental evidence of slip in hexadecane: Solid interfaces*, Phys. Rev. Lett. 85 (2000), pp. 980–983.
[535] R.C. Major, H.I. Kim, J.E. Houston, and X.Y. Zhu, *Tribological properties of alkoxyl monolayers on oxide terminated silicon*, Tribol. Lett. 14 (2003), pp. 237–244.
[536] B.P. Miller and J. Krim, *Sliding friction measurements of molecularly thin ethanol and pentanol films: How friction and spreading impact lubricity*, J. Low Temp. Phys. 157 (2009), pp. 252–267.
[537] T.S. Coffey, M. Abdelmaksoud, and J. Krim, *A scanning probe and quartz crystal microbalance study of the impact of C60 on friction at solid–liquid interfaces*, J. Phys. Condens. Matter, Special Issue 13 (2001), pp. 4991–4999.
[538] D.W. Brenner, D.L. Irving, A.L. Kingon, and J. Krim, *Multiscale analysis of liquid lubrication trends from industrial machines to micro-electrical-mechanical systems*, Langmuir 23(18) (2007), pp. 9253–9257.
[539] T.S. Coffey and J. Krim, *C-60 molecular bearings and the phenomenon of nanomapping*, Phys. Rev. Lett. 96(18) (2006), art#186104.
[540] N. Forster, *Rolling contact testing of vapor phase lubricants. III. Surface analysis*, Tribol. Trans. 40 (1999), pp. 1–9.
[541] M. Suzuki, *Characterization of monolayer and bilary (polymer monolayer) structures for their use as a lubricant*, Thin Solid Films 160 (1988), pp. 453–462.
[542] L.E. Bailey, C.W. Frank, D. Johannsmann, A. Laschitsch, and G.W. Tyndall, *Frictional properties of perfluoropolyether monolayers investigated with quartz resonators*, Appl. Phys. Lett. 78(17) (2001), pp. 2601–2603.
[543] M.K. Banerjee, V.V. Krylov, G. McHale, and M.I. Newton, *Surface acoustic wave resonances in the spreading of viscous fluids*, Phys. Rev. B 59(12) (1999), pp. 8262–8270.
[544] W.D. Luedtke and U. Landman, *Structure, dynamics and thermodynamics of passivated gold nanocrystals and their assemblies*, J. Phys. Chem. 100 (1996), pp. 13323–13329.

[545] L.J. Lewis, P. Jensen, and J.L. Barrat, *Melting, freezing and coalescence of gold nanoclusters*, Phys. Rev. B 56 (1997), pp. 2248–2257.
[546] P. Deltour, J.L. Barrat, and P. Jensen, *Fast diffusion of a Lennard-Jones cluster on a crystalline surface*, Phys. Rev. Lett. 78(24) (1997), pp. 4597–4600.
[547] V.N. Antonov, A.S. Bhatti, J.S. Palmer, and J.H. Weaver, *Nanostructure diffusion and aggregation on desorbing rare-gas solids: Slip on an incommensurate lattice*, Phys. Rev. B 60(20) (2003), art#205418.
[548] I.G. Marchenko and I.M. Neklyudov, *Study of the mobility of small copper clusters on a xenon buffer layer at temperatures of 30–70 K*, Low Temp. Phys. 32(10) (2006), pp. 957–960.
[549] E.I. Altman and R.J. Colton, *Interaction of C60 with noble metal surfaces: Adsorption of fullerenes on Cu(111) and Ag(111) surfaces*, Surf. Sci. 295 (1993), pp. 13–33.
[550] V. Bortolani, M. Brigazzi, A. Franchini, and G. Santoro, *Simulations of the temperature dependence of static friction at the N-2/Pb interface*, J. Phys.: Condens. Matt. 19(30) (2007), art#305014.
[551] J.F. Jia, S.C. Li, Q.K. Xue, and Y.F. Zhang, *Quantum size effects induced novel properties in two-dimensional electronic systems: Pb thin films on Si(111)*, J. Phys. Soc. Jpn. 76(8) (2007), art#082001.
[552] G.C. Dong, T.Z. Han, J.F. Jia, Q.T. Shen, Q.K. Xue, and Y.F. Zhang, *Adhesion modulation by quantum size effects in Pb/Si(111) system*, Appl. Phys. Lett. 89(18) (2006), art#183109.
[553] I.B. Altfeder, J. Hu, A. Voevodin, and J. Krim, *Magic-sized diamond nanocrystals*, Phys. Rev. Lett. 102 (2009), art#136104.
[554] J.G. Dash, *Films on Solid Surfaces: Physics and Chemistry of Physical Adsorption*, Academic Press, New York, 1975, 284 pp.
[555] R.D. Boutchko and L.W. Bruch, *Brownian friction of gas molecules on the graphite surface*, Phys. Rev. B 59(16) (1999), pp. 10992–10995.
[556] M. Enachescu, R.J.A. van den Oetelaar, R.W. Carpick, D.F. Ogletree, C.F.J. Flipse, and M. Slameron, *Atomic force microscopy study of an ideally hard contact: The diamond(111) tungsten carbide interface*, Phys. Rev. Lett. 81(9) (1998), pp. 1877–1880.
[557] S.K. Sinha (ed.), *Ordering in Two-Dimensions*, North Holland, New York, 1980.
[558] J.A. Venables, *Introduction to Surface and Thin Film Processes*, Cambridge University Press, Cambridge, 2000, p. 116.
[559] H. Brune, J. Chevrier, F. Comin, and E. Riedo, *Nanotribology of carbon based thin films: The influence of film structure and surface morphology*, Surf. Sci. 477(1) (2001), pp. 25–34.
[560] M. Lucas, Z. Zhang, I. Palaci, C. Klinke, E. Tosatti, and E. Riedo, *Hindered rolling and friction anisotropy in supported carbon nanotubes*, Nat. Mater. 8 (2009), pp. 876–881.
[561] K.S. Nagapriya, O. Goldbart, I. Kaplan-Ashiri, G. Seifert, R. Tenne, and E. Joselevich, *Torsional stick–slip behavior in WS(2) nanotubes*, Phys. Rev. Lett. 19 (2008), art#195501.
[562] A.R. Konicek, D.S. Grierson, P.U.P.A. Gilbert, W.G. Sawyer, A.V. Sumant, and R.W. Carpick, *Origin of ultralow friction and wear in ultrananocrystalline diamond*, Phys. Rev. Lett. 100(23) (2008), art#235502.
[563] C. Lee, Q.Y. Li, W. Kalb, X.Z. Liu, H. Berger, R.W. Carpick, and J. Hone, *Frictional characteristics of atomically thin sheet*s, Science 328 (2010), pp. 76–80.
[564] R.A. Trasca, M.W. Cole, T. Coffey, and J. Krim, *Gas absorption on a C-60 monolayer*, Phys. Rev. E 77(4) (2008), art#041603.
[565] R. Luthi, E. Meyer, H. Haefke, L. Howald, W. Gutmannsbauer, and H.J. Guntherodt, *Sled-type motion on the nanometer-scale-determination of dissipation and cohesive energies of C-60*, Science 266(5193) (1994), pp. 1979–1981.
[566] T. Sakurai, X.D. Wang, T. Hashizume, V. Yurov, H. Shinohara, and H.W. Pickering, *Adsorption of fullerenes on Cu (111) and Ag (111) surfaces*, Appl. Surf. Sci. 87/88 (1995), pp. 405–413.
[567] S.E. Campbell, G. Luengo, V.I. Srdanov, F. Wudl, and J.N. Israelachvili, *Very low viscosity at the solid–liquid interface induced by adsorbed C-60 monolayers*, Nature 382(6591) (1996), pp. 520–522.
[568] Q. Liang, O.K.C. Tsui, Y.B. Xu, H.N. Li, and X.D. Xiao, *Effect of C-60 molecular rotation on nanotribology*, Phys. Rev. Lett. 90 (2003), art#146102.
[569] H.N. Li, Q. Liang, and X.D. Xiao, *Friction and adhesion between C-60 single crystal surfaces and AFM tips: Effects of the orientational phase transition*, J. Phys. Chem. B 100(1) (2006), pp. 403–409.

[570] R. Maboudian and R.T. Howe, *Stiction reduction processes for surface micromachines*, Tribol. Lett. 3 (1997), pp. 215–221.
[571] B.P. Miller, N.D. Theodore, M.J. Brukman, K.J. Wahl, and J. Krim, *A nano- to macroscale tribological study of PFTS and TCP lubricants for Si MEMS applications*, Tribol. Lett. 38 (2010), pp. 69–78.
[572] T.M. Mayer, M.P. deBoer, N.D. Shinn, P.J. Clews, and T.A. Michalske, *Chemical vapor deposition of fluoroalkylsilane monolayer films for adhesion control in microelectromechanical systems*, J. Vac. Sci. Technol. B 18(5) (2000), pp. 2433–2440.
[573] S. Onclin, B.J. Ravoo and D.N. Reinhoudt, *Engineering silicon oxide surfaces using self-assembled monolayers*, Angew. Chem. Int. Ed. Engl. 44 (2005), pp. 6282–6304.
[574] D.B. Asay, M.T. Dugger, J.A. Ohlhausen, and S.H. Kim, *Macro- to nano-scale wear prevention via molecular adsorption*, Langmuir 24 (2008), pp. 155–159.
[575] D.B. Asay, M.T. Dugger, and S.H. Kim, *In-situ vapor-phase lubrication of MEMS*, Tribol. Lett. 29 (2008), pp. 67–74.
[576] A.L. Barnette, D.B. Asay, D. Kim, B.D. Guyer, H. Lim, M.J. Janik, and S.H. Kim, *Experimental and density functional theory study of the tribochemical wear behavior of SiO_2 in humid and alcohol vapor environments*, Langmuir 25 (2009), pp. 13052–13061.
[577] B. Bhushan (ed.), *NSF/AFOSRlASME Workshop on Tribology Issues and Opportunities in MEMS*, Kluwer Academic Publishers, Dordrecht, the Netherlands, 1997.
[578] M.J. Brukman, G. Oncins Marco, T.D. Dunbar, L.D. Boardman, and R.W. Carpick, *Nanotribological properties of alkanephosphonic acid self-assembled monolayers on aluminum oxide: Effects of fluorination and substrate crystallinity*, Langmuir 22 (2006), pp. 3988–3998.
[579] H.I. Kim, V. Boiadjiev, J.E. Houston, X.Y. Zhu, and J.D. Kiely, *Tribological properties of self-assembled monolayers on Au, SiO_x and Si surfaces*, Tribol. Lett. 10 (2001), pp. 97–101.
[580] X.Y. Zhu and J.E. Houston, *Molecular lubricants for silicon-based microelectromechanical systems (MEMS): A novel assembly strategy*, Tribol. Lett. 7 (1999), pp. 87–90.
[581] B.J. Briscoe and D.C.B. Evans, *The shear properties of Langmuir–Blodgett layers*, Proc. Math. Phys. Eng. Sci. 380 (1982), pp. 389–407.
[582] J. Seto, T. Nagai, C. Ishimoto, and H. Watanabe, *Frictional properties of magnetic media coated with Langmuir–Blodgett films*, Thin Solid Films 134 (1985), p. 101.
[583] Y.N. Zhang, F. Hanke, V. Bortolani, M. Persson, and R.Q. Wu, *Why sliding friction of Ne and Kr monolayers is so different on the Pb (111) surface*, Phys. Rev. Lett. 106(23) (2011), art#236103.
[584] V. DePalma and N. Tillman, *Friction and wear of self-assembled trichlorosilane monolayer films on silicon*, Langmuir 5 (1989), pp. 868–872.
[585] R.W. Carpick, D.Y. Sasaki, and A.R. Bums, *Large friction anisotropy of a polydiacetylene monolayer*, Tribol. Lett. 7(2–3) (1999), pp. 79–85.
[586] S.A. Joyce, R.C. Thomas, J.E. Houston, T.A. Michalske, and R.M. Crooks, *Mechanical relaxation of organic monolayer films measured by force microscopy*, Phys. Rev. Lett. 68 (1992), pp. 2790–2793.
[587] C.D. Frisbie, L.F. Rozsnyai, A. Noy, M.S. Wrighton, and C.M. Lieber, *Functional group imaging by chemical force microscopy*, Science 265 (1994), pp. 2071–2074.
[588] J.B.D. Green, M.T. McDermott, M.D. Porter, and L.M. Siperko, *Nanometer-scale mapping of chemically distinct domains at well-defined organic interfaces using frictional force microscopy*, J. Phys. Chem. 99 (1995), pp. 10960–10965.
[589] E. Barrena, S. Kopta, D.F. Ogletree, D.H. Charych, and M. Salmeron, *Relationship between friction and molecular structure: Alkylsilane lubricant films under pressure*, Phys. Rev. Lett. 82 (1999), pp. 2880–2883.
[590] P. Cao, R. Colorado, M. Graupe, T.R. Lee, S.S. Perry, O.E. Shmakova, L. Shuang, I. Wenzl, and X.P. Yan, *Local packing environment strongly influences the frictional properties of mixed CH3- and CF3-terminated alkanethiol SAMs on Au(111)*, Langmuir 21(3) (2005), pp. 933–936.
[591] X. Xiao, J. Hu, D.H. Charych, M. Salmeron, *Chain length dependence of the frictional properties of alkylsilane molecules self-assembled on mica studied by atomic force microscopy*, Langmuir 12(2) (1996), pp. 235–237.
[592] X.D. Xiao, X.C. Xie, Y. Xiong, and L. Zuo, *Enhanced lubricity in mixed alkanethiol monolayer*, J. Phys. Chem. B 109(48) (2005), pp. 22971–22975.

[593] W.R. Ashurst, C. Yau, C. Carraro, R. Maboudian, and M.T. Dugger, *Dichlorodimethylsilane as an anti-stiction monolayer for MEMS: A comparison to the octadecyltrichlorosilane self-assembled monolayer*, J. Microelectromech. Syst. 10(1) (2001), pp. 41–49.

[594] E. Barrena, C. Ocal, and M. Salmeron, *Molecular packing changes of alkanethiols monolayers on Au(111) under applied pressure*, J. Chem. Phys. 113 (2000), pp. 2413–2418.

[595] J. Klein, E. Kumacheva, D. Mahalu, D. Perahia, and L.J. Fetters, *Reduction of frictional forces between solid-surfaces bearing polymer brushes*, Nature 370(6491) (1994), pp. 634–636.

[596] A. Lio, D.H. Charych, and M. Salmeron, *Comparative atomic force microscopy study of the chain length dependence of frictional properties of alkanethiols on gold and alkylsilanes on mica*, J. Phys. Chem. B 101 (1997), pp. 3800–3805.

[597] E. Meyer, R.M. Overney, D. Brodbeck, L. Howald, R. Luthi, J. Frommer, and H.-J. Gunngherodt, *Friction and wear of Langmuir–Blodgett films observed by friction force microscopy*, Phys. Rev. Lett. 69(12) (1992), pp. 1777–1780.

[598] P.T. Mikulski and J.A. Harrison, *Periodicities in the properties associated with the friction of model self-assembled monolayers*, Tribol. Lett. 10(1–2) (2001), pp. 29–35.

[599] U. Srinivasan, *Alkyltrichlorosilane-based self-assembled monolayer films for stiction reduction in silicon micromachines*, J. Microelectromech. Syst. 7 (1998), pp. 252–260.

[600] M.J. Stevens, M.R. Houston, R.T. Howe, and R. Maboudian, *Thoughts on the structure of alkylsilane monolayers*, Langmuir 15 (1999), pp. 2773–2778.

[601] T.A. Witten, L. Leibler, and P.A. Pincus, *Stress-relaxation in the lamellar copolymer mesophase*, Macromolecules 23 (1990), pp. 824–829.

[602] G. Luengo, F.J. Schmitt, R. Hill, and J. Israelachvili, *Thin film rheology and tribology of confined polymer melts: Contrasts with bulk properties*, Macromolecules 30(8) (1997), pp. 824–829.

[603] M. Chandross, G.S. Grest, and M.J. Stevens, *Friction between alkylsilane monolayers: Molecular simulation of ordered monolayers*, Langmuir 18(22) (2002), pp. 8392–8399.

[604] P.A. Schorr, T.C.B. Kwan, S.M. Kilbey, E.S.G. Shaqfeh, and M. Tirrell, *Shear forces between tethered polymer chains as a function of compression, sliding velocity and solvent quality*, Macromolecules 36 (2003), pp. 389–398.

[605] U. Raviv, S. Giasson, N. Kampf, J.F. Gohy, R. Jerome, and J. Klein, *Lubrication by charged polymers*, Nature 425 (2003), pp. 163–165.

[606] T. Kreer, K. Binder, and M.H. Muser, *Friction between polymer brushes in good solvent conditions: Steady state sliding vs. transient behavior*, Langmuir 19 (2003), pp. 7551–7559.

[607] N. Kampf, U. Raviv, and J. Klein, *Normal and shear forces between adsorbed and gelled layers of chitosan, a naturally occurring cationic polyelectrolyte*, Macromolecules 37 (2004), pp. 1134–1142.

[608] W. Hartung, T. Drobek, S. Lee, S. Zurcher, and N.D. Spencer, *The influence of anchoring-group structure on the lubricating properties of brush-forming graft copolymers in an aqueous medium*, Tribol. Lett. 31 (2008), pp. 119–128.

[609] J.B. Sokoloff, *Theory of the observed ultralow friction between sliding polyelectrolyte brushes*, J. Chem. Phys. 129 (2008), art#014901.

[610] J.B. Sokoloff and I. Webman, *Theory of depinning of monolayer films adsorbed on a quartz crystal microbalance*, Phys. Rev. E 77 (2008), art#042601.

[611] U. Raviv, S. Giasson, N. Kampf, J.F. Gohy, R. Jerome, and J. Klein, *Normal and frictional forces between surfaces bearing polyelectrolyte brushes*, Langmuir 24 (2008), pp. 8678–8687.

[612] M. Chandross, C.D. Lorenz, M.J. Stevens, and G.S. Grest, *Simulations of nanotribology with realistic probe tip models*, Langmuir 24(4) (2008), pp. 1240–1246.

[613] D.L. Irving and D.W. Brenner, *Diffusion on a self-assembled monolayer: Molecular modeling of a bound plus mobile lubricant*, J. Phys. Chem. B 110 (2006), pp. 15426–15431.

[614] R.L. Jones, B.L. Harrod, and J.D. Batteas, *Intercalation of 3-phenyl-1-proponal into OTS SAMs on silica nanoasperities to create self-repairing interfaces for MEMS lubrication*, Langmuir 26 (2010), pp. 16355–16361.

[615] W. Neeyakorn, M. Varma, C. Jaye, J.E. Burnette, S.M. Lee, R.J. Nemanich, C.S. Grant, and J. Krim, *Dynamics of vapor-phase organophosphates on silicon and OTS*, Tribol. Lett. 27 (2007), pp. 269–276.

[616] D. Fuhrmann, B.N.J. Persson, E. Tosatti, G. Witte, and C. Woll, *Low-frequency adsorbate vibrational relaxation and sliding friction*, Phys. Rev. B 59(18) (1999), pp. 11777–11791.
[617] Y.Z. Hu, H. Wang, and T. Zhang, *Simulations on atomic-scale friction between self-assembled monolayers: Phononic energy dissipation*, Tribol. Int. 40(4) (2007), pp. 680–686.
[618] P.E. Sheehan and C.M. Lieber, *Nanotribology and nanofabrication of MoO_3 structures by atomic force microscopy*, Science 272 (1996), pp. 1158–1161.
[619] M. Hirano, K. Shinjo, R. Kanko, and Y. Murata, *Observation of superlubricity by scanning tunneling microscopy*, Phys. Rev. Lett. 78(8) (1997), pp. 1448–1451.
[620] J.S. Ko and A.J. Gellman, *Friction anisotropy at Ni(100)/Ni(100) interfaces*, Langmuir 16 (2000), pp. 8343–8351.
[621] E.F. McFadden and A.J. Gellman, *Recent progress in ultrahigh vacuum tribometry*, Tribol. Lett. 4(2) (1998), pp. 155–161.
[622] C.M. Mancinelli and A.J. Gellman, *Friction anisotropy at Pd(100)/Pd(100) interfaces*, Langmuir 20 (2004), pp. 1680–1687.
[623] T.S. Coffey, *Nanotribology fundamentals: Predicting the viscous coefficient of friction*, Ph.D. diss., North Carolina State University, 2004.
[624] P. Mohandas, C.P. Lusher, V.A. Mikheev, B. Cowan, and J. Saunders, *Interfacial friction of submonolayer helium films adsorbed on the surface of graphite*, J. Low. Temp. Phys. 101 (1995), pp. 481–488.
[625] S.M. Winder, *Quartz crystal microbalance measurements of sliding friction of inert gas films on lead, copper, nickel, and graphene surfaces*, Ph.D. diss., North Carolina State University, Raleigh, NC, 2003.
[626] J. Krim and R.P. Behringer, *Friction, force chains and falling fruit*, Phys. Today 62 (2009), pp. 66–67.
[627] A.P. Merkle and L.D. Marks, *Comment on friction between incommensurate crystal*, Philos. Mag. Lett. 87(8) (2007), pp. 527–532.
[628] M. Kisiel, E. Gnecco, U. Gysin, L. Marot, S. Rast, and E. Meyer, *Suppression of electronic friction on Nb films in the superconducting state*, Nat. Mater. 10 (2011), pp. 119–122.
[629] J.N. Ding, Y.G. Meng, and S.Z. Wen, *The tribological properties of $YBa_2Cu_3O_7$ films in ambient environment*, Wear 250 (2001), pp. 311–317.

Appendix 1. Cumulative summary of slip time data

Table A.1. Cumulative slip time data.

Adsorbate	Preplate	Substrate	Technique	T (K)	Reference	τ (ns)					
						$\Theta = 0.2$	$\Theta = 0.5$	$\Theta = 1$ (liquid)	$\Theta = 1$ (solid)	$\Theta = 2$	$\Theta = 4 - 5$
N_2 (nitrogen)		Au(111)	QCM	77.4	[508]		3	4		8	
N_2 (nitrogen)		Au(111)	QCM	77.4	[176]			4		7	
Xe (xenon)		Au(111)	QCM	110	[508]	1.7	1.1	0.7			
Xe (xenon)		Au(111)	QCM	80	[33]				1.2	4	
Xe (xenon)		Au(111)	QCM	113.6	[33]		1	2		5	
Kr (krypton)		Au-amorp	hQCM	77.4	[404]			4	50	100	
$(CH_3C_6H_4)\cdot 3PO_4$ (TCP)		Cr	QCM	300	[155]		1	0.9		0.9	
$(CH_3C_6H_4)\cdot 3PO_4$ (TCP)		Cr	QCM	573	[155]	>0	>0	>0		>0	
$(CH_3C_6H_4)\cdot 3PO_4$ (TCP)		Cr	QCM	673	[155]	0	0		0	0	0
$(CH_3C_6H_4)\cdot 3PO_4$ (TCP)	O_2	Cr	QCM	573	[514]	0	0		0	0	0
$(CH_3C_6H_4)\cdot 3PO_4$ (TCP)		Cr	QCM	673	[514]	0	0		0	0	0
O_2 (oxygen)	TCP	Cr	QCM	573	[514]	0	0		0	0	
CO (carbon monoxide)		Cu	Resistivity		[447]		0.039(E)				
O_2 (oxygen)		Cu	Resistivity		[447]		0.007(E)				
C_6H_5I (iodobenzene)		Cu(111)	STM-QCM	300	[272]	0	0		0	0	0
C_6H_6 (benzene)		Cu(111)	STM-QCM	300	[272]			>0	>0		
C_8H_{18} (*n*-octane)		Cu(111)	QCM	300	[623]		1.5	0.9		0.8	
CH_3OH (methanol)	C60 monolayer	Cu(111)	QCM	300	[539]	10	7	3.6			
CH_3OH (methanol)	C60 rotating bilayer	Cu(111)	QCM	300	[539]	3	4	1.9			
Kr (krypton)		Cu(111)	QCM	77.4	[355]			7	11		
Kr (krypton)	C60 fixed bilayer	Cu(111)	QCM	77.4	[539]	10	4	3			
Kr (krypton)	C60 monolayer	Cu(111)	QCM	77.4	[539]	10	4	3			
Xe (xenon)		Cu(111)	QCM	77.4	[356]				15.5	30	
$(CH_3C_6H_4)\cdot 3PO_4$ (TCP)		Fe	QCM	300	[155]	2	1.75	1.75		1.5	
$(CH_3C_6H_4)\cdot 3PO_4$ (TCP)		Fe	QCM	380–450	[155]	>0	>0	>0		>0	
$(CH_3C_6H_4)\cdot 3PO_4$ (TCP)		Fe	QCM	500–673	[155]	0	0	0		0	0
$(CH_3C_6H_4)\cdot 3PO_4$ (TCP)		Fe	QCM	673	[514]	0	0		0	0	0
$(CH_3C_6H_4)\cdot 3PO_4$ (TCP)		Fe	QCM	573	[514]	0	0		0	0	0
$(CH_3C_6H_4)\cdot 3PO_4$ (TCP)	O_2	Fe	QCM	573	[514]	∼0.001	∼0.001		∼0.001	∼0.001	∼0.001
$(CH_3C_6H_4)\cdot 3PO_4$ (TCP)	O_2	Fe	QCM	673	[514]	∼0.001	∼0.001		∼0.001	∼0.001	∼0.001
O_2 (oxygen)	TCP	Fe	QCM	573	[514]	∼0.001	∼0.001		∼0.001	∼0.001	
^{4}He(helium)		Graphite	QCM	0.45	[486]				20	7,80	
^{4}He(helium)		Graphite	QCM	1.0	[486]				20	8,80	
^{4}He(helium)		Graphite	QCM	1.25	[486]				20	8.5,70	

(*Continued*)

Table A.1. Continued

Adsorbate	Preplate	Substrate	Technique	T (K)	Reference	τ (ns) $\Theta = 0.2$	$\Theta = 0.5$	$\Theta = 1$ (liquid)	$\Theta = 1$ (solid)	$\Theta = 2$	$\Theta = 4 - 5$
^{4}He(helium)		Graphite	QCM	1.5	[486]					9, 60	
^{4}He(helium)	^{4}He solid monolayer	Graphite	QCM	0.75	[486]			Inifinite			
^{4}He(helium)		Graphite	Torsion. Osc.	0.05–2	[624]					>0	
C_6H_6 (benzene)		Graphite	HeSE	140	[128]		0.00045				
^{4}He (helium)		Graphite	QCM	<4 K	[484,485]			>0			
Kr (krypton)		Graphite	QCM	85.8	[476]		0&60(C)		0&20 (IC)	10,300	
Kr (krypton)		Graphite	QCM	85.8	[476]		0&60(C)		0&60(C)		
^{3}He (helium)		Hectorite	QCM	0.5–2.0	[490]				>0		
^{3}He (helium)		Hectorite	QCM	0.15–4	[490]					>0	
^{3}He (helium)		Hectorite	QCM	0.15–4	[490]					>0	
^{3}He (helium)		Hectorite	QCM	0.5–2.5	[481]				>0		
CO (carbon monoxide)	Ni	Resistivity			[447]	0.014(E)					
H (hydrogen)		Ni	Resistivity		[447]		0.001(E)				
N_2 (nitrogen)		Ni	Resistivity		[447]		0.046(E)				
Kr (krypton)		Ni(111)	QCM	77.4	[355]			0.26	0.78		
Xe (xenon)	Graphene	Ni(111)	QCM	77.4	[356]		2		1.7		
Xe (xenon)		Ni(111)	QCM	77.4	[356]		0.4		0.47	0.2	
N_2 (nitrogen)		Pb	QCM	7.2	[510]				0		
C_8H_{18} (*n*-octane)		Pb(111)	QCM	300	[623]			0.6		0.9	
CO		Pb(111)	QCM	7.2	[492]	0	0		0		
H_2O (water)		Pb(111)	QCM	7.2	[420]			τ (SC)> τ (N)			
Kr (krypton)		Pb(111)	QCM	6.5	[491]	0	0		0	0	0
N_2 (nitrogen)		Pb(111)	Theory		[115,323]				2–20(E)		
N_2 (nitrogen)	Air	Pb(111)	QCM	77.4	[166]			1.5		1.2	2
N_2 (nitrogen)	Air	Pb(111)	Resistivity	7.2	[164]				1.3 (E)		
N_2 (nitrogen)		Pb(111)	QCM	9	[493]				0		
N_2 (nitrogen)		Pb(111)	QCM	15	[493]				0		
N_2 (nitrogen)		Pb(111)	QCM	19	[493]	0	0		0.05	0.12	
Ne (neon)		Pb(111)	QCM	5.4	[182]	0	0				
Ne (neon)		Pb(111)	QCM	6.5	[182]	0	0.08		0.3		
Ne (neon)	1–3 Xe monolayers	Pb(111)	QCM	6.5	[491]	1	5		8		
Ne (neon)	1–4 Kr monolayers	Pb(111)	QCM	6.5	[491]	0	1		7		
Ne (neon)		Pb(111)	QCM	6.5	[491]	0	1		3		

(*Continued*)

Table A.1. Continued

						τ (ns)					
Adsorbate	Preplate	Substrate	Technique	T (K)	Reference	$\Theta = 0.2$	$\Theta = 0.5$	$\Theta = 1$ (liquid)	$\Theta = 1$ (solid)	$\Theta = 2$	$\Theta = 4 - 5$
^{4}He(helium)		Pb(111)n.	QCM	7.2	[420]						76
^{4}He(helium)		Pb(111)n.	QCM	7.2	[420]						87
Ar (argon)		Pb(111)n.	QCM	10–15	[493]	0	0		0	0	0
D_2 (deuterium)		Pb(111)n.	QCM	10–15	[493]			>0			
Kr (krypton)		Pb(111)n.	QCM	10–15	[493]	0	0		0	0	0
N_2 (nitrogen)	Air	Pb(111)n.	QCM	7.2	[165]				12		
N_2 (nitrogen)		Pb(111)n.	QCM	7.2	[420]					19	
N_2 (nitrogen)		Pb(111)n.	QCM	7.2	[420]					140 (magnet)	
N_2 (nitrogen)		Pb(111)n.	QCM	12	[419]				0	0	
Ne (neon)		Pb(111)n.	QCM	7.2	[462]		2.5	<5			
O_2 (oxygen)		Pb(111)n.	QCM	7.2	[492]			τ(SC) > τ(N) > 0			
Xe (xenon)		Pb(111)n.	QCM	10–15	[493]	0	0		0	0	0
Xe (xenon)		Pb(111)n.	QCM	77.4	[625]				0.7		
^{4}He(helium)	Air	Pb(111)s.c.	QCM	4.2	[166]			20		10	18
^{4}He(helium)		Pb(111)s.c	QCM	7.2	[420]						196
^{4}He(helium)		Pb(111)s.c.	QCM	7.2	[420]						1538
N_2 (nitrogen)	Air	Pb(111)s.c	QCM	7.2	[165]				29		
N_2 (nitrogen)		Pb(111)s.c.	QCM	7.2	[420]					40	
N_2 (nitrogen)		Pb(111)s.c	QCM	7.2	[420]					1190 (magnet)	
N_2 (nitrogen)		Pb(111)s.c.	QCM	7.2	[419]			τ(SC) > τ(N)			
Ne (neon)	Air	Pb(111)s.c	QCM	5.75	[166]						?50
Ne (neon)		Pb(111)s.c.	QCM	7.2	[462]		2.5				
C_2H_5 (ethanol)		Si	QCM	300	[536]		4	8.5		9	
C_5H_{12} (pentanol)		Si	QCM	300	[536]		4	6		8	
CF_3CH_2OH (TFE)		Si	QCM	300	[536]		1	3.5		2	
$(CH_3C_6H_4)\cdot 3PO_4$ (TCP)	OTS	Si-amorph	QCM	300	[615]	0.05					0.48
$(CH_3C_6H_4)\cdot 3PO_4$ (TCP)		Si-amorph	QCM	300	[615]	0	0	0.1		0.9	0.9
TBBP	OTS	Si-amorph	QCM	300	[615]	0.1					0.24
TBBP		Si-amorph	QCM	300	[615]	0	0.05	0.1		0.3	0.3
PFPE	SiO_x/Si	Blowoff	300		[216]		0.0004				
$(CH_3C_6H_4)\cdot 3PO_4$ (TCP)		Si-poly	QCM	300	[615]	0	0	0.1		0.12	0.14
TBBP		Si-poly	QCM	300	[615]	0	0	0.2		0.25	